

**DEVELOPMENT OF NEW ORGANIC PROBES FOR
OPTICAL DETECTION OF METAL IONS:
SYNTHESIS, CHARACTERIZATION AND SENSING
STUDIES**

Thesis
submitted for the degree of
DOCTOR OF PHILOSOPHY (SCIENCE)
MARCH-2023

by

MR. SAMIK ACHARYYA



Department of Chemistry
Jadavpur University, Kolkata ~ 700 032
India



Date: 29/08/2023

CERTIFICATE FROM THE SUPERVISOR(S)

This is to certify that the thesis entitled “Development of new organic probes for optical detection of metal ions: Synthesis, characterization and sensing studies” submitted by Mr. Samik Acharyya, M.Sc., who got his name registered on 09.08.2019 for the award of Ph.D. (Science) degree of Jadavpur University, is absolutely based upon his own work under the supervision of Dr. Tapan Kumar Mondal and that neither this thesis nor any part of it has been submitted for either any degree / diploma or any other academic award anywhere before.

It is also certified that he has fulfilled all the requirements of the regulations relating to the nature and period of research.

Tapan K. Mondal
29/08/2023

Dr. Tapan Kumar Mondal (supervisor)

Dr. TAPAN KUMAR MONDAL
Professor
Department of Chemistry
Jadavpur University
Kolkata-700032

Signature of the Supervisor and date with official seal

“What is research but a blind date with knowledge?”

~Will Harvey.

Dedicated to

*My parents, my teachers, my
wife and close friends...*

ACKNOWLEDGEMENTS

In my life and its tiring fights, in the endless dawns until the twilight,

I glance to my friends, by my side and we hum as we trudge

: 'Friendship is the might..... friendship is the light...'

The long journey, perhaps too long, is at last coming to an end. There is no wonder in that. Everything has an end. An era ends just as quickly as does a second. But the wonder is the journey itself, in which I have experienced myriads of events and the feelings and the emotions attached with each one of them. There has been pain and elation, achievements and inaction, satisfaction and frustration, content and discontent, a few successes and lots of failures. But I did learn from every incident I experienced in my life as a research fellow. To me, my Ph.D. days are the second best days of my life. 'Second best' because, nothing can beat the school days as you all will agree.

Some of the people I have met during this time will each hold a special place in my heart. The foremost name to be mentioned will be my research supervisor Dr. Tapan Kumar Mondal, Professor, Department of Chemistry, Jadavpur University, Kolkata-700032. My head will always bow in front of him in a sense of veneration and gratitude. Countless thanks to him for allowing me to pursue my Ph.D. in his research group. He guided me like a captain of a ship through an ocean of problems and difficulties that I have faced throughout the course of my research work.

I would also like to express my gratitude to Dr. Deblina Sarkar, my ex-lab mate and a good friend, for helping me gain a foothold in the "chemosensor" field of research, Dr. Saswati Gharami for her friendship and immense help in every way possible and Dr. Lakshman Patra and Dr. Subrata Jana for sharing the same dreams together, no matter how hopeless they might seem and for ardent companionship during my time at the laboratory.

I express my gratitude to the faculty members of Department of Chemistry, Jadavpur University, Prof. Subratanath Koner, Head, Department of Chemistry, Prof. Subenoy Chakraborty, Dean of Science, JU, Prof. Saurabh Das, Section-In-Charge, Inorganic Chemistry Section and all other faculty members of Department of Chemistry, Jadavpur University. I am indebted to all the teaching as well as non-teaching staff members of this department and university for their help and support.

I express my affection and immense gratitude to all my past and present labmates namely, Dr. Ajoy Kr. Pramanik, Dr. Sujan Biswas, Subhankar Kundu, Dr. Puspendu Roy, Dr. Apurba Sau Mondal, Dr. Chandan Kumar Manna, Mr. Biswajit Bera, Mr. Akash Das, Mr. Rahul Naskar, Mr. Atanu Maji, Mr. Sandipan Mandal, Mr. Subrata Mondal, Mr. Amitav Biswas, Mr. Arpan Halder, Ms. Moumita Ghosh, Mr. Chandrasekhar Mandi and last but not the least, Dr. Krishnendu Aich for their constant help and support throughout my research journey. They made my research journey easier and very much enjoyable. I will always cherish in solitude, all the beautiful memories I have made with them.

I also express my reverence and gratefulness to all my teachers in school especially Amal kanti sir, Pranab Maji sir and Niranjana Sir, during my graduation, Dr. Murari Priya Roy sir, Dr. Tania Das, Dr. Hrishikesh Chatterjee sir and Dr. Satya Ranjan Ghosh sir and all my Post Graduation teachers Dr. Rana Sen, Dr. Dinabandhu Kundu and especially Dr. Nirmalendu Sasmal for the rigorous training in practical organic chemistry during my M.Sc. Thanks to all of them for igniting my passion towards chemistry.

I would like to thank my wife for encouraging me and not letting my morale down during the concluding part of my research life.

Lastly, but most importantly with all the gratitude in my heart I would like to thank my father Sri Swapan Kumar Acharyya and my mother Smt. Shefali Acharyya for their constant encouragement, support and unflinching belief in me and my abilities. I will forever try, though unsuccessfully, to love them as fiercely as they love me.



(Samik Acharyya)

Department of Chemistry,

Jadavpur University.

CONTENTS

	PAGE NUMBER
PREFACE	i-iv
CHAPTER 1	1-48
A COMPENDIOUS STUDY INTRODUCING FLUORESCENCE TECHNIQUE AND MOLECULAR SENSORS: THE WAY THEY SENSE IONIC ANALYTES.	
1.1 INTRODUCTION.	2
1.2. SUPRAMOLECULAR CHEMISTRY: FROM MOLECULES TO SUPER-MOLECULES.	3
1.3. BINDING WITH SELECTION: MOLECULAR RECOGNITION.	3-4
1.4. CHEMOSENSORS AND CHEMOSIMETERS: WHAT THEY ARE?	5-6
1.4.1. TYPES AND SUB-TYPES OF CHEMOSENSORS: A CLASSIFICATION	5
1.4.2. OPTICAL CHEMOSENSORS	6
1.5. FLUORESCENCE TECHNIQUE: A ROBUST TECHNIQUE FOR DESIGNING CHEMOSENSORS.	6-22
1.5.1. JABLONSKI DIAGRAM: EXCITED STATE OF THE RECEPTOR MOLECULE	7-8
1.5.2. DIFFERENT FLUORESCENCE ENHANCING AND QUENCHING PROCESSES	8-18
1.5.3. TYPES AND MECHANISM OF FLUORESCENCE QUENCHING PROCESSES	18-22
1.6. CHEMICAL FORCES BEHIND HOST-GUEST BINDING: NON-COVALENT INTERACTIONS.	22-26
1.6.1 COULOMBIC INTERACTIONS	22-23
1.6.2. HYDROGEN BONDING	23-24
1.6.3. π - π STACKING	24-25
1.6.4. VAN DER WAALS FORCE	25-26
1.7. AN IDEAL CHEMOSENSOR AND DIFFERENT APPROACHES TO DESIGN ONE.	27-36
1.7.1. CRITERIA OF DESIGNING AN IDEAL	27-28

	CHEMOSENSOR	
	1.7.2. DIFFERENT SCHEMES IN DESIGNING A CHEMOSENSOR	28-35
	1.8. APPLICATIONS OF CHEMOSENSORS AS OPTICAL BIOSENSORS, IN LIVE-CELL IMAGING AND MOLECULAR LOGIC GATES.	35-42
	1.8.1. APPLICATION AS OPTICAL BIOSENSORS	36-37
	1.8.2. APPLICATION IN LIVE CELL IMAGING	37-39
	1.8.3. APPLICATION IN CONSTRUCTION OF MOLECULAR LOGIC GATES	39-41
	1.9. AIM OF THE THESIS	42
	1.10. REFERENCES	42-48
CHAPTER 2	INSTRUMENTATIONS AND TECHNIQUES	49-66
	2.1. INTRODUCTION	50
	2.2. METHODS OF CHARACTERIZATION	50-58
	2.2.1. HIGH RESOLUTION MASS SPECTROMETRY (HRMS) AND ELEMENTAL ANALYSIS	50-51
	2.2.2. INFRARED SPECTROSCOPY (IR)	51
	2.2.3. ¹H NMR SPECTROSCOPY	52-54
	2.2.4. ¹³C NMR SPECTROSCOPY	54
	2.2.5. UV-VIS ABSORPTION SPECTROSCOPY	54-55
	2.2.6. FLUORESCENCE SPECTROSCOPY	55-57
	2.2.7. FLUORESCENCE LIFETIME MEASUREMENT	57
	2.2.8. SINGLE CRYSTAL X-RAY DIFFRACTION TECHNIQUE	58
	2.3. INSTRUMENTATION SEGMENT OF THE SPECTROSCOPIC TECHNIQUES	59-63
	2.3.1. NMR TECHNIQUE	59
	2.3.2. IR TECHNIQUE	59-60
	2.3.3. HRMS TECHNIQUE	60-61
	2.3.4. UV-VIS TECHNIQUE	61-62
	2.3.5. FLUORIMETRY	62
	2.3.6. FLUORESCENCE LIFETIME TECHNIQUE	63
	2.4. SOME ESSENTIAL ANALYTICAL METHODS TO STUDY THE CHEMOSENSORS	64-66
	2.4.1. QUANTUM YIELD MEASUREMENT	64
	2.4.2. CALCULATION OF BINDING CONSTANT OF	64

	SYNTHESIZED LIGAND	
	2.4.3. DETERMINATION OF LIMIT OF DETECTION OF SYNTHESIZED CHEMOSENSORS	65
	2.5. REFERENCES	65-66
CHAPTER 3	AN EFFICIENT FLUORESCENCE “TURN-ON” CHEMOSENSOR COMPRISING OF COUMARIN AND RHODAMINE MOIETIES FOR AL³⁺ AND Hg²⁺	67-89
	3.1. INTRODUCTION	69
	3.2. BASIS OF PRESENT WORK	69
	3.3. RESULTS AND DISCUSSIONS	70-79
	3.3.1. SYNTHESIS OF HL	70
	3.3.2. SPECTRAL CHARACTERIZATION AND ANALYSIS OF HL	70-71
	3.3.3. CATION SENSING STUDIES: UV-VIS SPECTROSCOPY STUDIES	71-72
	3.3.4. CATION SENSING STUDIES: FLUORESCENCE EMISSION STUDIES	73-75
	3.3.5. BINDING STUDIES OF HL WITH AL ³⁺ AND Hg ²⁺	75-76
	3.3.6. EFFECT OF PH ON EMISSION PROPERTIES	76-77
	3.3.7. PROBABLE SENSING MECHANISM	77
	3.3.8. DFT CALCULATIONS	78-79
	3.4. EXPERIMENTAL	79-81
	3.4.1. MATERIALS AND METHODS	79-80
	3.4.2. SYNTHESIS OF THE RECEPTOR HL	80
	3.4.3. GENERAL METHOD FOR UV-VIS AND FLUORESCENCE TITRATION	81
	3.4.4 COMPUTATIONAL METHODS	81
	3.5. CONCLUSIONS	81-82
	3.6. REFERENCES	82-84
	APPENDIX	85-89
CHAPTER 4	A THIOETHER CONTAINING REVERSIBLE FLUORESCENCE “TURN-ON” CHEMOSENSOR FOR SELECTIVE DETECTION OF ZINC(II): APPLICATIONS IN LIVE CELL IMAGING AND INHIBIT LOGIC GATE.	90-125
	4.1. INTRODUCTION	92
	4.2. BASIS OF PRESENT WORK	93
	4.3. RESULTS AND DISCUSSIONS	93-107

4.3.1. SYNTHESIS OF H ₂ L	93-94
4.3.2. SPECTRAL CHARACTERIZATION AND ANALYSIS OF H ₂ L	94
4.3.3. CATION SENSING STUDIES: UV-VIS SPECTROSCOPY STUDIES	94
4.3.4. CATION SENSING STUDIES: FLUORESCENCE EMISSION STUDIES	95-98
4.3.5. BINDING STUDIES WITH H ₂ L AND ZN ²⁺ AND DETECTION LIMIT OF H ₂ L	98-100
4.3.6. LIFETIME DECAY PROFILE OF THE RECEPTOR H ₂ L	100-101
4.3.7. PH STUDY	101-102
4.3.8. APPLICATION AS LOGIC GATE	102-103
4.3.9. PROBABLE SENSING MECHANISM	103-104
4.3.10. MOLECULAR CRYSTAL STRUCTURE OF H ₂ L COMPLEX	104
4.3.11. ELECTRONIC SPECTRA AND DFT CALCULATION	105
4.3.12. CELL BIO-IMAGING	106-107
4.4. EXPERIMENTAL	107-112
4.4.1. MATERIALS AND METHODS	107-108
4.4.2. SYNTHESIS OF THE RECEPTOR H ₂ L	108
4.4.3. GENERAL METHOD FOR UV-VIS AND FLUORESCENCE TITRATION	108-110
4.4.3.1. RECORDING ABSORPTION SPECTRA	108
4.4.3.2. RECORDING EMISSION SPECTRA	109
4.4.3.3. JOB'S PLOT BY FLUORESCENCE METHOD	109
4.4.3.4. DETERMINATION OF FLUORESCENCE QUANTUM YIELDS (Φ) OF H ₂ L AND ITS ZN ²⁺ COMPLEX	109
4.4.3.5. DETERMINATION OF DETECTION LIMIT	110
4.4.3.6. DETERMINATION OF BINDING CONSTANT FROM FLUORESCENCE TITRATION DATA	110
4.4.4. COMPUTATIONAL METHOD	110-111
4.4.5. LIVE CELL IMAGING	111
4.5.6. CRYSTALLOGRAPHIC STUDIES	111
4.5. CONCLUSIONS	112

	4.6. REFERENCES	113
	APPENDIX	116-125
CHAPTER 5	NOVEL PYRIDYL BASED AZO-DERIVATIVE FOR THE SELECTIVE AND COLORIMETRIC DETECTION OF NICKEL(II)	126-149
	5.1. INTRODUCTION	128
	5.2. BASIS OF PRESENT WORK	128
	5.3. RESULTS AND DISCUSSIONS	129-137
	5.3.1. SYNTHESIS OF H₂L	129
	5.3.2. SPECTRAL CHARACTERIZATION AND ANALYSIS OF H₂L AND H₂L-Ni²⁺	129-130
	5.3.3. CATION SENSING STUDIES: UV-VIS SPECTROSCOPY STUDIES	130-135
	5.3.4. ELECTRONIC SPECTRA AND DFT CALCULATION	135-137
	5.4. EXPERIMENTAL	137-140
	5.4.1. MATERIALS AND METHODS	137
	5.4.2. SYNTHESIS OF THE RECEPTOR H₂L	137-138
	5.4.3. SYNTHESSES OF THE H₂L-Ni²⁺ COMPLEX	138
	5.4.4. GENERAL METHOD FOR UV-VIS STUDIES	138-140
	5.4.4.1. UV-VIS METHOD	139
	5.4.4.2. JOB'S PLOT BY UV-VIS METHOD	139
	5.4.4.3. DETERMINATION OF DETECTION LIMIT	139
	5.4.4.4. DETERMINATION OF ASSOCIATION CONSTANT	139
	5.4.5. COMPUTATIONAL METHOD	140
	5.5. CONCLUSIONS	140
	5.6. REFERENCES	140-142
	APPENDIX	143-149
CHAPTER 6	A NEW COUMARIN-BASED "TURN-ON" PROBE FOR THE SELECTIVE AND DISTINCT FLUORESCENCE RESPONSE TOWARDS AL³⁺	150-180
	6.1. INTRODUCTION	152-153
	6.2. BASIS OF PRESENT WORK	153
	6.3. RESULTS AND DISCUSSIONS	154-165
	6.3.1. SYNTHESIS OF HMBH	154

6.3.2. SPECTRAL CHARACTERIZATION AND ANALYSIS OF HMBH	154-155
6.3.3. CATION SENSING STUDIES: UV-VIS SPECTROSCOPY STUDIES	155
6.3.4. CATION SENSING STUDIES: FLUORESCENCE EMISSION STUDIES	155-157
6.3.5. BINDING STUDIES OF HMBH WITH Al^{3+}	157-161
6.3.6. EFFECT OF PH ON EMISSION PROPERTIES	161-162
6.3.7. DIP-STICK EXPERIMENT: DETECTION OF Al^{3+} USING TLC PLATE	162-163
6.3.8. PROBABLE SENSING MECHANISM	163-164
6.3.9. DFT CALCULATIONS	164-165
6.4. EXPERIMENTAL	165-168
6.4.1. MATERIALS AND METHODS	165-166
6.4.2. SYNTHESIS OF 2-HYDROXYBENZOHYDRAZIDE (1)	166
6.4.3. SYNTHESIS OF (E)-2-HYDROXY-N'-((4-HYDROXY-2-OXO-2H-CHROMEN-3-YL)METHYLENE)-BENZOHYDRAZIDE (HMBH)	167
6.4.4. GENERAL METHOD FOR UV-VIS AND FLUORESCENCE TITRATION	167-168
6.4.4.1. UV-VIS METHOD	167
6.4.4.2. FLUORESCENCE METHOD	167
6.4.4.3. JOB'S PLOT BY FLUORESCENCE METHOD	168
6.4.5. COMPUTATIONAL METHODS	168
6.5. CONCLUSIONS	168-169
6.6. REFERENCES	169-172
APPENDIX	173-180
CHAPTER 7	
A NEW ESIPT-ICT MEDIATED DUAL CHANNEL FLUORESCENCE "TURN-ON" SWITCH FOR SELECTIVE AND SEQUENTIAL DETECTION OF Zn^{2+}	181-212
7.1. INTRODUCTION	183-184
7.2. BASIS PRESENT WORK	184
7.3. RESULTS AND DISCUSSIONS	185-193
7.3.1. SYNTHESIS OF HBSA	185
7.3.2. SPECTRAL CHARACTERIZATION AND ANALYSIS OF HBSA	185-186

7.3.3. CATION SENSING STUDIES: UV-VIS SPECTROSCOPY STUDIES	186-187
7.3.4. CATION SENSING STUDIES: FLUORESCENCE EMISSION STUDIES	187-189
7.3.5. BINDING STUDIES OF HBSA WITH Zn^{2+}	189-190
7.3.6. EFFECT OF PH ON EMISSION PROPERTIES	191
7.3.7. PROBABLE SENSING MECHANISM	191-192
7.3.8. DFT CALCULATIONS	192-193
7.4. EXPERIMENTAL	193-196
7.4.1. MATERIALS AND METHODS	193
7.4.2. SYNTHESIS OF (E)-4-(HYDRAZONO(PHENYL)METHYL)BENZENE-1,3-DIOL (1)	193-194
7.4.3. SYNTHESIS OF 4-((Z)-((E)-4-(DIETHYLAMINO)-2-HYDROXYBENZYLIDENE) - HYDRAZONO) (PHENYL) METHYL)BENZENE-1,3-DIOL (HBSA)	194-195
7.4.4. GENERAL METHOD FOR UV-VIS AND FLUORESCENCE TITRATION	195-196
7.4.4.1. UV-VIS METHOD	195
7.4.4.2. FLUORESCENCE METHOD	195
7.4.4.3. JOB'S PLOT BY FLUORESCENCE METHOD	195-196
7.4.5. COMPUTATIONAL METHODS	196
7.5. CONCLUSIONS	196
7.6. REFERENCES	197-203
APPENDIX	204-212
LIST OF PUBLICATION	213

PREFACE

PREFACE

The present research work of designing and synthesizing novel colorimetric and fluorescence chemosensors has found a prominent place in modern research. The area of this research field lies at the interface of many different research fields such as chemistry, physics, biology, environmental sciences and Medicine etc. A chemosensor or a molecular sensor is a compound, a molecule of which is capable of detecting a specific analyte by identifying and attributing changes in one or more of its properties, such as absorption, emission etc. The field has been recently found to have biological applications as in live cell imaging which helps in the purpose of detection of certain ions and analytes in various cancer cells. The current field has some applications in modern drug delivery systems too.

As the name suggests, the submitted thesis work entitled, **“Development of new organic probes for optical detection of metal ions: Synthesis, characterization and sensing studies”** contains novel design and synthesis of several colorimetric and fluorescence chemosensor molecules with rigorous spectral studies and binding studies with respect to the particular ionic analyte along with other coexisting ionic analytes. These newly fabricated molecules have been found to behave as chemosensors for certain environmentally and biologically important ionic analytes. Thorough spectral study viz. HRMS, IR- Studies, ^1H as well as ^{13}C NMR, UV-Vis and fluorescence has helped in determining the structure of the receptor and by various analytical studies the binding of the receptors and the ions has also been confirmed. Biological application of these molecules as bio-markers in live-cell imaging studies has also been investigated. This thesis consists of seven chapters based on the design, synthesis, spectral characterization and spectral study of sensing properties of the novel molecular sensors. Theoretical calculations based on Density Function Theory have often been used to ascertain the sensing mechanism of these chemosensors. A few of them also has been found to have application as molecular logic-gates.

PREFACE

Chapter 1 serves as a brief introduction to the basic concepts of the present research work. It gives the basic definition of a chemosensor along with its classification. It explains the basic concept of different non-covalent forces involved in host-guest binding. The necessary criteria for the designing of molecular probes are also incorporated in this chapter. A concise literature survey of various reported chemosensors based on several molecular mechanisms have been discussed elaborately.

Chapter 2 is about the instruments and methods that were used during the course of the present research work. It serves as a brief description of instrumented procedures such as HRMS, IR, ^1H , ^{13}C NMR, UV-Vis, fluorescence detection, lifetime decay measurement, crystallography etc. In this chapter, basic theory behind some of the relevant analytical procedures are also illustrated, such as measuring the limit of detection of the chemosensor, calculation of quantum yield and also derivation of association constant or binding constant.

Chapter 3 briefly describes the synthesis and characterization of a fluorescence “turn-on” receptor (HL) for both Al^{3+} and Hg^{2+} ions. The receptor is based on Rhodamine and coumarin moieties. The absorption, emission properties and cation sensing properties have been studied thoroughly. The structure has been optimized by computational methods and TDDFT and DFT calculations have also been done.

Chapter 4 demonstrates the design, synthesis and characterization of a thioether containing fluorescence “turn-on” probe (H_2L) for the selective detection of Zn^{2+} in DMSO:water, 1:5 medium. The probe may be used reversibly and an INHIBIT logic gate was constructed using Zn^{2+} and EDTA as the chemical inputs. The chapter also contains live-cell imaging studies using the ligand H_2L , Zn^{2+} solution and MCF-7 cell line.

PREFACE

Chapter 5 presents a selective colorimetric chemosensor for Ni^{2+} ion, based on a pyridyl azo derivative and its synthesis, characterization, photo-physical properties and various cation sensing studies. DFT and TDDFT calculations also have been done to ascertain its structure and spectral tendencies.

Chapter 6 introduces the fabrication of a new coumarin-based “turn-on” probe HMBH for the selective and distinct fluorescence response towards Al^{3+} along with its synthesis, characterization and cation sensing studies. The fluorescence “turn-on” probe upon binding selectively with Al^{3+} shows a great fluorescence enhancement at $\lambda_{\text{max}} = 456 \text{ nm}$. DFT and TDDFT computations have also been done to obtain the optimised structure of the ligand and the metal complex and their spectral properties.

Chapter 7 illustrates the synthesis, characterization, spectral studies, cation sensing studies of a novel fluorescence “Turn-on” probe (HBSA) for the selective detection of Zn^{2+} ion. Fluorescence titration clearly states that HBSA upon binding with Zn^{2+} shows an emission peak at 529 nm with slight blue shift in emission intensity. The limit of detection is in the order of 10^{-9} M for Zn^{2+} which clearly indicates high efficiency of HBSA in detecting Zn^{2+} ion. Electronic structure and sensing mechanism have been interpreted by DFT and TDDFT calculations.

To describe in a nutshell, the present thesis deals with the synthesis and characterization of a few novel organic molecules which have the capability to recognize and bind selectively with certain environmentally and biologically important metal ions along with the receptors’ application in live cell imaging and also in construction of molecular logic gates. I would like to note that few of these works have already been published in reputed international journals, a list of which has been given at the end of this thesis.

PREFACE

In keeping with the general practice, due acknowledgement through proper citation has been made while reporting facts and scientific observations, whenever the findings of other investigators is used. I further proclaim that I am responsible for any unintentional error or lacunae in this thesis and any such error is deeply regretted. I hope it will not fail to intrigue its readers.

Samik Acharyya
(Samik Acharyya)

Department of Chemistry

Jadavpur University

A compendious study introducing
fluorescence technique and
molecular sensors: the way they
sense ionic analytes.

CHAPTER 1

1.1. Introduction

Although the chemists knew about coordination compounds since 18th century but any satisfactory theory was unavailable that could explain the observed properties of these compounds. The foundation stone was laid by Alfred Werner with his pioneering theory, published in 1893 based on which scientists and researchers could carry out their research. The field of coordination chemistry then branched off countless times into a plethora of various research fields including the one relevant here, 'coordination chemistry of artificial molecular sensors and chemoreceptors'. In fact, after the development of the supramolecular chemistry in the late 1970s and the path breaking work of Pedersen, Cram and Lehn, a systematic research pattern for the fabrication of metal ion receptors was established. Although the coordination chemistry, as we know it, is mostly related to transition metals, the current field is not only limited to chemoreception of transition-metal ions but extends to various other metal ions like- Al, Zn, Hg, Cu, Ni etc. that are relevant in environmental science and human biology in some way or the other. A variety of probes has been fabricated in recent history of research in this field that can detect any particular analyte. But the search is always on, for a probe with even lower limit of detection, lower cost for synthesis and better thermodynamic and kinetic aspect of the binding reaction between the probe and the analyte. Therefore, in recent years, requirement for designing chemosensors for fast, on-time and cost-effective monitoring of environmental samples has seen a constant increase over time. The area of the field of research on chemosensors has expanded exponentially in terms of funding, numbers of papers published and the number of active researchers worldwide. In comparison with the traditional analytical tools and methods chemical sensors are portable, simple to use, works in-situ and most importantly can detect analytes at much lower concentrations. [1,2] These features enable chemosensors to carry about real-time measurements and the errors occurring possibly due to sample transportation and sample storage can be greatly minimized [3].

CHAPTER 1

1.2 Supramolecular chemistry: From molecules to super-molecules.

As it was proposed by J. M. Lehn, supramolecular chemistry can be subtitled as the “chemistry beyond the molecules”. Its main focus has always been on the chemical systems containing a number of non-covalent assemblies of molecular subunits or components and their steric and stereoelectronic aspects. The objects of interest in supramolecular chemistry are supramolecular entities or “supermolecules” possessing features similar to those of the constituent molecules themselves. It can be said that molecules are to supermolecules what atoms are to molecules and that the non-covalent interactions are to supermolecules what covalent bonds are to molecules. So, just like the fact that molecular chemistry is based on the covalent bond formation, supramolecular chemistry is reliant on the weaker and reversible non-covalent interactions between molecules. Supramolecular assemblies have microscopic organization with macroscopic characteristics in them viz. mesomorphic phases, solid state structures, films, layers, membranes, vesicles, micelles etc. [4] Nature has many quintessential examples of the various structures, properties and functions, which can be achieved by supramolecular systems. The concept of supramolecular chemistry gives wings to the idea of molecular recognition.

1.3. Binding with selection: Molecular recognition.

Molecular recognition is a phenomenon that is quite common in various biological processes. It is also common in chemistry and material sciences. [5] Molecular recognition can be defined by the selective binding of a certain molecule or a certain ionic analyte with a receptor through non-covalent interactions like hydrogen bonding, π - π interactions, hydrophobic forces, van der Waals forces and ligand-metal coordination, the last one being the most relevant here. [6] Molecular recognition forms the basis of development of a chemosensor. It is one of the two major processes that occur during detection of an analyte by a chemosensor molecule. The other one being signal transduction. On the basis of this the overall structure of a chemosensor can be imagined to be an

CHAPTER 1

ensemble of three components- a receptor, a transducer unit and a spacer. The role of the receptor is to selectively bind with an analyte. The role of the transducer is to send a signal upon binding of receptor and specific analyte. And the role of the spacer is to work as a stereo-electronic link between the two. In molecule recognition the receptor probe is also denominated as ‘the host’ and the analyte is called ‘the guest’ and the binding event is often termed as ‘host-guest interaction’. [7] The molecular recognition is dependent upon the shape, size, chemical properties and electronic requirements of the host and the guest. [8]

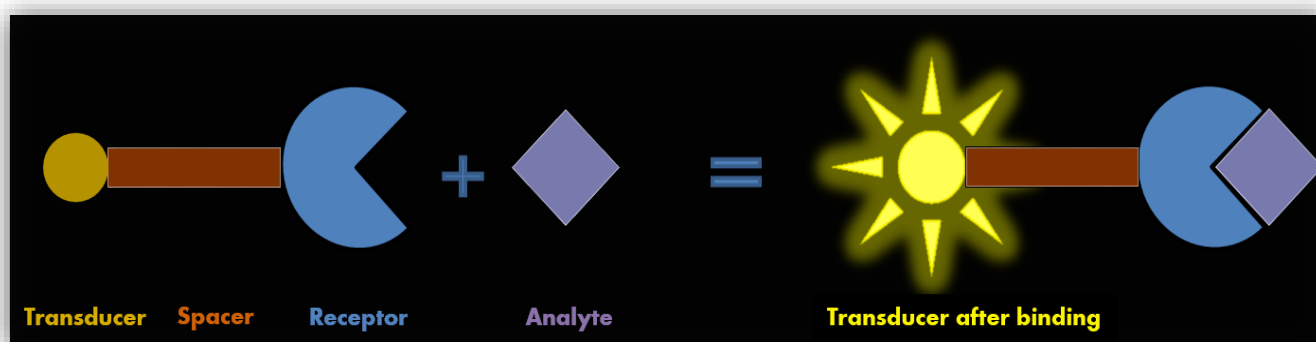
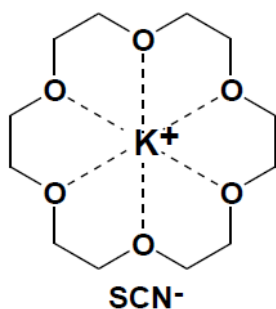
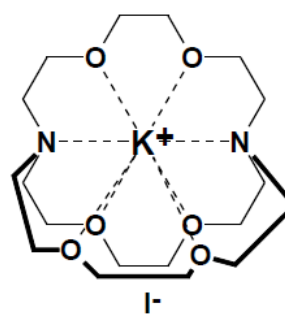


Fig. 1.3.1: The binding event or Host-Guest Interaction

In his pioneering work C. J. Pederson first introduced the concept of molecular recognition. [9] Pederson created crown ether macrocycles and then Lehn synthesized macrobicyclic ethers to bind and recognize cationic and anionic species, molecules etc. [10] Thus the “Host-Guest” chemistry started its journey with the crown ether serving as a molecular host to the cationic guests. [11]



Macrocyclic ether: Pedersen



Macrobicyclic ether: Lehn

Fig.

1.3.2:

The Macrocyclic and macrobicyclic ethers designed by Pederson and Lehn.

CHAPTER 1

1.4. Chemosensors and chemodosimeters: what they are?

Chemosensors are basically synthesized molecules that can bind with certain analytes selectively, reversibly, quickly and strongly enough which is accompanied by a concurrent change in one or more properties (viz. redox potential, absorption or fluorescence emission spectra) that can be monitored through an instrument or naked eye. [12,13] Based on the nature of change in properties of the binding molecule the chemosensors are termed as redox chemosensors or optical chemosensors etc.

1.4.1. Types and sub-types of chemosensors: a classification.

The classification of chemosensors can be done in a number of ways (Fig 1.4.1). According to their *modus operandi* the transducers may be stratified into two major groups: (i) “physical” and (ii) “chemical” sensors. They can also be classified into sub groups such as electrochemical, optical, electrical, magnetic, mass sensitive and thermometric indicating the type of change associated with the detection. [14] There can be two types of optical chemosensors, when they are broadly classified on the basis of the change occurring after the addition of the chemical species or analyte (viz. metal ion) to the receptor molecule. When the probe, acting as an indicator dye undergoes an absorption spectral change in the visible region of the electromagnetic spectra upon binding with the analyte, it is called a colorimetric chemosensor. The probe is called a fluorescence chemosensor when it undergoes a change in its fluorescence emission spectra upon binding with the analyte.

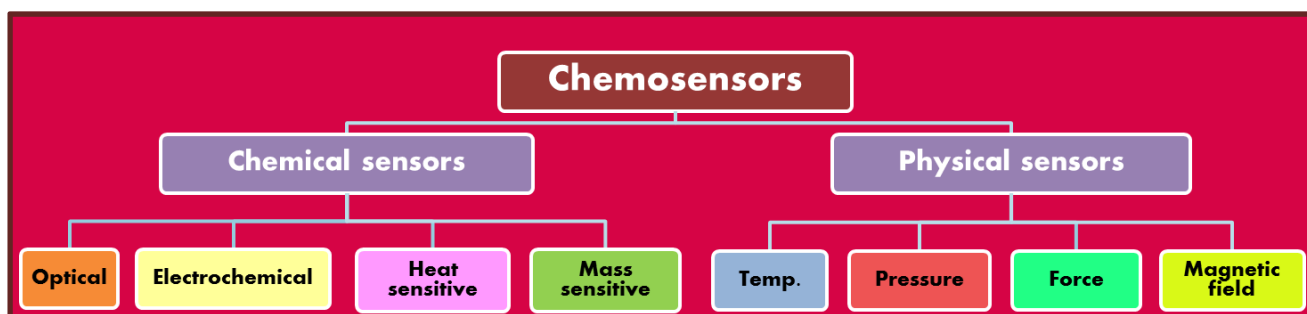


Fig. 1.4.1: Classification of sensors

CHAPTER 1

1.4.2. Optical chemosensors

Our main area of focus is concerned with optical chemosensors which, as we previously proposed, consists of a few important elements 1) The receptor part, 2) The Spacer and 3) The transducer part. The receptor part is also called the recognition element and it is the part where identification of the analyte takes place upon its selective binding. The role of the transducer part or element is to send upon recognition, an optical signal that is detectable by a detector instrument. To design an efficient optical sensor a few criterions should be kept in mind-

- a) The optical signal given out by the transducer part should have high signal-to-noise ratio.
- b) There should be a considerable change of signal upon exposure to the analyte.
- c) The material or compound acting as sensor should be chemically stable.
- d) The indicator should be unreactive under uv-vis light.
- e) It is desirable that the sensor material does not get destroyed or change irreversibly upon reacting with the analyte.
- f) The chemicals and the materials used to synthesize the sensor should be cost effective.
- g) The sensor should be able to bind with the analyte quickly enough for real-time detection.
- h) The fabrication of the sensor should be done with resources having minimal chemical hazard.

One can easily understand that meeting all these criteria together in a single optical chemosensor is a near impossible task and many of the existing ones have one or more limitations. Hence, there is always room at the top and the chemosensor research still thrives on this quest for designing the perfect one for each individual analyte.

1.5. Fluorescence Technique: a robust technique for designing chemosensors.

Chemosensors based on fluorescence technique shows reliable results even when performed in varied conditions and with excellent reproducibility. Fluorescent receptors often show improved

CHAPTER 1

sensitivity which makes them capable of detection in minute levels. These chemosensors commonly show great selectivity towards the specific analyte because it is highly unlikely that the other co-existing analytes would have same effects on the fluorescence properties of the receptor as the target analyte. [15-18] There can be broadly two types of receptors based on fluorescence technique one is the on/off type in which only the complexed or the non-complexed species is fluorescent and another is the type where a significant change is observed in its emission pattern such as wavelength, intensity etc. The on/off type can be divided into two sub-types one is called “Turn-On” where fluorescence is turned on upon complexation with the specified analyte and the other is called “Turn-Off” where fluorescence of the receptor is quenched upon complexation with the analyte. The turning on and quenching of the fluorescence can also occur due to some kind of irreversible chemical change occurring upon addition of the analyte [19]. In fluorescence technique we can also measure the lifetime of the fluorescence excited states, polarization and energy transfer.

1.5.1. Jablonski diagram: Excited state of the receptor molecule.

Jablonski diagram is a schematic diagram showing the various energy transfer and relaxation processes which occur in the time hiatus between absorption and emission or non-emission of light energy. The several molecular processes which occur in the excited state of the molecule are explained by this diagram [20]. The Jablonski diagram is shown in Fig. 1.5.1. The symbols S_0 , S_1 and S_2 represent the singlet ground electronic state, the first, and the second singlet excited electronic states respectively. While belonging to a particular electronic energy state, a fluorophore may exist in a range of vibrational energy levels, denoted by 0, 1, 2 etc. Since electronic transitions are very fast compared with nuclear motions according to Frank-Condon principle, the displacement of the nucleus becomes insignificant during electronic transitions. At room temperature most of the molecules populate the lower vibrational states, if not the lowest, of the electronic ground state. When the fluorophore molecules at S_0 absorb light, they are excited to the higher vibrational levels of either S_1 or S_2 . Internal conversion or IC of the excited state happens when molecules undergo transition from S_2 to S_1 . Fluorescence is the emission of light energy during transition from the S_1 to S_0 state. Conversion from singlet spin state S_1 to triplet spin state T_1 is called intersystem crossing or ISC. Low intensity emission of long-duration during conversion from the triplet excited state, T_1 to

CHAPTER 1

singlet ground state S_0 is termed as phosphorescence. The rate constant for triplet to singlet emission i.e., phosphorescence are much smaller than that for fluorescence because this transition is spin-forbidden.

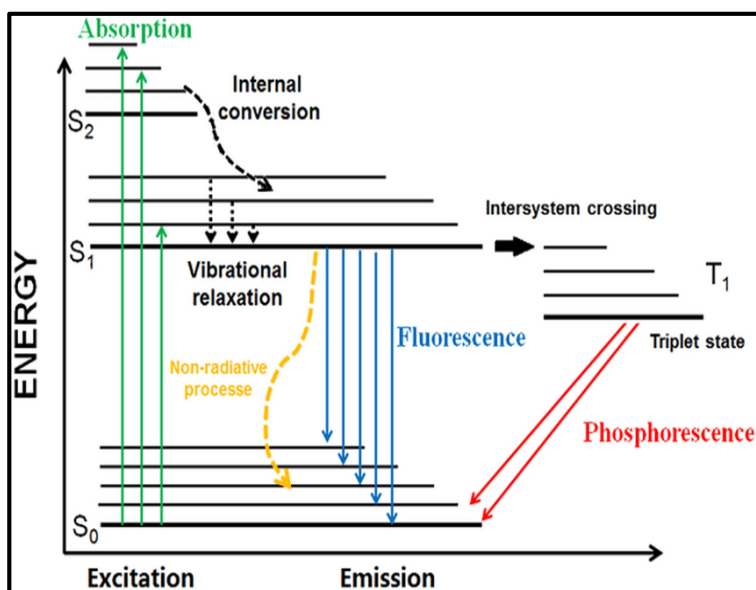


Fig. 1.5.1. Jablonski diagram: Energy transfer and relaxation processes occurring in the excited state of the molecule.

1.5.2. Different fluorescence enhancing and quenching processes.

Various fluorescence enhancing and fluorescence quenching processes play an important role in shaping the final emission pattern of the receptor molecule and the host-guest complex. In this segment these processes are briefly described.

1.5.2.1. Fluorescence resonance energy transfer (FRET)

Fluorescence resonance energy transfer process is the intermolecular dipole-dipole coupling mediated transfer of energy from an excited molecular fluorophore (Donor) to another ground state fluorophore (Acceptor) [21] (Fig. 1.5.2). The extent of energy transfer is proportional to the extent of spectral overlap between the absorption curve of the acceptor fluorophore and the emission curve of

CHAPTER 1

the donor (Fig. 1.5.3). The spectral overlap is given by the Förster distance and the rate of energy transfer $k_t(r)$ is follows

$$k_t(r) = (1/\tau_d)(R_0/r)^6$$

where 'r' is the distance between the donor (*D*) and acceptor (*A*) and ' τ_d ' is the lifetime of the donor in absence of energy transfer. The extent of energy transfer also depends on the distance *r*. Jablonski diagram shown in Fig. 1.5.2 represents the FRET process ($D^* + A \rightarrow D + A^*$).

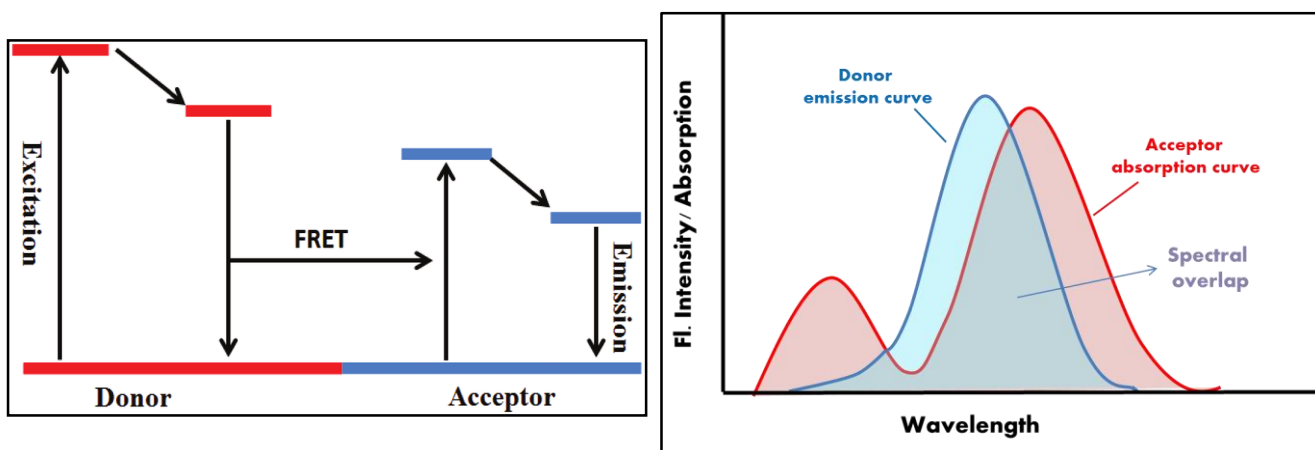


Fig. 1.5.2: Jablonski diagram showing FRET and Fig. 1.5.3: Spectral overlap.

In the year 2010 Jian-Fa Zhu et. al. reported a FRET based fluorescence chemosensor containing spiropyran and 8-amino quinoline moieties. The fluorescence turn-on is explained on the basis of CHEF (Chelation Enhanced Fluorescence) and FRET relay between the two fluorophore moieties of the receptor. FRET occurs in this sensing molecule by excitation of the quinoline unit at 370 nm. Following an increase in the concentration of Zn^{2+} , the low frequency fluorescent peak at 645 nm enhances with concurrent reduction of its high frequency fluorescent peak at 470 nm (associated with the quinoline moiety). A distinctive isosbestic point at 570 nm is evident from fluorescence titration curve. [22]

CHAPTER 1

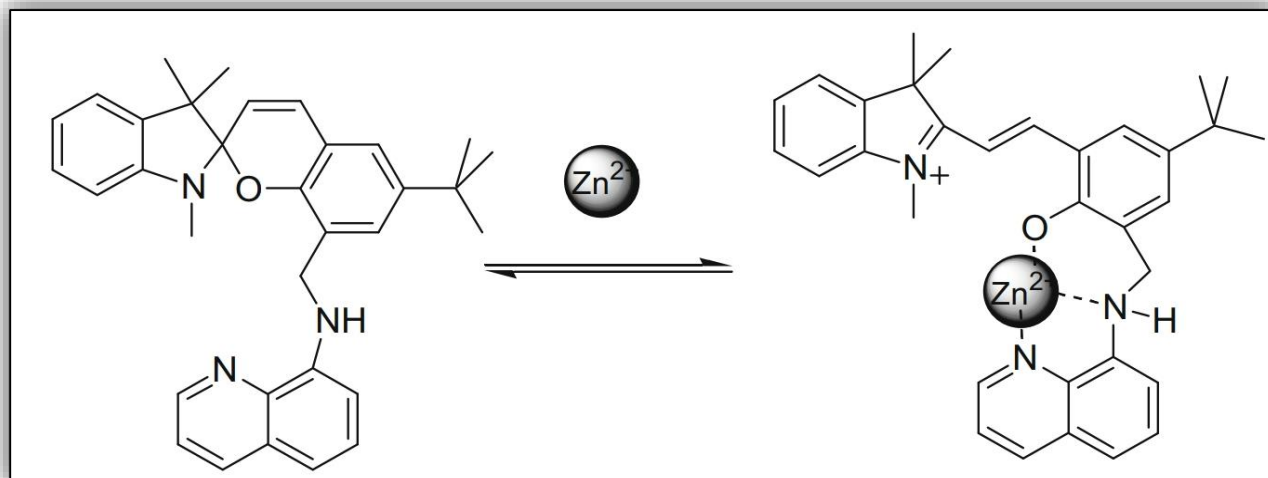


Fig. 1.5.4: complexation of Zn^{2+} with the spiropyran-quinoline receptor (Jian-Fa Zhu et. al.)

After a few years in 2014, another receptor based on dual fluorophore units, namely dansyl and rhodamine B, was reported by Jingyu Piao et. al. In this receptor the sensing mechanism of $Fe(III)$ ions has been attributed to the ‘off-on’ FRET occurring between the donor dansyl unit and the rhodamine unit as the acceptor. Significant spectral overlap between the emission spectra of the dansyl moiety (broad emission band at 450-600 nm) and absorption spectra of the rhodamine B moiety after binding with Fe^{3+} is evident from the experimental results. This FRET turn-on may be a resultant factor due to the spirolactam ring opening associated to complexation of rhodamin receptor with the Fe^{3+} ion. Excitation at 420 nm gives rise to an intense emission peak at 578 nm and a comparatively weak one at about 507 nm in the fluorescence spectrum of the Fe^{3+} complex. [23]

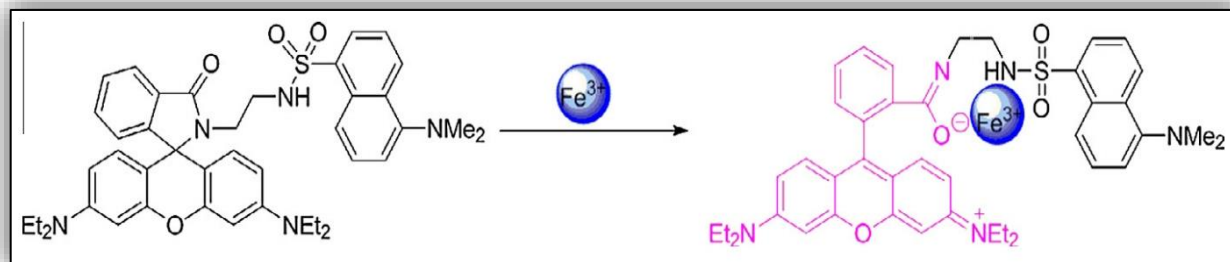


Fig. 1.5.5: Binding of $Fe(III)$ to the dansyl-rhodamine B receptor reported by Jingyu Piao et. al.

CHAPTER 1

Very recently, Kanhu Charan Behera et. al. reported a pyrene-rhodamine FRET couple which acts as a detector for picric acid. As in other rhodamine based sensors in this case also the rhodamine part is the acceptor and the pyrene moiety is the donor in FRET. The Pyrene-rhodamine FRET couple is spaced by a 1,3- diamminopropane linker with high spatial flexibility which allows optimum probe-analyte interaction. It was found from the steady state and lifetime data that the FRET occurs through-space by singlet-singlet excitation energy transfer as a mode of dipole-dipole interaction between the excited donor (D^*) and acceptor (A) couple. Among the dual fluorescence output channel, i.e, the pyrene (at 428 nm) and the rhodamine (at 578 nm), the peak at 428 nm increases then decreases steadily upon gradual addition of picric acid and the peak at 578 nm appears only after addition of 2.0 equivalent of the analyte. [24]

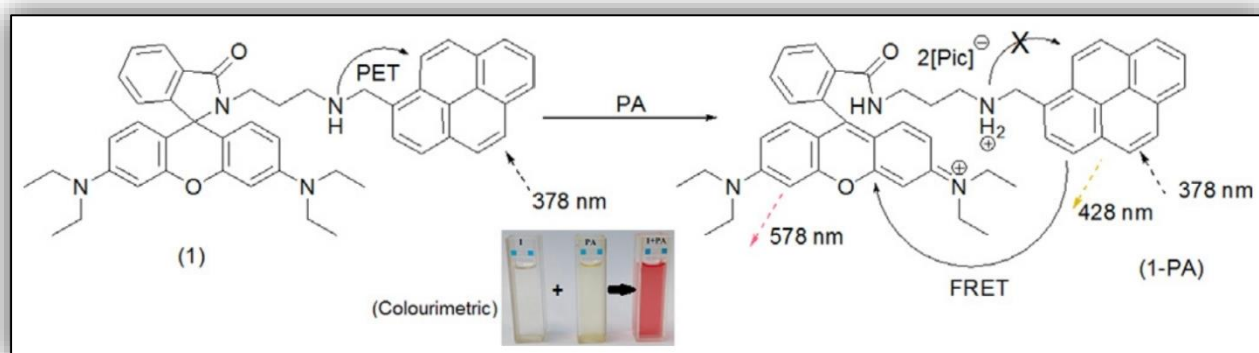


Fig. 1.5.6: Dansyl to Rhodamine FRET turn-on upon spirolactam ring opening (Behera et. al.)

1.5.2.2. Chelation enhanced fluorescence (CHEF) and Chelation enhanced quenching (CHEQ)

In Chelation enhanced fluorescence turn-on and quenching process, the geometry of the molecular structure of the fluorophore changes upon complexation with the metal ion. This brings upon changes to its stereo-electronic properties. But the CHEF effect is more common than the CHEQ as chelation causes more rigidity in the molecule causing the non-radiative relaxation processes to happen in much lower magnitude compared to the free receptor. Consequently, radiative relaxation or fluorescence emission gets turned on or increased in most of the cases. [25, 26] Along with

CHAPTER 1

hindering the roto-vibrational relaxation processes, chelation also negates the possibility of PET processes increasing the probability of fluorescence emission turn-on.

Zhiyong Zhang et. al. reported a phenylenevinylene terpyridine fluorescence chemosensor for both Cd(II) and Zn(II) metal ions in which the Cd(II) ion causes CHEF upon complexation whereas the Zn(II) ion causes CHEQ upon complexation with the receptor (mepvpt). When the chemosensor binds to Cd(II), the molecular structure becomes more planar and $S_3 \rightarrow S_0$ & $S_4 \rightarrow S_0$ radiative relaxation rates become higher than that of mepvpt leading to CHEF. In case of the Zn(II) complex, a new $S_4 \rightarrow S_0$ emission is initiated and high S_4 to triplet state ISC rates increase, which leads to CHQF. [27]

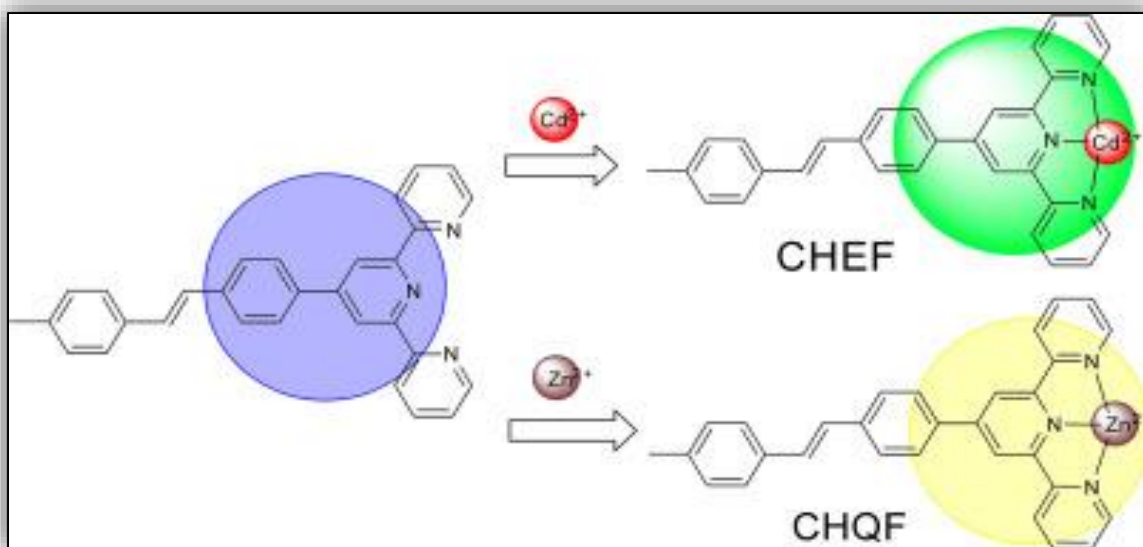


Fig. 1.5.7: A receptor reported by Zhang et.al. showing CHEF and CHEQ

In 2020, Luís Gustavo Teixeira Alves Duarte et al. reported a copper(II) sensor based on CHEQ. In this chemosensor, the quenching effect upon complexation with Cu(II) is explained on the basis of appearance of a faster and competitive non-radiative decay process due to the paramagnetic electronic configuration of Cu^{2+} ion and also by the electronic transitions due to ligand to metal charge transfer(LMCT). [28]

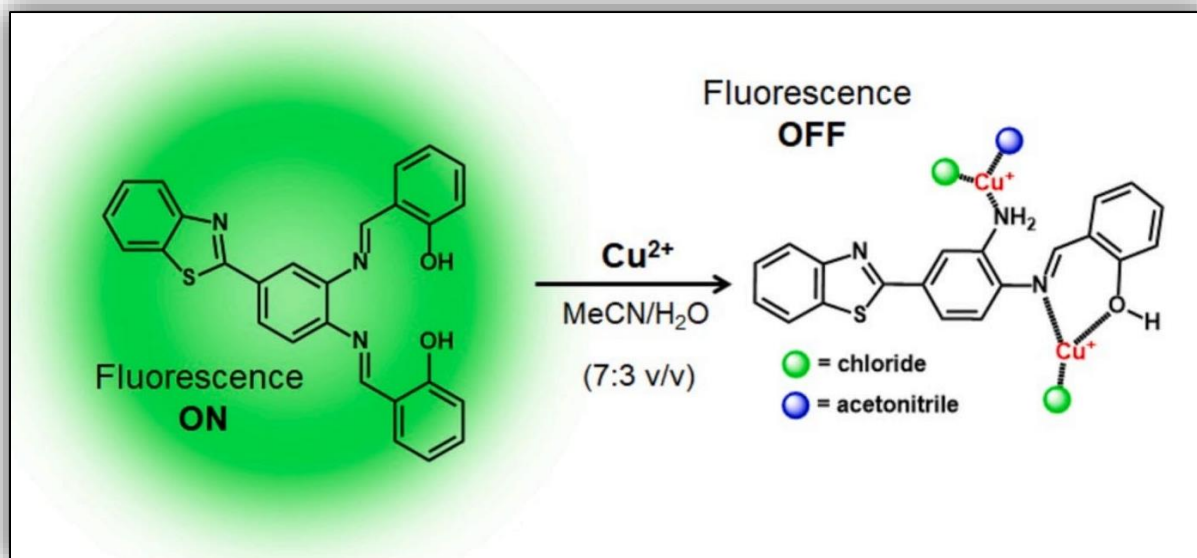


Fig. 1.5.8: Complexation of $\text{Cu}(\text{II})$ with the receptor reported by Duarte et al. leads to CHEQ.

1.5.2.3. Photo induced electron transfer process (PET)

Photo-induced Electron Transfer (PET) has been studied intensively and used widely for the purpose of sensing of cations and anions and is one of the most important factor in mechanisms of sensing in fluorescent chemosensors. In his pioneering work Weller described the thermodynamic basis for PET for intermolecular systems. [29] When an electron jumps to the lowest unoccupied molecular orbital (LUMO of the first excited state S_1) upon excitation and then comes back to the highest occupied molecular orbital (HOMO of the ground state S_0), the excess energy is emitted as light. This radiative relaxation is noted as fluorescence in a molecule. But after the photo-excitation of an electron from HOMO to LUMO, if a filled orbital from another part of the same molecule or from another molecular entity present in the vicinity lies in between the HOMO and the LUMO energetically i.e., if we have a donor group "D", a Photo induced Electron Transfer (PET) occurs from this filled donor orbital to the singly occupied HOMO of the fluorophore (Step 1). A further electron transfer from the singly occupied LUMO of the fluorophore to the donor orbital reinstates the stable ground state but without any fluorescence emission (Step 2) (Fig. 1.5.5).

CHAPTER 1

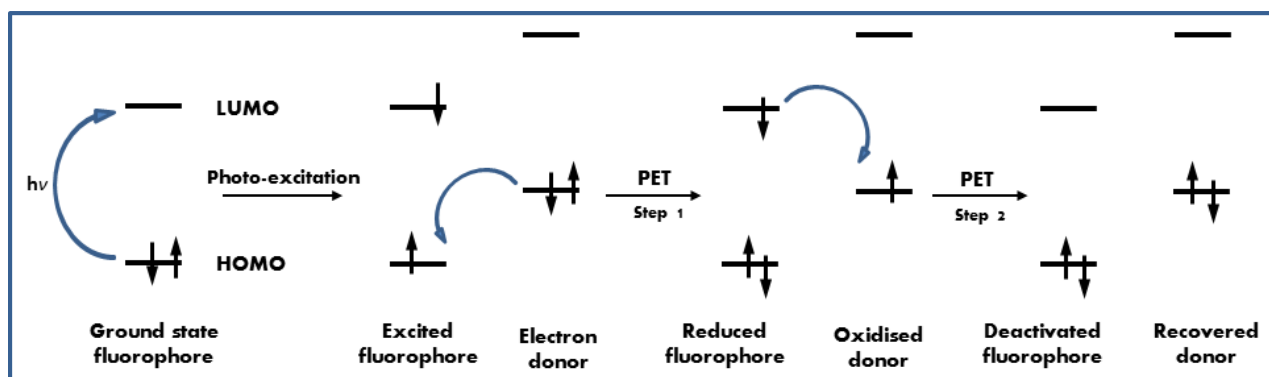


Fig. 1.5.9: FMO energy diagram showing steps of PET process.

In 2020 Pavel A. Panchenko et. al. reported a Zn^{2+} chemosensor based on PET turn-off upon complexation. The receptor comprised of two distinct units among which naphthalimide moiety is pretty common in previously reported PET based fluorescence chemoreceptors. [30] In the PET process occurring in the free receptor, the electron donation occurs from the filled HOMO which is localized on the the salicylidine moiety and the electron accepting half-filled HOMO (-1) belongs to the naphthalimide chromophore. This non-radiative process is disrupted in the Zn^{2+} -complex due to donation of electron pair on imine nitrogen to Zn^{2+} ion. Subsequently fluorescence gets turned on upon complexation with zinc ion. [31]

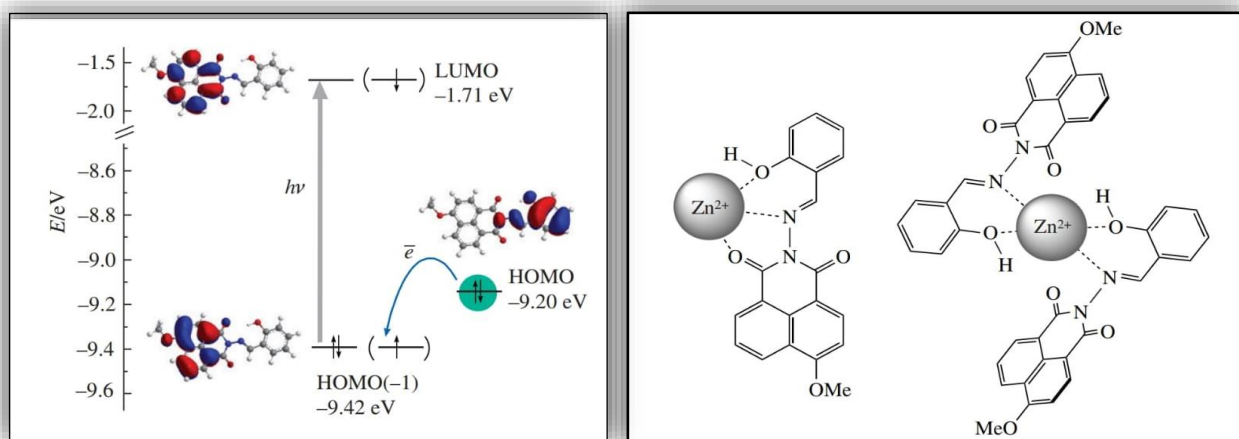


Fig. 1.5.10: a) MO diagram based on energy calculations showing PET process in the free receptor.

And b) two proposed modes of complexation of the receptor and Zn^{2+} reported by Pavel A.

Panchenko et. al.

CHAPTER 1

Xiao-li Yue et. al. reported a PET and ESIPT based Al^{3+} selective fluorescence chemosensor in the year 2017, which has a naphthalene unit and a pyridine carboxylic hydrazone unit attached via a Schiff base linkage. In the uncomplexed state, the imine nitrogen can donate its lone pairs to the half-filled HOMO associated to the acceptor naphthalene moiety in excited state turning PET on. But, the non-radiative decay route via PET gets inhibited in the Al(III) complex due to unavailability of the lone pairs of electrons on the imine nitrogen and fluorescence turn-on takes place. [32]

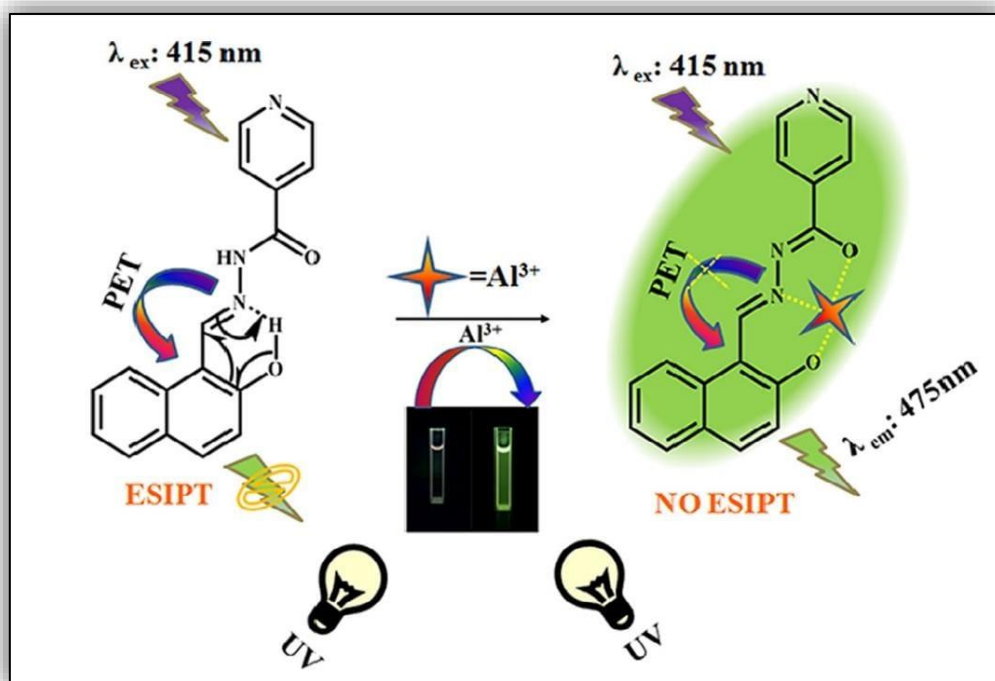


Fig. 1.5.11: Complete sensing scheme of the Al^{3+} receptor reported by Xiao-li Yue et. al.

1.5.2.4. Excited State Intramolecular Proton Transfer (ESIPT)

The ESIPT chromophores resembles the keto tautomer in terms of features unique to it. [33] But the ESIPT chromophores usually exist as the *cis*-enol form in the ground state and are stabilised by the intramolecular hydrogen bonding. According to Frank-Condon principle, upon excitation, the singlet excited state of the enol form gets populated with no relaxation in geometry. Then due to a fast ESIPT process, the excited singlet state of the *cis*-keto form gets populated. This *cis*-keto form is stabilised by intramolecular H-bonding as well. The ESIPT process is much faster compared to the fluorescence emission or radiative relaxation. Therefore, when the ESIPT chromophores show

CHAPTER 1

fluorescence, it happens mainly due to the S_1 to S_0 electron transfer in the keto tautomer with a few exceptions (Fig. 1.5.12) [33]. The singlet excited state (S_1) of the *cis*-keto form may also undergo deactivation by isomerizing to the excited *trans*-keto form and then by undergoing Internal Conversion (Fig. 1.5.13) [34]. Generally, large Stokes shift is observed for the ESIPT chromophores. ESIPT process has been the centre of attention due to its application in several fields such as molecular probes [35], luminescent materials [36], logic gates [37] etc.

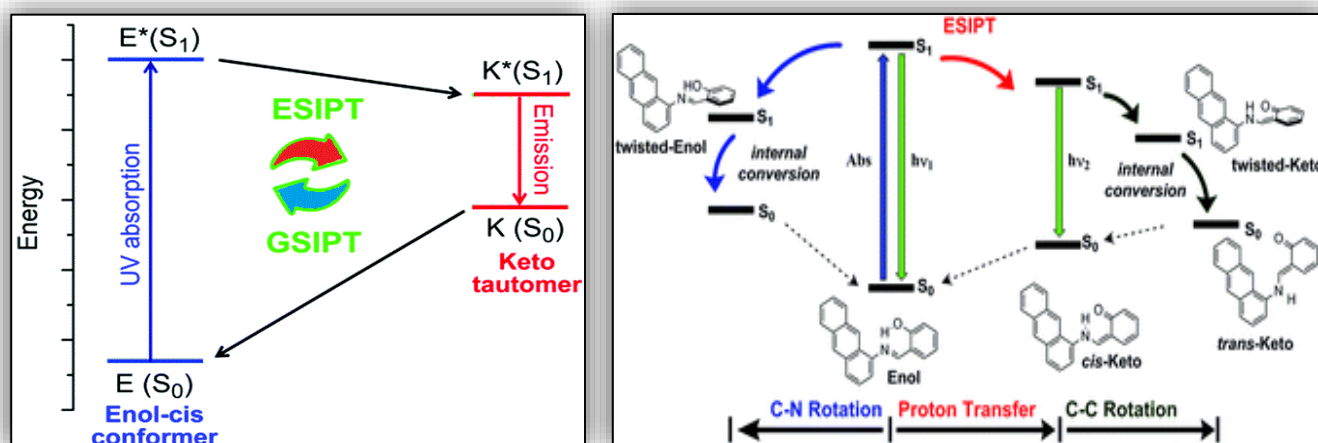


Fig. 1.5.12 and 1.5.13: Energy Profile diagram of ESIPT and deactivation of excited keto form [34]

In 2015, Zhaodi Liu et.al. reported a fluorescence chemosensor for Mg^{2+} ion based on ESIPT turn off. It has a hydroxynaphthaldehyde and an N-amminosuccinimide unit joined via Schiff-base linkage. The hydroxyl group situated at the ortho position to the imine functionality in the naphthalene ring induces ESIPT and causes stabilization to the enol and keto form of the receptor. Both the forms are in equilibrium and quite competitive in terms of respective concentrations. Upon selective coordination of Mg^{2+} ion to the receptor in an alcohol solvent the ESIPT between the imine nitrogen and the keto oxygen gets eliminated and hence the radiative decay i.e., fluorescence turns on. [38]

CHAPTER 1

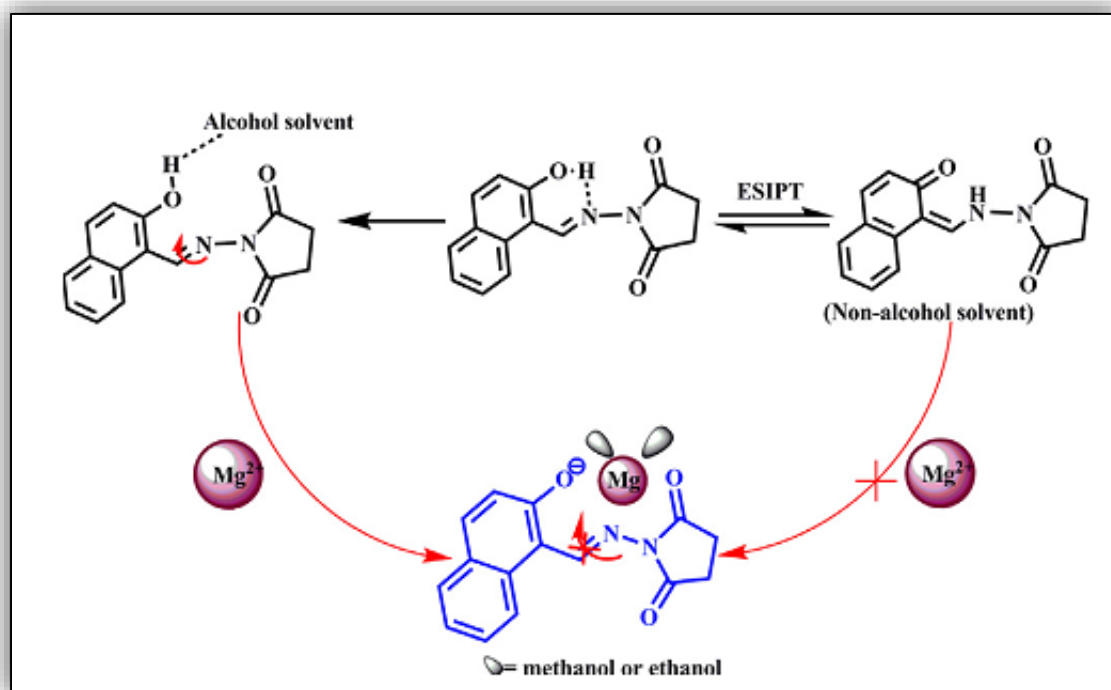


Fig. 1.5.14: The ES IPT process and ES IPT turn-off during the binding of Mg²⁺ with the receptor reported by Zhaodi Liu et.al.

Another ES IPT based fluorescence turn-on receptor was reported in 2017 by Caixia Yuan et. al. Upon specific coordination of Zn²⁺ to the receptor the ES IPT occurring in its free state gets hindered. The same has been confirmed by various studies like, DFT calculations, p-NMR, pH effect etc. by the investigators. Presence of an intermolecular hydrogen bonding between the phenolic -OH hydrogen and the imine nitrogen evident in the X-ray diffraction crystallographic structure also strongly suggest possibility of an ES IPT going on. But tetrahedral coordination of zinc (II) with two molecules of the receptor ends the possibility of conversion of the more stable and strongly emitting enol form into a weakly emitting keto form in the excited state(ES IPT). Hence, a significant increase in fluorescence intensity is seen in case of Zn²⁺ complex. [39]

CHAPTER 1

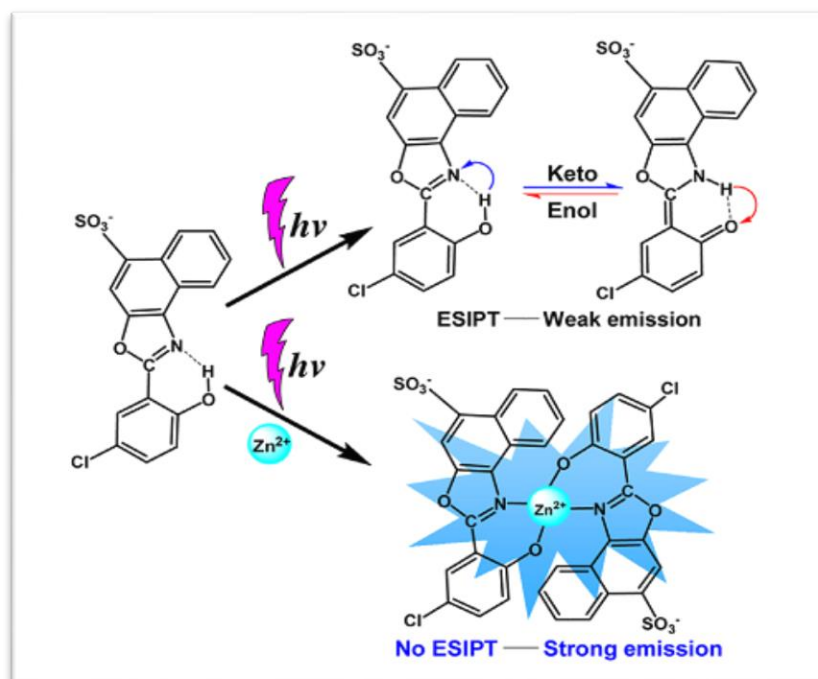


Fig. 1.5.15: The ESIPT turn-off upon binding of Zn^{2+} with the receptor reported by Caixia Yuan et.al.

1.5.3. Types and mechanism of fluorescence quenching processes.

Quenching is the photo-chemical processes that lead to a decrease in fluorescence intensity. These processes can happen during the lifetime of excited state. Quenching may occur due to collisional quenching, electron transfer, excited state reactions or due to formation of complexes in the ground state. There are mainly two types of quenching processes: (1) collisional or dynamic quenching and (2) static quenching.

1.5.3.1. Dynamic or Collisional quenching

Collisional quenching occurs upon collision of the excited state fluorophore with some other molecule in solution, called the quencher. The energy transfer from the excited state fluorophore to the quencher upon collision leads to deactivation and fluorescence quenching. Jablonski diagram shown in figure 1.5.8 represents the quenching process due to collision. The decrease in intensity due to collisional quenching is represented by Stern-Volmer equation:

CHAPTER 1

Bimolecular quenching: - $[F^* + Q \rightarrow F + Q^* \text{ (or } Q)]$; Rate of quenching = $k_q [F^*][Q]$

$$\text{Stern-Volmer equation: } F/F_0 = 1 + K [Q] = 1 + k_q \tau_0 [Q]$$

where K is the Stern-Volmer quenching constant, k_q is the bimolecular quenching rate constant, τ_0 is the lifetime of the excited state of the fluorophore in absence of the quencher, and $[Q]$ is the quencher concentration. The constant K mainly represents the sensitivity of the fluorophore to a quencher. A variety of molecules such as oxygen, halide ions, halogens, amines and certain amides like acrylamide etc. can act as fluorescence quenchers. Elements with high atomic weight strongly enhances the rate of intersystem crossing (i.e. the interchange of singlet and triplet states or vice versa) thereby quenching the fluorescence. This relaxation mechanism is hence known as the External heavy atom effect. Quenching by heavy atoms occur due to spin-orbit coupling also. Collisional quenching diminishes the lifetime of the fluorophore.

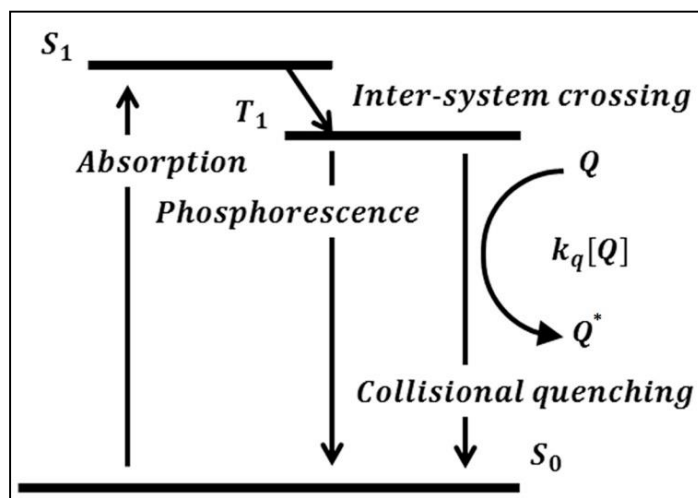


Fig. 1.5.16: Jablonski diagram showing collision quenching

1.5.3.2. Static quenching

The fluorophore may also form in its ground state, a stable complex with an additional molecule acting as a quencher. The fluorophore is said to be statically quenched when this ground-state

CHAPTER 1

complex is non-fluorescent. In such cases, the variation of the fluorescence emission intensity as a function of the concentration of the quencher is expressed by the equation:

$$F_0/F = 1 + K_a[Q], \text{ } K_a = \text{association constant of the complex.}$$

Unlike the dynamic quenching, static quenching (Figure 1.5.9) does not decrease the lifetime of the sample as the fluorophore molecules remaining un-complexed are able to emit after excitation. So they will have normal excited state properties. So, the quencher basically reduces the number of fluorophores which can emit upon excitation and consequently the emission from the sample is reduced.

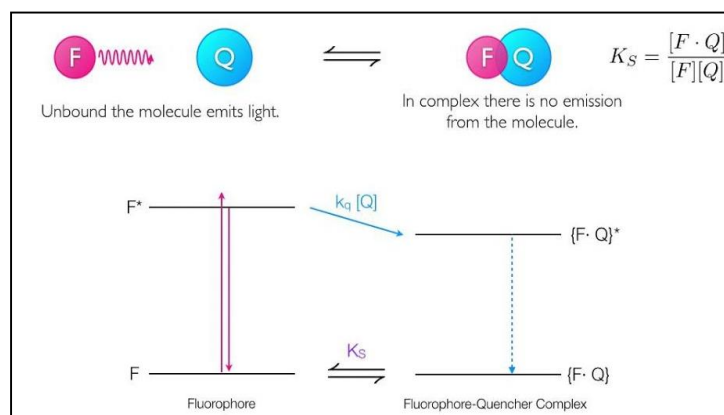


Fig. 1.5.17: Simple mechanism of dynamic quenching.

In 2017 L.Wang et al. extensively studied the fluorescence quenching of phenanthrene, 9-phenanthrol and naphthalene upon treatment with different forms of humic acid as chemical quencher molecules. [40] He studied the comparative quenching abilities of original humic acid, hydrolysed, decarboxylated and bleached forms of humic acid. He also used the Freundlich Model to ascertain the binded and unbound concentration of the emitter molecule with the help of HPLC and subsequently found out the contribution of dynamic quenching in the total quenching process. The amount of dynamic quenching was quantified by subtracting the concentration of quencher bound fluorescent chemical (obtained from HPLC) from the total concentration of the quenched fluorescent chemical (obtained from the fluorescence quenching studies).

CHAPTER 1

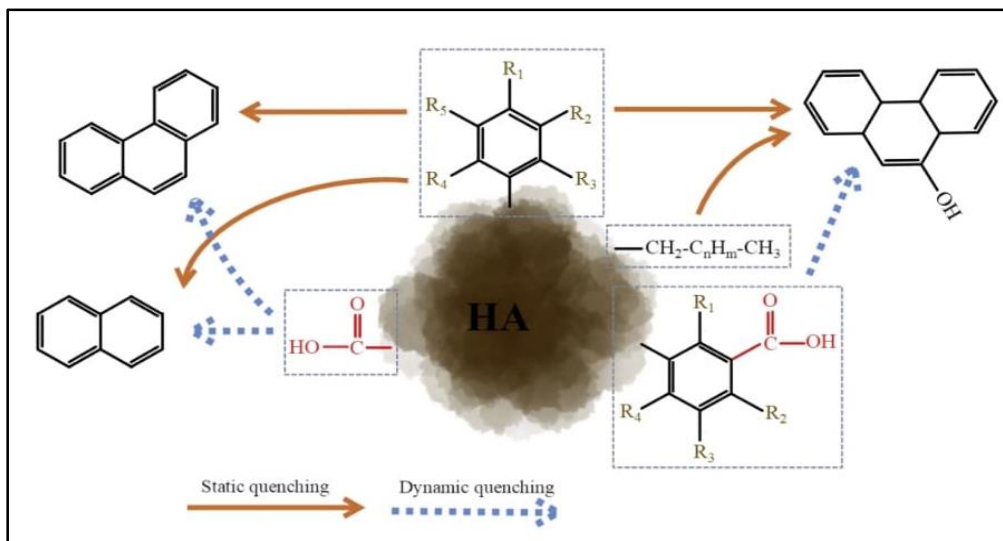


Fig. 1.5.18: Schematic representation of the interaction between different functional groups of Humic Acid quencher and the different fluorescent molecules used by L. Wang et al. [40]

In 2019, E. Ciotta et al. studied the quenching of the unfolded fullerene nanoparticles (referred as UFNPs) upon addition of Cu(II) salts. [41. a)] It was demonstrated that the quenching effect is independent of the anionic part of the Cu(II) salt added. Therefore, the Cu²⁺ ion can be considered as the quenching agent in this case. In their previous work [41. b), c)] they also showed that upon addition of copper ion UV-Vis spectral change is observed but the lifetime of the UFNPs does not change. This fact hints at complexation between UFNPs and Cu²⁺ ions in the ground state and demonstrates the static nature of the overall quenching process.

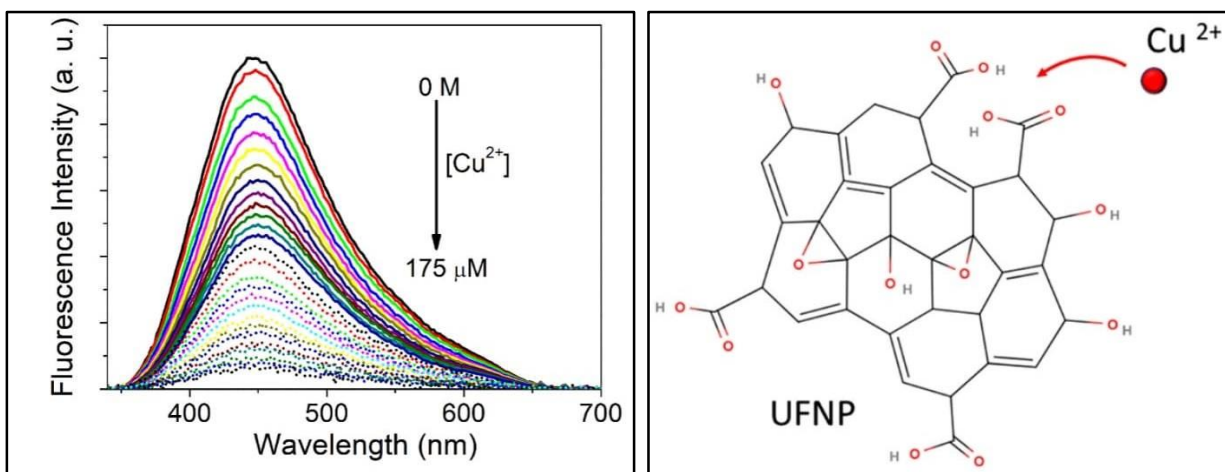


Fig. 1.5.19 and 1.5.20: Fluorescence quenching curve and schematic representation of complexation of UFNP and Cu²⁺ ions.

1.6. Chemical forces behind host-guest binding: Non-covalent interactions.

The binding event, one of the most important step in supramolecular chemistry and chemosensing is reliant on various attractive and, very much undesirably, repulsive non-covalent chemical forces. The term, “non-covalent forces” covers a vast mélange of attractive and repulsive forces. The most relevant ones, along with a succinct statement about their energies, are described below.

- (1) Coulombic interactions [ion-ion interaction (100-350 kJ/mole), dipole-dipole (5-50 kJ/mole)], ion-dipole (50-200 kJ/mole);
- (2) Hydrogen bonding (4-120 kJ/mole) interactions;
- (3) π - π stacking (0-50 kJ/mole) interactions;
- (4) Van der Waals forces (< 5 kJ/mole).

CHAPTER 1

1.6.1. Coulombic interactions

Coulombic interactions involve Electrostatic attraction forces between two opposite charges in an ion pair or partially developed charges on dipolar molecules. Ion-ion interactions {Figure 1.6.1(a)} are basically non-directional, but in case of ion-dipole and dipole-dipole interactions the dipoles must properly align themselves for effective binding. Many cation receptors (crown ethers, cryptands and spherands) and anion receptors (protonated or alkylated polyammonium macrobicycles) have been designed to hold the guest in place based on such ion-dipole interactions.

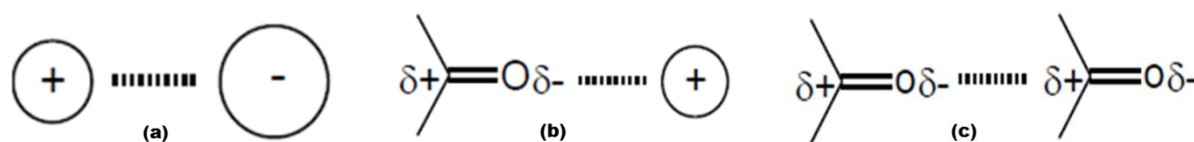


Fig. 1.6.1: Electrostatic interactions (a) ion-ion (b) ion-dipole and (c) dipole-dipole.

1.6.2. Hydrogen bonding

Hydrogen bonding is a special type among all the non-covalent interactions. Although it is called a 'bond' it is not considered to be a proper one. By definition, hydrogen bond is a force of attraction working between an electronegative atom and a hydrogen atom covalently bonded with another electronegative atom of the same or a different molecule. Hydrogen bond plays a crucial role in molecular recognition. Hydrogen Bonding can be classified into two types, 1) intermolecular hydrogen bonding, where hydrogen bond occurs between different molecules and 2) intramolecular hydrogen bonding, where bonding occurs within a single molecule. This bond is weaker (characteristic hydrogen bond 5-30 kJ/mole) than ionic or covalent bonds but it is stronger than Vander Waals force.

Biological systems like the DNA double helix have been found to be highly reliant on hydrogen bonds for its structure. In other words, hydrogen bonds can be said to be the basis of our mere existence and are also the basis of secondary, tertiary and quaternary structures of proteins (Fig. 1.6.2 and 1.6.3). Hydrogen bonds have been the major binding interaction in many receptors designed to co-ordinate neutral organic species such as small alcohols, amides etc. and even anions.

CHAPTER 1

By exploiting the precision and directional nature of the hydrogen bonds, individual components may be spatially arranged in order to build complex molecular architectures.

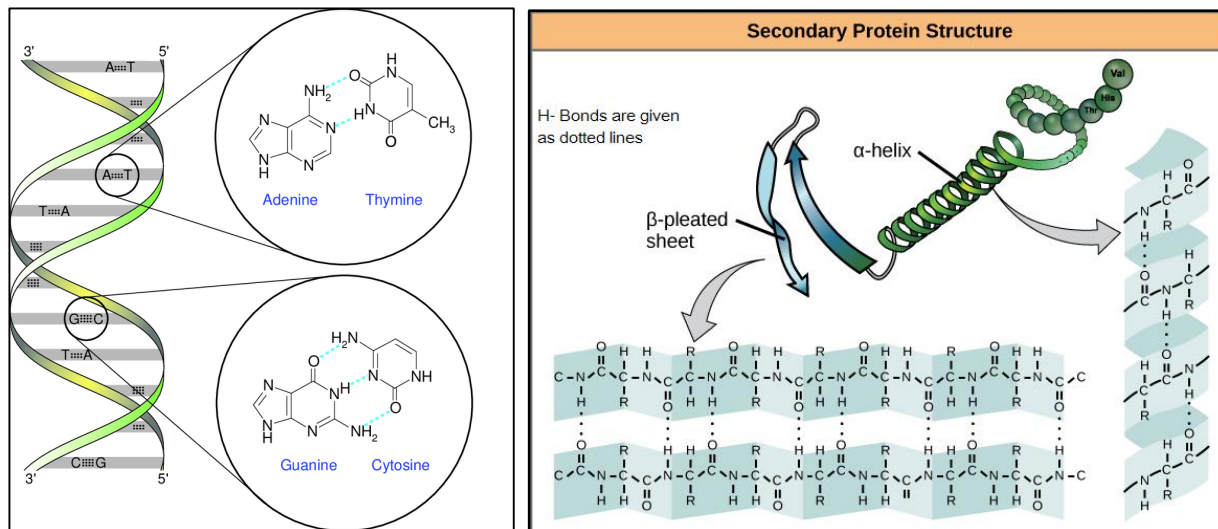


Fig. 1.6.2 & 1.6.3: Hydrogen bonding in DNA double helix and secondary structure of protein.

1.6.3. π - π stacking

The first synthetic application of a π -stacking interaction was postulated by E. J. Corey in 1972 for the chiral reduction of ketone during the synthesis of prostaglandins. But recently, organic chemists are increasingly using the term π -stacking in host-guest chemistry.

π -stacking interaction is a type of non-covalent interaction which occurs when two separate π -conjugate systems come in close vicinity and align themselves parallel causing intermolecular interaction between p-orbitals (Figure 1.6.4). This p-p interaction can occur “face-to-face” (‘sandwich’), “edge-to-face” (T-shaped) or in “offset” (‘parallel-displaced’) manner. The compounds containing aromatic moieties stacked with each other by aromatic interactions make a large influence on molecule based crystal structure in solid state molecular recognition [42], porphyrin aggregation etc. [43] In Zimmerman’s molecular tweezers [44] the π - π interactions is thought to be associated with a parallel-displaced geometry. The crystal structures show that the two tweezers form complex with each other but with minimal π -overlap in its stacking interactions. [45]

CHAPTER 1

The biological role of π - π interactions is evident in the repeated base pair stacking in DNA, the interaction of drugs with DNA and in folding of a protein molecule. [46]

The exact nature of π -stacking interaction is still a matter of debate. Among various proposed models to explain the observations, the electron donor-acceptor (EDA) model suggests that the strong attraction arises because of electronic interaction between an electron donor and electron acceptor whereas according to a charge transfer (CT) model, a CT complex is claimed to be formed due to association of a good electron donor and an acceptor which is characterized by a charge transfer transition band in the UV-vis absorption spectrum. [47]

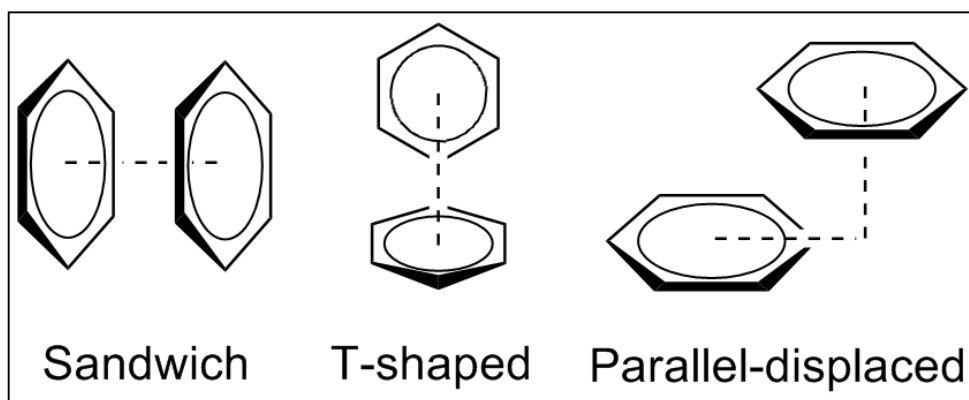


Fig. 1.6.4: Different modes of π -stacking interactions: (a) Sandwich (face to face), (b) T-shaped (edge to face) and (c) Parallel-displaced (offset).

1.6.4. Van der waals force

Van der Waals force is a relatively weak electric force of attraction that exists in gases, in liquefied and solidified gases, and in almost all organic liquids and solids as the main intermolecular force. This kind of forces are named for the Dutch physicist Johannes Diderik van der Waals, who in 1873 first postulated these intermolecular forces in developing a theory to account for the properties of real gases. Solids that are held together by van der Waals forces characteristically have lower melting points and are softer than those held together by the stronger ionic, covalent, and metallic bonds because The energy of this force of attraction is much less than other bonding interactions even less than hydrogen bonding interactions.

CHAPTER 1

Van der Waals forces may arise from three sources. **First**, if some of the molecules are permanent electric dipoles. The tendency of such permanent dipoles to align with each other results in a net attractive force. This can be called the **dipole-dipole type**. **Second**, the presence of permanent dipoles may temporarily induce polarization in other nearby nonpolar molecules. The attractive force resulting from the interaction of a permanent dipole with a neighboring induced dipole may be called the **dipole-induced dipole type**. **Third**, when there are no permanent dipoles present (e.g., in the noble gas argon or the organic liquid benzene), a force of attraction still arises due to fluctuating polarization of an atoms or a molecule and subsequent induction upon another nearby atom or molecule. These Van der Waals forces can be called **fluctuating dipole-induced dipole type**. In supramolecular chemistry these forces provide additional stabilization to the binding of a hydrophobic guest into the hydrophobic cavity.

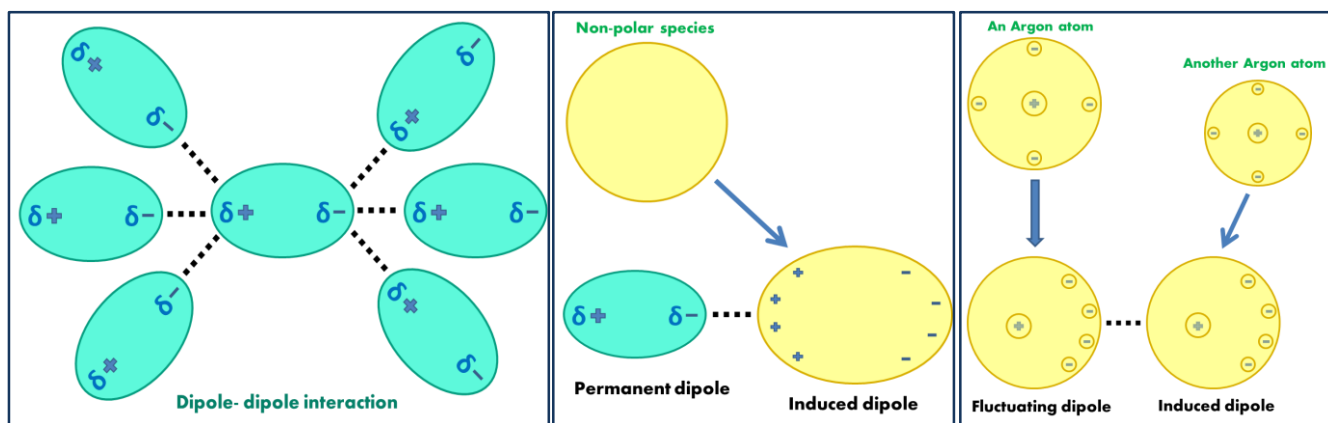


Fig. 1.6.5: Types of Van der waals' forces: a) dipole-dipole; b) dipole-induced dipole; c) fluctuating dipole-induced dipole type.

CHAPTER 1

1.7. An ideal chemosensor and different approaches to design one.

1.7.1. Criteria of designing an ideal chemosensor

As the pioneering works in the chemosensor field suggests, the chemistry of synthetic receptors were broadly associated with detection of transition metal ions. But the chemistry of chemo-receptors today is not only restricted to transition metal ions but has expanded to all types of cationic, anionic or neutral substrates of organic, inorganic and even biological origin. The effectiveness of complexation between the receptor and the substrate depends upon various types of interactions as we have already discussed in the previous section. Now in order to design an ideal receptor for any substrate the chemist needs to stick to a few basic criteria, as it is mentioned hereunder:

The chemist needs...

- (1) To consider steric effects between receptor and substrate and use it advantageously. E.g. A concave domain or a cavity and convex domain or a bulge in the structure of the receptor and the substrate.
- (2) To look for Presence of additional binding interactions in complementary binding sites in the correct configuration on the receptor and on substrate in order to attain complementary electronic and nuclear distribution.
- (3) To design several interaction sites when non-covalent interactions are the principal forces of binding.
- (5) To achieve high photo stability and high selectivity of the receptor.
- (6) To ensure that the receptor has satisfactory shelf life.
- (7) To make sure that both the host and the guest love (both are solvophilic) or, if the case is so, hate (both are solvophobic) the solvent or medium.
- (8) To keep the chemistry of synthesis as green as possible.

CHAPTER 1

Hypothesized receptors may be synthesized either by multistep total synthesis of the target receptor molecule or by regio-specific functionalization of certain easily available small molecules. Simpler synthetic design having limited number of recognition elements leads to simple sensing patterns. Structural units that may react to or be perturbed by external factors should be avoided. The investigations relevant to this thesis are focused on *endo*-receptors in which the binding sites are situated inside a molecular cavity. [48] For a certain host molecule, guest molecules are taken into consideration only after evaluating all the probable recognition elements.

1.7.2. Different schemes in designing a chemosensor

The selectivity of any receptor for its specified guest, e.g. a particular cation, depends upon the ratio between the receptor's binding affinity towards a specified cation and other competing cations. Thus an efficient host boasts of a stronger affinity for a single particular guest cation compared to other coexisting cations. As the extent of selectivity of a host is controlled by a vast number of factors like size of guest ions and binding site, and functional behaviour of host and guest molecule, electronic charge distribution throughout the host molecule, solvent polarity etc., designing and synthesizing a selective and efficient host molecule is a very taxing task.

1.7.2.1. Changes in absorption spectra upon binding with cations or anions

Even if the chemoreceptor does not have any fluorophore attached to it or if it has no fluorescence properties at all, it may still be able to detect an ionic analyte. When a certain ionic species selectively brings about particular changes to the absorption spectra of a chromophore giving rise to new absorption peaks, the colorimetric change is observable under naked eye and the molecule can act as a colorimetric chemosensor to that ion. This is the basic approach and does not have the benefit of fluorescence technique.

In 2021, Yongjie Ding et al. reported a dual chemosensor for the colorimetric detection of Fe^{2+} and fluorescence detection of Al^{3+} [49]. In this quinolone based receptor the absorption band at 344 nm experienced a red shift to 363 nm upon addition of Fe^{2+} and a new band appears in the visible region at around 670 nm giving rise to the colorimetric change from faint yellow to dark green. Such visible change is not seen in presence of other coexisting cations making the receptor a good chemosensor

CHAPTER 1

for the selective colorimetric detection of Fe(II). In 2017 another colorimetric sensor for Fe(II) and Fe(III) ions was reported by Ju Byeong Chae et. al. wherein addition of Fe²⁺ and Fe³⁺ ions cause distinct changes to the absorption spectra of the receptor with extinction of the peak at 430 nm and evolution of a new bands at 350 nm and 490 nm with an isosbestic point at 382 nm. [50]

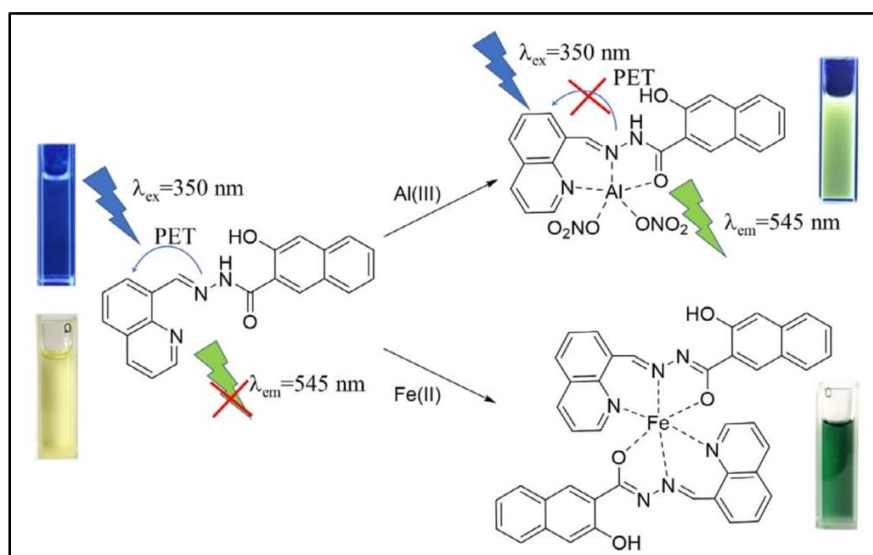


Fig. 1.7.1: Basic sensing scheme of the receptor reported by Yongjie Ding et al.

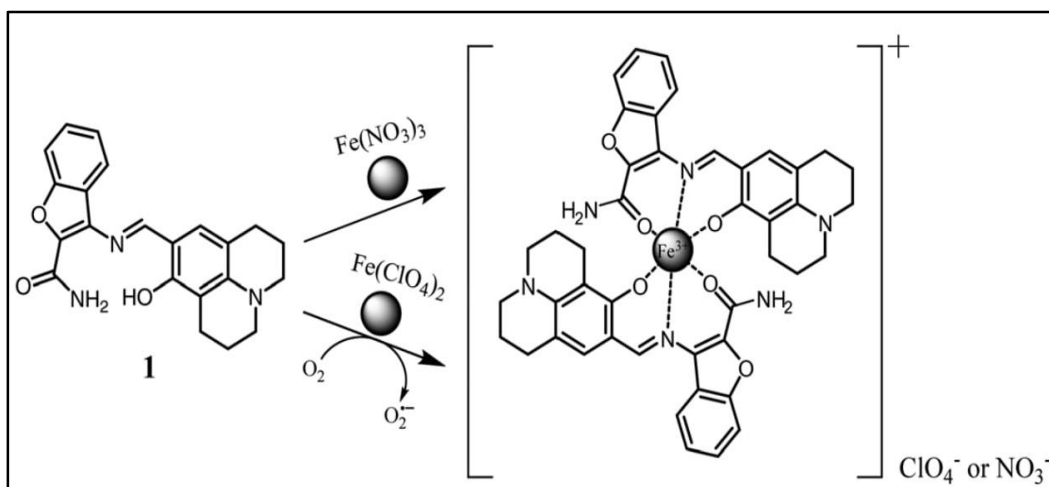


Fig. 1.7.2: Binding mode of the receptor reported by Ju Byeong Chae et al.

CHAPTER 1

1.7.2.2. Fluorescence turn-on and turn-off upon binding with ionic analytes

In this approach researchers often work with known fluorophores or precursors to a fluorophore eg. Fluoresceins, hydroxy coumarines, amino coumarines, Rhodamine-6G, Rhodamine-B, chromenes etc. These fluorophore moieties can be functionalized into various novel compounds with proper binding sites by incorporating new functional groups and new moieties by organic reactions. Subsequently if a certain ionic analyte selectively and significantly changes the emission spectra of the novel receptor upon binding, it can be said to work as a chemosensor towards that ion. One can also plan to turn off the fluorescence of the receptor fluorophore by some reaction whereafter a certain analyte once again selectively turns on the fluorescence upon complexation. A third scenario is also possible where the chemoreceptor is fluorescent and the ionic analyte quenches the fluorescence upon binding.

In 2014 S. Tong et. al. reported a Rhodamine based mercury ion chemosensor associated with a fluorescence turn-on upon addition of Hg^{2+} ion to the free receptors namely Rs-Naph and Rb-Naph and the receptors taken in an up-conversion $\beta\text{-NaYF}_4: \text{Y(III)/Er(III)}$ excitation host. In presence of Hg(II) ions new emission bands at 578 nm and 580 nm are observed for Rs-Naph and Rb-Naph respectively. [51]

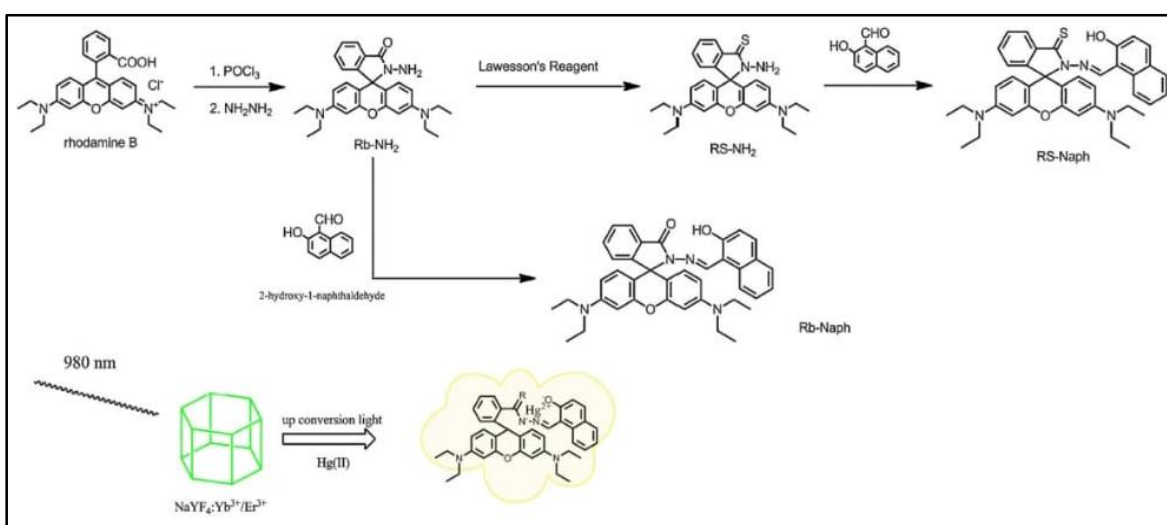


Fig. 1.7.3: Synthesis and binding scheme of the receptor reported by S. Tong et. al.

CHAPTER 1

Very recently in 2022 H. Kim et. al. reported a fluorescence turn-on chemosensor that can act as a dual chemosensor for both Zn^{2+} and Hg^{2+} ions based on naphthalene and carbothiamide moieties. The reported chemosensor namely NTHC can detect Zn^{2+} ions and Hg^{2+} in different solvent mediums, respectively buffer (pH=7.0) for Zn^{2+} and DMSO:buffer (99:1, v/v) for Hg^{2+} . Upon addition of Zn^{2+} a fluorescence band at 448 nm drastically increases in intensity and in case of fluorescence titration with Hg^{2+} a band at 460 nm increases in intensity. [52]

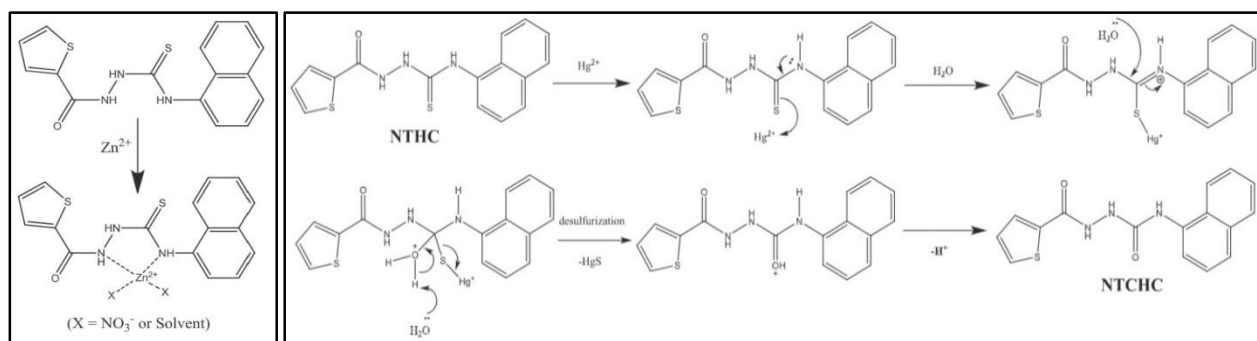


Fig. 1.7.4 a) and b): Binding of receptor with Zn^{2+} ions and sensing of Hg^{2+} ions by desulfurization technique in the chemosensor reported by H. Kim et. al.

In 2015 E. Senkuytu et. al. reported a fluorescent turn-off chemosensor for Fe^{3+} and Cu^{2+} ions based on amine substituted fluorenylidene bridged cyclotriphosphazenes. [53] The presence of both Fe^{3+} and Cu^{2+} ions decrease the intensity of distinct emission band at 370 nm corresponding to the receptor molecule. In the same year W. Cui et al. reported a fluorescence turn-off for the detection of silver ion. The receptor molecule is structurally based on a conjugate polymer containing 2,3-di(pyridine-2-yl) quinoxaline. [54] Upon addition of Ag^+ ions to the polymerized sensing material colorimetric changes occur along with changes to the emission spectra. The emission peak at 525 nm rapidly diminishes in terms of intensity as soon as silver ion is added to the receptor ensemble.

CHAPTER 1

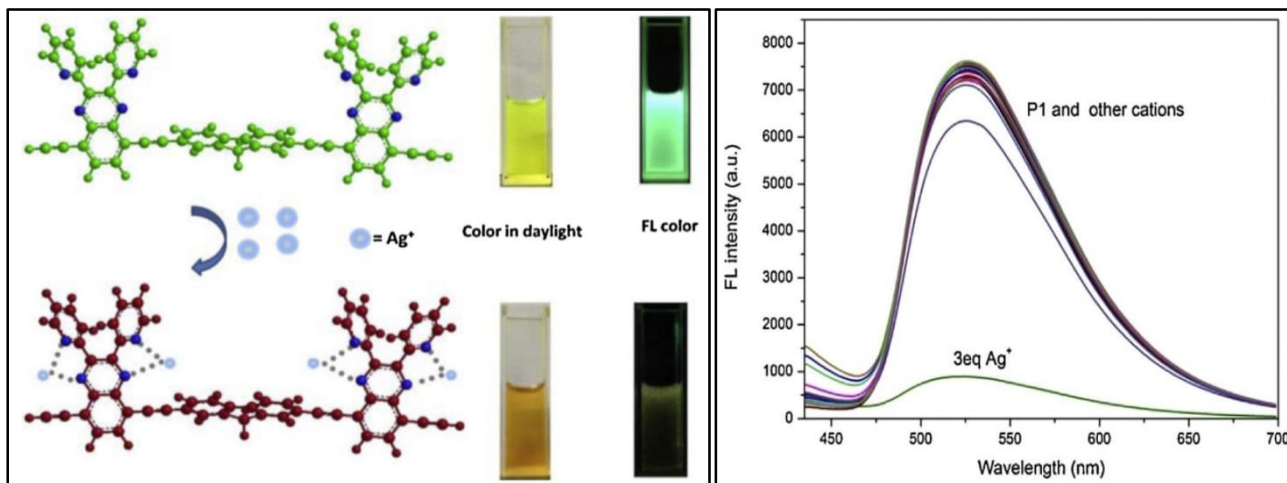


Fig. 1.7.5 a) and b): Sensing scheme for sensing of Ag^+ ions and the fluorescence curve upon addition of 3 equivalents of Ag^+ in the chemosensor reported by W. Cui et. al.

1.7.2.3. Sequential fluorescence turn-on or turn-off upon de-complexation of the receptor and the analyte

In some cases, sequential addition of a second analyte sets the receptor free from the receptor-analyte ensemble by forming insoluble compound or a stronger complex with the first analyte and subsequently the emission behavior of the receptor emerges once again. If the freeing of the receptor happens with selectivity for a certain second analyte, the complex between the receptor and the first analyte is said to act as a sequential chemosensor to the second ionic analyte. For eg. S^{2-} and I^- ions can free a receptor from its Hg^{2+} ion complex, F^- ions can free a receptor from its Al^{3+} ion complex, and Cl^- ions can free an Ag^+ ion receptor from its complex etc.

Jaewon Kim et al. reported a sequential chemosensor for chloride ions in which the silver ion complexes of the various substituted benzimidazole compounds are used. [55] The sensing event is associated with addition of chloride ions to the silver complex and subsequent fluorescence turn-on due to liberation of the benzimidazole molecule following precipitation of silver ions as silver chloride. The optimum benzimidazole derivative shows an emission maximum at about 344 nm. Upon addition of Ag^+ ions the fluorescence gets quenched and after sequential addition of Cl^- ions the receptor gets freed and fluorescence gets turned on once again.

CHAPTER 1

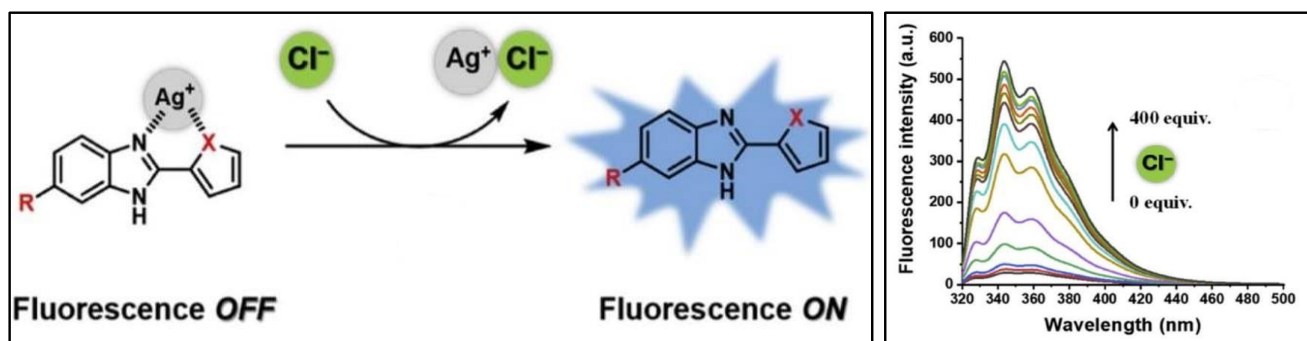


Fig. 1.7.6 a) and b): Sensing scheme for sensing of Cl⁻ ions and the fluorescence titration curve upon addition of Cl⁻ to the chemosensor reported by J. Kim et al.

In 2014, Yong-Sheng Mi et al. synthesized and characterized a rhodamine-quinolone based chemosensor (named as REQ). The receptor had the ability to detect both Al³⁺ and F⁻ ions sequentially. [56] Upon gradual addition of Al³⁺ solution to the buffer solution containing the receptor REQ, the fluorescence intensity increases alongside the increment in the concentration of the Al³⁺ ions and an emission maximum can be observed at 584 nm. This indicates prominence of the open ring form of the rhodamine moiety in the Al³⁺ complex. But after sequential addition of Fluoride(F⁻) ions the more stable fluoride complex of the aluminium ion(AlF₆³⁻) is formed and the receptor is freed. This causes the lactam ring in the rhodamine moiety to reform and results in the quenching of the fluorescence maxima at 584 nm.

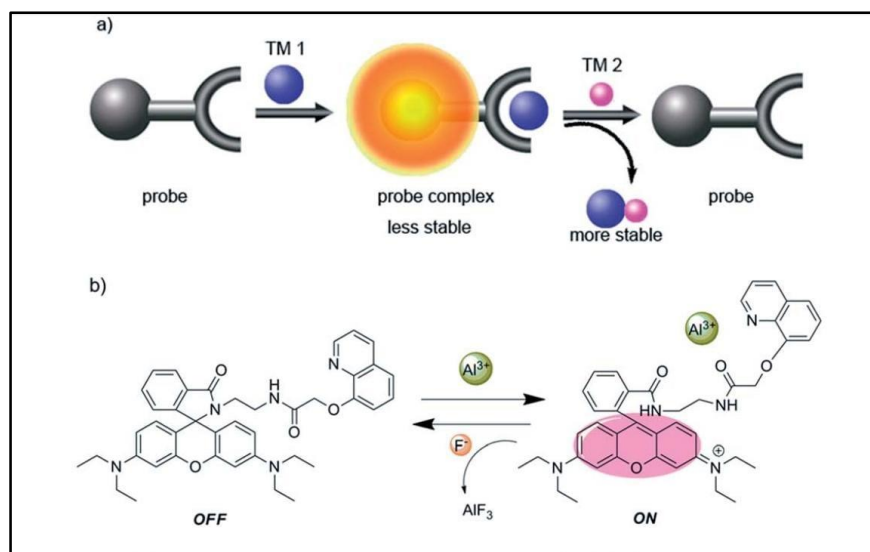


Fig. 1.7.7 a) and b): Scheme for sequential sensing of Al³⁺ and F⁻ ions by the chemosensor reported by Y-Sheng Mi et al.

CHAPTER 1

1.7.2.4. Approaches to design host molecules for anionic analytes

1.7.2.4.1 Binding site-signaling subunit approach for anionic analytes

In this approach Many anionic sensors are designed by covalent attachment of signaling subunits and anion binding sites. [57] The moment the coordination site binds the anion, the properties of the signaling subunit changes giving rise to alterations either in the absorption behaviour (chromogenic chemosensor) or in its emission behavior (fluorogenic chemosensor). (Figure 1.7.1)

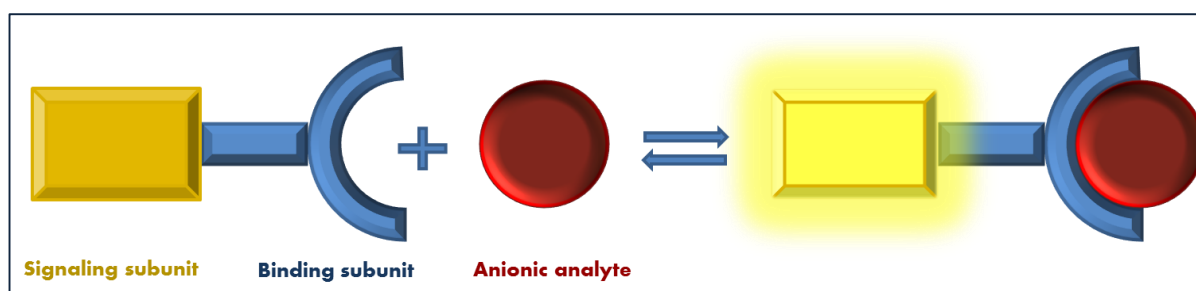


Fig. 1.7.1: Binding site-signaling subunit approach

1.7.2.4.2 Displacement approach for anionic analytes

Here in this approach, upon addition of a target anion to the solution containing the non-covalently attached binding subunit-transducing indicator ensemble (Receptor-Indicator ensemble), a displacement reaction occurs. The binding site coordinates the incoming anion whereas the signaling subunit or the Indicator returns to the solution retrieving the spectral behavior in its free state. If the signaling subunit or free indicator has different than that of the molecular ensemble, then the anion binding process is associated to a signaling event.

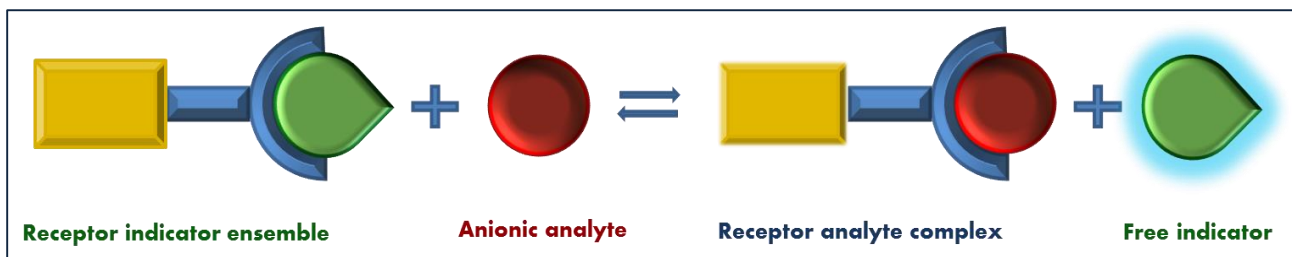


Fig. 1.7.8: Displacement approach for anionic analytes

CHAPTER 1

1.7.2.4.3. Chemodosimeter approach

Chemodosimeters are inherently different from chemosensors in the way that they are designed based on irreversible chemical reactions that accompany the transduction event. [58, 59] So, chemodosimeters may not be reversible or reusable but they are very selective towards a specific anionic or cationic analyte. [60]

A chemodosimeter may function in two ways, one in which the anion reacts by forming covalent bond with the chemodosimeter and therefore is attached to product. In the second type, the anion initiates and catalyzes a chemical reaction. The reaction of the anionic analyte with the chemodosimeters can either turn –on fluorescence or inflict a ratiometric change in the emission curve. Figure 1.8 represents the types of a chemodosimeter graphically.

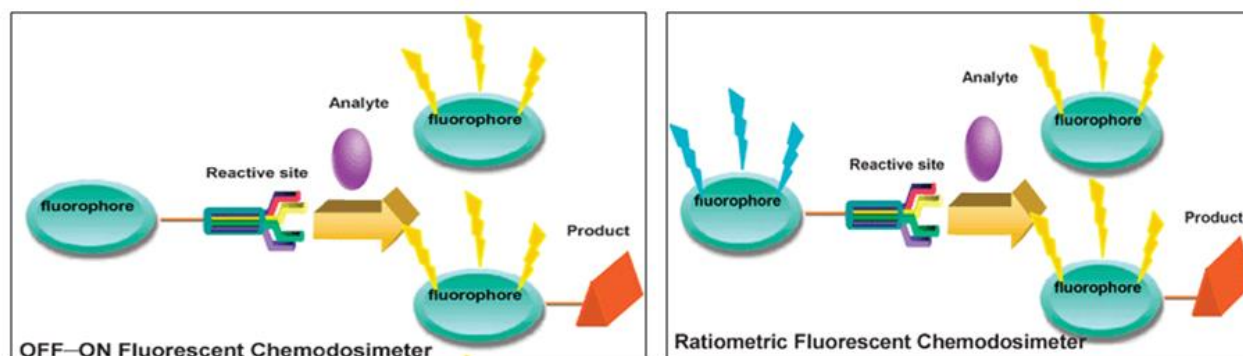


Fig. 1.7.9: Types of chemodosimeters.

1.8. Applications of chemosensors as optical biosensors, in live-cell imaging and molecular logic gates

Chemosensors have been known to offer a variety of applications. Out of these applications, a few that are relevant to this thesis is discussed briefly in the ensuing segment.

1.8.1. Application as optical biosensors

Biosensors are analytical devices that consists of a fixed biological sensing element and a transducer element. The detection of biomolecules in a complex sample is achieved by converting the chemical signal into an optical or electrical signal produced by the physio-chemical transducer. Quantifying the strength of the signal we can also deduce the analyte concentration. [61 a), b)] The sensing event is initiated by molecular recognition of the targeted analyte. The detection process is associated with the stereo-electronic interaction between the analyte and the sensing element and its effect on the transducer. [62] The factors that are assessed for the selection of the proper biological sensing element, are the specificity towards a particular analyte, ease of storage, operational and environmental stability. The choice is also dictated by the type of analyte to be detected such as heavy metal ions, small organic compounds, antigens, microbes, hormones or nucleic acids etc. Some common biological sensing element that have been used widely may be classified into enzymes, antibodies, DNA, receptors, organelles and microorganisms. Even cells or tissues of both plant and animals have been used as biological sensing elements. [63, 64]

In 2015, Giorgi Shtenberg et al. designed and fabricated a simple optical biosensor for trace heavy metals using enzymatic activity inhibition. The target enzyme has been immobilized on the surface of the pore walls of PSi nanostructures. Specific interaction between the target enzyme and the heavy metal ions modifies the enzymatic activity negatively. This interaction makes the real-time monitoring of heavy metal ions possible by translating into a shift in the reflectivity spectrum of the PSi film as its effective optical thickness (EOT) changes. The enzyme used in this activity inhibition sensing concept is horseradish peroxidase (HRP). It is one of the most important peroxidases in biotechnological research. In absence of heavy metal ions, the enzymatic action upon the substrate molecules gives insoluble products which is deposited in the nanopores on the PSiO₂ film and causes a substantial redshift in the EOT. But this EOT shift is not observed in presence of heavy metal ions which interact with the enzyme and decreases its action thereby (see fig. 1.8.1). [65]

CHAPTER 1

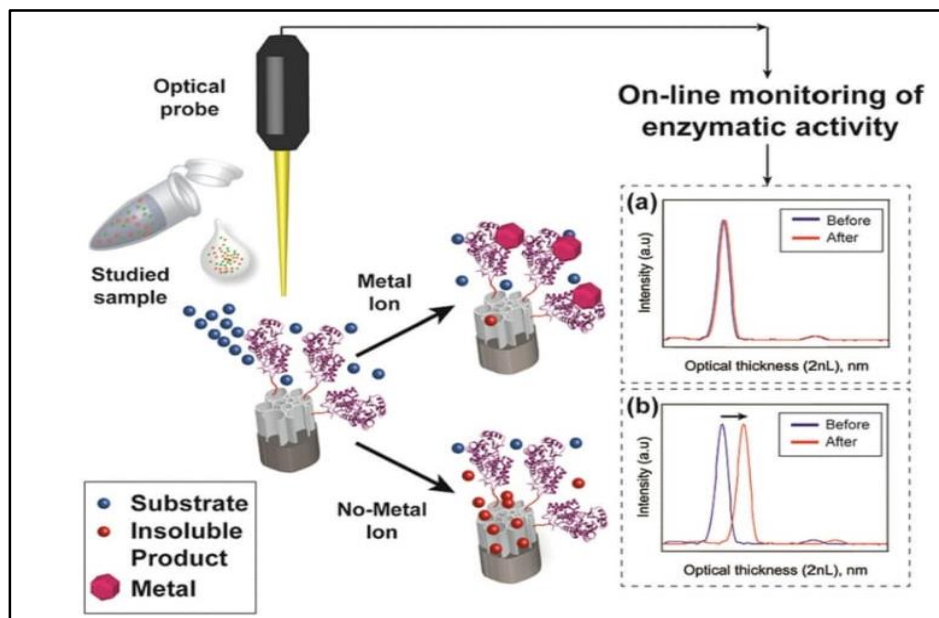


Fig. 1.8.1: Schematic representation of the sensing of the heavy metal ions by monitoring the optical thickness. a) No red shift in EOT in presence of metal ions and b) Red shift in EOT in absence of heavy metal ions. [65]

1.8.2. Application in live cell imaging

Various metal ions like Copper (Cu^{2+}), zinc (Zn^{2+}), aluminium (Al^{3+}) and iron (Fe^{3+}) have a crucial role in biology and also in the intracellular activities. [66]. Cu^{2+} is involved in mitochondrial respiration and neuronal functions, Zn^{2+} works as the active centers of many enzymes, Al^{3+} has long been suspected to be a neurotoxic agent causing Alzheimer's disease, whereas both Fe^{2+} and Fe^{3+} is essential for oxygen delivery and electron transport. [67, 68, 69] Therefore, it is very important to trace these metal ions in the intra-cellular region as well as in solution phase. In the recent chemosensor research various receptors have been used for live cell imaging studies to explore their capability to detect various metal ions *in-vivo*.

In 2018, Ezhumalai et al. synthesized a couple of turn-on macrocyclic chemosensors for Al^{3+} ion. Live cell imaging studies were done with KB cells (papilloma). The receptors namely 'me1' and 'dm2' exhibited good cell membrane permeability. Upon addition of Al^{3+} ions the intracellular

CHAPTER 1

concentration of Al^{3+} increases and fluorescence gets turned on due to PET turn-off and the cells appear fluorescent under confocal microscope (see fig. 1.8.2.). [70]

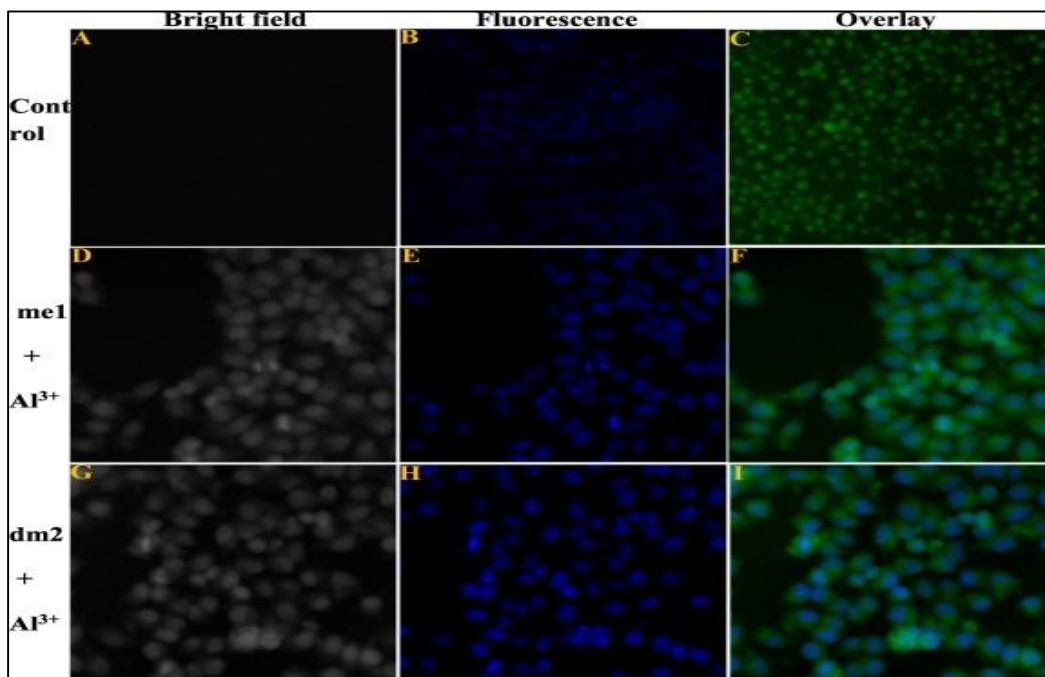


Fig. 1.8.2: Fluorescence images of KB cells treated with compounds ‘me1’ and ‘dm2’, and $\text{Al}(\text{NO}_3)_3$ under bright field, fluorescence field and the overlay of the two. [70]

Subsequently in 2022, Pranabendu Das et al. reported a piperazine based Schiff base chemosensor for the detection of $\text{Zn}(\text{II})$, $\text{Cu}(\text{II})$ and F^- . The live cell imaging studies has been done with HeLa cells which have been incubated with the bare chemosensor(HL) and subsequently with $\text{Zn}(\text{II})$. The addition of triggers blue fluorescence in the intra cellular region showing that the chemosensor can detect $\text{Zn}(\text{II})$ in the intracellular environment. (see fig 1.8.3.) [71]

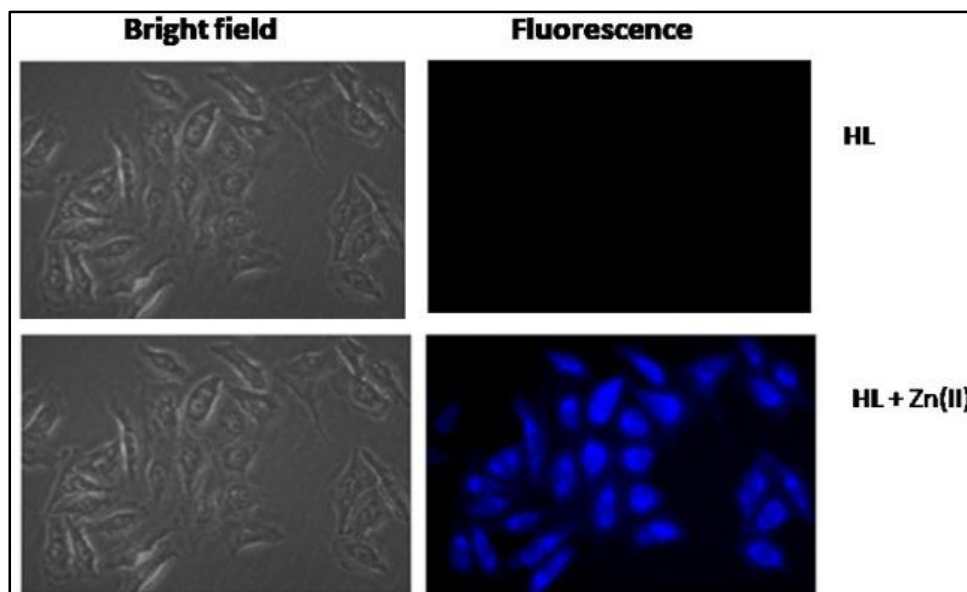


Fig. 1.8.3: Fluorescence microscopy images of HeLa cells incubated with HL and HL- Zn(II).[71]

1.8.3. Application in construction of molecular logic gates

In recent times construction of molecular logic gates has been an area of interest in chemosensor research. [72-74] It may have various applications such as in digital information security, molecular arithmetic, construction of memory devices and drug action. A molecular logic gate, used as a digital building block, may be constructed when there is more than one chemical input that corresponds to a single signal output giving rise to a logic function viz. AND, OR, NAND or INHIBIT. [75]

In 2022, P. Das et al. reported construction of an INHIBIT logic gate with three chemical inputs viz. the free ligand(HL), Zn(II) ion and EDTA and the fluorescence emission at 459 nm as a single output. The Zn(II) ion turns on the emission at 459 nm upon its addition to the free receptor. On further addition of EDTA, it forms a stronger complex with Zn(II) and frees the receptor again turning the emission output off. EDTA has been used as a chemical output via an inverter. The fig. 1.8.4 shows the inhibit logic gate and the relevant truth table. [76]

CHAPTER 1

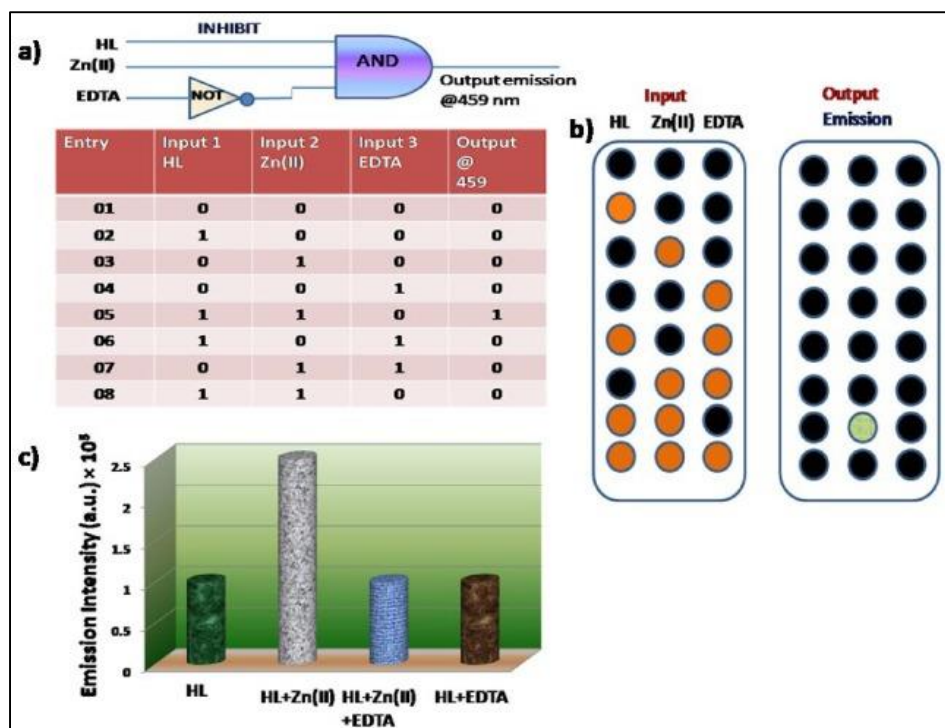


Fig. 1.8.4: The logic circuit and the truth table for the chemosensor reported by P. Das et al. [76]

In 2008, D. Zhang et al. reported a merocyanin receptor marked 'L' which was used to construct a few unique logic circuits having NAND, NOR and INHIBIT functions. The polarity of the solvent is the first input (Input value is '1' when a high polarity solvent is used and '0' when a low polarity solvent is used) and the second input is either H^+ concentration or Hg^{2+} in case of different logic gates. The two output signals are the fluorescence emissions at 470 nm and 520 nm (output is regarded as '1' when the relative intensity is over 70-80% and '0' when it is below 10-30%). Both H^+ and Hg^{2+} concentrations lead to fluorescence quenching of the ligand but only when high polarity solvent is used. The molecular logic circuits and the truth tables are schematically represented in the fig. 1.8.5 and fig. 1.8.6. [77]

CHAPTER 1

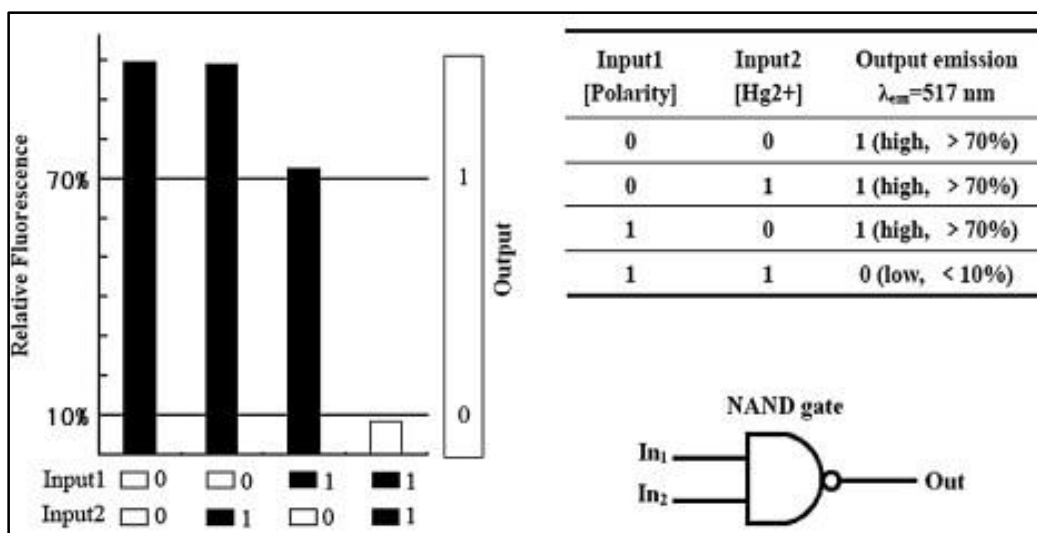


Fig. 1.8.5: The NAND logic gate reported by D. Zhang et al. and the corresponding truth table. [77]

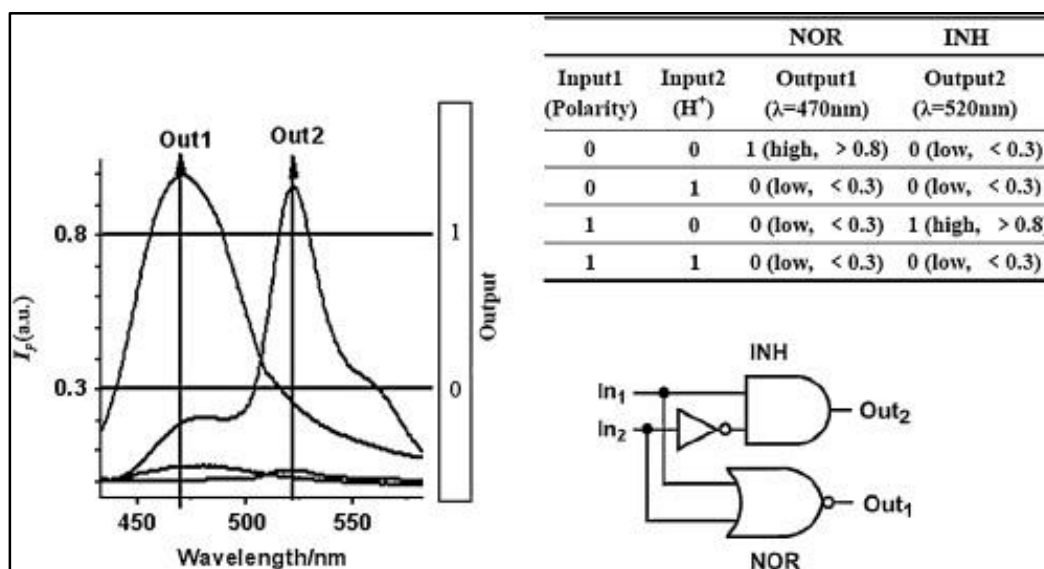


Fig. 1.8.6: The NOR and INHIBIT logic gate reported by D. Zhang et al. and the corresponding truth table. [77]

CHAPTER 1

1.9. Aim of the thesis

The aim of the present thesis is to explain, to its readers, how the chemosensor research works and to demonstrate how to conceptualize and develop chemosensors for selective determination of toxic and biologically relevant metal ions. It also consists of a complete body of research work on metal ion chemosensors along with their application in modern science. Keeping in mind the ever-increasing need to develop efficient, selective and low-cost chemosensors for the detection of metal ions, a few novel efficient aluminium, mercury, nickel and zinc ion sensors have been synthesized using economically viable routes. The chemosensors binds with the selective metal ions very quickly along with a visible change in most cases and hence have the benefit of real time, naked-eye detection. In comparison with the conventional methods, which require expensive analytical instruments that are difficult to transport, these chemosensors are far superior for on-field sample analysis. They all have comparatively lower limit of detection than their predecessors. This enables them to detect metal ions in biological and environmental samples even when these ions are present in very minuscule quantities. The optical sensors presented here are also found to be effective in the metal ion concentration ranges prescribed by WHO. Most of the chemosensors in this thesis are reversible in nature and can be reused. This thesis also duly notes the application of the chemosensors as optical biosensor, in live cell imaging studies, construction of certain molecular logic gates and in development of easy detection tools such as ‘dip sticks’.

1.10. References

1. L.Prodi , F. Bolletta, M. Montalti, N. Zaccheroni, *Coord. Chem. Rev*, 2000, **205**, 59–83.
2. O. S. Wolfbeis, editor, *Optical Sensors*, Industrial, Springer: Germany (2004)
3. B. R. Eggins. *Chem. Sens. Biosens*, John Wiley & Sons (2002).
4. J. G. Vos, R. T. Forster, T. E. Keyes *Interfacial supramolecular assemblies*, New Jersey, John Wiley, 2003.

CHAPTER 1

5. A. K. Mahapatra, S. S. Ali, K. Maiti, S. Mondal, R. Maji, S. Manna, S. K. Manna, M. R. Uddin and S. Mandal, *RSC Adv.*, 2016, **6**, 113219.
6. M. R. Lockett, H. Lange, B. Breiten, A. Heroux, W. Sherman, D. Rappoport, P. O. Yau, P. W. Snyder, G. M. Whitesides, *Angew. Chem. Int. Ed.*, 2003, **52** (30), 7714–7717.
7. (a) G. A. Jeffrey, *An Introduction to Hydrogen Bonding*, Oxford University Press: Oxford, 1997; (b) H. Dugas, *Bio-organic Chemistry*, Springer Verlag, New York, Inc. 1996; (c) J. M. Lehn, *Supramolecular Chemistry*, Weinheim, New York, Basel. Cambridge, Tokyo: VCH, 1995. 3.
8. (a) F. Vogtle, *Supramolecular chemistry, An Introduction*; Wiley & Sons: Chichester, 1993; (b) P. D. Beer, P. A. Gale and D. K. Smith, *Supramolecular Chemistry*, Oxford University Press, New York, 1999. (c) S. H. Gellman, *Chem. Rev.* 1997, **97**, 1231; (d) T. Schrader and A. D. Hamilton, *Functional Synthetic Receptors*, Wiley-VCH, Weinheim, 2005. (e) A. D. Hamilton, *Supramolecular Control of Structure and Reactivity (Perspective in supramolecular Chemistry)*, Wiley, New York, 1996.
9. C. J. Pedersen, *J. Am. Chem. Soc.* 1967, **89**, 2495.
10. (a) J. -M. Lehn, *Pure Appl. Chem.* 1978, **50**, 871; (b) J. -M. Lehn, *Acc. Chem. Res.* 1978, **11**, 49.
11. (a) D. J. Cram and J. M. Cram, *Science* 1974, **183**, 803; (b) D. J. Cram and J. M. Cram, *Container Molecules and Their Guests*, Royal Society of Chemistry, Cambridge, 1994; (c) J. -M. Lehn, *Angew. Chem.* 1988, **100**, 91; (d) J. -M. Lehn, *Science*, 1985, **227**, 849.
12. A.P. de Silva, H.Q.N. Gunaratne, T. Gunnlaugsson, A.J.M. Huxley, C.P. McCoy, J.T. Rademacher, T.E. Rice, *Chem. Rev.* 1997, **97**, 1515.
13. A.W. Czarnik, editor, *Fluorescent Chemosensors for Ion and Molecule Recognition*, A.C.S, Washington, 1992.
14. Y. -Q. Weng, F. Yue and Y. -R. Zhong, *Inorg. Chem.*, 2007, **46**, 7749.
15. D. Buccella, J. A. Horowitz, S. J. Lippard, *J. Am. Chem. Soc.*, 2011, **133**, 4101.
16. M. Montalti, L. Prodi, N.J. Zaccheroni, *Materials Chemistry* 15 (2005) 2810.
17. A. P. de Silva, H. Q. N. Gunaratne, C. P. McCoy, *Nature*, 1993, **364**, 42.

CHAPTER 1

18. Z. Liu, W. He, Z. Guo, *Chem. Soc. Rev.*, 2013, **42**, 1568.
19. Y. Xiang, A. Tong, P. Jin and Y. Ju, *Org. Lett.*, 2006, **8**, 2863.
20. Jablonski A. 1935. Über den Mechanisms des Photolumineszenz von Farbstoffphosphoren, *Z. Phys.*, **94**, 38–46.
21. Strickler SJ, Berg RA. 1962. Relationship between absorption intensity and fluorescence lifetime of molecules. *J ChemPhys*, **37**, 814.
22. Jian-Fa Zhu, Han Yuan, Wing-Hong Chan, Albert W. M. Lee, *Tet. Lett.*, 2010, **51**, 3550–3554.
23. Jingyu Piao, Jia Lv, Xin Zhou, Tong Zhao, Xue Wu, *Spectrochimica Acta Part A*, 2014, **128**, 475–480.
24. Kanhu Charan Behera, Debajani Mallick, Braja Narayan Patra, Bamaprasad Bag, *Spectrochimica Acta Part A*, 2022, **271**, 120934
25. Formica, Mauro; Fusi, Vieri; Giorgi, Luca; Micheloni, Mauro, *Coord. Chem. Rev.*, 2012, **256** (1–2): 170–192.
26. Elena Pazos, Olalla Va'zquez, Jose' L. Mascaren'as and M. Eugenio Va'zquez, *Chem. Soc. Rev.*, 2009, **38**, 3348–3359
27. Zhiyong Zhang, Chengjun Wang, Zhongzhi Zhang, Yijing Luo, Shanshan Sun, Guangqing Zhang, *SpectrochimiaActa Part A*, 2019, **209**, 40-48.
28. Luís Gustavo Teixeira Alves Duarte, Felipe Lange Coelho, Jose Carlos Germino, Gabriela Gamino da Costa, Jonatas Faleiro Berbigier, Fabiano Severo Rodembusch, Teresa Dib Zambon Atvars, *dyes and pigments*, 2020, **181**, 108566.
29. A. Weller, *Pure Appl. Chem.* 1968, **16**, 115.
30. Soon Young Kim, Jong-In Hong, *Tetrahedron Lett.*, 2009, **50**, 2822-2824.
31. Pavel A. Panchenko, Pavel A. Ignatov, Marina A. Zakharko, Yurii V. Fedorov and Olga A. Fedorova, *Mendeleev Commun.*, 2020, **30**, 55–58.
32. Xiao-li Yue, Zhao-qing Wang, Chao-rui Li, Zheng-yin Yang, *Tetrahedron Letters* 2017, **58**, 4532–4537.

CHAPTER 1

33. T. Iijima, A. Momotake, Y. Shinohara, T. Sato, Y. Nishimura and T. Arai, *J. Phys. Chem. A.*, 2010, **114**, 1603.
34. Wilver A. Muriel, Rodrigo Morales-Cueto and William Rodríguez-Córdoba, *Phys. Chem. Chem. Phys.*, 2019, **21**, 915-928.
35. J. S. Wu, W. M. Liu, J. C. Ge, H. Y. Zhang, P. F. Wang, *Chem. Soc. Rev.*, 2011, **40**, 3483.
36. S. Park, J. E. Kwon, S. H. Kim, J. Seo, K. Chung, S. Y. Park, D. J. Jang, B. M. Medina, J. Gierschner, S. Y. Park, *J. Am. Chem. Soc.*, 2009, **131**, 14043.
37. V. Luxami, S. Kumar, *New J. Chem.*, 2008, **32**, 2074.
38. Zhaodi Liu, Huajie Xu, Shuisheng Chen, Liangquan Sheng, Hong Zhang, Fuying Hao, Pengfei Su, Wenlong Wang, *Spectrochimica Acta Part A*, 2015, **149**, 83-89.
39. Caixia Yuan, Shiyang Li, Yanbo Wu, Liping Lu, Miaoli Zhu, *Sensors and Actuators B*, 2017, **242**, 1035–1042.
40. Lin Wang, Hao Li, Yu Yang, Di Zhang, Min Wu, Bo Pan, Baoshan Xing, *Water Research*, 2017, **122**, 337-344.
41. a) E Ciotta, P. Proposito, R. Pizzoferrato, *Journal of Luminiscence*, 2019, **206**, 518-522; b) E. Ciotta, S. Paoloni, M. Richetta, P. Proposito, P. Tagliatesta, C. Lorecchio, I. Venditti, I. Fratoddi, S. Casciardi, R. Pizzoferrato, *Sensors*, 2017, **17**, 1-15; c) E. Ciotta, P. Proposito, P. Tagliatesta, C. Lorecchio, L. Stella, S. Kaciulis, P. Soltani, E. Placidi, R. Pizzoferrato, *Sensors*, **18**, 2018, 1-15.
42. a) Lei Liu, Ran Ding, Yue yuan Mao, Bing qing Sun, *Chem. Phys. Lett.*, 2022, **793**, 139393, b) G. R. Desiraju, Eds. *Crystal Design: Structure and Function, Perspective in Supramolecular Chemistry*, Vols. 7, John Wiley & Sons Ltd.: New York, NY, 2003, c) G. R. Desiraju and A. Gavezzotti, *Chem. Commun.* 1989, 621.
43. (a) B. Askew, P. Ballester, C. Buhr, K. S. Jeong, S. Jones, K. Parris, K. Williams and J. Jr. Rebek, *J. Am. Chem. Soc.* 1989, **111**, 1082; (b) A. D. Hamilton and D. Van Engen, *J. Am. Chem. Soc.* 1987, **109**, 5035; (c) A. Sygula, F. R. Fronczek, R. Sygula, P. W. Rabideau and M. M. Olmstead, *J. Am. Chem. Soc.* 2007, **129**, 3842.
44. S. C. Zimmerman, C. M. VanZyl and G. S. Hamilton, *J. Am. Chem. Soc.* 1989, **111**, 1373.

CHAPTER 1

45. S. C. Zimmerman, M. Mrkisch and M. Baloga, *J. Am. Chem. Soc.* 1989, **111**, 8528.
46. (a) S. K. Burley and G. A. Petsko, *Science*, 1985, **229**, 23; (b) S. K. Burley and G. A. Petsko, *Adv. Protein Chem.* 1988, **39**, 125; (c) U. Derewenda, Z. Derewenda, E. J. Dodson, G. G. Dodson, C. D. Reynolds, G. D. Smith, C. Sparks and D. Swenson, *Nature*, 1989, **338**, 594; d) Maria G. Khrenova, Alexander V. Nemukhin, Vladimir G. Tsirelson, *Chemical Physics*, 2019, **522**, Pages 32-38.
47. (a) D. Gust and T. A. Moore, *Topics Curr. Chem.*, 1991, **159**, 103; (b) H. M. Colquhoun, J. F. Stoddart, D. J. Williams, J. B. Wolstenholme and R. Zarzycki, *Angew. Chem. Int. Edn. Engl.*, 1981, **20**, 1051.
48. C. J. Pedersen, *Angew. Chem. Int. Ed. Engl.*, 1988, **27**, 1021.
49. Yongjie Ding, Chunxiang Zhao, Pengcheng Zhang, Yahong Chen, Weiwu Song, Guanglu Liu, Zengchen Liu, Lin Yun, Ruiqi Han, *J. Mol. Struct.*, 2021, **1231**, 129965.
50. Ju Byeong Chae, Hyo Jung Jang, Cheal Kim, *Photochem. Photobiol. Sci.*, 2017, **16**, 1812.
51. Senmiao Tong, Liqin Zhang, Liu Bing, Lita Yi, *sensors and Actuators B*, 2014, **203**, 157-164.
52. Hyeongjin Kim, Minji Lee, Jae Jun Lee, Eun Ki Min, Ki-Tae Kim, Cheal Kim, *Journal of Photochem. And Photobiology A: Chemistry*, 2022, **428**, 113882.
53. Elif Senkuytu, Esra Tanriverdi Ecik, Mahmut Durmus, Gonul Yenilmez Ciftci, *Polyhedron*, 2015, **101**, 223-229.
54. Wei Cui, Lingyun Wang, Gang Xiang, Lixia Zhou, Xiaoning An, Derong Cao, *Sensors and Actuators B*, 2015, **207**, 281-290.
55. Jaewon Kim, Suji Lee, Sudeok Kim, Minhyuk Jang, Hohjai Lee, Min Su Han, *Dyes and Pigments*, 2020, **177**, 108291.
56. Yong-Sheng Mi, Dong-Ming Liang, Ya-Ting Chen, Xu-Biao Luo, Jian-nan Xiang, *RSC Adv.*, 2014, **4**, 42337.
57. R. A. Bissell, A. P. de Silva, H. Q. N. Gunaratne, P. L. M. Lynch, G. E. M. Maguire and K. R. A. S. Sandanayake, *Chem. Soc. Rev.*, 1992, **21**, 187.

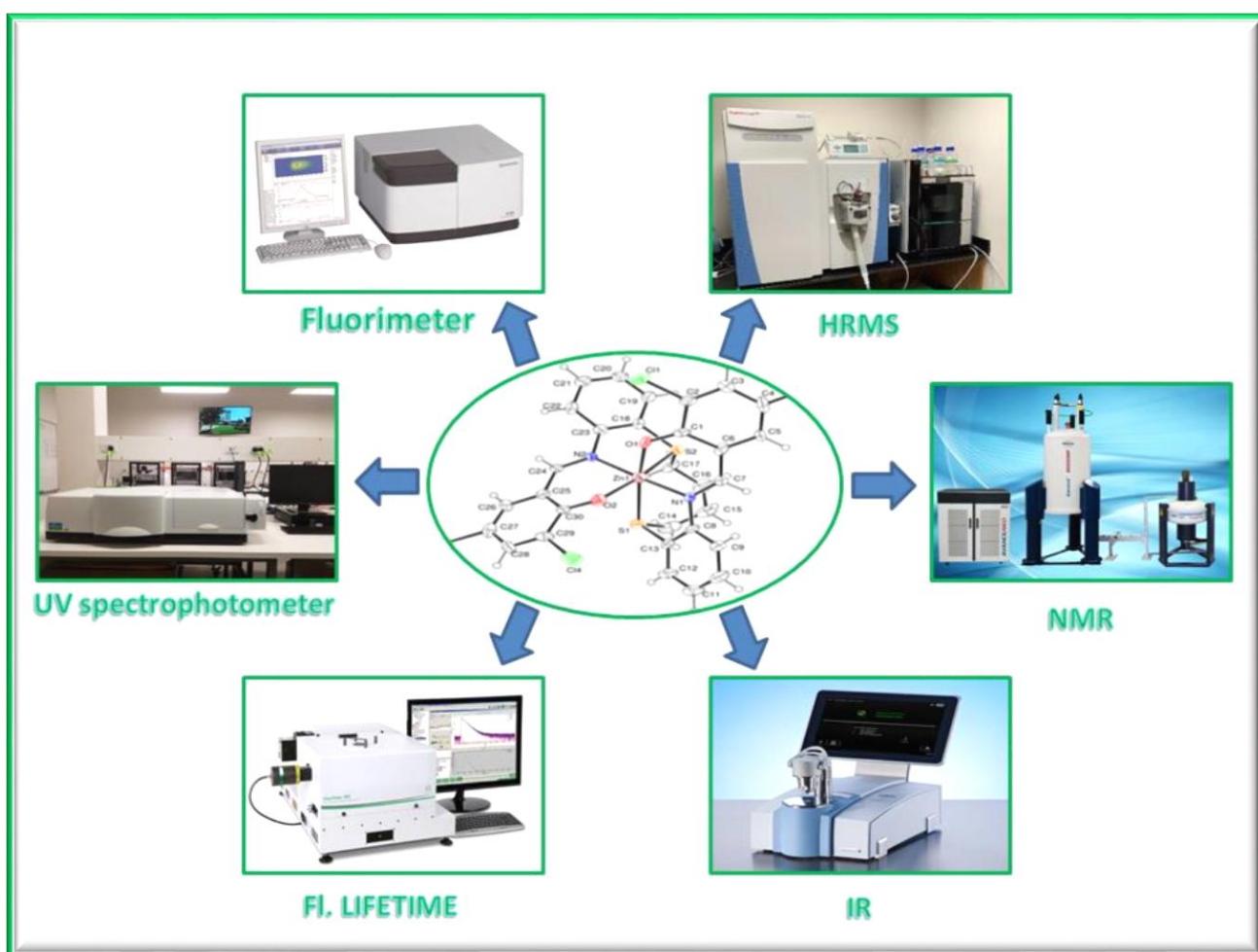
CHAPTER 1

58. Kuljit Kaur, Rajnish Saini, Ashwani Kumar, Vijay Luxami, Navneet Kaur, Prabhpreet Singh, Subodh Kumar, *Coord. Chem. Rev.*, 2012, **256(17-18)**, 1992-2028.
59. M.-Y. Chae and A. W. Czarnik, *J. Am. Chem. Soc.*, 1992, **114**, 9704.
60. (a) V. Dujols, F. Ford and A. W. Czarnik, *J. Am. Chem. Soc.*, 1997, **119**, 7386; (b) A. P. de Silva, T. S. Moody and G. D. Wright, *Analyst*, 2009, **134**, 2385.
61. (a) P. Damborský, J. Švitel and J. Katrlík, *Essays Biochem.*, 2016, **60**, 91; (b) Chen Chen and Junsheng Wang, *Analyst*, 2020, **145**, 1605.
62. Chen Chen and Junsheng Wang, *Analyst*, 2020, **145**, 1605.
63. S. F. D'Souza, *Biosens. Bioelec.*, 2001, **16**, 337.
64. E. M. Bosch, J. R. A. Sanchez, S. F. Rojas and B. C. Ojada, *Sensors*, 2007, **7**, 797.
65. Giorgi Shtenberg, Naama Massad-Ivanir and Ester Segal, *Analyst*, 2015, **140**, 4507.
66. J. Zheng, X. Mao, J. Ling, Q. He, J. Quan, *Biological Trace Element Research*, 2014, **160 (1)**, 15-23.
67. S. Krupanidhi, A. Sreekumar, C.B. Sanjeevi, *Indian Journal of Medical Research*, 2008, **128 (4)**, 448-461.
68. J.R. Walton, *Neurotoxicology*, 2006, **27 (3)**, 385-394.
69. V. Gujar, V. Pundge, D. Ottoor, *Journal of Luminescence*, 2015, **161**, 87-94.
70. Ezhumalai, Dhineshkumar, Mathivanan, Iyappan, Chinnadurai, Anbuselvan, *Spectrochimica Acta Part A*, 2018, **199**, 209-219.
71. Pranabendu Das, Swati Singh Rajput, Manik Das, Soumik Laha, Indranil Choudhuri, Nandan Bhattacharyya, Arindam Das, Bidhan Chandra Samanta, Md. Mehboob Alam, Tithi Maity, *Journal of Photochemistry & Photobiology A*, 2022, **427**, 113817.
72. P.A. De Silva, N.H.Q. Gunaratne, C.P. McCoy, *Nature*, 1993, **364**, 42-44.
73. J. Qin, Z. Yang, *J. Photochem. Photobiol.*, 2016, **324**, 152-158.
74. W.T. Huang, Y. Shi, W.Y. Xie, H.Q. Luo, N.B. Li, *Chem. Commun.* 2011, **47**, 7800-7802.

CHAPTER 1

75. Debrupa Biswas, Nandagopal Bar, Sumana Pal, SwapanKumar Mazumder, Arindam Ray, Shreyashi Chowdhury, GourabKanti Das, Pranesh Chowdhury, *Journal of Molecular Structure*, 2022, **1252**, 132166.
76. Pranabendu Das, Swati Singh Rajput, Manik Das, Soumik Laha, Indranil Choudhuri, Nandan Bhattacharyya, Arindam Das, Bidhan Chandra Samanta, Md. Mehboob Alam, Tithi Maity, *Journal of Photochemistry & Photobiology A*, 2022, **427**, 113817.
77. Dong Zhang, Jianhua Su, Xiang Ma, He Tian, *Tetrahedron*, 2008, **64**, 8515–8521.

Instrumentations and techniques



2.1. Introduction

The nascent step in designing a chemosensor is the creation of a scheme and devising a plan for synthesis of the targeted molecular chemosensor. The actual synthesis follows the first step which is carried out in the wet laboratory. This chapter talks about the steps thereafter and more specifically the instruments and techniques required in those steps. Characterization of the synthesized probe and the metal complexes mentioned throughout this thesis is done with instrumental methods such as HRMS, IR, $^1\text{H-NMR}$, $^{13}\text{C-NMR}$, X-ray diffraction crystallography etc. A plethora of photo-physical instruments or techniques such as UV-VIS Spectrophotometer or UV-Vis spectroscopy, Fluorimetry, Time-resolved fluorimetry or Lifetime decay fluorimeter and pH-meters for pH-studies etc. are used in the sensing studies of the chemoreceptor. Single crystal X-ray diffraction method is used to determine the structure of the chemosensor molecule in the cases where single crystal of the compound has been obtained.

2.2. Methods of characterization

Thorough characterization of the purified synthesized receptor molecule was carried out using the different techniques as described below.

2.2.1. High resolution mass spectrometry (HRMS) and Elemental analysis

High Resolution Mass Spectrometry is an essential part of the characterization process after the synthesis step. From the molecular ion peak given in the HRM spectra we can know the molecular weight of the synthesized compound and compare it with that of the desired chemosensor. We can also comment about the structural composition of the synthesized molecule by recognizing mass fragments in the spectra.

In this technique, sample molecules are bombarded with a beam of electrons having high energy. As a result, the molecules ionize and break up into many a number of fragments. Some of them are positive ions. Each type of ion has a particular m/z ratio i.e., mass to charge ratio. For most ions, the charge is one and thus m/z ratio is basically the molecular mass of the ion. A distinct signal is obtained for each value of m/z which corresponds to the mass of the particular fragment. The

CHAPTER 2

intensity of each signal corresponds to the relative abundance of the ion generating the signal. The Intensity of the most intense peak in the structure is taken as 100% and it is known as the base peak.

Elemental analysis is also a proven technique which gives the percentage of elements like C, H and N present in a compound. In this thesis all the HRMS data were recorded on Waters (Xevo G2 Q-TOF) mass spectrometer and the elemental analysis was carried out in a 2400 Series-II CHN analyzer, Perkin Elmer, USA.

2.2.2. Infrared Spectroscopy (IR spectra)

Infra-red spectroscopy is another potent method which gives ample information indicating the structure of synthesized probes. Unlike UV-VIS spectrum which consists of moderately few peaks, the IR technique produces a spectrum including a great number of absorption bands from which a lot of information may be collected about a particular structure. Upon absorption of infra-red radiation, the various bonds in a molecule begin to bend and stretch. The most significant infra-red region is from 2.5 μ to 15 μ in which molecular vibrations can be detected and measured. The absorption of IR radiations can be assigned either in terms of wavelength (λ) or in terms of wave number (ν).

Mostly, IR spectra of various samples are plotted as absorbance or percent transmittance versus wave number. The correlation between wave number and wavelength is as follows:

$$\text{Wave number} = 1/\text{wavelength (in cm)}$$

Band intensity is either expressed in terms of absorbance (A) or transmittance (T).

$$A = \log_{10}(1/T)$$

When a molecule absorbs IR radiation it causes excitation of that molecule from a lower to the higher vibrational energy level. These vibrational energy levels are connected with a number of narrowly spaced rotational levels. Among all the bonds in a molecule only those associated with a change in dipole moment upon vibration are eligible to absorb in the IR frequency region. In case of such bonds, vibrational transitions accompany dipole moment change and are called IR-active transitions. The compounds having such a vibrational transition will be called IR-active compounds. Thus IR spectroscopy is also termed as vibrational-rotational spectroscopy.

All the IR data in this thesis were recorded on a RX-1 PerkinElmer spectrophotometer and samples were prepared as KBr pellets.

CHAPTER 2

2.2.3. ^1H -NMR Spectroscopy: waltz with a proton

^1H as well as ^{13}C NMR spectroscopies are the most useful analytical techniques to characterize the structure of a newly synthesized chemosensor. Nuclear magnetic resonance is a phenomenon which occurs when the magnetic energy of the protium nucleus or some other type of nuclei, under an external static magnetic field, interacts with the oscillating magnetic field of an electromagnetic radiation. Among all the spectroscopic methods, the NMR spectroscopy uses electromagnetic wave with the lowest frequency for excitation. The sample nucleus absorbs electromagnetic energy in the radio-wave region. The absorption peaks appear at different frequencies depending upon the type of proton or other nuclei contained in the sample compound.

It is a nondestructive technique and gives response in molar ratio, which allows structure elucidation of the desired molecules. In this method the protons in an organic or inorganic molecule are exposed to a powerful magnetic field. Under the influence of that external magnetic field the different protons then start their waltz like dance like a spinning top or to be more scientific, start to precess at different frequencies. [1] Now these precessing protons can either align themselves in parallel or in anti-parallel orientation with respect to the external magnetic field. Now when these precessing protons are irradiated with steadily changing radio frequencies, protons undergo transition from low-energy parallel state to high-energy anti-parallel state. This transition only occurs when they find a match between the transition energy and the energy of the radiation. In that case absorption occurs and a signal is obtained. The spectrum obtained by this experiment is called nuclear magnetic resonance spectrum. In an NMR spectrum, magnetic field strengths applied for all the types of protons are measured and the corresponding absorption peaks are plotted. The total number of signals at different field strengths indicates the types of the different sets of equivalent protons present in the sample molecule. The position of the signals in the total field range of the spectrum helps us to know if the protons are adjacent to any particular electron attracting or electron releasing group.

When a molecule is placed in a magnetic field, the electrons also circulate the protons thereby producing secondary magnetic fields. When this induced field is in opposition with the external magnetic field, the proton is said to be shielded. When shielding occurs the protons undergo transition at a higher magnetic field and are said to be shifted upfield. Deshielding effect makes the proton to absorb radio frequency at a lower magnetic field and hence are said to be shifted downfield. These shifts are called chemical shifts. For determining chemical shifts of protons of various natures in a molecule, the signal for tetramethylsilane (TMS) is taken as a reference. For a

CHAPTER 2

particular proton in a molecule, NMR signal appears at a particular field strengths compared to a reference signal from TMS. The chemical shift is the difference in the signal position of a particular proton with respect to the reference signal given by the TMS protons. It is measured in equivalence frequency and expressed as δ value. Its unit is ppm (parts per million) as is evident from the units taken in the numerator and the denominator.

$$\delta = (v_{\text{sample}} - v_{\text{TMS}}) / \text{operating frequency}$$

(unit of numerator in hertz and denominator in megahertz)

The solvent used must have no protons so that it does not give absorption of its own in NMR spectrum. Conventionally deuterated solvents like CDCl_3 and DMSO-D_6 are used as deuterium is effectively NMR silent in the operating frequency range of proton NMR. [2]

In an NMR spectrum, the area under each peak is proportional to the number of protons in each set of protons present in the studied compound. Often due to the coupling of different protons in the surroundings of the absorbing proton, a signal undergoes splitting to form multiplets. Importantly the separation between the midpoints of the two adjacent peaks in a multiplet is usually called the J-coupling constant. The coupling constants are generally expressed in Hz.

In case of NMR titration, inferences about the stability of the host-guest complex can be drawn by determining the association constant from analysis of the chemical shift values. The exact stoichiometry of a receptor molecule can be determined by simply plotting the chemical shift versus host-guest mole ratio when the binding constant is large and exchange is fast. When broad range of binding constants is considered and dynamic exchange between the free host and the complex is fast on the NMR time scale, Job's method is usually adopted for the stoichiometry of the complex. If it is slow on the NMR time scale, the stoichiometry of the complex is apparent [2].

Each and every ^1H NMR spectra of all the synthesized chemosensors, their metal complexes and other associated compounds were recorded on a Bruker 300 MHz instrument.

CHAPTER 2

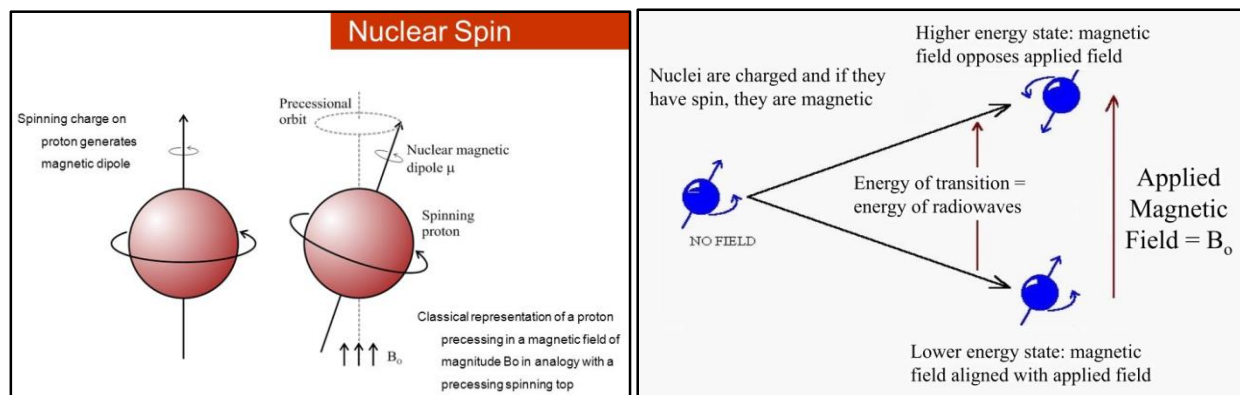


Fig 2.1: The waltz of a proton: Larmor precession & **Fig 2.2:** NMR spin energy levels under external magnetic field (B_0).

2.2.4. ^{13}C NMR Spectroscopy: waltz of the other kind

^{13}C -NMR is comparatively a young technique. There are prominent differences between the ^1H and ^{13}C spectra both in the form of recording as well as in application. The nuclear spin quantum number is denoted by I and its value for C^{12} nucleus is equal to zero. So, being non-magnetic it does not give rise to NMR signal. On the contrary, C^{13} has a spin quantum number equal to $\frac{1}{2}$ and it is NMR active but with natural abundance of 1.11% only. Every C^{13} signal couples strongly with the directly attached protons and also couples with the protons which are in two to four bonds distance from it. The value of the coupling constants changes in accordance to the distance between C^{13} and the proton. For almost all organic molecules, complete C^{13} spectra appear in the range of 0-200 ppm. The common internal standard used for ^{13}C NMR is tetramethylsilane TMS.

All the ^{13}C NMR spectra of the synthesized compounds in the thesis was recorded on a Bruker 300 MHz instrument.

2.2.5. UV-Vis absorption spectroscopy

The foremost step in the ion sensing studies of the chemo-receptors is the study of changes in the absorption spectra of the ligand upon gradual addition of the specific ionic analytes that is being sensed along with the other co-existing ions. The specific changes in the absorption spectra indicates complexation and are often associated with a colorimetric change i.e., alteration in its color.

CHAPTER 2

The wavelength range in which absorption is studied is between 200-700 nm (UV-Visible range), hence the name. Since, radiation in this range can inflict electronic transition, the alternate title for this technique is Electronic spectroscopy. For visible and ultra-violet spectrum, electronic excitations leads to the promotion of electrons from a lower energy molecular orbital to a higher energy molecular orbital. Compounds which absorb in the visible range appears colored to the human eye and any change in the spectrum of such compound results in change of color.

In the UV-Vis plot or the absorption spectrum, the wavelength (nm) is taken in the x-axis and the absorbance (a.u.) is taken in the y-axis as a function of the former. Generally the spectrum consists of a number of absorption bands. There are two laws explaining the absorption changes by the molecules. These are: (i) Lambert's law and (ii) Beer's law.

As a combination of these two laws, the Lambert-Beer's law can be stated as:

$$I(\nu) = I_0(\nu)10^{-\epsilon(\nu)cl}$$

Where $I_0(\nu)$ and $I(\nu)$ are the intensity of incident light and transmitted light respectively at the frequency ν , ϵ is the molar extinction coefficient or absorptivity at frequency ν which can be expressed in $L(\text{liters})\text{mol}^{-1}\text{cm}^{-1}$, c is the concentration of solution in moles litre^{-1} and l is the path length (cm) of the absorbing medium.

For a UV-Vis experiment, absorption spectra of the solvent in which the sample is dissolved, is recorded at first. Now one can eliminate the contribution of the solvent from the absorption spectra of the probe itself so that no solvent peaks are recorded. This process is called as baseline correction. The samples of desired concentration are then taken in a quartz cuvette and the absorption spectrum measurement is carried out. All the electronic spectra reported in this thesis were recorded in a Perkin Elmer Lambda 750 spectrophotometer.

2.2.6. Fluorescence Spectroscopy

The emission spectra of the synthesized probes were also recorded and analyzed to check if the probe has the scope of being a fluorescent chemosensor. If a specific and reproducible change in the emission spectra of the probe is observed upon addition of a selective analyte then various detailed studies (viz. Fluorescence titration, competition study, pH study, fluorescence lifetime measurements) are required to ascertain the sensing pattern of the receptor.

CHAPTER 2

A brief study of the Jablonski diagram reveals the fundamentals of photoluminescence processes that occur in various molecules. Jablonski diagram illustrates a variety of processes that occur between absorption and emission of light energy by complex molecular systems. It demonstrates various radiative and non-radiative processes which occur in the excited state of the molecule [3]. The Jablonski diagram is shown in Figure 2.2. The symbols S_0 , S_1 and S_2 signifies respectively the singlet, ground, first and second electronic states. At each of these electronic energy levels, there exists a number of vibrational energy levels, represented as by 0, 1, 2, etc. The electronic transitions occur in about a femtosecond. The displacement of the nucleus is irrelevant in such a small time span. This is demonstrated in Frank-Condon principle. The fluorophores do not populate the higher or excited vibrational levels at normal temperatures. Hence, absorption and emission take place mostly from or to the lowest vibrational energy states. The fluorophore gets excited to some higher vibrational level of either S_1 or S_2 upon absorption of light energy. When the molecules jump from S_2 to S_1 the process is called internal conversion. When the molecules undergo radiative relaxation from S_1 to S_0 state emission of light energy occurs and the process is termed fluorescence. Conversion of S_1 to T_1 is called intersystem crossing due to change in spin. Emission of light occurring during spin forbidden transition from the triplet ground state to singlet ground state is termed as phosphorescence [4]. As phosphorescence is spin forbidden the rate constants for such emission are much smaller than those for fluorescence.

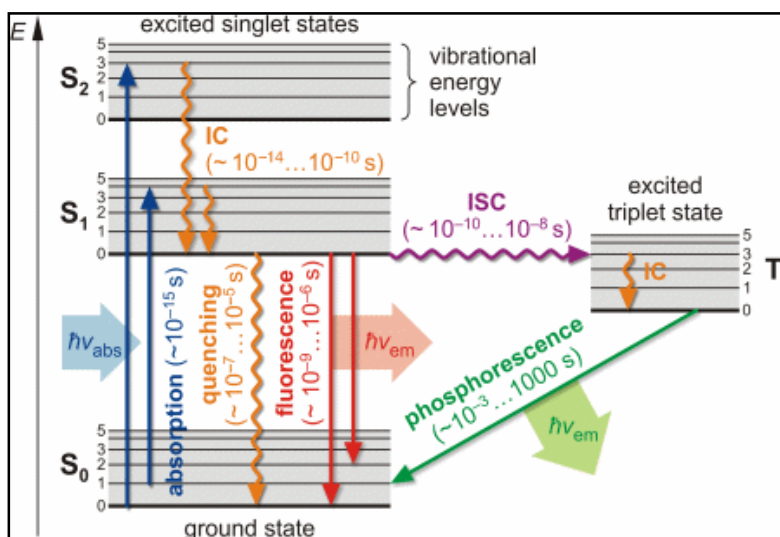


Fig. 2.3: Jablonski diagram demonstrating all the excitation and relaxation processes involved in photoluminescence.

CHAPTER 2

For a typical fluorescence measurement, the samples of desired concentration were prepared in quartz cuvette and the emission spectra were recorded without any baseline correction as in this case contribution in the photo-luminescence spectra from the solvent part is negligible. All the fluorescence spectral data reported in this thesis were recorded with the aid of Shimadzu RF-6000 fluorescence spectrophotometer at room temperature (298 K).

2.2.7. Fluorescence lifetime measurement

Fluorescence lifetime of an excited state is the characteristic average time a molecule stay in that excited state before undergoing decay. The Fluorescence lifetime decay curve is plotted against time for a particular emission wavelength which arises upon excitation at a particular wavelength. In general, a fluorescent molecule exhibits a single exponential decay and the relationship between their emission intensity and time can be expressed as:

$$I(t) = I(0) \exp(-kt)$$

Where, $I(0)$ and $I(t)$ are the fluorescence intensity at the original stage ($t = 0$) i.e., the moment when excitation stops and at any given time 't' respectively; k is the rate constant describing the decay processes. Both radiative and non-radiative decays affect the rate constant, k .

A radiative decay rate constant is k_r which is characterized by lifetime τ_r and a non-radiative decay rate constant is k_{nr} , characterized by lifetime τ_{nr} . So, the equation of lifetime derived given as:

$k = k_r + k_{nr} = 1/\tau_r + 1/\tau_{nr} = 1/\tau$ and the equation becomes,

$$I(t) = I(0) \exp (-t/\tau)$$

One can obtain the overall fluorescence lifetime τ , by fitting a single exponential decay to the experimental fluorescence decay curve.

For a typical measurement, the samples of desired concentration were prepared in quartz cuvette and the emission spectra were recorded. The lifetime measurement of synthesized probes is a valuable tool to study further about these sensors. All the lifetime decay measurement in this thesis work was done using time-correlated single photon counting set up from Horiba Jobin-Yvon. The emission decay data were collected on a Hamamatsu MCP photomultiplier (R3809) and were analyzed by using IBH DAS6 software. The goodness of fit was evaluated by χ^2 criterion and visual inspection of the residuals of the fitted function to the data. Generally, fluorescence has a lifetime of a few nanoseconds (ns), while spin-forbidden phosphorescence has a lifetime in the order of microsecond (μ s) to millisecond (ms).

2.2.8. Single crystal X-ray diffraction technique

Single crystal X-ray diffraction provides various important data like, unit cell dimensions, bond-lengths, bond-angles and details of site-ordering etc. about the internal lattice of crystalline substances in a non-destructive way. Next step is the single-crystal structure refinement or in other words ‘solving of crystal structure’ where the data generated from the X-ray analysis is interpreted and refined to obtain the crystal structure.

In 1912, Max von Laue discovered that the spacing of planes in the crystal lattice of crystalline substances act as three-dimensional diffraction gratings for X-ray wavelengths. X-ray diffraction has emerged as a familiar procedure for the study and deduction of crystal structures and atomic spacing. In X-ray diffraction constructive interference occurs between monochromatic X-rays, that are produced by a cathode ray tube, and a crystalline sample. X-rays from the source are usually filtered to generate monochromatic radiation and directed towards the sample compound. The rays incident upon the sample produces constructive interference only when conditions satisfy Bragg's Law ($n\lambda = 2d\sin\theta$). Where, ‘ λ ’ denotes the wavelength of electromagnetic radiation, ‘ θ ’ is the diffraction angle and ‘ d ’ is the lattice spacing in a crystalline sample. After diffraction, the X-rays are then detected, processed and counted. By altering the geometry of the incident rays, the orientation of the mounted crystal and the detector, all possible diffraction possibilities of the lattice should be attained [5]. All diffraction methods are based on generation of X-rays in an X-ray tube. A vital component of all diffraction is the angle between the incident and diffracted rays.

Single crystals were mounted on glass fibers with epoxy cement as described in relevant thesis work. X-ray analysis was done using Apex II CCD diffractometer with fine-focus sealed tube graphite-monochromated Mo $K\alpha$ radiation ($\lambda = 0.71073 \text{ \AA}$) at room temperature. The data was processed with SAINT and corrected for absorption using SADABS [6]. The structures were solved by direct method using the program SHELXTL [7] and was refined by full-matrix least squares technique on F2 using anisotropic displacement parameters for all non-hydrogen atoms. Hydrogen atoms were included in the refinement process as per the riding model. The Mercury 3.0 software was used for the analysis of bond distances and angles.

2.3. Instrumentation segment of the spectroscopic techniques

2.3.1. NMR technique

Nuclear magnetic resonance spectrophotometer makes use of a magnet, a radio-frequency, a detector and an amplifier. The detection system is used to note down that energy is being transferred from the radio-frequency beam to the nucleus. The sample under examination is taken in a glass tube which is positioned between the pole faces of a magnet. A radio-frequency source is made to fall on the sample. It can be completed by feeding energy into a coil placed around the sample tube. A signal is detected if the nuclei in the sample resonates with the source. Energy is transferred from the source via nuclei to the detector coil. The output from the detector can be directed to a cathode ray oscillograph or to a strip of chart recorder after amplification.

The instrumentation technique is shown in Figure 2.4.

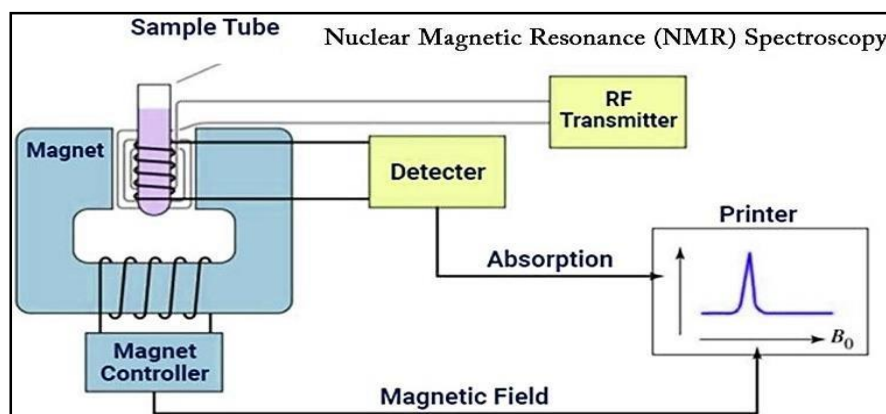


Fig. 2.4: Schematic diagram of instrumentation of NMR spectroscopy.

2.3.2. IR technique

In common IR instruments the source of Infra-red light used for scanning is Nernst glower. It is basically a rod containing the sintered mixture of the oxides of Zirconium, Ytterbium and Erbium. The rod produces Infra-red radiations when it is electrically heated to 1500°C.

Silicon carbide may also be used in the rod to produce Infra-red radiations. Optical prisms or gratings is used to obtain monochromatic light. For prism material, glass or quartz cannot be used since they absorb strongly through most of the IR-region. Sodium chloride or certain alkali metal halides are commonly used as cell containers or for prism materials as these are transparent to most of the IR region under consideration. Light from the source is split into two beams. One of the beams

CHAPTER 2

is passed through the sample under examination and is called the sample beam. The other beam is called the reference beam. When the beam passes through the sample, it becomes less intense due to the absorption of certain frequencies. Now there will be a difference in the intensities of the two beams. Intensities of the bands can be recorded as a linear function T (transmittance) against the corresponding wave-number.

The instrumentation technique is illustrated in Figure 2.5.

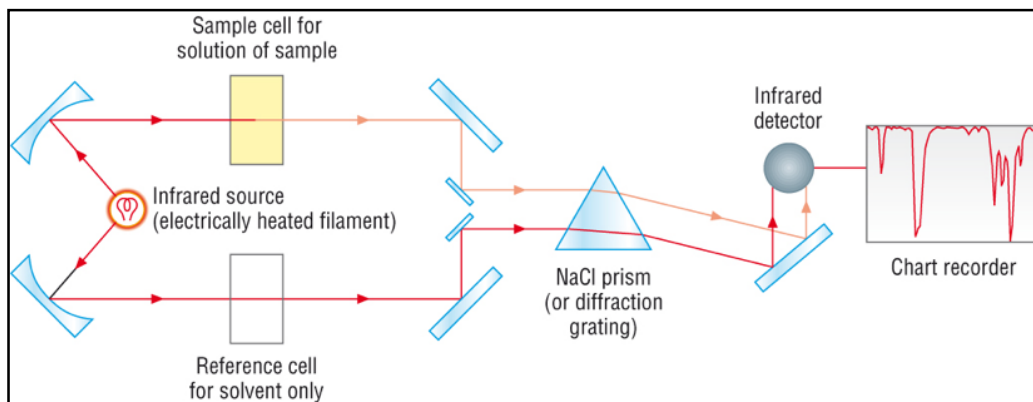


Fig. 2.5: Schematic representation of instrumentation of IR spectroscopy.

2.3.3. HRMS technique

The instrumentation of mass spectrometer consists of three main parts:

(a) Ion source. The first and a significant step of achieving a mass spectrum is to ionize the sample compound. The common procedure used for the fabrication of ion in mass spectrometer is by the bombardment of electrons. The bombarding electrons are generated from an electrically heated tungsten filament. A few milligram of the substance is produced as vapor in the source at an operating pressure of 10^{-6} mm. The vapor is permitted to pass through a slit into the ion chamber. Here it is bombarded by a flow of electrons produced by a tungsten filament. Due to bombardment, the molecules generally lose one electron to form a parent ion radical. But if the energy of the bombarding electron is around 70 eV, additional energy is consumed in fragmenting the parent ion. This results in the formation of fragment ions or the daughter ions.

(b) Quadrupole Mass filter. The positively charged ions generated in the ion chamber are accelerated by pertaining an acceleration potential. These ions then go through the mass filter or the mass analyser. Here the fragmented ions are differentiated on the basis of their m/z ratio and their mass to charge ratio is measured.

CHAPTER 2

(c) **Ion detector.** The ions which are separated by the mass analyser, are detected and measured electrically. The ions pass through the collecting slit one after the other and fall on the detector. The instrumentation technique is shown in Figure 2.6.

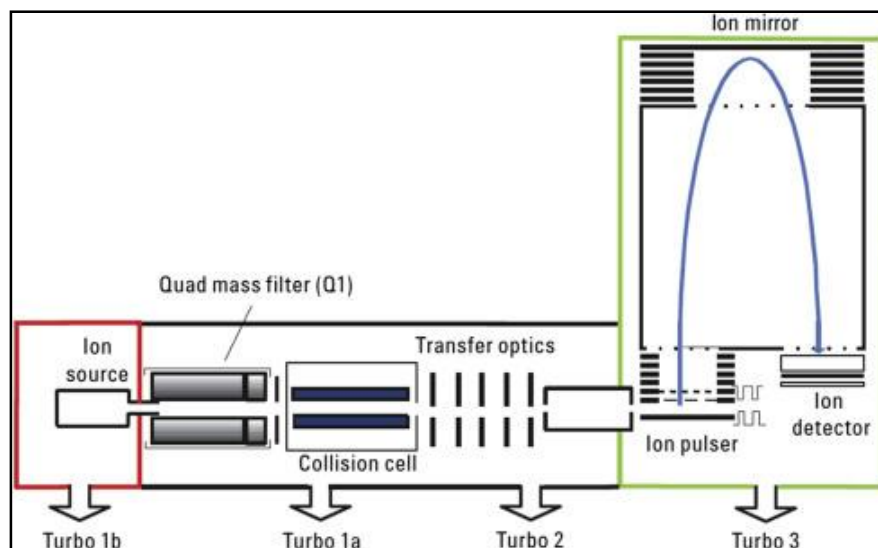


Fig. 2.6: Schematic of instrumentation of High resolution mass spectrometry.

2.3.4. UV-Vis technique

The roll of a spectrophotometer is to detect the percentage transmittance of light radiation when light of a constant intensity and frequency range is passed through the sample compound taken in solution phase. Thus, the instrument compares the intensity of the transmitted light with that of the incident light or light transmitted through the pure solvent.

The modern UV-Vis spectrometers consist of a few key parts viz. the source of light, a monochromator filter, a detector, an amplifier and the data recording devices. The most popular sources of light are hydrogen-deuterium discharge lamp and tungsten Filament lamp. These two lamps cover the whole frequency range of the UV-Vis region. Most spectrophotometers are double beam instruments. The primary source of light is divided into two beams of equal intensity by a beam splitter. One of which passes though the sample and the other through the reference. A schematic representation is given below in Figure 2.7. which shows the detailed instrumentation of a ultra-violet spectrophotometer.

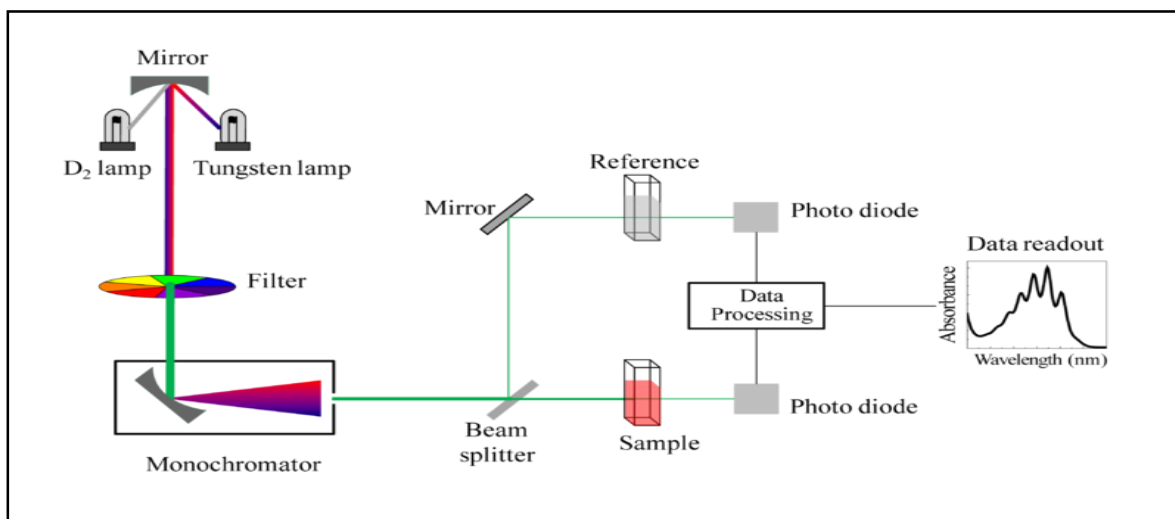


Fig. 2.7: Schematic presentation of different parameters involved in absorption spectra measurement

2.3.5. Fluorimetry

A fluorimeter is a device that measures the intensity and its distribution throughout the wavelength range visible to human eye. After excitation by a certain wavelength of light generally from UV region of the spectrum the fluorophore undergoes radiative relaxation and emits visible light which is then detected, quantified and represented digitally by a detector-computer assembly. Modern fluorimeters can detect the emission from a fluorescent molecule in very minute concentrations.

The basic components of a fluorometer are an excitation source, an excitation monochromator, a sample chamber, where a cuvette containing the sample solution is placed, an emission monochromator and a detector. Most commercial instruments use the right angle detector approach as it reduces the background noise. In normal instrumentation mode, the sample compound is excited with polarized light and the intensity of the emitted fluorescence by that compound is measured by a polarizer analyser. A schematic representation of the fluorimeter instrument is shown in Figure 2.8 which demonstrates the detailed instrumentation.

CHAPTER 2

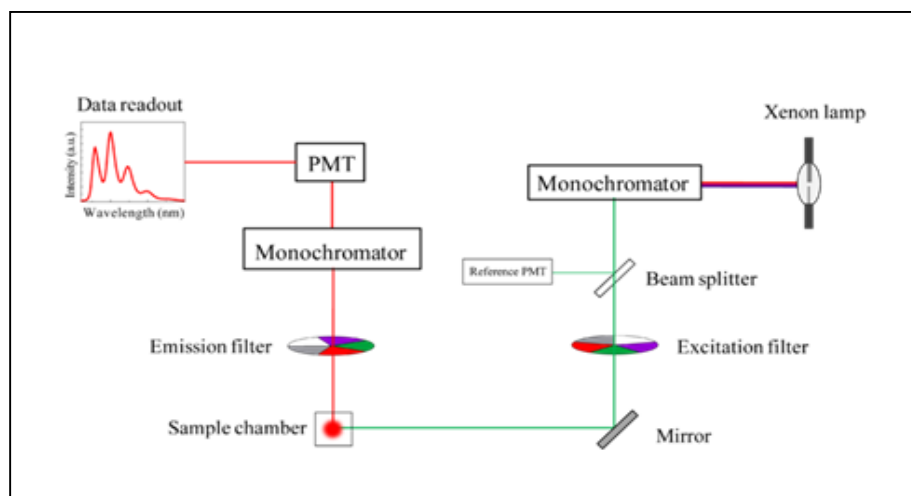


Fig. 2.8: Schematic representation of a fluorimeter.

2.3.6. Fluorescence lifetime technique

The Fluorescence lifetime instruments record the life time of the excited state of a certain fluorophore over the course of many events. To reconstruct the lifetime decay profile a technique known as TCSPC or time-correlating single photon counting is used. It is a method of comparing the timing of a pulsed excitation source, like a laser or a LED, with the timing of the arrival of single photons on a detector. It requires many a repetition of pulses of excitation source and photons detected to achieve a required statistical data precision. The instrumentation of a TCSPC-fluorescence lifetime machine is shown schematically in the following diagram (Figure 2.9).

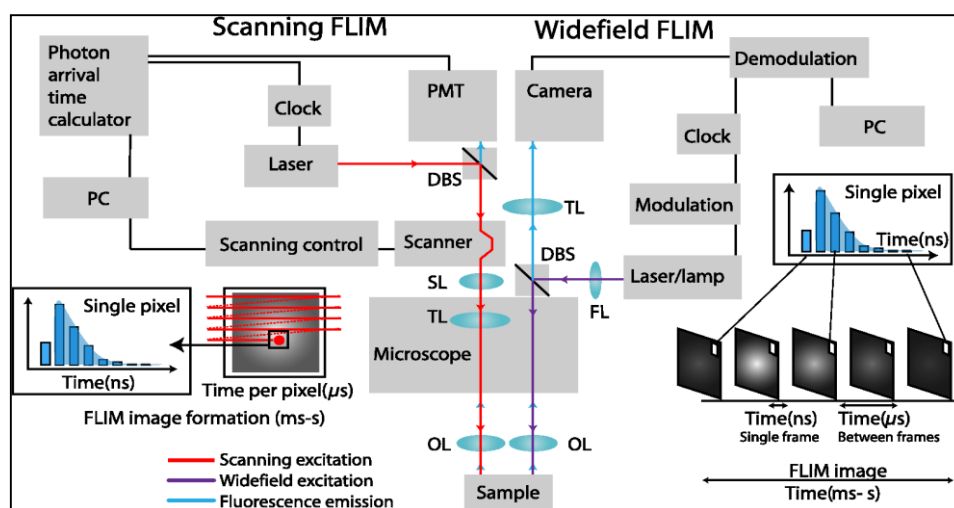


Fig. 2.9 Schematic diagram of a TCSPC instrument

2.4. Some essential analytical methods to study the chemosensors

2.4.1. Quantum yield measurement

Photoluminescence quantum yield is the efficiency, of a luminescent particle, of converting absorbed light into emitted light, i.e.,

$$\text{Quantum Yield} = \text{number of emitted photons} / \text{number of absorbed photons}$$

Quantum yield is alternately named as quantum efficiency (QE) or fluorescence efficiency. The value of Quantum yield may vary between 0 and 1. Higher the quantum yield, brighter is the emission. To measure the quantum yield of a sample one needs to compare its emission with a reference dye with known quantum yield or one can also measure the absolute quantum yield. To measure the Quantum yield, the absorbance of both the sample and the reference dye were recorded. Thereafter, emission spectra were recorded using the maximal excitation wavelengths and the integrated areas of the spectra were calculated further. The quantum yields were then measured by using the following equation:

$$\Phi_x = \Phi_s \times \left(\frac{I_x}{I_s}\right) \times \left(\frac{A_s}{A_x}\right) \times \left(\frac{n_x}{n_s}\right)^2$$

Where, x & s designate the unknown and standard solution respectively, ϕ is the quantum yield, I is the integrated area under the fluorescence spectra, A is the absorbance and n is the refractive index of the solvent.

The selection of the reference dye was varied throughout the thesis work according to the position of the absorbance peaks in each case. All the absorption and fluorescence spectra were recorded using Perkin Elmer Lambda 750 spectrophotometer and Shimadzu RF-6000 fluorescence spectrophotometer respectively.

2.4.2. Calculation of binding constant of synthesized ligand

The binding constant or the association constant of a receptor is the parameter that determines if the probe is stable enough to successfully bind with the specific analyte or not. Binding constant (K_a) was calculated from the fluorescence intensity data according to the Benesi-Hildebrand equation. The relevant equation that is stated below.

CHAPTER 2

$$1/(F-F_0) = 1/\{K_a(F_{\min/\max}-F_0) [M^{n+}]^x\} + 1/[F_{\min/\max}-F_0]$$

Here F_0 , F and $F_{\min/\max}$ indicate the emission in absence of, at any intermediate and at infinite concentration of the analyte respectively. K_a is the binding constant and $[M^{n+}]$ is the concentration of the analyte (in most cases, the metal ion with which the probe binds). When $1/(F-F_0)$ was plotted against $1/[M^{n+}]$ for any particular sensor, the value of K_a was obtained as the ratio of intercept and slope of the curve (see the Benesi-Hildebrand equation). When the plot of $1/(F-F_0)$ vs. $1/[M^{n+}]$ gives a straight line it indicates 1:1 complexation of the probe with the corresponding metal.

2.4.3. Determination of limit of detection of synthesized chemosensors

The value of limit of detection or LOD value determines the sensitivity of a chemosensor towards a specific analyte. Hence it is a very important term in the field of chemosensors and chemodosimeters. The lower is the LOD value of a chemosensor, the greater will be its ability to sense the analyte in very minuscule concentrations. Especially in case of toxic analytes, the low detection limit value is very desirable as the receptor should be able to detect such analytes in concentration levels much lower than its permissible values.

The LOD value of each receptor was calculated based on the fluorescence titration curve obtained by gradual addition of the analyte into the ligand solution. To determine the S/N ratio, the emission intensity of the probe itself was measured repeatedly for 10 times and the standard deviation of blank measurements was determined. So the limits of detection of the desired probes were determined by using the following equation throughout the thesis work:

$$DL = K \times Sb_1/S$$

Where $K = 2$ or 3 (we take 3 in this case); Sb_1 is the standard deviation of the blank solution; S is the slope of the calibration curve.

2.5. References

1. William Kemp, Organic Spectroscopy, 3rd Ed., 2008, **Chapter 3**, 104-165.
2. Marc Loudon, Jim Parise, Organic Chemistry, 7th Ed., 2021, **Chapter 13**, 611-612.
3. A. Jablonski, *Z. Phys.*, 1935, **94**, 38.
4. J. R. Lakowicz, *Plenum Press*, 1983, 496.

CHAPTER 2

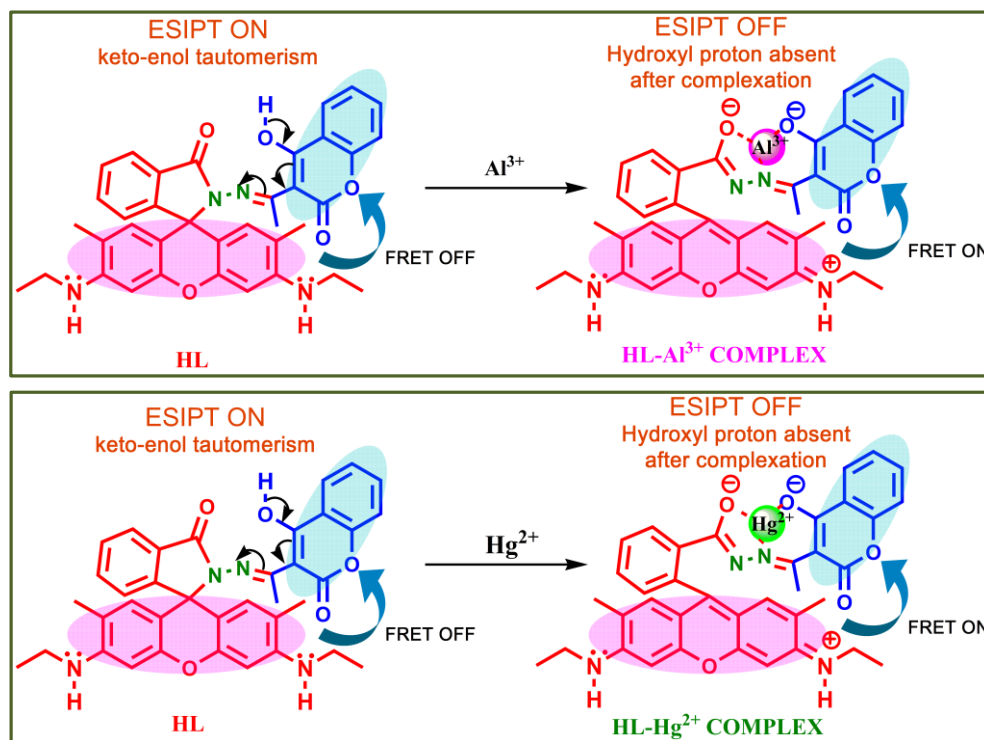
5. C. P. Gomez and R. A. Jacobson, John Wiley & Sons, Inc., 2012.
6. Bruker. APEX2, SAINT and SADABS. Bruker AXS Inc., Madison, Wisconsin, USA. 2009.
7. Sheldrick G. M. A short history of SHELX. *Acta Cryst.* 2008, **64**, 112.

An Efficient Fluorescence “Turn-On”
Chemosensor Comprising of
Coumarin and Rhodamine Moieties
for Al³⁺ and Hg²⁺

An Efficient Fluorescence “Turn-On” Chemosensor Comprising of Coumarin and Rhodamine Moieties for Al³⁺ and Hg²⁺

Abstract

A potent fluorescence ‘turn-on’ receptor (HL) based on rhodamine and coumarin moieties for the detection of Hg²⁺ and Al³⁺ is synthesized by condensation of rhodamine 6G hydrazide and 4-hydroxy-3-acetylcoumarin. In presence of Al³⁺ and/or Hg²⁺ the receptor (HL) exhibits deep pink colouration and a sharp band at 528 nm is appeared in UV–Vis titration. Upon gradual addition of Al³⁺ and/or Hg²⁺ to the solution of HL significant enhancement of fluorescence intensity is observed at 564 nm in MeCN:H₂O (1:5, v/v) medium. The receptor is strongly bound to Al³⁺ and/or Hg²⁺ and the association constants (K_a) are found to be 1.74×10^4 and 1.04×10^4 M⁻¹ for Al³⁺ and Hg²⁺ respectively.



3.1. Introduction

Mercury is considered to be one of the most toxic heavy metals and can cause serious environmental and health problem [1,2]. It may have adverse effect on human nervous system, digestive and immune systems including lungs, kidneys, skin, eyes, brain and nervous system [3-5]. According to the Environmental Protection Agency (EPA) the limit of inorganic mercury(II) level in drinking water should be less than 2 ppb [6,7]. On the other hand, aluminum is one of the most common metals in nature and has abundant use in electrical, food packaging and food processing industry which causes easy bioaccumulation of the metal in human body and plants [8-11]. Aluminium has neurotoxic effects and has long been suspected as one of the factors causing the Alzheimer's and Parkinson's disease [12]. Al^{3+} can cause osteomalacia [13] and also acts as a metalloestrogen facilitating the gene-expression in breast cancer cell and therefore its growth [14-17]. The World Health Organization (WHO) prescribed the average human intake of aluminium as around 3-10 mg/day and its limit in drinking water should be less than 7.41 μM [18-21]. Therefore, facile and financially viable methods of detecting Hg^{2+} and Al^{3+} in environmental and biological samples has become a matter of utmost interest. Detection by measuring luminescence property is simple, highly sensitive, quick and reversible in nature [22-24].

3.2. Basis of present work

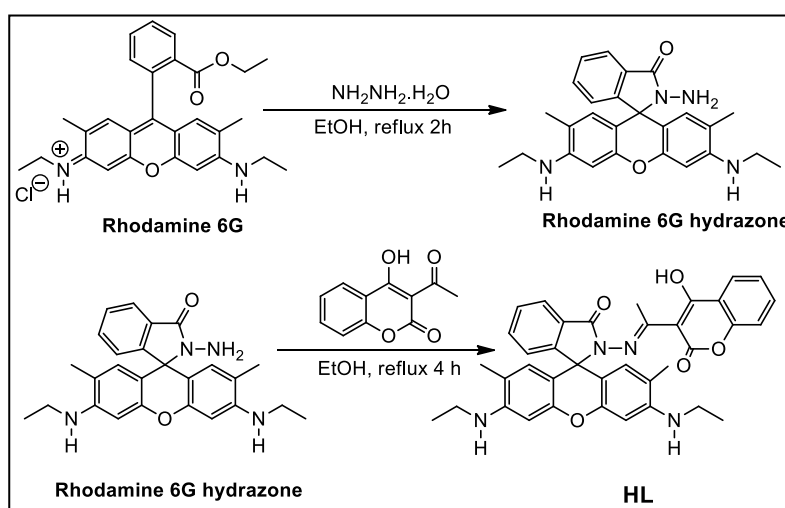
Till date very few chemosensors are reported comprising of coumarin and rhodamine moieties that can detect Al^{3+} and/or Hg^{2+} [25-28]. Herein, the reported chemosensor, 3-(1-(rhodamine-6G-hydrazidimino)ethyl)-4-hydroxy-2H-chromen-2-one (HL) was synthesized following an economically cheap route. It can detect both Al^{3+} and Hg^{2+} with high selectivity in solution phase and also has the benefit of being reversible. Both the metal ions i.e., Hg^{2+} and Al^{3+} induce huge increase in emission intensity, but the emission intensity is quenched significantly in presence of F^- and S^{2-} for Hg^{2+} and Al^{3+} respectively.

CHAPTER 3

3.3. Results and discussions

3.3.1 Synthesis of HL

The synthesis of HL was carried out via a two stepped process. In the first step rhodamine 6G hydrazone was synthesized by reacting rhodamine 6G with hydrazine hydrate in ethanol following the reported procedure [40]. The rhodamine 6G hydrazone was then condensed with 3-acetyl-4-hydroxycoumarin in ethanol under reflux to form the Schiff base HL (Scheme 3.1).



Scheme 3.1: Synthesis of rhodamine 6G hydrazone and the receptor HL

3.3.2 Spectral characterization and analysis of HL

IR spectrum of HL in KBr pellets showed stretching at 1721 cm^{-1} corresponding to the δ -lactone $\text{C}=\text{O}$, stretching at 1689 cm^{-1} and 1638 cm^{-1} for the keto $\text{C}=\text{O}$ of the rhodamine moiety and for the imine $\text{C}=\text{N}$ respectively (Fig. S1). $^1\text{H-NMR}$ spectra were taken in CDCl_3 solvent showed a peak at $\delta 14.95$ for the hydrogen bonded enolic OH proton (Fig. S2), which was absent in the metal complexes $[\text{HL-Al}^{3+}]$ and $[\text{HL-Hg}^{2+}]$, indicative of the coordination with the metal through O and N donor site of HL. The aromatic protons appeared in the range, 8.05-6.26 ppm as expected. Slight downfield shift of the protons of the aromatic zone in the $[\text{HL-Al}^{3+}]$ and $[\text{HL-Hg}^{2+}]$ complexes in comparison with the free HL is attributed to the coordination of the receptor with Al^{3+} and Hg^{2+} ions.

CHAPTER 3

The mass spectra of free ligand showed m/z peak at 615.3093 corresponding to $[\text{HL} + \text{H}]^+$ and that of the complexes $[\text{HL}-\text{Al}^{3+}]$ and $[\text{HL}-\text{Hg}^{2+}]$ showed m/z peak at 765.3854 for $\text{H}^+[\text{Al}(\text{HL}-\text{H})(\text{NO}_3)_2]$ and 855.2132 for $\text{Na}^+[\text{Hg}(\text{HL}-\text{H})(\text{H}_2\text{O})]$ respectively (Fig. S4).

3.3.3 Cation sensing studies: UV-Vis spectroscopy studies

Free receptor HL exhibits a strong absorbance band at 302 nm along with a shoulder at 338 nm, in 1:5, v/v MeCN:H₂O in neutral pH (pH=7.2). As shown in Figs. 3.1 and 3.2, upon addition of aqueous solution of Al^{3+} and Hg^{2+} to the solution of HL, a new peak arose at 528 nm and became intense with increasing the concentrations of metal ions. During the addition of Al^{3+} and Hg^{2+} beautiful colour change (red pink) was observed due to the formation of coordination compounds by opening the spirolactam ring of HL (Fig. 3.3). The effect of other metal ions i.e, Na^+ , K^+ , Ca^{2+} , Mg^{2+} , Mn^{2+} , Fe^{3+} , Cr^{3+} , Co^{2+} , Ni^{2+} , Cu^{2+} and Cd^{2+} on the UV-Vis spectrum of HL has also been studied, but no significant changes are observed except for Cu^{2+} (Fig. 4). The selectivity and sensitivity of HL towards Al^{3+} and Hg^{2+} were examined by adding different metal ions to the HL solution. It shows specific selectivity towards Al^{3+} and Hg^{2+} in $\text{CH}_3\text{CN}/\text{H}_2\text{O}$ (1:5, v/v) solution, whilst no significant change was observed with other competing metal ions except Cu^{2+} (Fig. 3.4).

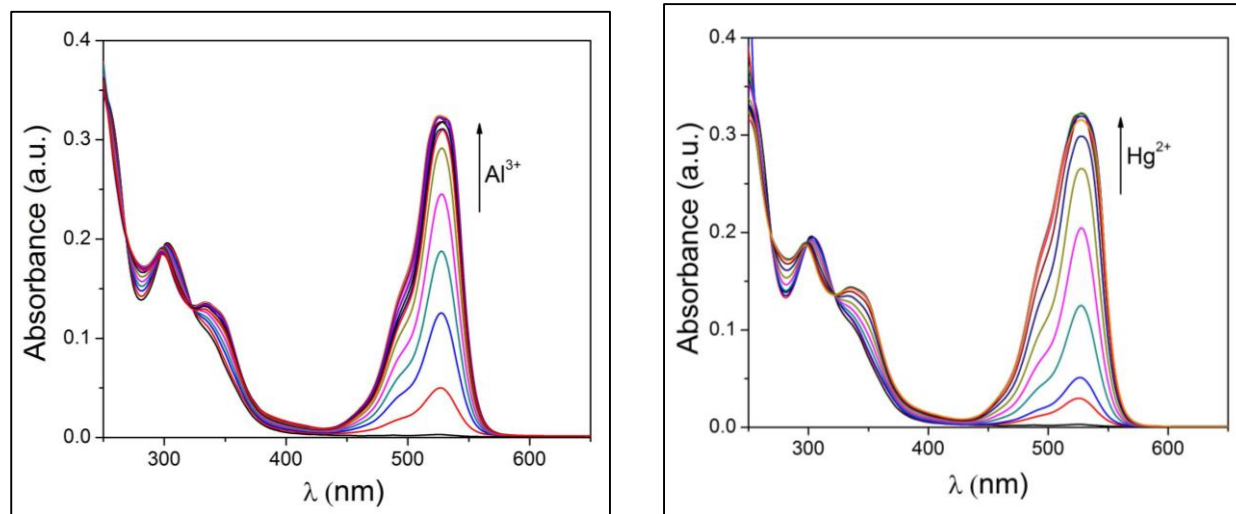


Fig. 3.1 and 3.2: Change in UV-Vis spectrum of HL (10 μM) upon gradual addition of Al^{3+} (20 μM) and Hg^{2+} in $\text{CH}_3\text{CN}/\text{H}_2\text{O}$ (1:5, v/v, pH = 7.2)

CHAPTER 3

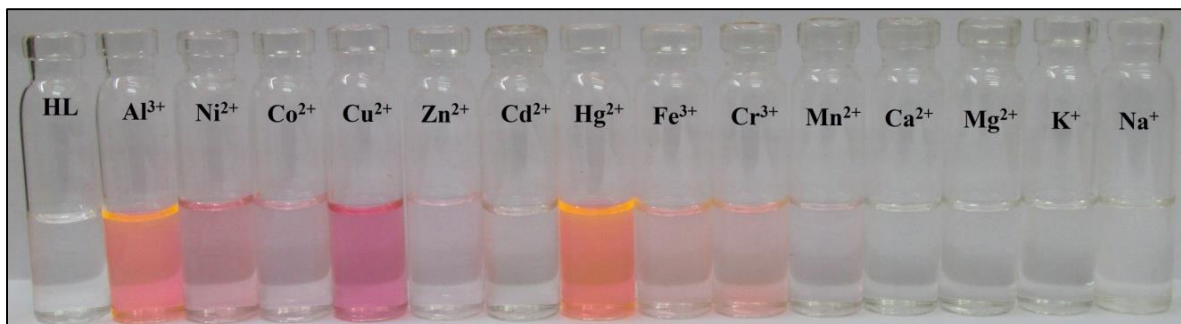


Fig. 3.3: Visual changes in colour of HL in presence of different cations

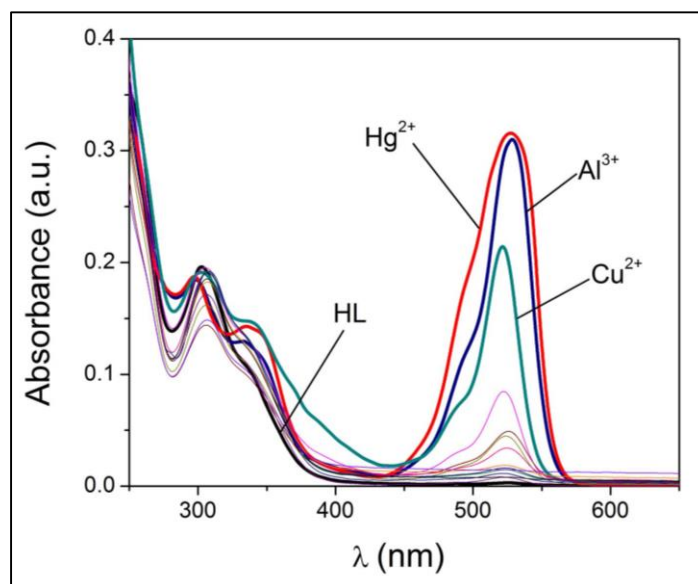


Fig. 3.4: Change in UV-Vis spectrum of HL (10 μM) in presence of various cations (20 μM) in $\text{CH}_3\text{CN}/\text{H}_2\text{O}$ (1:5, v/v, pH = 7.2)

3.3.4 Cation sensing studies: Fluorescence emission studies

The metal ion sensing property of HL was also investigated by monitoring the changes in fluorescence properties upon addition of several metal ions such as Na^+ , K^+ , Ca^{2+} , Mg^{2+} , Al^{3+} , Mn^{2+} , Fe^{3+} , Cr^{3+} , Co^{2+} , Ni^{2+} , Cu^{2+} , Cd^{2+} and Hg^{2+} in $\text{CH}_3\text{CN}/\text{H}_2\text{O}$ (1:5, v/v, pH = 7.2). The free receptor (HL) exhibits a very weak emission band at 550 nm upon excitation at 338 nm with very poor emission quantum yield $\phi = 0.005$. With the addition of Al^{3+} and/or Hg^{2+} remarkable enhancement of fluorescence intensity is observed. For Al^{3+} the fluorescence intensity enhanced by 47 fold ($\phi = 0.131$), while for Hg^{2+} enhancement was 34 fold ($\phi = 0.097$) with emission $\lambda_{\text{max}} = 564$ nm (Figs. 3.5 and 3.6). The increase in fluorescence intensity is accompanied by the opening of spirolactam ring of the receptor upon chelation with Al^{3+} and Hg^{2+} .

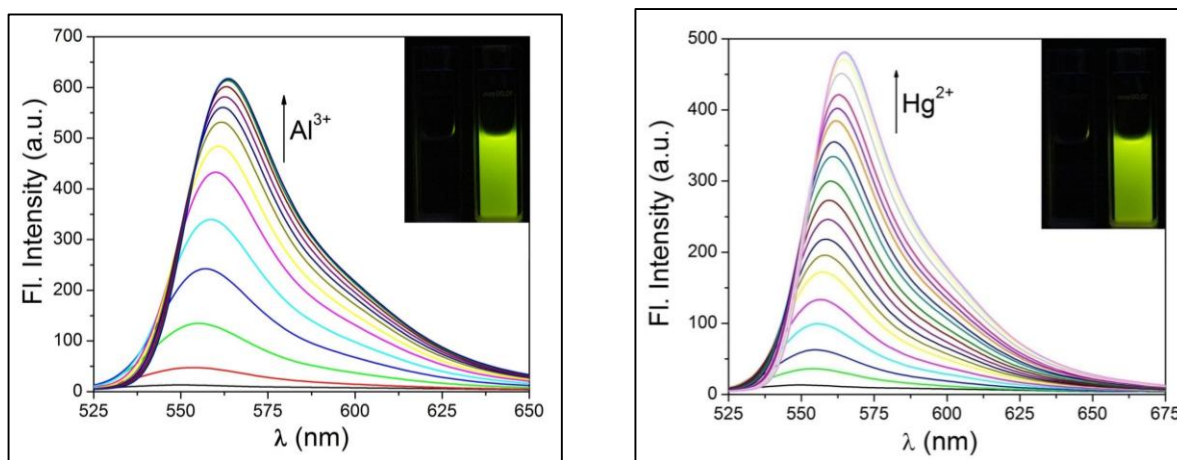


Fig. 3.5 and 3.6: Change in emission spectrum of HL (10 μM) upon gradual addition of Al^{3+} (20 μM) and Hg^{2+} (20 μM) in $\text{CH}_3\text{CN}/\text{H}_2\text{O}$ (1:5, v/v, pH = 7.2). Inset shows the visual effect of addition of Al^{3+} to HL in UV light.

Notably, the addition of excess other metal ions including Cu^{2+} , caused insignificant changes in fluorescence intensity (Fig. 3.7). These enhancements of fluorescence reflect a strong selective OFF-ON fluorescent signaling property of HL for Al^{3+} and Hg^{2+} .

CHAPTER 3

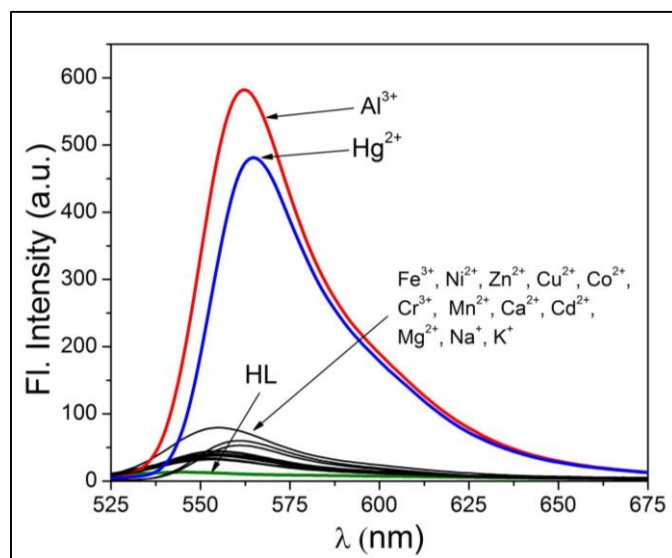


Fig. 3.7: Change in emission spectrum of HL (10 μM) upon gradual addition of different cations (20 μM) in $\text{CH}_3\text{CN}/\text{H}_2\text{O}$ (1:5, v/v, pH = 7.2)

However, on gradual addition of F^- to HL-Al^{3+} and S^{2-} to HL-Hg^{2+} solutions, fluorescent intensity at 564 nm gradually decreases (Figs. 3.8 and 3.9). The quenching of fluorescence intensity for HL-Al^{3+} and HL-Hg^{2+} is very selective for F^- and S^{2-} respectively, other anions have no significant effect on fluorescence intensity.

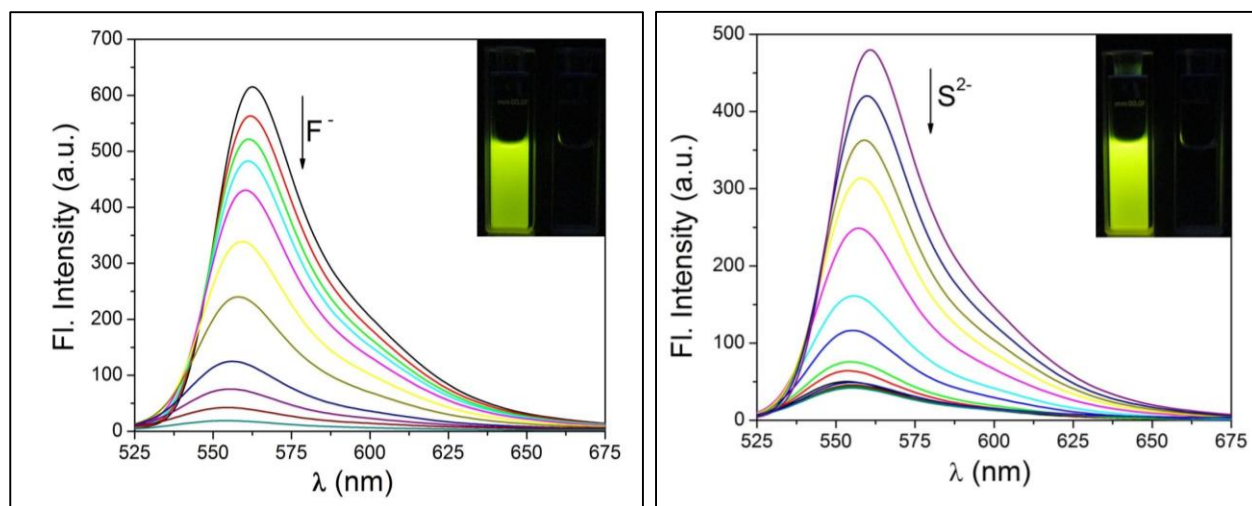


Fig. 3.8 and 3.9: Change in emission spectrum of HL-Al^{3+} complex (10 μM) upon addition of F^- (20 μM) and Change in emission spectrum of HL-Hg^{2+} complex (10 μM) upon addition of S^{2-} (20 μM) in $\text{CH}_3\text{CN}/\text{H}_2\text{O}$ (1:5, v/v, pH = 7.2)

CHAPTER 3

Fluorescence emission intensity of HL was measured in presence of different metal ions i.e., Na^+ , K^+ , Ca^{2+} , Mg^{2+} , Al^{3+} , Mn^{2+} , Fe^{3+} , Cr^{3+} , Co^{2+} , Ni^{2+} , Cu^{2+} , Cd^{2+} and Hg^{2+} in MeCN:H₂O (1:5, v/v, pH=7.2) but there is hardly any increase in emission intensity except for Al^{3+} and Hg^{2+} . Then to these solutions Al^{3+} was added which then shows obvious fluorescent enhancements (Fig. 3.10). Similar fluorescence enhancement was also seen when Hg^{2+} was added to HL solution in presence of various other metals (Fig. 3.11). Thus the synthesized receptor HL is highly efficient in detection of Al^{3+} and Hg^{2+} even in presence of other metals and thus it can detect Al^{3+} and Hg^{2+} in biological or environmental samples where other metals usually co-exist with them.

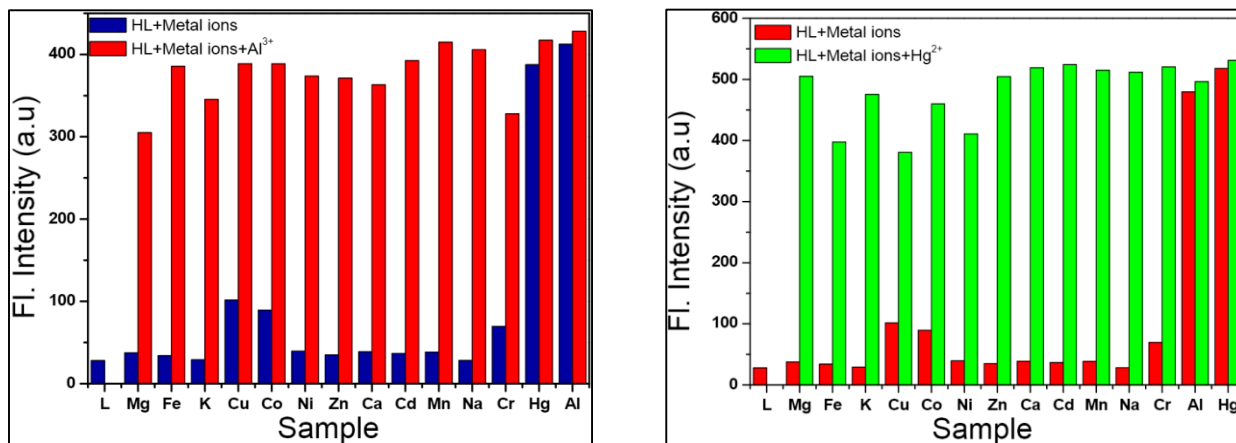


Fig. 3.10 and 3.11: competition study- Emission intensity of HL Upon addition of various metals and effect of subsequent addition of Al^{3+} and Hg^{2+}

3.3.5 Binding studies of HL with Al^{3+} and Hg^{2+}

Jobs plot for complexations of HL with Al^{3+} and Hg^{2+} with emission intensity taken on Y-axis shows a maximum in the plot corresponding to ~0.5 mole fraction indicating 1:1 complex formations of HL with Al^{3+} and Hg^{2+} (Figs. S5 and S6). From emission spectral change, limit of detection of the chemosensor for Al^{3+} and Hg^{2+} were determined using the equation $\text{LOD} = K \times \text{SD}/S$ where SD is

CHAPTER 3

the standard deviation of the blank solution and S in the slope of the calibration curve (Figs. S9 and S10). The limit of detection for Al^{3+} was found to be about 6.05×10^{-8} M and for Hg^{2+} and the same was found to be 7.557×10^{-8} M. These results clearly demonstrate that the chemosensor is highly efficient in sensing Al^{3+} and Hg^{2+} even in very minute level. Among all other common metal ions, Al^{3+} and Hg^{2+} resulted in pronounced fluorescence enhancement and the association constants (K_a) were determined by the fluorescence titration method for HL with Al^{3+} and Hg^{2+} . The association constants were found to be 1.74×10^4 and $1.04 \times 10^4 \text{ M}^{-1}$ for Al^{3+} and Hg^{2+} respectively by the Benesi-Hildebrand equation (Figs. S11 and S12).

3.3.6 Effect of pH on emission properties

The effect of pH on the emission intensity of the receptor (HL) in absence and presence of Al^{3+} and Hg^{2+} were studied. In case of HL there is hardly any change in fluorescence intensity in the pH range 4-12 (Fig. 3.12). Below pH 4 a sharp increase in fluorescence intensity is observed due to protonation of hydroxy O atoms and imine N preventing the excited state intramolecular proton transfer (ESIPT) process. ESIPT is more dominant as a relaxation process than fluorescence. So only when it stops relaxation happens through fluorescence route and we observe an increase in fluorescence intensity [41]. For similar reason on addition of 1.2 equivalents of Al^{3+} and Hg^{2+} the fluorescence intensity increases. The fluorescence intensity first increases with the increase of pH and maximum at pH range 6-8. But, on further increase in pH fluorescence intensity drops drastically due to the dissociation of metal complexes at $\text{pH} > 8$. Thus, the receptor (HL) is efficient in detection of Al^{3+} and Hg^{2+} in the biologically relevant pH range (6-7).

CHAPTER 3

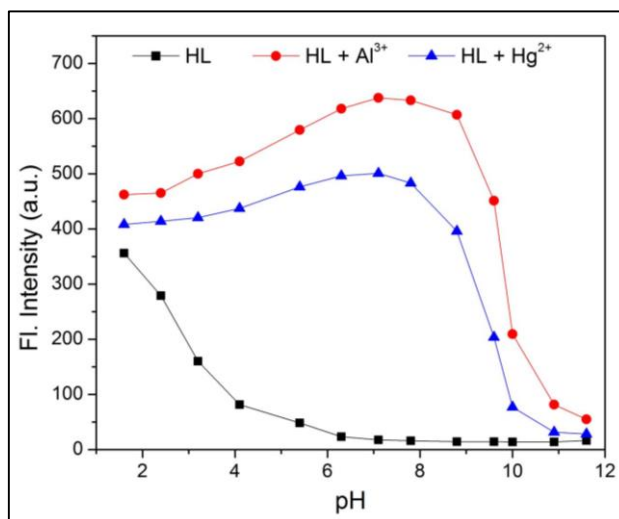


Fig. 3.12: Effect of pH on fluorescence intensity of receptor HL (-■-■-), HL+Al³⁺ (-●-●-) and HL+Hg²⁺ (-▲-▲-)

3.3.7 Probable sensing mechanism

The fluorescence “turn-on” upon addition of both Al³⁺ and Hg²⁺ can be attributed to the opening of the spirolactam ring of the Rhodamine-6G hydrazide moiety which establishes a long conjugation between the Rhodamine and the coumarin moieties. The complexation also eliminates the hydroxyl proton which switches off the non-radiative ESIPT process. There may also be a possibility of “FRET turn-on” from Rhodamine (donor) to Coumarin (acceptor) upon complexation with the metal ion (see Fig.3.13)

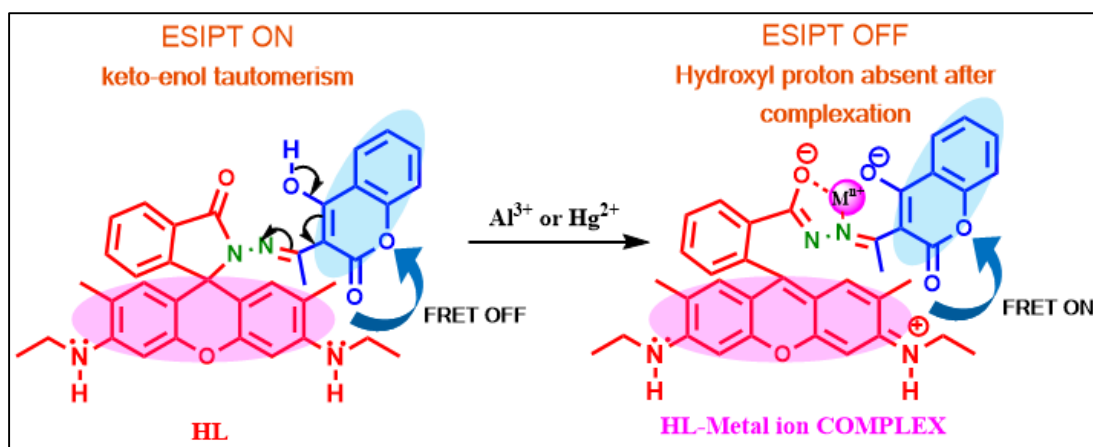


Fig.3.13: Probable sensing scheme.

CHAPTER 3

3.3.8 DFT calculations

To know the electronic structures of free receptor, HL and its complexes with Al^{3+} and Hg^{2+} , geometry optimizations were carried out using DFT method. The optimized structures of HL, HL- Al^{3+} and HL- Hg^{2+} are shown in Fig. 3.14. The HOMO-LUMO energy gap for free receptor (3.86 eV) is significantly reduced upon complexations with Al^{3+} (2.83 V) and Hg^{2+} (2.85 V), and are reflected in the UV-Vis spectra of the complexes. To get depth inside into the changes in absorption spectrum of HL upon addition of Al^{3+} and Hg^{2+} , TDDFT calculations by TDDFT/CPCM method in acetonitrile were carried out. The calculated vertical electronic excitations are noted in Table 3.1. The absorption bands of free receptor at 303 and 338 nm correspond to HOMO \rightarrow LUMO and HOMO-2 \rightarrow LUMO transitions respectively. In complexes the HOMO \rightarrow LUMO transition is red shifted compare to free receptor and appeared at 519 nm HL- Al^{3+} and 514 nm for HL- Hg^{2+} .

Compounds	$\lambda_{\text{calc.}}$ (nm)	E (eV)	f	Key excitations	$\lambda_{\text{expt.}}$ (nm)
HL	350.8	3.5347	0.3202	(81%)HOMO \rightarrow LUMO	338
	305.6	4.0566	0.1296	(86%)HOMO-2 \rightarrow LUMO	303
HL- Al^{3+}	519.4	2.3869	0.6637	(77%)HOMO \rightarrow LUMO	530
	499.4	2.4828	0.0993	(69%)HOMO \rightarrow LUMO+1	491
	353.8	3.5045	0.2177	(89%)HOMO-2 \rightarrow LUMO	346
HL- Hg^{2+}	514.3	2.4106	0.6649	(92%)HOMO \rightarrow LUMO	527
	472.8	2.6222	0.1253	(95%)HOMO-1 \rightarrow LUMO	493
	353.7	3.5057	0.2207	(87%)HOMO-3 \rightarrow LUMO	344

Table 3.1: Calculated vertical excitations of HL, HL- Al^{3+} and HL- Hg^{2+} by TDDFT/CPCM method.

CHAPTER 3

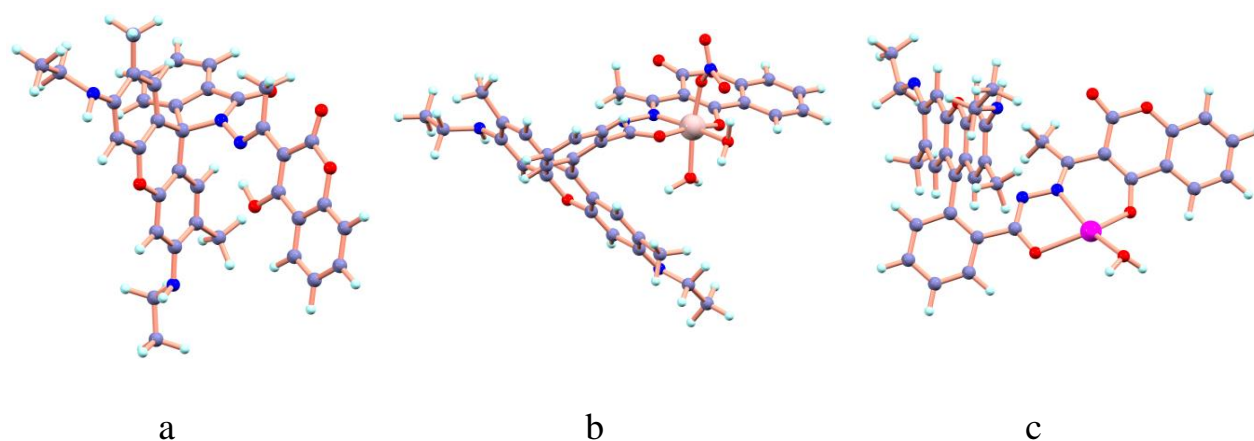


Fig. 3.14: Optimized structures of (a) HL, (b) HL-Al³⁺ and (c) HL-Hg²⁺ by DFT/B3LYP method

3.4. Experimental

3.4.1 Materials and methods

Rhodamine-6G hydrochloride and 4-hydroxycoumarin were purchased from Sigma Aldrich. All other organic chemicals and inorganic salts were purchased from Merck and used without further purification.

Elemental analysis was carried out in a 2400 Series-II CHN analyzer, Perkin Elmer, USA. HRMS mass spectra were recorded on Waters (Xevo G2 Q-TOF) mass spectrometer. Infrared spectra were taken on a RX-1 Perkin Elmer spectrophotometer with samples prepared as KBr pellets. Electronic spectral studies were performed on a PerkinElmer Lambda 750 spectrophotometer. Luminescence property was measured using PerkinElmer LS 55 fluorescence spectrophotometer at room temperature (298 K). NMR spectra were recorded using a Bruker (AC) 300 MHz FTNMR spectrometer of ~0.05 M solutions of the compounds in CDCl₃.

The luminescence quantum yield was determined using Coumarin-120 laser dye as reference. The compound and the reference dye were excited at the same wavelength, maintaining nearly equal absorbance (~0.1), and the emission spectra were recorded. The area of the emission spectrum was

CHAPTER 3

integrated using the software available in the instrument and the quantum yield was calculated according to the following equation:

$$\phi_S/\phi_R = [A_S / A_R] \times [(Abs)_R / (Abs)_S] \times [\eta_S^2/\eta_R^2]$$

Here, ϕ_S and ϕ_R are the luminescence quantum yields of the sample and reference, respectively. A_S and A_R are the areas under the emission spectra of the sample and the reference respectively, $(Abs)_S$ and $(Abs)_R$ are the respective optical densities of the sample and the reference solution at the wavelength of excitation, and η_S and η_R are the values of refractive index values for the respective solvent used for the sample and reference.

Fluorescence lifetimes were measured using a time-resolved spectrofluorometer from IBH, UK. The instrument uses a picoseconds diode laser (NanoLed-03, 370 nm) as the excitation source and works on the principle of time-correlated single photon counting. The goodness of fit was evaluated by χ^2 criterion and visual inspection of the residuals of the fitted function to the data.

3.4.2 Synthesis of the receptor HL

Rhodamine-6G hydrochloride (0.480 g, 1.0 mmol) was taken in ethanol and refluxed with an excess of hydrazine monohydrate (3.0 mL) for 2 h and kept for cooling overnight. Rhodamine-6G hydrazide was obtained as a pink precipitate. 3-Acetyl-4-hydroxy-2H-chromen-2-one (0.204 g, 1.0 mmol) and rhodamine-6G hydrazide (0.429 g, 1.0 mmol) was refluxed together in ethanol medium. The product was collected by evaporation of solvent under reduced pressure. Yield was 75%.

Calc. for C₃₇H₃₄N₄O₅ (HL): Calc. (%) C 72.195, H 5.528, N 9.105. Found (%), C 71.967, H 5.524, N 9.098.

¹H NMR data (CDCl₃, 300 MHz): δ 14.9526 (1H, s), 8.028 (1H, m), 7.942 (1H, m), 7.855 (1H, d, J= 6.741 Hz), 7.602(2H, m), 7.477 (1H, m), 7.097 (2H, m), 6.369 (1H, s), 6.303 (2H, s), 6.212 (1H, s), 4.14 (4H, q, J=7.8), 2.37 (3H, s), 2.17 (6H, s), 1.07 (6H, t, J=7.1).

IR data (KBr) (cm⁻¹): 3386, ν (O-H); 1722 and 1689, ν (C=O); 1638, ν (C=N).

HRMS data: calc. for C₃₇H₃₅N₄O₅ [M + H]⁺ (*m/z*): 615.70; found: 615.31.

CHAPTER 3

3.4.3 General Method for UV-Vis and Fluorescence Titration

3.4.3.1 Recording absorption and emission spectra

Stock solution of the receptor HL (10 μM) in [(MeCN/H₂O), 1:5, v/v] (at 25°C) using HEPES buffered solution at pH=7.2 was prepared. Solutions of the guest cations using their chloride salts in the order of 100 μM were prepared in deionized water. The changes in absorption and emission spectra were monitored by gradual addition of solutions of different cations to HL solution (10 μM). Aqueous solutions of different anions (100 μM) were added to HL-Al³⁺ and HL-Hg²⁺ solutions (10 μM) and spectra were recorded by means of UV-Vis and fluorescence methods.

3.4.3.2 Job's Plot by Fluorescence Method

A series of solutions containing HL (10 μM) and metal salt (10 μM) were prepared so that the volume remained constant (4 mL) each with Al³⁺ and Hg²⁺. MeCN:H₂O (1:5, v/v) was used as solvent at pH 7.2 using HEPES buffer. Job's plots were drawn by plotting ΔF versus mole fraction of Al³⁺ and Hg²⁺ [ΔF = change of emission intensity at 564 nm].

3.4.4 Computational methods

All calculations were carried out at the B3LYP [29-31] level using Gaussian 09 software [32]. The 6-31+G(d) basis set was assigned for all the elements except for Hg. For Hg, Lanl2DZ basis set with effective core potential was used [33]. The geometries of HL, HL-Al³⁺ and HL-Hg²⁺ were fully optimized using DFT method in singlet ground state. Vertical electronic excitations based on B3LYP optimized geometries were computed using the time-dependent density functional theory (TDDFT) formalism [34-36] in acetonitrile using conductor-like polarizable continuum model (CPCM) [37-39].

3.5. Conclusions

An efficient and selective fluorescent 'turn-on' chemosensor (HL) based on coumarin and rhodamine moieties for the detection of Hg²⁺ and Al³⁺ has been successfully synthesized. The

CHAPTER 3

colorimetric and fluorogenic detections of Al^{3+} and/or Hg^{2+} have been carried out by UV-Vis and fluorescence methods respectively. The limit of detection for both the metal ion was found to be in the order of 10^{-8} M and so it can be used as an efficient probe for the detection of trace level of Hg^{2+} and Al^{3+} in solution.

3.6. Reference

1. P. Grandjean, P. Weihe, R.F. White, F. Debes, *Environ Res.*, 1998, **77**, 165-172.
2. D.W. Boening, *Chemosphere*, 2000, **40**, 1335-1351.
3. X. Zhang, Y. Xiao, X. Qian, *Angew Chem Int Ed.*, 2008, **47**, 8025-8029.
4. V. K. Bhardwaj, H. Sharma, N. Kaur, N. Singh, *New J. Chem.*, 2013, **37**, 4192-4198.
5. Y. Wang, F. Yang, X. R. Yang, *Biosens. Bioelectron.*, 2010, **25**, 1994-1998.
6. Mercury Update: Impact on Fish Advisories; EPA Fact Sheet EPA-823-F-01-001; Environmental Protection Agency, Office of Water: Washington, DC, 2001.
7. Y. Jiao, L. Zhang, P. Zhou, *Talanta*, 2016, **150**, 14-19.
8. M. K. Hamdy, O. R. Noyes, *Appl. Microbiol.*, 1975, **30**, 424-432.
9. M. G. Sont, S. M. White, W. G. Flamm, G. A. Burdock, *Regul. Toxicol. Pharmacol.*, 2001, **33**, 66-79.
10. J. Exley, *J. Inorg. Biochem.*, 2005, **99**, 1747-1748.
11. D. Sarkar, A. Pramanik, S. Biswas, P. Karmakar, T. K. Mondal, *RSC Adv.*, 2014, **4**, 30666-30672.
12. J. R. Walton, *Neuro Toxicology*, 2006, **27**, 385-394.
13. G. C. Woodson, *Bone*, 1998, **22**, 695-598.

CHAPTER 3

14. P. D. Darbre, *J. Inorg. Biochem.*, 2005, **99**, 1912-1919.
15. G. D. Fasman, *Coord. Chem. Rev.*, 1996, **149**, 125-165.
16. P. D. Darbre, *Morphologie*, 2014, **100**, 65-74.
17. P. D. Darbre, F. Mannello, C. Exley, *J. Inorg. Biochem.*, 2013, **128**, 257-261.
18. B. Valeur, I. Leray, *Coord. Chem. Rev.*, 2000, **205**, 3-40.
19. G. Berthon, *Coord. Chem. Rev.*, 2002, **228**, 319-341.
20. Z. Krejpcio, R. W. Wojciak, *Pol. J. Environ. Stud.*, 2002, **11**, 251-254.
21. J. Barcelo, C. Poschenrieder, *Environ. Exp. Bot.*, 2002, **48**, 75-92
22. S. Yoon, E. W. Miller, Q. He, P. H. Do, C. J. Chang, *Angew Chem.*, 2007, **119**, 6778-6781.
23. S. Yoon, A. E. Albers, A. P. Wong, C. J. Chang, *J. Am. Chem. Soc.*, 2005, **127**, 16030-16031.
24. D. T. Quang, J. S. Kim, *Chem. Rev.*, 2010, **110**, 6280-6301.
25. L. Cao, C. Jia, Y. Huang, Q. Zhang, N. Wang, Y. Xue, D. Du, *Tetrahedron Lett.*, 2014, **55**, 4062-4066.
26. G. He, X. Zhang, C. He, X. Zhao, C. Duan, *Tetrahedron*, 2010, **66**, 9762-9768.
27. S. Adhikari, S. Mandal, A. Ghosh, S. Guria, D. Das, *Sens. Actuators B Chem.*, 2016, **234**, 222-230.
28. J. Park, S. Angupillai, Y. A. Son, *Mol. Cryst. Liq. Cryst.*, 2015, **662**, 103-113.
29. A. D. Becke, *J. Chem. Phys.*, 1993, **98**, 5648-5652.
30. C. Lee, W. Yang, R. G. Parr, *Phys. Rev. B*, 1988, **37**, 785-789.
31. D. Andrae, U. Haeussermann, M. Dolg, H. Stoll, H. Preuss, *Theor. Chim. Acta*, 1990, **77**, 123-141.
32. M. J. Frisch, G. W. Trucks, H. B. Schlegel, G. E. Scuseria, M. A. Robb, J. R. Cheeseman, G. Scalmani, V. Barone, B. Mennucci, G. A. Petersson, H. Nakatsuji, M. Caricato, X. Li, H. P.

CHAPTER 3

Hratchian, A. F. Izmaylov, J. Bloino, G. Zheng, J. L. Sonnenberg, M. Hada, M. Ehara, K. Toyota, R. Fukuda, J. Hasegawa, M. Ishida, T. Nakajima, Y. Honda, O. Kitao, H. Nakai, T. Vreven, J. A. Montgomery, Jr., J. E. Peralta, F. Ogliaro, M. Bearpark, J. J. Heyd, E. Brothers, K. N. Kudin, V. N. Staroverov, R. Kobayashi, J. Normand, K. Raghavachari, A. Rendell, J. C. Burant, S. S. Iyengar, J. Tomasi, M. Cossi, N. Rega, J. M. Millam, M. Klene, J. E. Knox, J. B. Cross, V. Bakken, C. Adamo, J. Jaramillo, R. Gomperts, R. E. Stratmann, O. Yazyev, A. J. Austin, R. Cammi, C. Pomelli, J. W. Ochterski, R. L. Martin, K. Morokuma, V. G. Zakrzewski, G. A. Voth, P. Salvador, J. J. Dannenberg, S. Dapprich, A. D. Daniels, Ö. Farkas, J. B. Foresman, J. V. Ortiz, J. Cioslowski and D. J. Fox, Gaussian, Inc., Wallingford CT, 2009.

33. P. J. Hay, W. R. Wadt, *J. Chem. Phys.*, 1985, **82**, 270-283.

34. R. Bauernschmitt, R. Ahlrichs, *Chem. Phys. Lett.*, 1996, **256**, 454-464.

35. R. E. Stratmann, G. E. Scuseria, M. J. Frisch, *J. Chem. Phys.*, 1998, **109**, 8218-8224.

36. M. E. Casida, C. Jamorski, K. C. Casida, D. R. Salahub, *J. Chem. Phys.*, 1998, **108**, 4439-4449.

37. V. Barone, M. Cossi, *J. Phys. Chem. A*, 1998, **102**, 1995-2001.

38. M. Cossi, V. Barone, *J. Chem. Phys.*, 2001, **115**, 4708-4717.

39. M. Cossi, N. Rega, G. Scalmani, V. Barone, *J. Comput. Chem.*, 2003, **24**, 669-681.

40. Y. Xiang, A. J. Tong, P. Y. Jin, Y. Ju, *Org. Lett.*, 2006, **8**, 2863.

41. S. Tobita, M. Yamamoto, N. Kurahayashi, R. Tsukagoshi, Y. Nakamura, H. Shizuka, *J. Phys. Chem. A*, 1998, **102**, 5206-5214.

CHAPTER 3

APPENDIX

CHAPTER 3

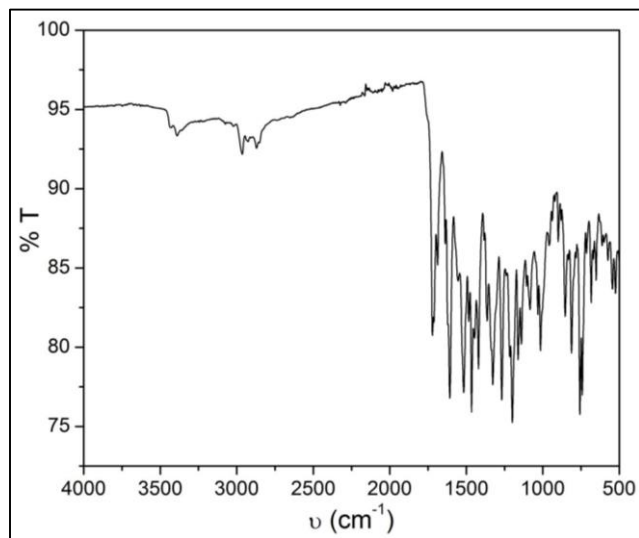


Fig. S1: IR spectrum of HL in KBr

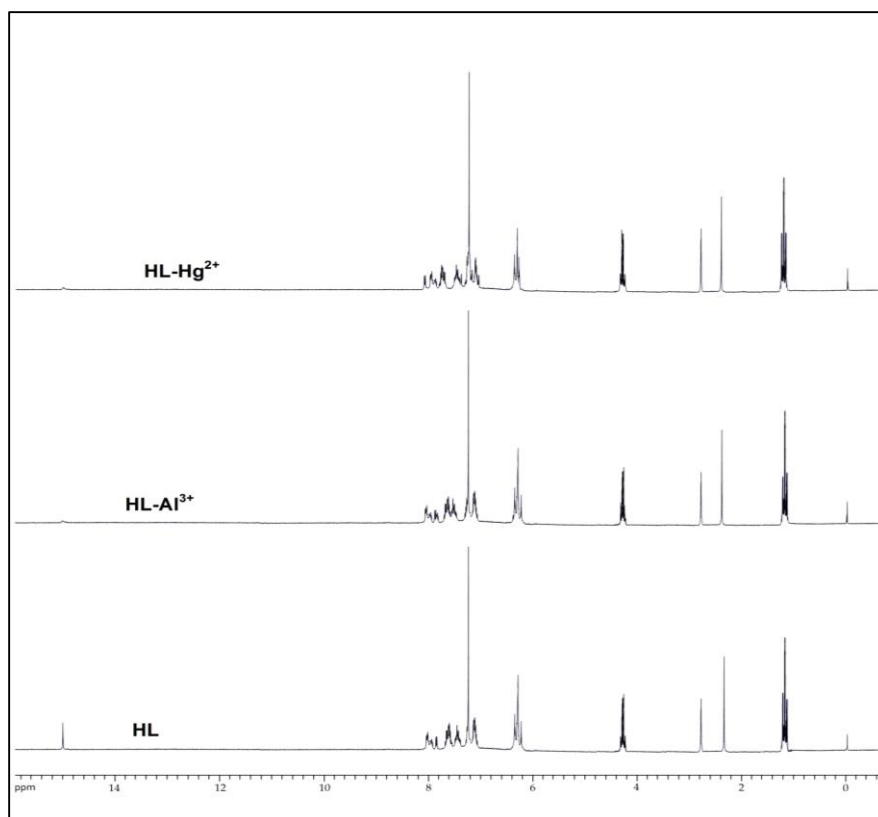


Fig. S2: ^1H NMR spectra of HL, HL- Al^{3+} and HL- Hg^{2+} in CDCl_3

CHAPTER 3

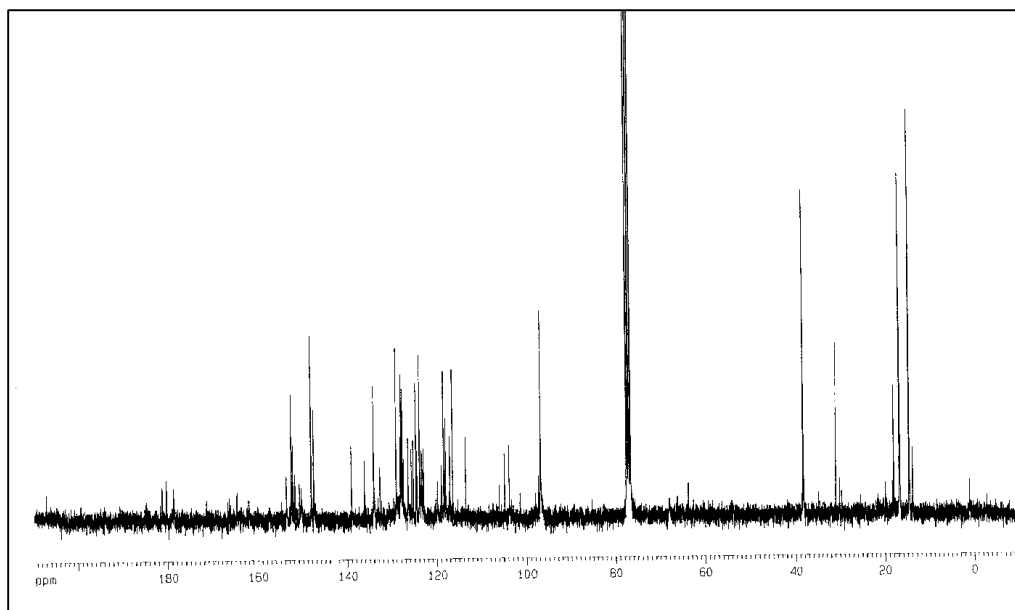


Fig. S3: ^{13}C NMR spectrum of HL in CDCl_3

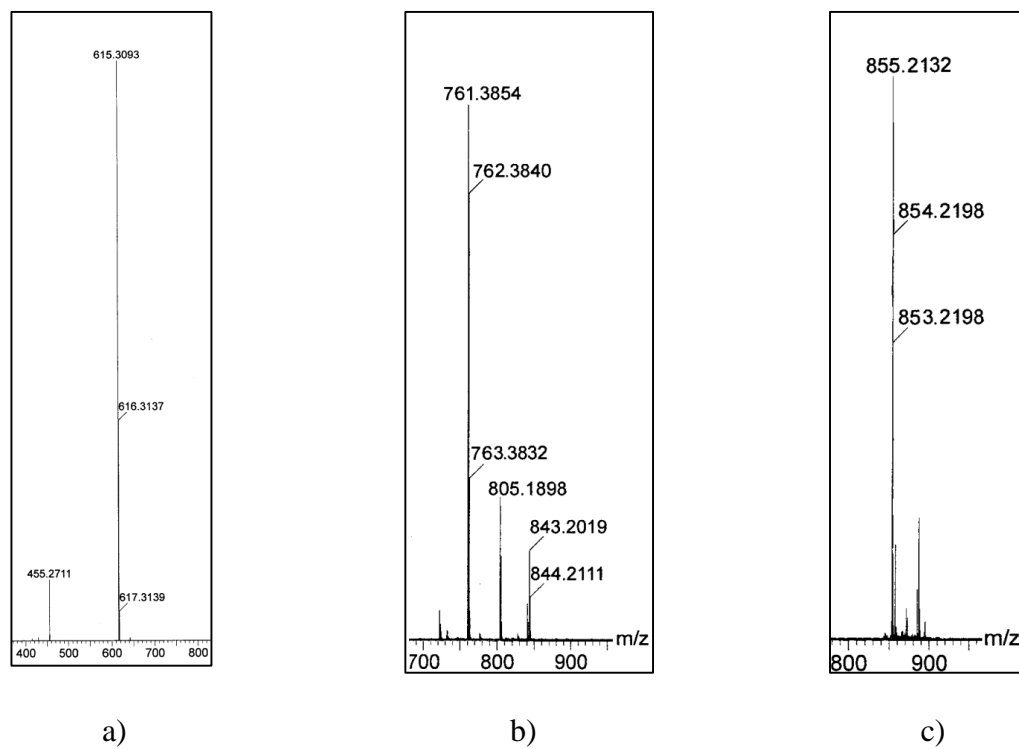


Fig. S4: HRMS spectra of (a) HL, (b) HL-Al^{3+} and (c) HL-Hg^{2+} in acetonitrile

CHAPTER 3

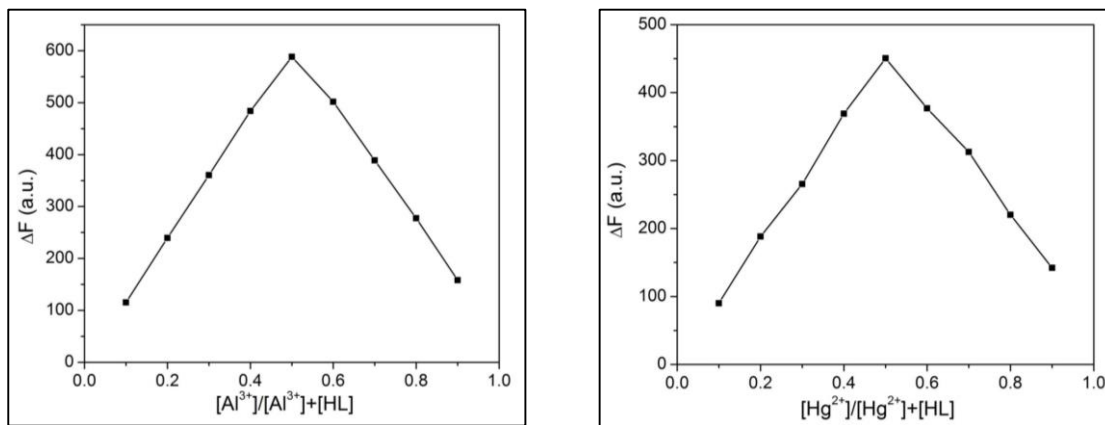


Fig. S5: and S6: Job's plot diagram of receptor (HL) for Al³⁺ and Hg²⁺ by fluorescence method.

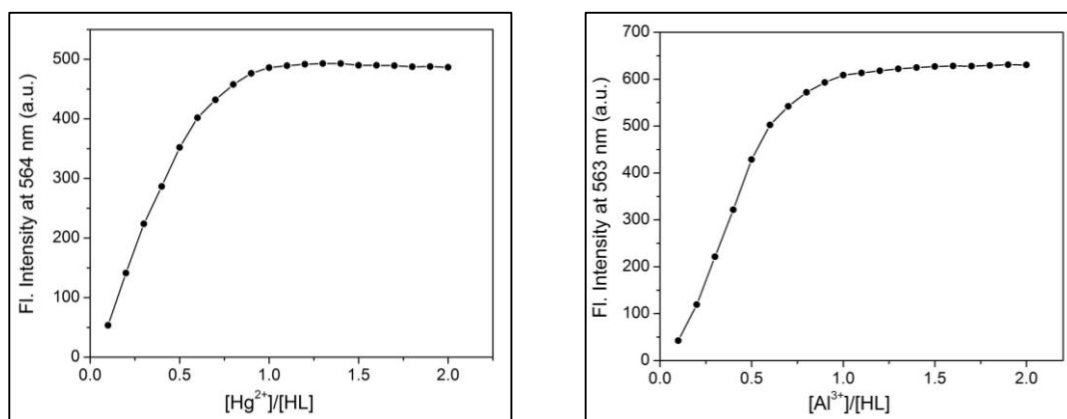


Fig. S7 and S8: Mole ratio plot of receptor (HL) for Hg²⁺ and Al³⁺ by fluorescence method.

CHAPTER 3

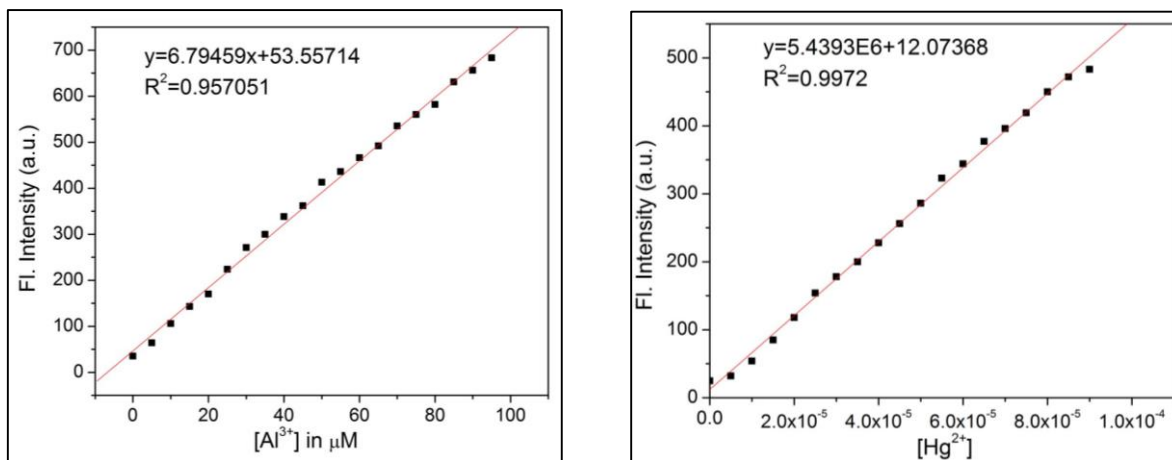


Fig. S9 and S10: Linear response curve of HL at 564 nm depending on the concentration Al^{3+} and Hg^{2+}

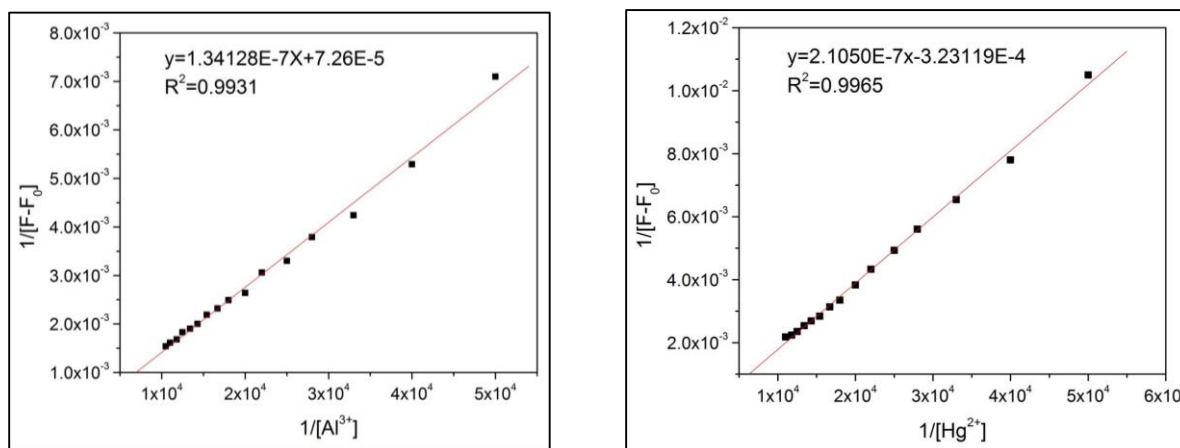


Fig. S11 and S12: Linear plot for the determination of association constant of HL- Al^{3+} and HL- Hg^{2+} complexes following Benesi-Hildebrande equation using fluorescence titration data.

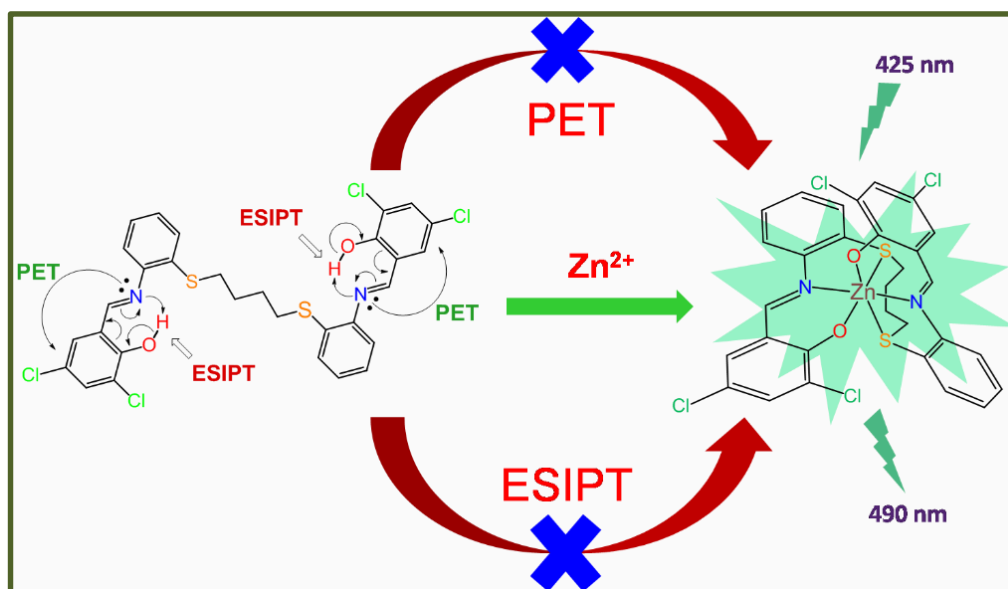
A thioether containing reversible fluorescence “turn-on” chemosensor for selective detection of zinc(II): Applications in live cell imaging and inhibit logic gate.

CHAPTER 4

A thioether containing reversible fluorescence “turn-on” chemosensor for selective detection of zinc(II): Applications in live cell imaging and inhibit logic gate.

Abstract

A new fluorescence probe (H₂L) is designed and synthesized for efficient and selective detection of zinc(II). H₂L exhibits fluorescence “turn-on” response with substantial enhancement of emission intensity with Zn²⁺ even in presence of other coexisting cations found in various environmental and biological samples. The calculated value of limit of detection (LOD) is 1.73×10⁻⁹ M. Exploiting the reversibility of the probe in presence of EDTA an INHIBIT logic gate is constructed with Zn²⁺ and EDTA as chemical inputs. DFT and TDDFT calculations are used to interpret electronic structure and elucidate the sensing mechanism. Cytotoxicity assay by MTT method with human breast cancer cell line (MCF-7) reveals that H₂L has negligible cytotoxicity and was used in live cell imaging



4.1. Introduction

Zn(II) is the second most abundant transition metal in human body after iron [1, 2] and plays indispensable roles in biological systems including regulation of cell growth, apoptosis, neural signal transmissions and catalysis [3, 4]. Disturbance of zinc level in the human body may cause a series of diseases, Parkinson's disease, Alzheimer's disease, metabolic disorder, prostate cancer etc. [5–7]. Excess intake of Zn(II), also may lead to diabetes, superficial skin diseases and even prostate cancer [5]. The above facts strongly advocate for the necessity of developing new and cost effective methods for efficient detection minuscule level of Zn(II) in biological samples. Fluorescent technique has recently gained profound attention as a powerful detection tool for non-invasive detection of metal ions because of its simplicity, sensitivity and reversible nature [8–10]. Recently, a good number of fluorescent probes are designed, based mostly on quinoline [11, 12], coumarin [12, 13], BINOL [14], fluorescein [15,16] and bipyridyl [17] fluorophores for effective detection of Zn(II). However, many of them require complex synthesis procedures involving drastic reaction conditions and expensive chemicals. The present chemosensor (H₂L) is prepared by simple Schiff base condensation reaction of 3,5-dichlorosalicylaldehyde and 2,2-(butane-1,4-diylbis(sulfanediyl))dianiline in methanol. Schiff bases are known to be a good complexing agent and extensively used for fluorogenic detection of metal ions [18, 19] and anions [20–22]. In recent years, Schiff bases of salicylidene derivatives are extensively used for the recognition of metal ions and anion sensing [23–25]. Moreover, the thioether containing fluorescence probes are known to be very efficient for selective detection of Zn(II) [26, 27]. In the present case the thioether containing chemosensor, H₂L exhibits significant and selective fluorescence enhancement in presence of Zn(II) in DMSO:H₂O (1:5, v/v) solution at pH 7.2. In presence of Zn(II), fluorescence intensity of H₂L enhanced significantly at 490 nm and an intense green fluorescence is observed under UV light. The structure of L–Zn²⁺ is confirmed by single crystal X-ray diffraction method. The cytotoxicity of the present probe towards human breast cancer cell lines (MCF-7) is studied and the probe is utilized for fluorescence live cell imaging.

4.2. Basis of present work

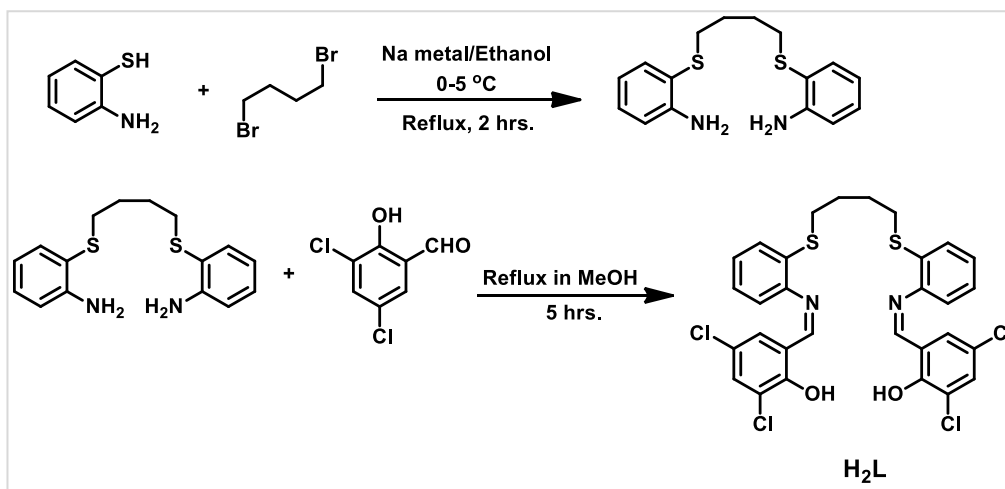
As discussed in the introductory section, due to escalated need for development of fluorescent receptors for the detection of Zn^{2+} ion, a number of fluorescent chemosensors has been reported till date. In 2017, Wen-Kui Dong et al. reported a Schiff base turn-on fluorescent sensor for Zn^{2+} . Upon addition of Zn^{2+} to the receptor the non-radiative PET process stops and the fluorescence gets turned on. [28] Very recently, Kettalu Ananthan Karthick et al. reported a novel pyridoxal based fluorescence sensor for selective turn-on fluorescent in presence of Zn^{2+} . [29] Vijay Kumar et al. also recently reported a turn-on fluorescence sensor capable of detecting Zn^{2+} based structurally on naphthalimide rings. [30] But, as discussed in the introduction and ensuing section 4.3.5 the present thioether based chemosensor has the advantage of high detection limit and application as a biomarker.

4.3. Results and discussion

4.3.1 Synthesis of H₂L

Synthetic procedure of formation of H₂L involves two very economic viable and easy steps. In the first step 2-aminothiophenol is alkylated with 1,4-dibromobutane. The alkylated product, in which two 2-aminothiophenol molecules are joined with a four carbon alkyl bridge, is then subjected to Schiff base condensation with 3,5-dichlorosalicylaldehyde in 1:1 molar ratio under refluxing condition for 5 hours to form the chemosensor H₂L (Scheme 4.1). The receptor H₂L is characterized by elemental and mass spectral analysis along with several other spectroscopic techniques (IR, UV-vis and NMR) (Figs. S1–S4).

CHAPTER 4



Scheme 4.1: Synthesis of receptor H₂L

4.3.2 Spectral characterization and analysis of H₂L

In IR spectrum of H₂L, imine (C=N) stretching frequency appears at 1590 cm⁻¹ and the aromatic double bonds appear at 1532–1494 cm⁻¹. The OH stretching frequency appears at 3281, 3591 and 3716 cm⁻¹ while the bands at 2843 and 3005 cm⁻¹ appear due to –CH stretching (Fig. S1). In ¹H-NMR spectrum of the sensor H₂L, OH protons appear at δ13.19 ppm which is absent in the L-Zn²⁺ complex due to coordination of H₂L to the Zn²⁺ ion (Fig. S4). The imine proton appears at δ8.54 ppm. The aromatic protons in the receptor appear as expected in the region δ7.16–7.44 ppm. In the L-Zn²⁺ complex, all aromatic protons appear at a bit downfield compared to that of H₂L, which can be clearly explained due to the coordination of Zn²⁺ with H₂L. Mass spectrum shows m/z peak corresponding to [H₂L+H⁺] at 651.47 (Fig. S2) while for L-Zn²⁺ complex, the peaks at 714.91 corresponds to [Zn(H₂L)+H⁺] species (Fig. S3) supporting 1:1 complex formation.

4.3.3 Cation sensing studies: UV-Vis spectroscopy studies

The probe (H₂L) (10 μM) showed a strong absorbance band at 361 nm in DMSO:H₂O (1:5, v/v, pH = 7.2) solution. Upon gradual addition of aqueous solution of Zn²⁺ (20 μM) into it, the absorbance at 361 nm decreased with generation of a new absorption band at 406 nm. The formation of this new

CHAPTER 4

absorption band may be due to the coordination of H₂L with Zn²⁺. A distinct isosbestic point appeared at 390 nm (Fig. 4.1).

The absorption spectral changes of H₂L were also studied in presence of other metals i.e., Na⁺, K⁺, Ca²⁺, Mg²⁺, Mn²⁺, Fe³⁺, Al³⁺, Cr³⁺, Co²⁺, Ni²⁺, Cu²⁺, Cd²⁺ and Hg²⁺ (Fig. 4.2). Only Ni²⁺ showed a change in the absorption spectrum other than Zn²⁺ but no abrupt change was observed for any other metal ions.

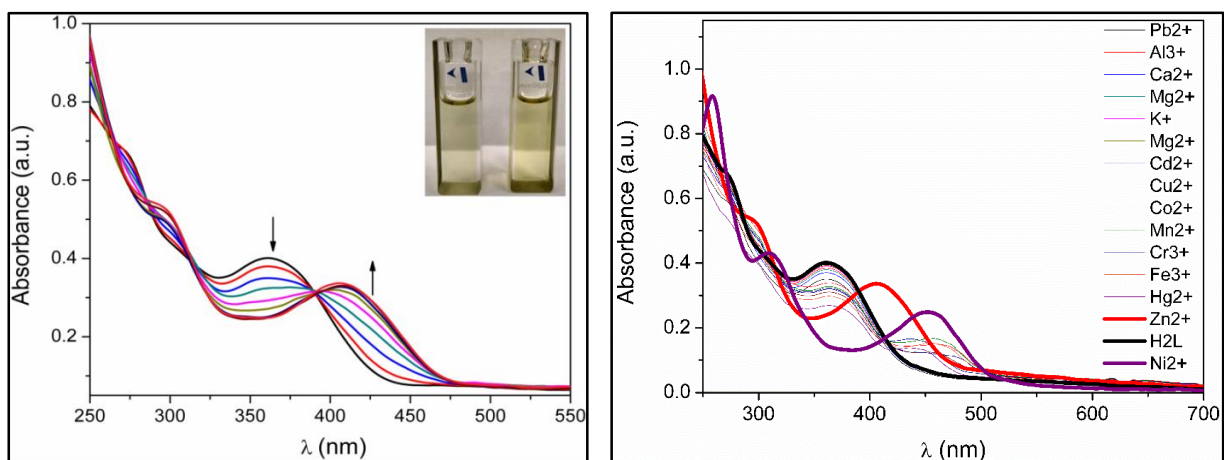


Fig. 4.1 and 4.2: Change in UV-Vis spectrum of H₂L upon gradual addition of Zn²⁺ and Change in absorption spectra of H₂L (10 μM) upon addition of different metal ions, i.e., Na⁺, K⁺, Ca²⁺, Mg²⁺, Mn²⁺, Fe³⁺, Cr³⁺, Al³⁺, Co²⁺, Ni²⁺, Hg²⁺, Cu²⁺, Pb²⁺ and Cd²⁺ (40 μM) in DMSO:H₂O (1:5, v/v) using HEPES buffered solution at pH =7.2.

4.3.4 Cation sensing studies: Fluorescence emission studies

The chemosensor, H₂L (10 μM) shows very weak emission band with a maxima (F₀) at around 556 nm ($\phi_F = 0.005$) in DMSO:H₂O (1:5, v/v, pH = 7.2) solution in the absence of metal ions. Gradual addition of Zn²⁺ (20 μM) to the probe solution showed a “turn-on” emission response with a blue shift of the emission intensity by ~ 66 nm at 490 nm ($\phi_F = 0.265$) (Fig. 4.3). Further, on addition of EDTA into L-Zn²⁺ solution, fluorescent intensity at 490 nm gradually diminishes due to the chelation of Zn²⁺ with EDTA resulting in the release of the free probe H₂L (Fig. 4.4). This observation proves the reversible nature of H₂L indicating to the fact that our synthesized probe can

CHAPTER 4

be reused, making it very viable economically. The enhancement of emission intensity upon addition of Zn^{2+} followed by quenching of fluorescence intensity upon addition of EDTA reflects a strong selective OFF-ON-OFF fluorescent signaling property of the ligand.

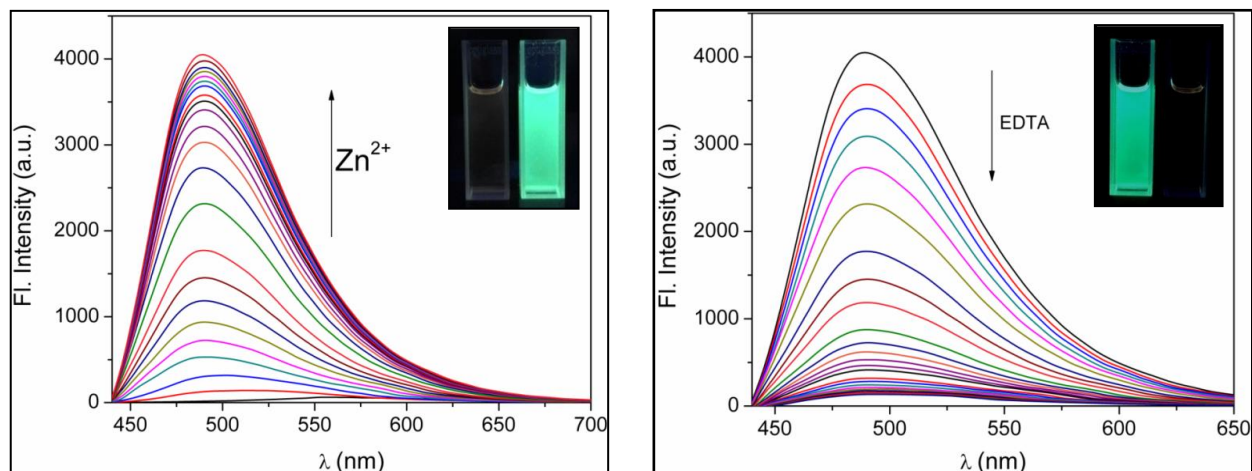


Fig. 4.3 and 4.4: Change in emission spectrum of H₂L (10 μM) upon gradual addition of 100 μM Zn^{2+} in 1:5, v/v DMSO:H₂O and Change in emission spectrum of H₂L-Zn²⁺ upon gradual addition of EDTA in 1:5, v/v DMSO:H₂O.

Fluorescence emission intensity of H₂L (10 μM) was also studied in presence of other metal ions, i.e; Na^+ , K^+ , Ca^{2+} , Mg^{2+} , Al^{3+} , Mn^{2+} , Fe^{3+} , Cr^{3+} , Co^{2+} , Ni^{2+} , Cu^{2+} , Cd^{2+} and Hg^{2+} (20 μM) in DMSO:H₂O (1:5, v/v, pH = 7.2) but there is hardly any change in emission intensity of H₂L except for Cd^{2+} . In presence of Cd^{2+} , H₂L shows slight increase in the fluorescence intensity. In case of Cd^{2+} , fluorescence intensity increases about 7 fold (Fig. 4.5). But this emission enhancement is merely negligible compared to the huge and sharp “turn-on” emission enhancement of 64 fold in presence of Zn^{2+} .

CHAPTER 4

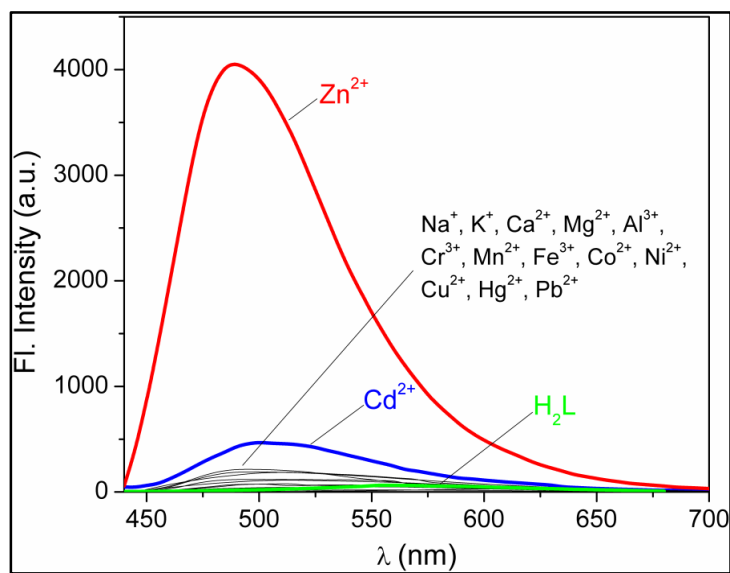


Fig. 4.5: Change in emission intensity of H₂L (10 μM) upon addition of different metal ions, i.e., Na⁺, K⁺, Ca²⁺, Mg²⁺, Mn²⁺, Fe³⁺, Cr³⁺, Al³⁺, Co²⁺, Ni²⁺, Hg²⁺, Cu²⁺, Pb²⁺ and Cd²⁺ (40 μM) in DMSO/H₂O (1/5, v/v) using HEPES buffered solution at pH=7.2.

The competition study revealed that in presence of Zn²⁺, the emission intensity of Cu²⁺, Fe³⁺ and Cr³⁺ were changed but for the other metal ions, there is hardly any changes in the emission intensity (Fig. 4.6). Thus the synthesized receptor (H₂L) is highly efficient in detecting Zn²⁺ in presence of other metals and in addition to that it can detect zinc in biological or environmental samples where other metals usually co-exist with Zn²⁺.

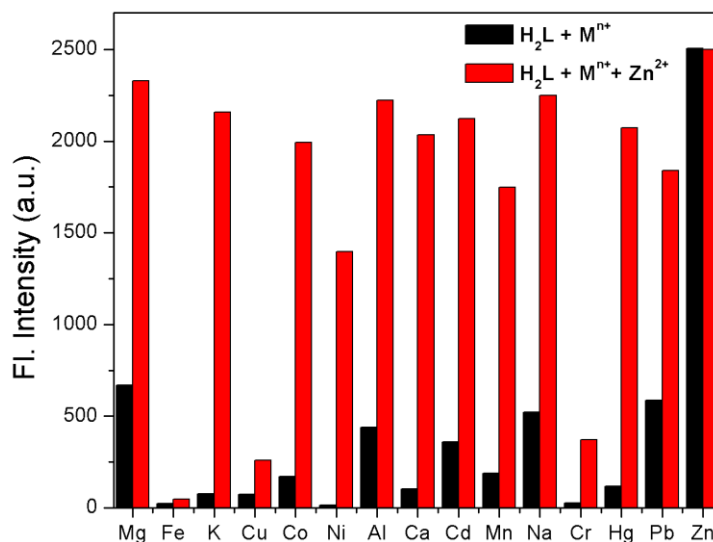
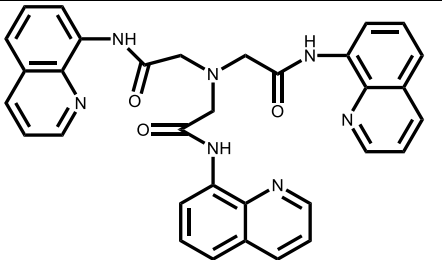


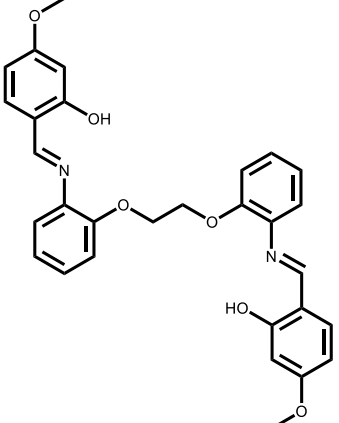
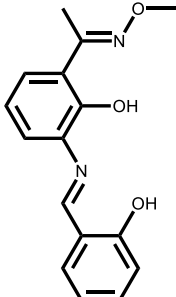
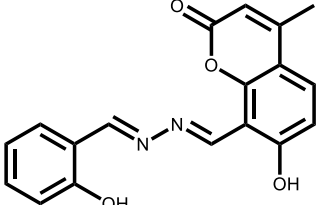
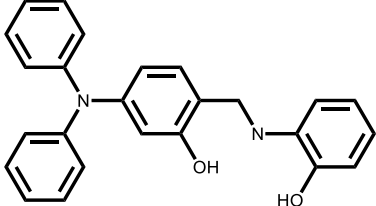
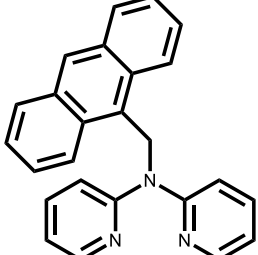
Fig. 4.6: Competition study using fluorescence method after addition of different analytes (40 μM) in the solution of H₂L (10 μM) in presence of Zn²⁺ (40 μM).

4.3.5 Binding studies with H₂L and Zn²⁺ and Detection limit of H₂L

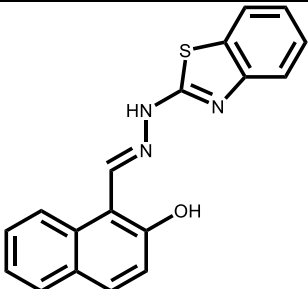
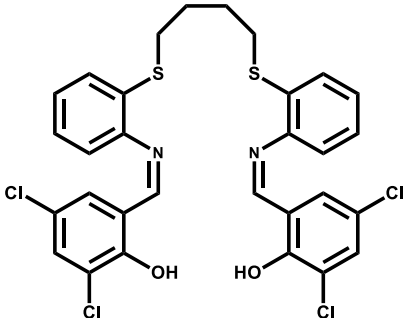
Job's plot of emission intensity shows maxima at ~0.5 mole fraction of the analyte indicating 1:1 complex formation of H₂L with Zn²⁺ (Fig. S5). From emission spectral change, limit of detection of the sensor, H₂L is determined for Zn²⁺ using the equation $LOD = K \times SD/S$, where SD is the standard deviation of the blank solution and S is the slope of the linear response curve (Fig. S6). The limit of detection for Zn²⁺ is found to be 1.73×10^{-9} M from fluorescent spectral titration. This clearly demonstrates that H₂L is highly efficient in sensing Zn²⁺ even in very minuscule levels. The association constant (K_a) has been determined by plotting the fluorescence intensity as a function of Zn²⁺ concentration to a suitable computer-fit non-linear program. From the non-linear plot the association constant (K_a) is found to be 6.91×10^4 M⁻¹ (Fig. S7). In Table 4.1, we have compared the limit of detection and association constant values of some previously reported Zn²⁺ sensors with our synthesized probe (H₂L).

Serial	Structure of chemosensors	Limit of Detection (LOD)	Association constant (K_a)	Reference
1		3.20×10^{-6} M	4.00×10^4 M ⁻¹	[28]

CHAPTER 4

2		$1.80 \times 10^{-8} \text{ M}$	$1.24 \times 10^4 \text{ M}^{-1}$	[29]
3		$1.44 \times 10^{-7} \text{ M}$	$2.25 \times 10^4 \text{ M}^{-1}$	[30]
4		$6.10 \times 10^{-8} \text{ M}$	$2.91 \times 10^3 \text{ M}^{-1/2}$	[31]
5		$3.43 \times 10^{-6} \text{ M}$	$1.30 \times 10^5 \text{ M}^{-1}$	[32]
6		$2.06 \times 10^{-6} \text{ M}$	$1.00 \times 10^5 \text{ M}^{-1}$	[33]

CHAPTER 4

7		$6.50 \times 10^{-7} \text{ M}$	$1.30 \times 10^4 \text{ M}^{-1}$	[34]
8		$1.73 \times 10^{-9} \text{ M}$	$6.91 \times 10^4 \text{ M}^{-1}$	Present work

4.3.6 Lifetime decay profile of the receptor H₂L

A nanosecond time-resolved fluorescence technique has been executed in order to observe the excited state behavior of H₂L and its complex with Zn²⁺ in DMSO:H₂O (1:5, v/v, pH = 7.2). The life time decay fit well in mono-exponential decay profile for free probe with life time of 0.77 ns ($\chi^2 = 1.01$), while for L-Zn²⁺ complex bi-exponential decay is observed with significant enhancement of average life time, $t_{av} = 2.67 \text{ ns}$ ($\chi^2 = 1.02$) (Fig. 4.5). The low fluorescence lifetime of the free probe (H₂L) may be due to the ESIPT effect. After complexation with Zn²⁺, structural rigidity appears in the probe and it shows the CHEF effect and ESIPT is also suppressed. Consequently, the emission lifetime increased significantly in the complex.

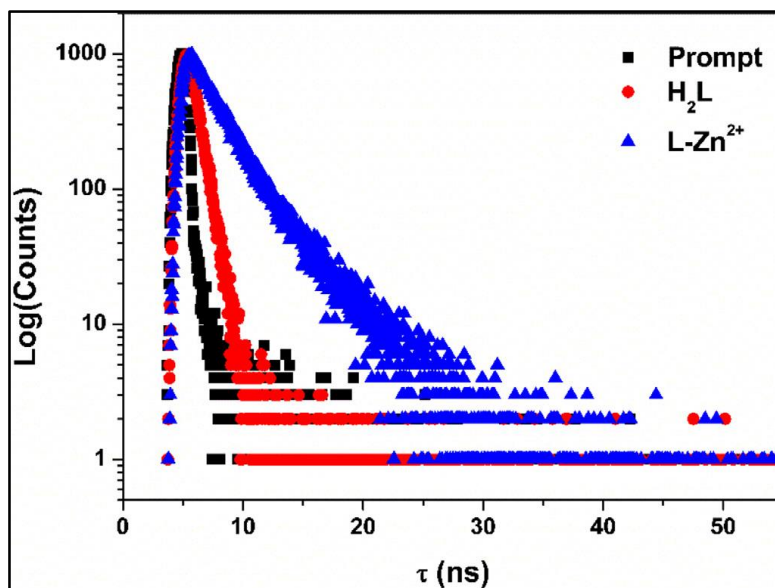


Fig. 4.7: Time-resolved fluorescence decay profile of H_2L (●), H_2L-Zn^{2+} complex (▲) and prompt (■) ($\lambda_{ex} = 370$ nm).

4.3.7 pH study

The effect of pH on the emission intensity of the receptor (H_2L) ($10 \mu M$) was studied in absence and presence of Zn^{2+} . In case of H_2L , emission intensity was slightly increased in the acidic pH range of 2.0–3.0 due to the protonation of the imine functionality preventing the excited state intramolecular proton transfer (ESIPT) process. There is again a decrease in fluorescence intensity from acidic to the near neutral pH range 4.0–7.0 where the intensity is really low (Fig. 4.6). Above pH 7.0, sharp increase in the emission intensity was observed due to deprotonation of phenolic hydroxyl group. As a result, the excited state intramolecular proton transfer (ESIPT) process gets hindered resulting in the enhancement of the fluorescence intensity [35, 36]. On addition of Zn^{2+} to the probe solution, the fluorescence intensity remained mostly unchanged at $pH < 4.0$, while there is an increase in fluorescence intensity as seen in the pH range 5.0–7.0. But, on further increase in pH, fluorescence intensity drops slowly due to the formation of $Zn(OH)_2$ at $pH > 8.0$ followed by the dissociation of the Zn^{2+} complex. Thus the receptor (H_2L) is efficient in detecting Zn^{2+} in the biologically relevant

CHAPTER 4

pH range (6.0–7.6). However, at low pH range ($\text{pH} \leq 4.0$), H_2L tends to combine with protons and at higher pH values ($\text{pH} \geq 8.0$), the ESIPT process gets hindered due to the deprotonation of phenolic hydroxyl group and hence in such extreme pH ranges, the receptor (H_2L) becomes ineffective in detecting Zn^{2+} .

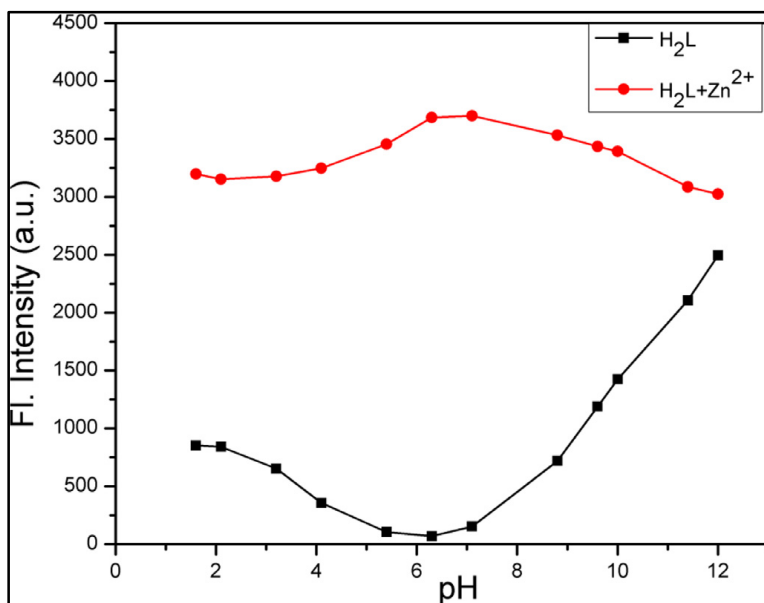


Fig. 4.8: Effect of pH on fluorescence intensity of receptor H_2L (---) and $\text{L} + \text{Zn}^{2+}$ (---) complex.

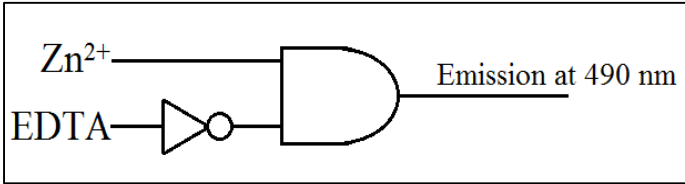
4.3.8 Application as logic gate

Molecular logic gate with biological and chemical compounds as inputs have surfaced as an alternative for silicon based logic gates. Several combinations of logic gates are used to execute arithmetic operations in semiconductor technology [37, 38]. The molecular logic gates, capable of carrying out Boolean logic operations in response to physical, chemical and biological inputs have become a fascinating topic for research in information technology. Moreover, logic gates with one or more chemical inputs have been developed to operate at the nano dimension [39, 40]. Several molecular logic function systems are reported recently [41, 42]. Here we have used our synthesized chemosensor H_2L as the basis of the molecular logic function with Zn^{2+} as well as the chelating

CHAPTER 4

agent EDTA as chemical inputs and emission mode at 490 nm as the output. Emission maxima at 490 nm appears as a result of coordination of H₂L with the metal Zn²⁺. Upon addition of EDTA to the above solution, the emission intensity at 490 nm again decreases. So it is noticed that, with two inputs as Zn²⁺ and EDTA, H₂L has the ability to exhibit INHIBIT function via emission output. An INHIBIT logic gate represents an AND gate with an inverter in one of its input. Only when Zn²⁺ is present and values of the other input i.e., EDTA is 0 then the emission at 490 nm is 1. Thus the emission maxima at 490 nm with Zn²⁺ and EDTA as chemical inputs can be explicated as a monomolecular circuit showing an INHIBIT logic function (Scheme 4.2).

Input		Output
IN1	IN2	OUT
Zn ²⁺	EDTA	Emission at 490 nm
0	0	0
0	1	0
1	0	1
1	1	0



Scheme 4.2. Truth table and the monomolecular circuit based on Zn²⁺ and EDTA as chemical inputs and emission mode at 490 nm as output.

4.3.9 Probable sensing mechanism

When Zn²⁺ is absent, H₂L shows a weak emission band at around 556 nm. Upon gradual addition of Zn²⁺ the receptor H₂L shows an excellent fluorescence intensity enhancement of 64-fold with new emission maxima at 490 nm. The quenching of emission intensity in free probe (H₂L) may be attributed due to the excited state intramolecular proton transfer (ESIPT) process and/or photo induced electron transfer (PET) process. The ESIPT and PET processes get inhibited due to the coordination with Zn²⁺ to the thioether sulphur atom, imine nitrogen atom and the disappearance of

CHAPTER 4

the proton of aromatic-OH group in L-Zn²⁺ complex. Moreover, the chelation enhanced fluorescence (CHEF) may also occur in the complex due to the rigid structure of L-Zn²⁺. (See Fig. 4.7)

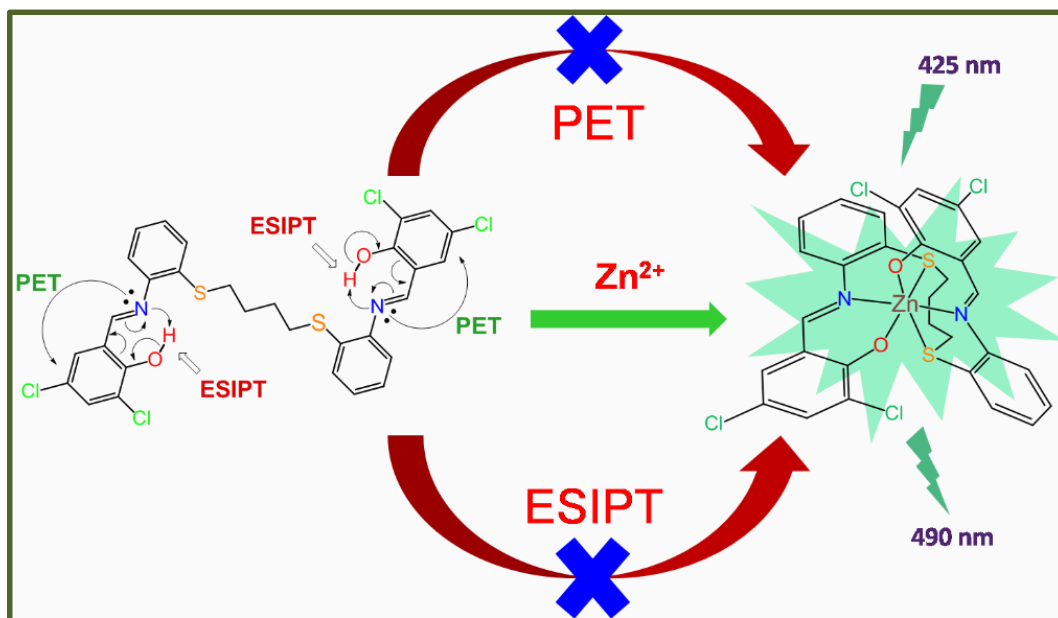


Fig. 4.9: Schematic representation of probable sensing mechanism.

4.3.10 Molecular crystal structure of H₂L complex

The 1:1 complexation of the probe (H₂L) with Zn²⁺ is further confirmed by single crystal X-ray structure of L-Zn²⁺ complex. The details of crystallographic data and refinement parameters are summarized in table S1. An ORTEP plot of L-Zn²⁺ complex along with the numbering scheme is shown in Fig. 4.8. The crystal structure exhibits a pseudo-octahedral geometry around Zn(II) center bonded with the receptor (H₂L) molecule in the di-anionic form in N₂S₂O₂-hexadentate binding fashion. The metal is coordinated to the ligand through the imine nitrogen atoms (N1 and N2),

CHAPTER 4

phenolic oxygen atoms (O1 and O2) and thioether-S atoms (S1 and S2), forming an octahedral complex. The selected bond distances and angles of complex are summarized in table S2.

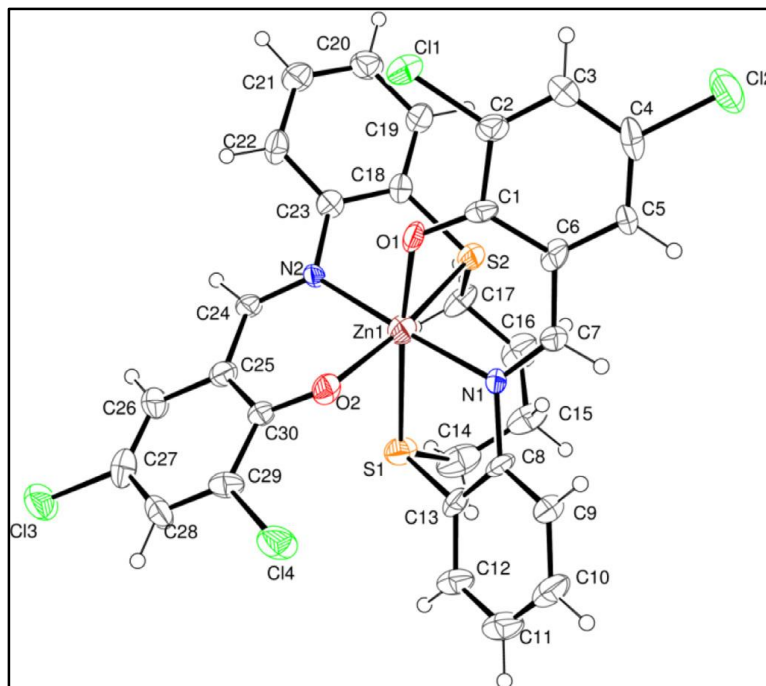


Fig. 4.10: ORTEP plot of H_2L-Zn^{2+} complex with 35% ellipsoidal probability.

4.3.11 Electronic spectra and DFT calculation

To gain a detailed insight into the electronic structure and electronic transition processes, geometry optimizations using density functional theory DFT and TDDFT calculations of free probe (H_2L) and $L-Zn^{2+}$ complex are carried out in B3LYP/6-31+G(d) method. The optimized structures of H_2L and $L-Zn^{2+}$ are shown in Fig. S8. Contour plots of H_2L and $L-Zn^{2+}$ are shown in Fig. S9 and S10 respectively. The energy and composition of some selected molecular orbitals of H_2L and $L-Zn^{2+}$ are summarized in table S3. The significant observation of DFT calculation is that the HOMO-LUMO energy gap of H_2L is significantly decreased from 3.65 eV to 3.22 eV in the Zn^{2+} complex, which is well corroborated with the HOMO-LUMO transitions of H_2L and $L-Zn^{2+}$. The HOMO→LUMO transition for the free probe is found to be at $\lambda = 382.6$ nm ($\lambda_{\text{expt}} = 361$ nm) for H_2L , while for $L-Zn^{2+}$ it is calculated to be at 422.2 nm ($\lambda_{\text{expt}} = 406$ nm).

CHAPTER 4

4.3.12 Cell bio-imaging

To further elaborate its practical application, the fluorescence probe is used for bio-imaging of human breast cancer cell lines (MCF-7). The cell viability study by MTT method revealed that the free probes (H₂L) has negligible toxicity at lower concentration levels on MCF-7 cell lines and IC₅₀ dose is found to be 52.4 μ M for the free probe (Fig. 4.9). For imaging study, MCF-7 cell lines treated with 15 μ M H₂L and Zn²⁺ solutions separately in six well plates. To visualize the morphological changes, the cells were stained with DAPI. For free probe, no significant fluorescence is observed under fluorescence microscope through green channel. But when the cells are incubated with both 15 μ M H₂L and Zn²⁺ and observed under fluorescence microscope a striking green fluorescence was observed through green channel (Fig. 4.10).

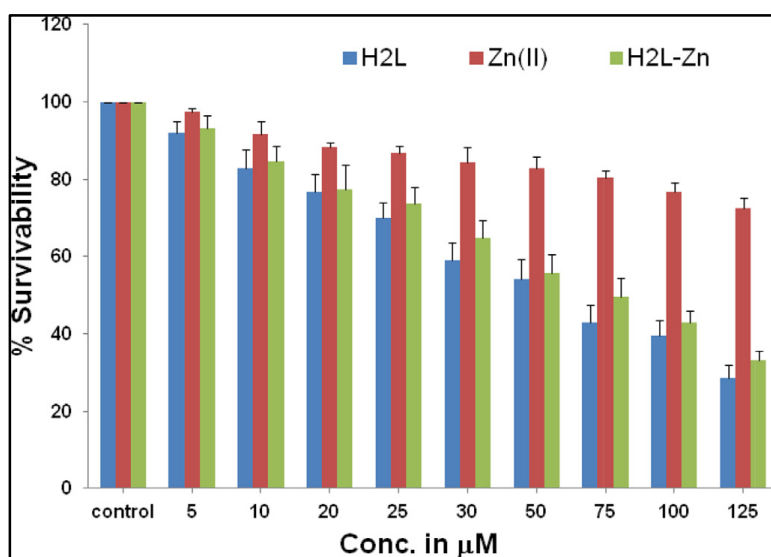


Fig. 4.11: MTT assay of Zn²⁺, H₂L and L-Zn²⁺ complex on MCF-7 cells.

CHAPTER 4

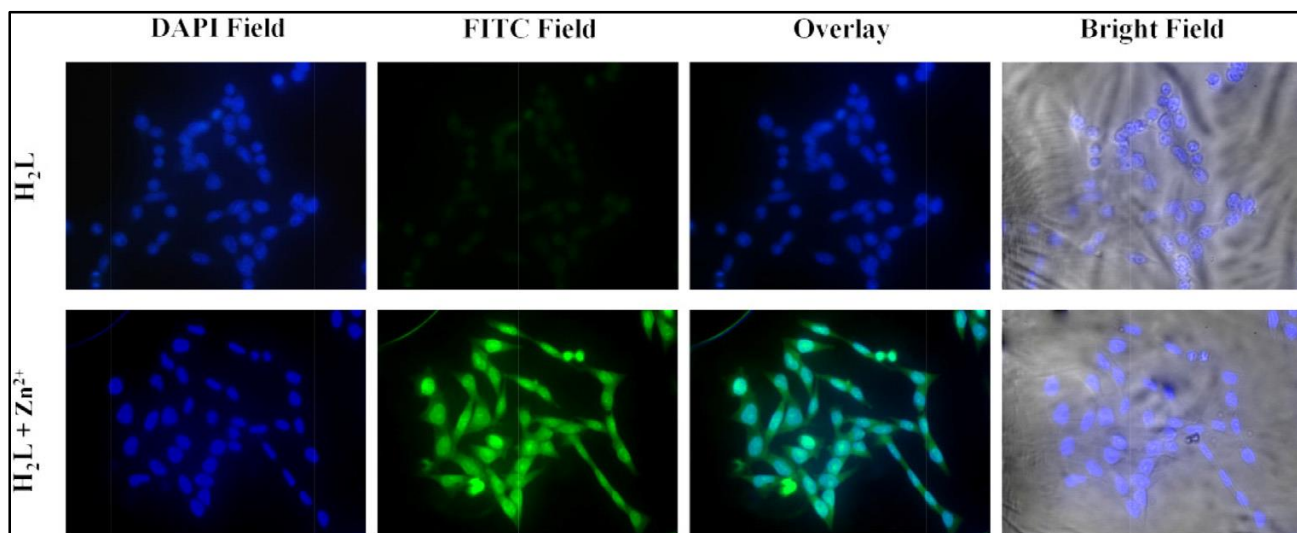


Fig. 4.12: Fluorescence image of MCF-7 cells after incubation with 15 μM H₂L and 15 μM L-Zn²⁺ complex. DAPI is used to stain the nucleus. Incubation period is 24 h.

4.4. Experimental

4.4.1 Materials and methods

2-Aminobenzenethiol and 1,4-dibromobutane were purchased from Sigma Aldrich and used without further purification. 3,5-Dichlorosalicylaldehyde was prepared from 2,4-dichlorophenol using the reported procedure [43]. All other reagents and solvents were purchased from commercial sources and used without any further purification.

Elemental analysis was carried out in a 2400 Series-II CHN analyzer, Perkin Elmer, USA. HRMS mass spectra were recorded on Waters (Xevo G2 Q-TOF) mass spectrometer. Infrared spectra were taken on a RX-1 Perkin Elmer spectrophotometer with samples prepared as KBr pellets. Electronic spectral studies were performed on a PerkinElmer Lambda 750 spectrophotometer. Luminescence property was measured using Shimadzu RF-6000 fluorescence spectrophotometer at room temperature (298 K). NMR spectra were recorded using a Bruker (AC)

CHAPTER 4

300 MHz FTNMR spectrometer of ~0.05 M solutions of the compounds in CDCl₃. Fluorescence lifetime measurements were carried out by using time-correlated single photon counting set up from Horiba Jobin-Yvon. The emission decay data were collected on a Hamamatsu MCP photomultiplier (R3809) and were analyzed by using IBH DAS6 software. The goodness of fit was evaluated by χ^2 criterion and visual inspection of the residuals of the fitted function to the data.

4.4.2 Synthesis of the receptor H₂L

Synthetic procedure of formation of H₂L involves two very economic cheap and easy steps. In the first step 2-aminothiophenol is alkylated with 1,4-dibromobutane using a reported technique [44]. Methanolic solution (20 ml) of the alkylated product (3.041 g., 10 mmol) is then added dropwise to the methanolic solution (20 ml) of 3,5-dichlorosalicylaldehyde (1.899 g., 10 mmol) with constant stirring. After the addition is complete the mixture is kept at refluxing condition for 10 h. After cooling the reaction mixture solvent was removed under reduced pressure using rotary evaporator. The solid mass thus obtained was recrystallized from dry methanol to get the pure ligand (H₂L). Yield was 3.942 g. (80%).

Anal. Calc. C₃₀H₂₄N₂Cl₄O₂S₂ (H₂L): C 55.39; H 3.72; N 4.31. Found: C 55.33; H 3.66; N 4.25.

IR data (KBr, cm⁻¹): 1590 ν (C=N); 2843 and 3005 ν (-CH); 3281, 3591 and 3716 ν (OH).

¹H NMR (300 MHz, CDCl₃): δ 13.19 (1H, s), 8.54 (1H, s), 7.15-7.44 (8H, m), 2.96 (2H, t, J = 6.99 Hz), 1.82 (1H, m).

HRMS (m/z): calculated for [M+H]⁺ = 651.4737; found = 651.4703.

4.4.3 General Method for UV-Vis and Fluorescence Titration

4.4.3.1 Recording absorption spectra

Stock solution of the receptor H₂L (10 μ M) in [(DMSO/H₂O), 1:5, v/v] (at 25°C) using HEPES buffered solution at pH = 7.2 was prepared. The solution of the guest cations using their chloride salts in the order of 100 μ M were prepared in deionized water. Solutions of various concentrations containing host and increasing concentrations of cations were prepared separately. The changes in

CHAPTER 4

UV-Vis spectra of receptor (10 μM) upon gradual addition of 100 μM metal ion solutions were recorded.

4.4.3.2 Recording emission spectra

Stock solution of the receptor H_2L (10 μM) in [(DMSO / H_2O), 1:5, v/v] (at 25°C) using HEPES buffered solution at pH=7.2 was prepared. To it ZnCl_2 (100 μM) solution was gradually added and fluorescence spectra were recorded. EDTA solution of 100 μM was added to the same solution where Zn^{2+} was added gradually to H_2L and fluorescence spectra were recorded. Chloride salts of Na^+ , K^+ , Ca^{2+} , Mg^{2+} , Mn^{2+} , Fe^{3+} , Cr^{3+} , Al^{3+} , Co^{2+} , Ni^{2+} , Cu^{2+} , Cd^{2+} and Hg^{2+} in DMSO : H_2O (1:5, v/v, pH=7.2) of 100 μM concentration were also added to the 10 μM H_2L solution and fluorescence spectra were recorded. To it further ZnCl_2 (40 μM) solution was added and spectra were recorded. For fluorescence study excitation wavelength used was 425 nm (excitation slit = 3.0 and emission slit = 3.0).

4.4.3.3 Job's plot by fluorescence method

For Job's plot experiment H_2L (20 μM) in (1:5, v/v) H_2O :DMSO and 20 μM ZnCl_2 were prepared as stock solution using HEPES buffer at pH 7.2. The concentration of each solution was varied keeping the total volume fixed at 5 mL. Fluorescence intensity was monitored at 490 nm. Job's plot were drawn by plotting ΔF as a function of mole fraction of Zn^{2+} (ΔF = change of intensity of the emission spectrum at 490 nm). The excitation wavelength used was 425 nm.

4.4.3.4 Determination of fluorescence Quantum Yields (Φ) of H_2L and its complex with Zn^{2+}

The luminescence quantum yield was determined using quinine sulfate ($\phi_s = 0.54$ in 0.5M H_2SO_4) as reference dye. The compounds and the reference dye were excited at the same wavelength and the emission spectra were recorded. The area of the emission spectrum was integrated and the quantum yield is calculated according to the following equation:

$$\Phi_x = \Phi_s \times \left(\frac{I_x}{I_s}\right) \times \left(\frac{A_s}{A_x}\right) \times \left(\frac{n_x}{n_s}\right)^2$$

CHAPTER 4

Where, x & s designate the unknown and standard solution respectively, ϕ is the quantum yield, I is the integrated area under the fluorescence spectra, A is the absorbance and n is the refractive index of the solvent.

The quantum yields of H_2L and $L-Zn^{2+}$ are determined using the above mentioned equation and the values are found to be 0.005 and 0.265 respectively.

4.4.3.5 Determination of detection limit

The detection limit was calculated based on the fluorescence titration. To determine the S/N ratio, the emission intensity of H_2L without Zn^{2+} was measured by 10 times and the standard deviation of blank measurements was determined. The detection limit of H_2L for Zn^{2+} was determined from the following equation¹:

$$DL = K \times Sb_1/S$$

Where $K = 2$ or 3 (we take 3 in this case); Sb_1 is the standard deviation of the blank solution; S is the slope of the calibration curve.

For Zn^{2+} : From the graph we get slope = 2.37×10^8 and Sb_1 value is 0.13703 . Thus using the formula we get the Detection Limit = 1.73×10^{-9} M i.e., H_2L can detect Zn^{2+} in this minimum concentration through fluorescence techniques.

4.4.3.6 Determination of binding constant from fluorescence titration data

Binding constant was calculated according to the Benesi-Hildebrand equation. K_a was calculated following the equation stated below.

$$1/(F-F_0) = 1/\{K_a(F_{max}-F_0) [M^{n+}]^x\} + 1/[F_{max}-F_0]$$

Here F_0 , F and F_{max} indicate the emission in absence of, at intermediate and at infinite concentration of metal ion respectively.

4.4.4 Computational method

Full geometry optimizations were carried out using the density functional theory (DFT) method at the B3LYP [45,46] level for the compounds. All calculations were performed with Gaussian 09 program package [47]. The calculations were aided by the Gauss View visualization program. All elements except aluminium were assigned 6-31+G(d) basis set. The vibrational frequency

CHAPTER 4

calculations were performed to certain that the optimized geometries represent the local minima and there were only positive eigen values. Vertical electronic excitations based on B3LYP optimized geometries were computed using the time-dependent density functional theory (TDDFT) formalism [48-50] in methanol using conductor-like polarizable continuum model (CPCM) [51-53].

4.4.5 Live cell imaging

4.4.5.1 Cell cytotoxicity assay

MCF-7 cells were evaluated for cytotoxicity with zinc chloride (Zn^{2+}), H_2L (receptor) and complex ($L-Zn^{2+}$) by the following protocol as described by Hamdi et al [54]. Cells were then seeded in 96-well plates at a density of 1×10^4 cells per well and cultivated in CO_2 incubator for 24 h after that. The cells were treated in aqueous medium while H_2L was dissolved in DMSO, but the final concentration of DMSO while treatment of cells was maintained below 1%. After treatment for 24 h, Methyl tetrazolium dye (MTT) (5 mg/ml) was added to each well and the plates were incubated in the dark at $37^\circ C$ for 2 h. Thus MTT was used to determine the cell viability and absorbance of MTT formazan was determined at 595 nm in spectrophotometer (Epoch Micro-plate Spectrophotometer, USA). Untreated cells were served as 100% viable.

4.4.5.2 Cell Bio imaging

MCF-7 cells were seeded for overnight on 22×22 mm glass cover slips. After 18 hours the cell media was discarded and fresh DMEM was added with adding H_2L and $L-Zn^{2+}$ respectively for 24 hours at a dose less than LD_{50} as found from cell cytotoxicity assay. After 24 hours the cell media was discarded and cells were washed with ice cold 1X Phosphate buffer saline for 5 times to remove any excess H_2L receptor present in the surroundings. Finally, the cover slip was mounted on a glass slide and observed under a fluorescent microscope (Leica DM4000 B, Germany) at 20x magnification.

4.4.6 Crystallographic studies

Details of crystal analysis, data collection and structure refinement data for $L-Zn^{2+}$ complex is given in Table S1. Crystal mounting was done on glass fibers with epoxy cement. A red, needle shaped single crystal of the $L-Zn^{2+}$, with dimensions of $0.18 \text{ mm} \times 0.08 \text{ mm} \times 0.06 \text{ mm}$ was selected. Single

CHAPTER 4

crystal data collection of the selected crystal was performed with an automated Bruker SMART APEX CCD diffractometer using graphite monochromatized Mo K_{α} radiation ($\lambda = 0.71073 \text{ \AA}$). Reflection data were recorded using the ω scan technique. The data was processed with SAINT and corrected for absorption using SADABS [55]. The structures were solved and refined by full-matrix least-squares techniques on F^2 using the SHELXTL program [56]. The absorption corrections were done by the multi-scan technique. All data were corrected for Lorentz and polarization effects, and the non-hydrogen atoms were refined anisotropically. Hydrogen atoms were included in the refinement process as per the riding model. Crystallographic data have been deposited at the Cambridge Crystallographic Data Centre with CCDC 1497208 for L-Zn²⁺. Copies of the data can be obtained free of charge on application to the CCDC, 12 Union Road, Cambridge CB2 IEZ, UK. Fax: +44-(0)1223-336033 or e-mail:deposit@ccdc.cam.ac.uk.

4.5 Conclusion

Synthesis of highly sensitive and selective chemosensor (H₂L) for the selective detection of Zn²⁺ is reported. Remarkable enhancement of fluorescence intensity upon addition of Zn²⁺ provides a useful detection technique for Zn²⁺. Reversibility of H₂L towards Zn²⁺ is checked upon incremental addition of EDTA into L-Zn²⁺. An INHIBIT logic gate is constructed using Zn²⁺ and EDTA as chemical inputs. Moreover, the chemosensor is efficient in detection of Zn²⁺ in presence of other metals. Further, the structure of L-Zn²⁺ complex is confirmed by single crystal X-ray crystallography. The developed chemosensor can also be utilized to detect Zn²⁺ in the intracellular region of human breast cancer cells (MCF-7).

CHAPTER 4

4.6. Reference

1. A.R.S. Alsalman, L.A. Almashhedy, M.H. Hadwan, *Biol. Trace Elem. Res.*, 2018, **184**, 340–349.
2. K. Hanaoka, Y. Muramatsu, Y. Urano, T. Terai, T. Nagano, *Chem. Eur. J.*, 2010, **16**, 568–572.
3. F. Virgili, R. Ambra, J. McCormack, E.E.A. Simpson, D. Ciarapica, L. Barnaba, E. Azzini, A. Polito, *Curr. Pharm. Des.*, 2018, **24**, 4131–4143.
4. I. Barroso, R. Farina, J.T. Guimaraes, *Clin. Biochem.*, 2018, **59**, 93–95.
5. A.S. Nakashima, R.H. Dyck, *Brain Res. Rev.*; 2009, **59**, 347–373.
6. K. Wojtunik-Kulesza, A. Oniszczyk, M. Waksmundzka-Hajnos, *Biomed. Pharma- cother.*, 2019, **111**, 1277–1289.
7. G. Lyubartseva, M.A. Lovell, *Biofactors*, 2012, **38**, 98–106.
8. M. Bath, N. Ahmed, *J. Photochem. Photobiol. A: Chem.*, 2019, **373**, 154–161.
9. A. Asaithambi, P. Biswanathamurti, K. Natarajan, *J. Photochem. Photobiol. A: Chem.*, 2019, **370**, 75–83.
10. Q. Wang, L. Jin, W. Wang, T. Hu, C. Chen, *J. Lumin.*, 2019, **209**, 411–419.
11. H. Song, Z. Zhang, *Dyes Pigm.*, 2019, **165**, 172–181.
12. G. Wu, Q. Gao, M. Li, X. Tang, K.W.C. Lai, Q. Tong, *J. Photochem. Photobiol. A: Chem.*, 2018, **355**, 487–495.
13. A. Bhattacharyya, S.C. Makhal, N. Guchhait, *Photochem. Photobiol. Sci.* 18 (2019) 2031–2041. [14] K. Zhang, S. Wu, D. Qu, L. Wang, *Tetrahedron Lett.*, 2016, **57**, 1133–1137.
15. K. Chantalakana, N. Choengchan, P. Yingyuad, P. Thongyoo, *Tetrahedron Lett.*, 2016, **57**, 1146–1149.
16. D. Wang, X. Xiang, X. Yang, X. Wang, Y. Guo, W. Liu, W. Qin, *Sens. Actuators B Chem.*, 2014, **201**, 246–254.
17. D. Wang, A.-M. Ren, L.-Y. Zou, J.-F. Guo, S. Huang, *J. Photochem. Photobiol. A: Chem.*, 2017, **341**, 20–30.
18. F. Nouri Moghadam, M. Amirasr, K. Eskandari, S. Meghdadi, *New J. Chem.*, 2019, **43**, 13536–13544.
19. A. Pandey, S.K. Asthana, A. Prakash, J.K. Roy, I. Tiwari, K.K. Upadhyay, *Dalton Trans.*, 2019, **48**, 2068–2076.
20. Ö. Şahin, Ü.Ö. Özdemir, N. Seferoğlu, B. Aydıner, M. Sarı, T. Tunç, Z. Seferoğlu, *Tetrahedron*, 2016, **72**, 5843–5852.

CHAPTER 4

21. S.K. Padhan, M.B. Podh, P.K. Sahu, S.N. Sahu, *Sens. Actuators B Chem.*, 2018, **255**, 1376–1390.
22. M. Chemchem, I. Yahaya, B. Aydiner, O. Doluca, N. Sefero ğlu, Z. Sefero ğlu, *Sens. Actuators B Chem.*, 2020, **305**, 127316.
23. M. Rahimi, A. Amini, H. Behmadi, *J. Photochem. Photobiol. A: Chem.*, 2020, **388**, 112-190.
24. P. Alreja, N. Kaur, *Inorg. Chim. Acta.*, 2018, **480**, 127–131.
25. S. Dalapati, M.A. Alam, S. Jana, S. Karmakar, N. Guchhait, *Spectrochim. Acta.*, 2013, **102**, 314–318.
26. C. Patra, A.K. Bhanja, C. Sen, D. Ojha , D. Chattopadhyay , A. Mahapatra , C. Sinha , *Sens. Actuators B Chem.*, 2016, **228**, 287–294.
27. C. Patra, C. Sen, A. Das Mahapatra, D. Chattopadhyay, A. Mahapatra, C. Sinha, *J. Photochem. Photobiol. A: Chem.*, 2017, **341**, 97–107.
28. W.-K. Dong, Sunday Folaranmi Akogun, Yang Zhang, Yin-Xia Sun, Xiu-Yan Dong, *Sensors and Act. B*, 2017, **238**, 723–734.
29. Kettalu Ananthan Karthick, Kalairajan Kaleeswari, C. Uma Maheswari, Gandhi Sivaraman, Bhaskaran Shankar, Arunachalam Tamilselvi, *J. Photochem, Photobiol.*, 2022, **428**, 113861.
30. Vijay Kumar, Devender Singh, Pramod Kumar, Garima Chaudhary, Amit P. Singh, Rajeev Gupta, *J. Mol. Struct.*, 2022, **1261**, 132901.
31. S. Goswami, A. K. Das, K. Aich, A. Manna, S. Maity, K. Khanra and N. Bhattacharyya, *Analyst*, 2013, **138**, 4593-4598.
32. A. K. Bhanja, C. Patra, S. Mondal, D. Ojha, D. Chattopadhyay and C. Sinha, *RSC Adv.*, 2015, **5**, 48997-49005.
33. W.K. Dong, S. F. Akogun, Y. Zhang, Y.-X. Sun, X.-Y. Dong, *Sens. Actuators B Chem.*, 2017, **238**, 723–734.
34. J.-H. Hu, Y. Suna, J. Qi, Q. Li, T.-B. Wei, *Spectrochim. Acta A Mol. Biomol. Spectrosc.*, 2017, **175**, 125–133.
35. S. Erdemir, S. Malkondu, *Sens. Actuators B Chem.*, 2013, **188**, 1225– 1229.
36. H. G. Lee, K. B. Kim, G. J. Park, Y. J. Na, H.Y. Jo, S. A. Lee, C. Kim, *Inorganic Chemistry Communications*, 2014, **39**, 61–65.
37. A. Gogoi, S. Samanta, G. Das, *Sens. Actuators B Chem.*, 2014, **202**, 788–794.
38. B. Sun, L. Liu, W. Liu, F. Meng, Q. Huang, *J. Lumin.*, 2020, **223**, 117-203.
39. Z. Qiao, Y. Wu, B. Tang, R. Perestrelo, R. Bhalla, *Tetrahedron Lett.*, 2019, **60**, 150-918.
40. A.K. Bhanja, C. Patra, S. Mondal, D. Ojha, D. Chattopadhyay, C. Sinha, *RSC Adv.*, 2015, **5**, 48997–49005.

CHAPTER 4

41. W.-K. Dong, S.F. Akogun, Y. Zhang, Y.-X. Sun, X.-Y. Dong, *Sens. Actuators B Chem.*, 2017, **238**, 723–734.
42. J.-H. Hu, Y. Suna, J. Qi, Q. Li, T.-B. Wei, *Spectrochim. Acta.*, 2017, **175**, 125–133.
43. S. Erdemir, S. Malkondu, *Sens. Actuators B Chem.*, 2013, **188**, 1225–1229.
44. H.G. Lee, K.B. Kim, G.J. Park, Y.J. Na, H.Y. Jo, S.A. Lee, C. Kim, *Inorg. Chem. Commun.*, 2014, **39**, 61–65.
45. A. Gogoi, S. Samanta, G. Das, *Sens. Actuators B Chem.*, 2014, **202**, 788–794.
46. M. Bahta, N. Ahmed, *J. Photochem. Photobiol. A: Chem.*, 2019, **373**, 154–161.
47. C. G. Densmore, H. Wheeler, R. Cohenour, T. W. Robison, D. Hasam, B. J. Cordova, P. C. Stark, E. N. Fuller, C. J. Cook, H. A. Weber, *Org. Process Res. Dev.*, 2007, **11**, 996–1003.
48. A. D. Becke, *J. Chem. Phys.*, 1993, **98**, 5648–5652.
49. C. Lee, W. Yang, R. G. Parr, *Phys. Rev. B.*, 1988, **37**, 785–789.
50. M. J. Frisch, G. W. Trucks, H. B. Schlegel, G. E. Scuseria, M. A. Robb, J. R. Cheeseman, G. Scalmani, V. Barone, B. Mennucci, G. A. Petersson, H. Nakatsuji, M. Caricato, X. Li, H. P. Hratchian, A. F. Izmaylov, J. Bloino, G. Zheng, J. L. Sonnenberg, M. Hada, M. Ehara, K. Toyota, R. Fukuda, J. Hasegawa, M. Ishida, T. Nakajima, Y. Honda, O. Kitao, H. Nakai, T. Vreven, J. A. Montgomery, Jr., J. E. Peralta, F. Ogliaro, M. Bearpark, J. J. Heyd, E. Brothers, K. N. Kudin, V. N. Staroverov, R. Kobayashi, J. Normand, K. Raghavachari, A. Rendell, J. C. Burant, S. S. Iyengar, J. Tomasi, M. Cossi, N. Rega, J. M. Millam, M. Klene, J. E. Knox, J. B. Cross, V. Bakken, C. Adamo, J. Jaramillo, R. Gomperts, R. E. Stratmann, O. Yazyev, A. J. Austin, R. Cammi, C. Pomelli, J. W. Ochterski, R. L. Martin, K. Morokuma, V. G. Zakrzewski, G. A. Voth, P. Salvador, J. J. Dannenberg, S. Dapprich, A. D. Daniels, Ö. Farkas, J. B. Foresman, J. V. Ortiz, J. Cioslowski and D. J. Fox, Gaussian, Inc., Wallingford CT, 2009.
51. R. Bauernschmitt, R. Ahlrichs, *Chem. Phys. Lett.* 1996, **256**, 454–464.
52. R. E. Stratmann, G. E. Scuseria, M. J. Frisch, *J. Chem. Phys.*, 1998, **109**, 8218–8224.
53. M. E. Casida, C. Jamorski, K. C. Casida, D. R. Salahub, *J. Chem. Phys.*, 1998, **108**, 4439–4449.
54. V. Barone, M. Cossi, *J. Phys. Chem. A*, 1998, **102**, 1995–2001.
55. M. Cossi, V. Barone, *J. Chem. Phys.*, 2001, **115**, 4708–4717.
56. M. Cossi, N. Rega, G. Scalmani, V. Barone, *J. Comput. Chem.*, 2003, **24**, 669–681.
57. Hamdi, C. Fischmeister, M. C. Puerta, P. Valerga, *Med. Chem. Res.*, 2011, **20**, 522–530.
58. Bruker. APEX2, SAINT and SADABS. Bruker AXS Inc., Madison, Winconsin, USA. 2009.
59. G. M. Sheldrick, A short history of SHELX. *Acta Cryst.*, 2008, **64**, 112–122.

CHAPTER 4

APPENDIX

CHAPTER 4

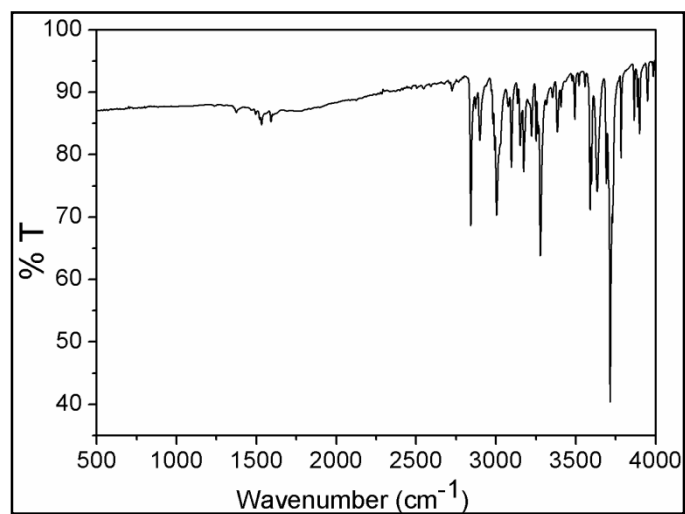


Figure S1: IR spectrum of the probe (H₂L)

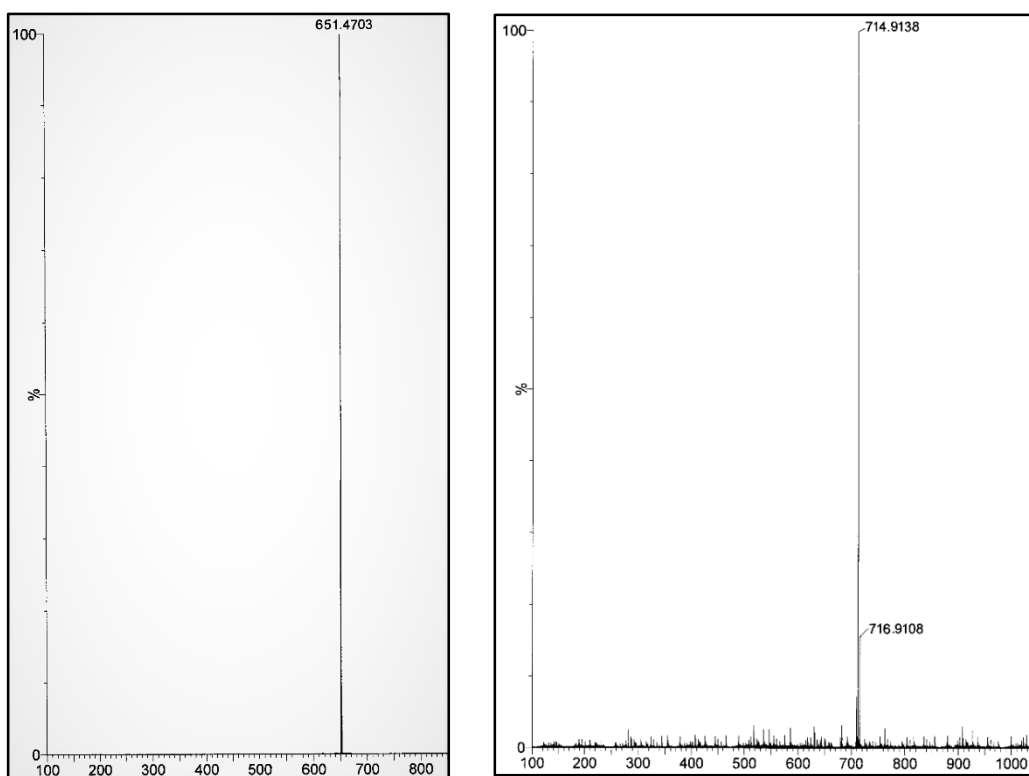


Figure S2 and S3: HRMS spectrum of the probe (H₂L) and L-Zn²⁺ complex

CHAPTER 4

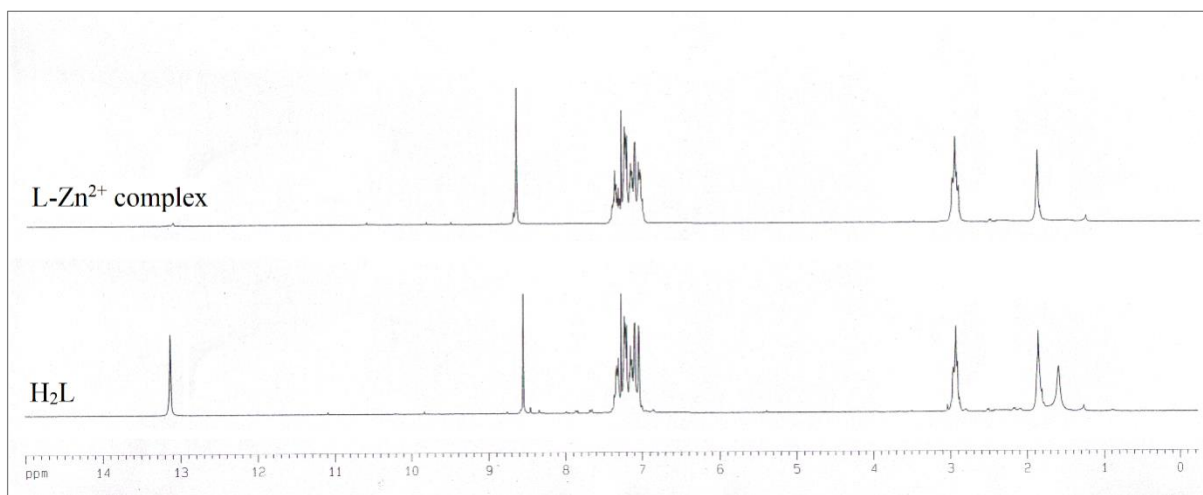


Figure S4: ^1H NMR (300 MHz) spectra of the probe (H_2L) and L-Zn^{2+} complex in CDCl_3

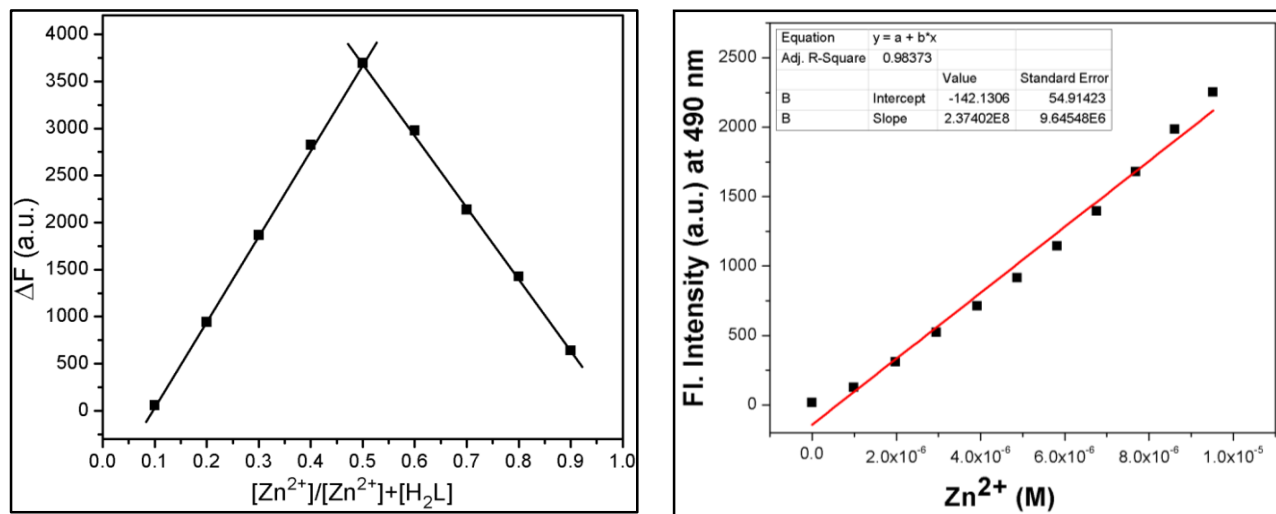


Figure S5 and S6: Job's plot of H_2L for Zn^{2+} and Linear response curve of H_2L at 490 nm depending on the Zn^{2+} concentration.

CHAPTER 4

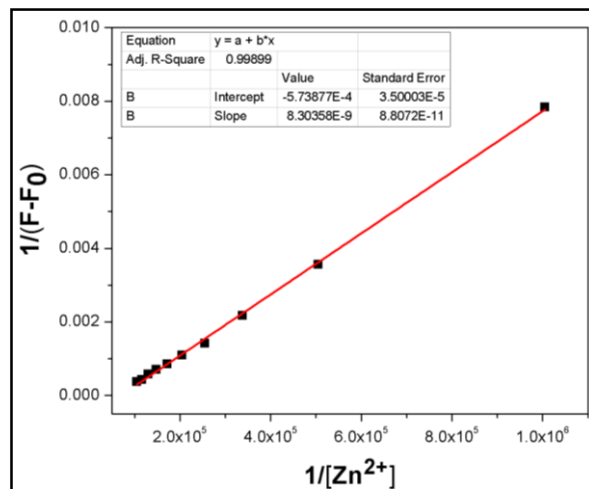


Figure S7: Determination of association constant of H₂L at 490 nm depending on the Zn²⁺ concentration using Benesi-Hildebrand equation.

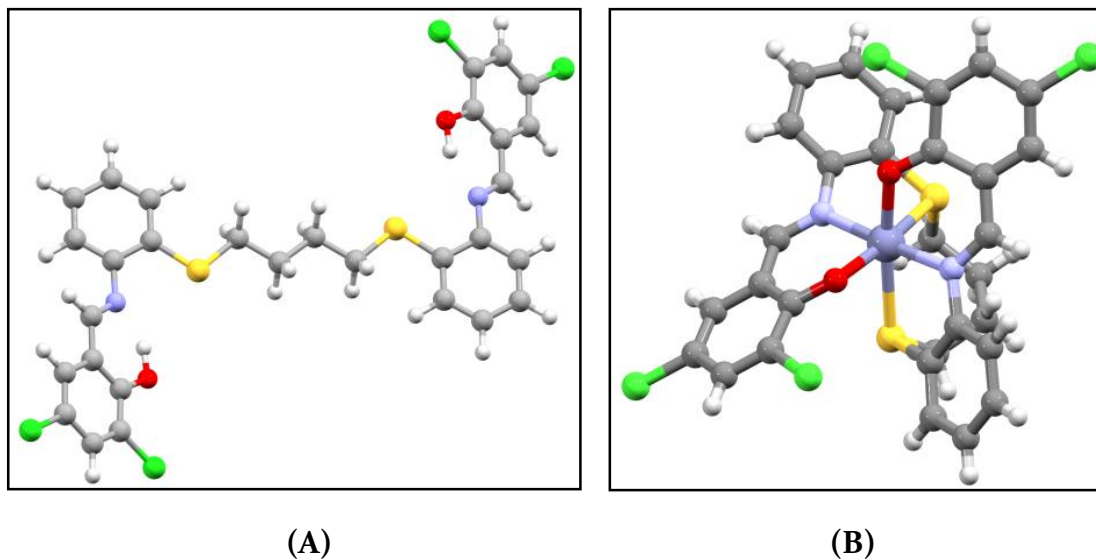


Figure S8. Optimized structure of (A) H₂L and (B) L-Zn²⁺ complex by DFT/B3LYP/6-31+G (d) method.

CHAPTER 4

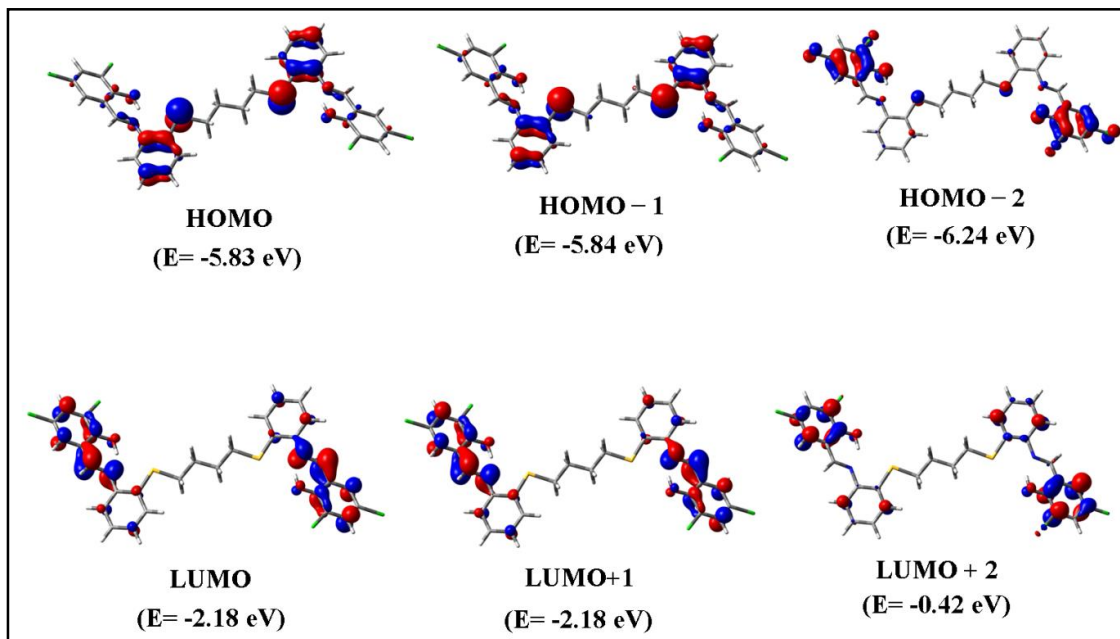


Figure S9. Contour plots of some selected molecular orbitals of H₂L

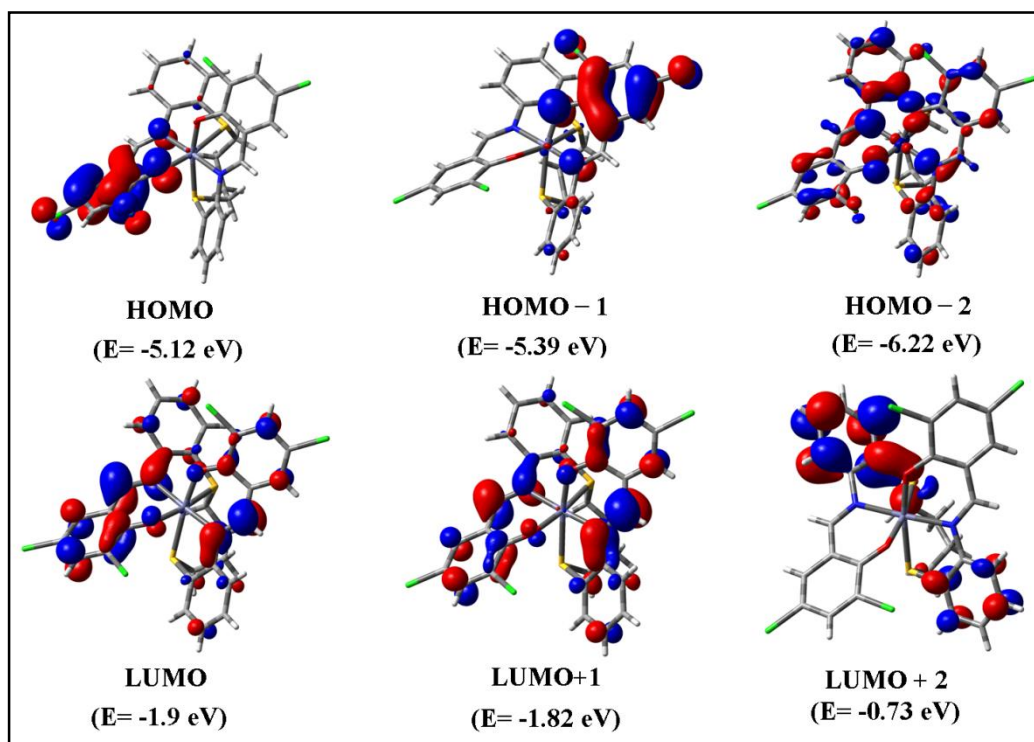


Figure S10. Contour plots of some selected molecular orbitals of L-Zn²⁺

CHAPTER 4

Table S1: Crystallographic data and refinement parameters of L-Zn²⁺

Formula	C ₃₀ H ₂₂ Cl ₄ N ₂ O ₂ S ₂ Zn
Formula Weight	713.79
Crystal System	<i>Monoclinic</i>
Space group	<i>P21/n</i>
a, b, c [Å]	7.939 (5), 17.404 (5), 20.076 (5)
α	90.000
β	95.318 (5)
γ	90.000
V [Å ³]	2762 (2)
Z	4
D(calc) [g/cm ³]	1.717
μ (Mo K α) [mm ⁻¹]	1.463
F(000)	1448
Absorption Correction	<i>multi-scan</i>
Temperature (K)	293
Radiation [Å]	0.71073
θ (Min-Max) [°]	2.14-20.14
Dataset (h; k; l)	-9 and 9; -20 and 19; -23 and 23
Total, Unique Data, R(int)	15899/4786/0.0821
Observed data [I > 2 σ (I)]	2674

CHAPTER 4

Nref, Npar	4786/370
R, wR ₂	0.0789, 0.2153
$\Delta q(\text{max})$ and $\Delta q(\text{min})$ [$e/\text{\AA}^3$]	0.626 and -0.930
Goodness of fit(S)	1.072

Table S2: Selected bond distances (\AA) and angles ($^\circ$) of L-Zn²⁺ complex

Bonds (\AA)	H ₂ L-Zn ²⁺
Zn1-O2	1.915(8)
Zn1-O1	1.996(8)
Zn1-N2	2.006(9)
Zn1-N1	2.020(9)
Zn1-S2	2.401(3)
Zn1-S1	2.504(4)
Angles ($^\circ$)	
O2-Zn1-O1	98.1(3)
O2-Zn1-N2	88.0(3)
O1-Zn1-N2	88.9(3)
O2-Zn1-N1	93.7(3)
O1-Zn1-N1	89.1(3)
N2-Zn1-N1	177.6(3)
O2-Zn1-S2	168.0(2)
O1-Zn1-S2	87.1(2)
N2-Zn1-S2	81.2(2)

CHAPTER 4

N1-Zn1-S2	97.2(3)
O2-Zn1-S1	79.7(3)
O1-Zn1-S1	171.0(2)
N2-Zn1-S1	99.7(3)
N1-Zn1-S1	82.4(3)
S2-Zn1-S1	96.83(13)

Table S3: Energy and compositions of some selected molecular orbitals of L-Zn²⁺

MO	Energy (eV)	% of composition		
		H ₂ L	Zn	Cl
LUMO+5	0.13	98	1	1
LUMO+4	0.08	97	2	1
LUMO+3	-0.69	100	0	0
LUMO+2	-0.73	99	1	1
LUMO+1	-1.82	99	0	1
LUMO	-1.9	99	1	1
HOMO	-5.12	86	1	13
HOMO-1	-5.39	87	1	12
HOMO-2	-6.22	94	2	5
HOMO-3	-6.31	92	1	7
HOMO-4	-6.51	92	2	7
HOMO-5	-6.64	87	2	11
HOMO-6	-7.0	94	2	3

CHAPTER 4

HOMO-7	-7.18	97	0	3
HOMO-8	-7.25	88	2	10
HOMO-9	-7.34	78	1	21
HOMO-10	-7.39	82	1	17

Table S4: Vertical electronic transitions calculated by TDDFT/B3LYP/CPCM method for H₂L and L-Zn²⁺ in DMSO

Compounds	E _{excitation} (eV)	λ _{excitation} (nm)	Osc. Strength (f)	Key transitions	Character
H ₂ L	3.2404	382.6	0.4634	(67%)HOMO→LUMO (28%)HOMO-1→LUMO	π(L)→π*(L)
	3.6223	342.3	0.3102	(47%)HOMO-3→LUMO+1 (48%)HOMO-2→LUMO	π(L)→π*(L)
	3.9365	315.0	0.0107	(38%)HOMO-5→LUMO (42%)HOMO-4→LUMO+1	π(L)→π*(L)
	3.9372	314.9	0.3001	(45%)HOMO-5→LUMO+1 (38%)HOMO-4→LUMO	π(L)→π*(L)
	4.5134	274.7	0.5393	(30%)HOMO-6→LUMO (30%)HOMO-7→LUMO+1	π(L)→π*(L)
	2.9368	422.2	0.1046	(98%)HOMO→LUMO	π(L)→π*(L)
	3.0179	410.8	0.0686	(96%)HOMO→LUMO+1	π(L)→π*(L)

CHAPTER 4

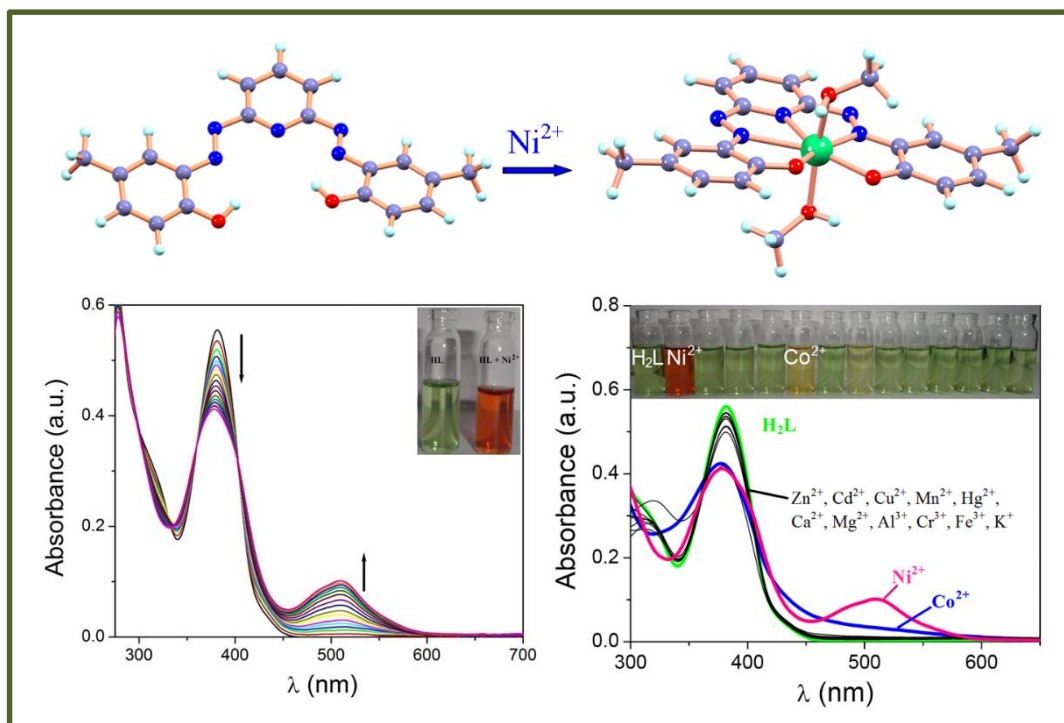
L-Zn ²⁺	3.0961	400.5	0.710	(95%)HOMO-1→LUMO	$\pi(L) \rightarrow \pi^*(L)$
	3.2068	386.6	0.2024	(94%)HOMO-1→LUMO+1	$\pi(L) \rightarrow \pi^*(L)$
	3.5888	345.5	0.0293	(42%)HOMO-2→LUMO+1	$\pi(L) \rightarrow \pi^*(L)$
	4.2578	291.2	0.0293	(88%)HOMO→LUMO+2	$\pi(L) \rightarrow \pi^*(L)$

Novel pyridyl based azo-derivative for the selective and colorimetric detection of nickel(II)

Novel pyridyl based azo-derivative for the selective and colorimetric detection of nickel(II)

Abstract

A highly sensitive and selective pyridyl based colourimetric chemosensor (H₂L) for the efficient detection of Ni²⁺ has been reported. The synthesized chemosensor H₂L is highly efficient in detecting Ni²⁺ even in presence of other metal ions that commonly co-exist with Ni²⁺ in several environmental as well as biological samples. H₂L also shows distinct colour change from green to deep red visible under naked eye due to specific binding with Ni²⁺. This colour change is actually obtained due to formation of a new band at 510 nm upon gradual addition of Ni²⁺. The cation sensing property of the receptor H₂L has been mainly studied by UV-Vis spectroscopy. Electronic structure of the H₂L-Ni²⁺ complex and sensing mechanism have been interpreted theoretically by DFT and TDDFT calculations.



5.1. Introduction

Recognition and sensing of metal ions has become an active field of research owing to its potential application in several fields which includes chemistry, bio-medicine, and environmental studies. [1,2] Detection of nickel(II) is highly important due to its toxic nature and widespread use in various industrial and catalytic processes. [3] Increased exposure to nickel(II) causes several diseases such as pneumonitis, dermatitis, asthma, several problems of the central nervous system and even cancer of the nasal cavity and lungs. [4,6] Thus the detection nickel(II) is of utmost importance in several biological, industrial and food samples. Most of industrial method of detection of nickel(II) depends on time consuming and involvement of sophisticated analytical techniques which includes atomic absorption or emission spectrometry, [7,8] liquid chromatography [9,10] and fluorometric chemosensors. [11,12] In spite of the fact that these methods are highly sensitive they are not convenient for “in-the-field” detection as they require expensive instruments which are very difficult to carry. Hence detection of nickel(II) using a very simple-to-use method, low cost and also very rapid, is of increasing demand. Colourimetric sensors comprises of a class of reagent which shows a distinctive colour change visible under ‘naked eye’, on selectively binding with certain specific analytes without the employment of sophisticated and expensive equipment. [13,14] Thus the development of colourimetric sensor for the easy and rapid detection of nickel(II) is a demanding field of research.

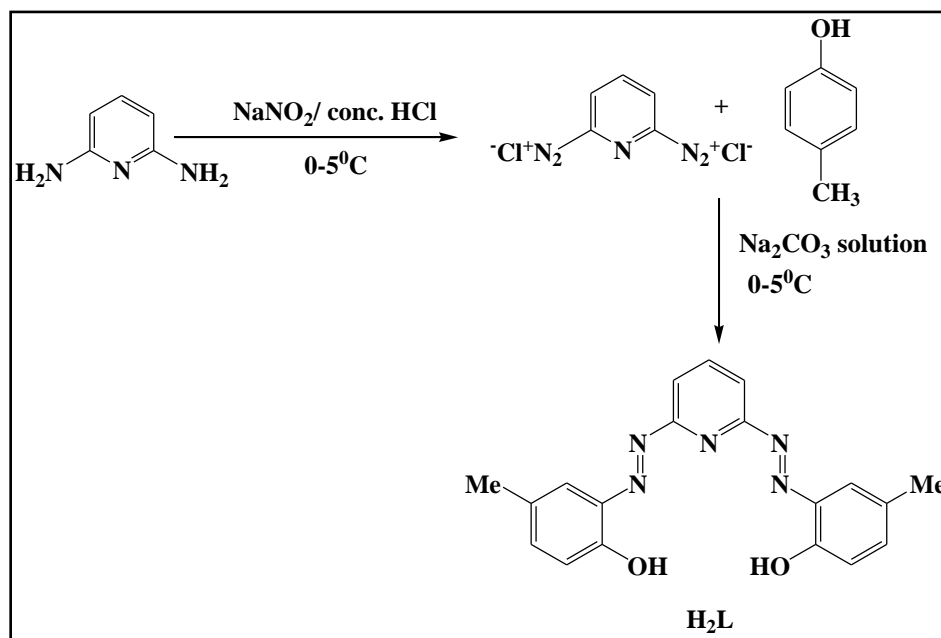
5.2. Basis of present work

Till date only a few efficient colorimetric chemosensor for the selective detection of Ni^{2+} have been reported. A quinoxaline based colourimetric and ratiometric chemosensor for the detection of nickel(II) has been reported by S. Goswami et.al. [15] Peralta-Domínguez et. al. reported a Schiff base derivative of cinnamaldehyde used efficient detection of nickel(II) by colourimetric method. [16] Several coumarin based colourimetric chemosensors for nickel(II) have been reported so far by Jiang et. al. and Wang et. al. [17,18]

5.3. Results and discussion

5.3.1 Synthesis of H₂L

The receptor H₂L (Scheme 5.1) has been synthesized by a very economically cheap and facile route which involves azo coupling of diazotized 2,6- Diaminopyridine with *p*-cresol in alkaline medium. The compound has been characterized by elemental and mass spectral analysis along with other spectroscopic techniques (IR, UV–Vis, NMR etc.) (*see Experimental Section*).



Scheme 5.1: Synthesis of pyridyl based chemosensor H₂L

5.3.2 Spectral characterization and analysis of H₂L and H₂L-Ni²⁺

IR spectra of the free receptor H₂L, shows a broad stretching at 1585 and 1417 cm⁻¹ corresponding to $\nu(\text{C}=\text{N})$ and $\nu(\text{N}=\text{N})$ respectively (Fig. S1). The stretching band at 3430 cm⁻¹ corresponds to $\nu(\text{O}-\text{H})$. In the H₂L-Ni²⁺ complex, the band at 3430 cm⁻¹ disappears due to co-ordination to the metal center while the $\nu(\text{C}=\text{N})$ and $\nu(\text{N}=\text{N})$ appeared at 1536 and 1407 cm⁻¹ again due to coordination (Fig.

CHAPTER 5

S2). HRMS spectrum of H₂L shows peak at 370.5 and 348.45 corresponding to H₂L+Na⁺ and H₂L+H⁺ respectively (Fig. S3). The HRMS spectrum of H₂L-Ni²⁺ complex shows a strong peak at 427.8 which corresponds to Na[Ni(L-2H)]⁺ species and a weak peak at 491.2 which corresponds to Na[Ni(L-2H)(MeOH)₂]⁺ (Fig. S4) supporting 1:1 complex formation. In the octahedral environment four coordination sites are satisfied by the N,N,O,O donors of H₂L while the remaining two coordination sites are occupied by two MeOH molecules which is used as solvent. The proposed octahedral geometry is further supported by the HRMS data. NMR spectrum of H₂L shows a singlet peak at 2.17 corresponding to the -CH₃ protons. The -OH peak appeared at the highly deshielded region of δ 14.50 and all the other aromatic protons appeared as expected in the deshielded zone of δ 6.61-8.17 (Fig. S5).

5.3.3 Cation sensing studies: UV-Vis spectroscopy studies

Stock solution of the receptor H₂L (10 μ M) in [(MeOH/H₂O), 1:1, v/v] (at 25°C) using HEPES buffered solution at pH = 7.4 was prepared. The solution of the guest cations using their chloride salts in the order of 100 μ M were prepared in deionized water. Solutions of various concentrations containing host and increasing concentrations of cations were prepared separately. The spectra of these solutions were recorded by means of UV-Vis methods.

Receptor H₂L (10 μ M) shows an absorbance band at 381 nm along with a shoulder at 316 nm. Addition of NiCl₂ (100 μ M) solution causes decrease in intensity of the absorption band at 381 nm and a new absorption band appears at 510 nm with a distinct isosbestic at around 402 nm (Fig. 5.1). The shoulder band of H₂L at 316 nm vanishes on addition of Ni(II) to it. This indicates the formation of a complex between the receptor H₂L and Ni²⁺. Due to the complexation with Ni²⁺, distinct colour change occurs from green to deep red.

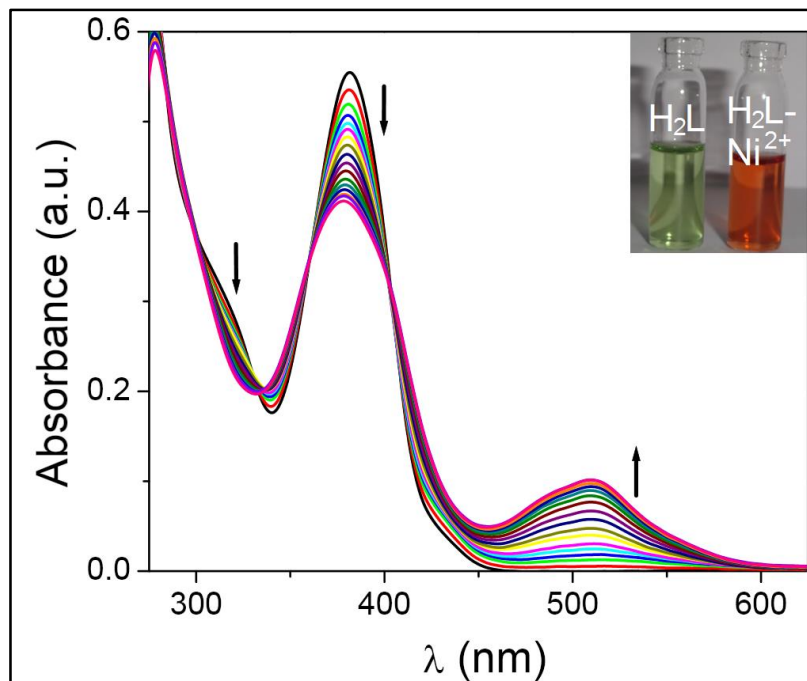


Fig. 5.1: Change in UV-Vis spectrum of HL (10 μM) upon gradual addition of 10 μM Ni^{2+} . Inset shows the visual effect of addition of Ni^{2+} to H_2L in ambient light.

Furthermore, the sensing ability of H_2L with Ni^{2+} at different pH has also been studied. At lower pH, the receptor H_2L has no significant response to Ni^{2+} in absorption spectroscopy may be due to protonation of the receptor H_2L . The absorbance at 510 nm is maximum and almost constant in the pH range 7.2 to 9.8, above pH 9.8 the absorbance is gradually decreased may due to hydrolysis (Fig. 5.2). Thus the receptor H_2L is also suitable in the detection of Ni(II) in the physiological pH of 7.4 as present in several biological samples.

CHAPTER 5

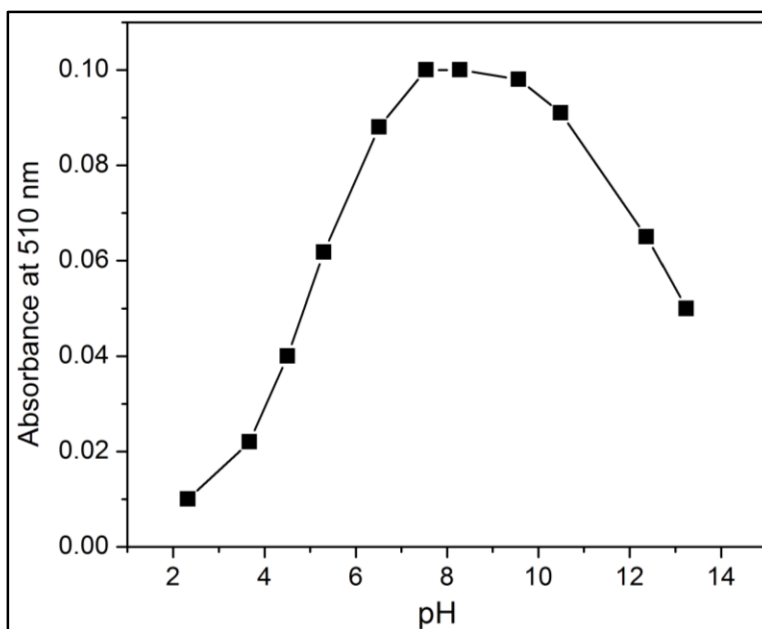


Fig. 5.2: Absorbance of H₂L at 510 nm in MeOH/H₂O (1:1, v/v) with different pH

From UV-Vis spectral change, limit of detection of the chemosensor H₂L for Ni²⁺ is determined using the equation $LOD = K \times SD/S$ where SD is the standard deviation of the blank solution and S in the slope of the calibration curve (Fig. 5.6). The limit of detection for Ni²⁺ is found to be 0.83 μ M from UV-Vis spectral titration. This result clearly demonstrates that the developed chemosensor is highly efficient in sensing Ni²⁺ even in very minute level and can serve as a highly efficient ‘naked-eye’ chemosensor for Ni(II). The association constant of Ni²⁺ for the receptor H₂L is found to be $1.27 \times 10^5 \text{ M}^{-1}$ (Fig. S6) based on UV-Vis spectral titration.

UV-Vis spectrum of H₂L is also studied in presence of other metals i.e, Ca²⁺, Mg²⁺, Mn²⁺, Fe³⁺, Al³⁺, Cr³⁺, Co²⁺, Zn²⁺, Cu²⁺, Cd²⁺ and Hg²⁺ but no significant changes are observed in either of the cases except to that in Co²⁺ (Fig. 5.3). Though Co²⁺ interferes only slightly but under naked eye, it shows only a very light yellow colour when added to H₂L compared to the bright deep red colour which H₂L shows in presence of only Ni(II).

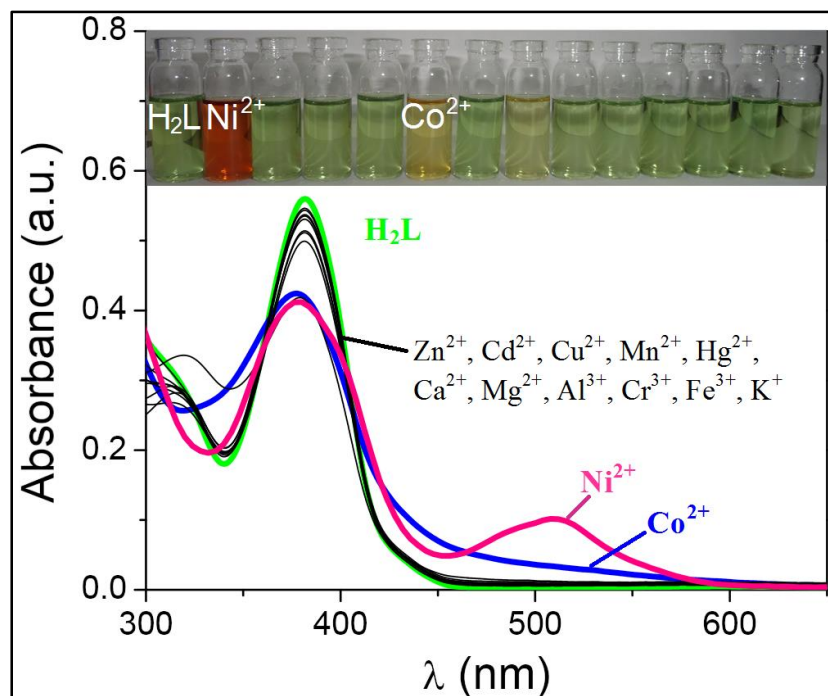


Fig. 5.3: UV-Vis spectra of chemosensor (H_2L) ($10\ \mu M$) upon addition of various metal ions i.e, Ca^{2+} , Mg^{2+} , Mn^{2+} , Fe^{3+} , Al^{3+} , Cr^{3+} , Co^{2+} , Zn^{2+} , Cu^{2+} , Cd^{2+} and Hg^{2+} ($20\ \mu M$). Inset shows the visual effect of addition of various metal ions to the receptor H_2L

The selectivity of H_2L for Ni^{2+} is studied in the presence of other metal ions such as Ca^{2+} , Mg^{2+} , Mn^{2+} , Fe^{3+} , Al^{3+} , Cr^{3+} , Co^{2+} , Zn^{2+} , Cu^{2+} , Cd^{2+} and Hg^{2+} . The intensity of the absorption band at 510 nm due to formation of H_2L-Ni^{2+} complex is not at all disturbed due to the presence of other metal ions simultaneously in solution (Fig. 5.4). Thus H_2L shows an excellent binding affinity for Ni^{2+} even in the presence of other metal ions and can detect Ni^{2+} very rapidly in other physiological as well as environmental samples where other metal ions like Ca^{2+} , Mg^{2+} , Mn^{2+} , Fe^{3+} , Al^{3+} , Cr^{3+} , Co^{2+} , Zn^{2+} , Cu^{2+} , Cd^{2+} and Hg^{2+} usually coexist with the analyte.

CHAPTER 5



Fig. 5.4: Absorbance intensity of chemosensor (H₂L) (10 μM) upon addition of 10 μM Ni²⁺ along with various metal ions i.e, Co²⁺, Cu²⁺, Zn²⁺, Hg²⁺, Cd²⁺, Mn²⁺, Mg²⁺, Ca²⁺, Al³⁺, Fe³⁺, Cr³⁺, K⁺ (20 μM)

Job's plot of the UV-Vis titration reveals that the maximum absorption at 510 nm corresponds to mole fraction at 0.5 (Fig. 5.5). Thus it clearly indicates that the complex formation between Ni²⁺ and H₂L has the stoichiometric ratio of 1:1. The mole ratio plot also reflects that the absorption intensity at 510 nm increases till the mole ratio of the analyte to the receptor H₂L reaches ~1.0, thus indicating 1:1 complex formation (Fig. S7).

For naked eyed detection, the distinct change in color has been observed at the minimum concentration of ~1 μM for Ni²⁺, which is much lower than the maximum contaminant level goal (MCLG = 1.7×10^{-5} M) reported by American Environmental Protection Agency (EPA) for Ni²⁺ in drinking water [30]. The detection limit determined by UV-Vis method is 8.3×10^{-7} M (Fig. 5.6).

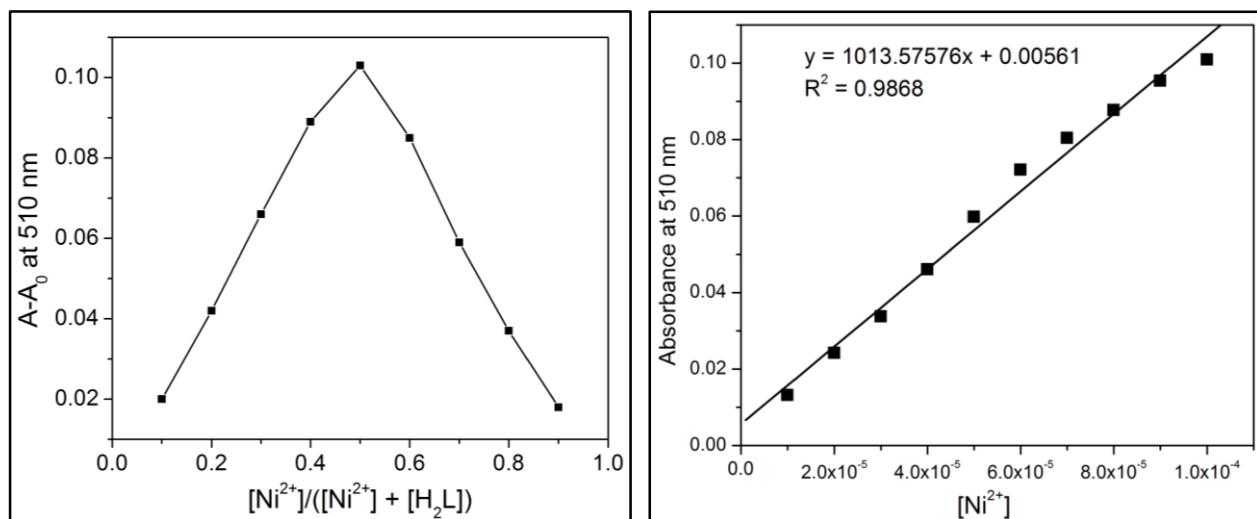


Fig. 5.5 and 5.6: Job's plot diagram of the receptor (H_2L) for Ni^{2+} at 510 nm and Linear response curve of H_2L at 510 nm depending on the Ni^{2+} concentration

5.3.4 Electronic spectra and DFT calculation

To get detailed insight into the interaction of H_2L with Ni^{2+} the DFT studies on H_2L and $\text{H}_2\text{L-Ni}^{2+}$ complex have been carried out. The optimized structure of H_2L is shown in Fig. 5.7. In an octahedral environment for the nickel(II) complex four coordination sites are occupied by the N,N,O,O donors of H_2L and the axial positions are occupied by coordinated methanol molecules (Fig. 5.8). The proposed geometry is supported by mass spectral analysis of $\text{H}_2\text{L-Ni}^{2+}$ complex and two electron paramagnetism of the complex. The contour plots of selected molecular orbitals of H_2L are shown in Fig. S8. The HOMO and HOMO-1 are π bonding in character and concentrated on the phenolate moieties, while HOMO-2 and HOMO-3 have non-bonding in character and concentrated on the azo($\text{N}=\text{N}$) functions. The LUMO and LUMO+1 have π anti-bonding in character with major

CHAPTER 5

contribution of $\pi^*(\text{N}=\text{N})$. The α -spin and β -spin molecular orbitals obtained in UB3LYP calculation of nickel complex are shown in Fig. S9 and Fig. S10 respectively. The HOMOs and LUMOs are mainly concentrated on the coordinated ligand with major contribution of $d\pi(\text{Ni})$ orbitals in β -spin LUMO+2 and LUMO+3.

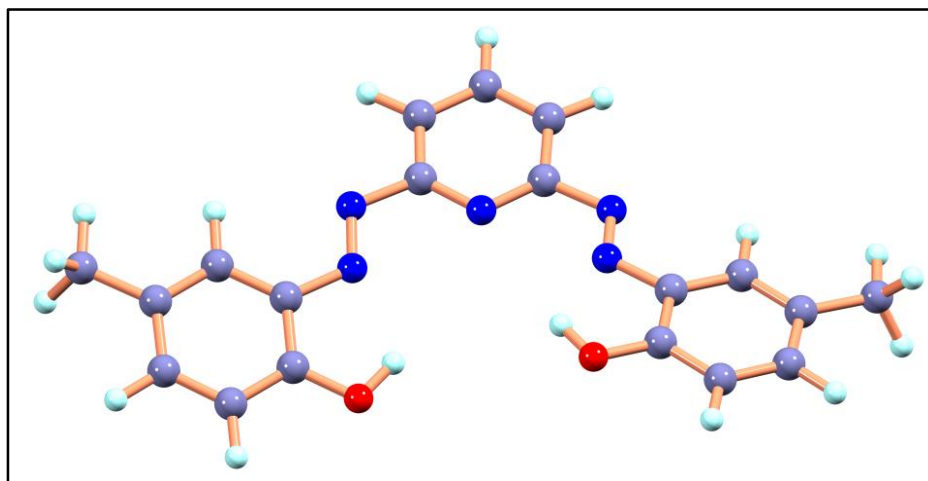


Fig. 5.7: Optimized structure of the receptor H₂L by DFT/B3LYP method

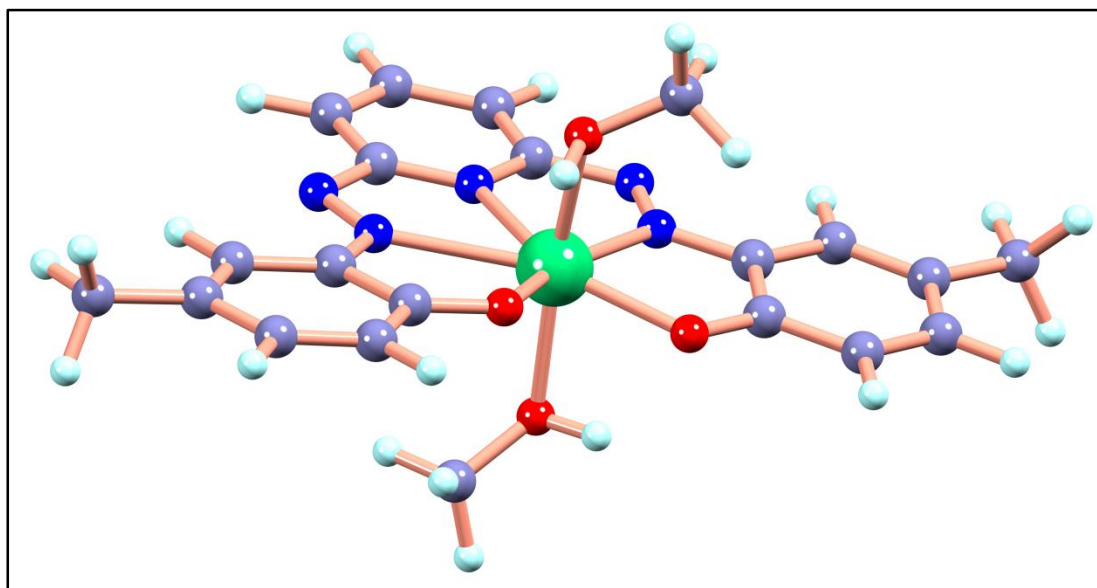


Fig. 5.8: Optimized structure of the H₂L-Ni²⁺ complex by DFT/B3LYP method

CHAPTER 5

The changes in electronic spectrum of H₂L upon complexation with Ni²⁺ have been interpreted by TDDFT calculations. In methanol H₂L shows two sharp bands at 382 nm and 273 nm along with two shoulders at 433 nm and 317 nm. The calculated band at 457 nm corresponds to the shoulder at 433 nm because of $n \rightarrow \pi^*$ transition. The sharp bands at 382 nm and 273 nm have $\pi \rightarrow \pi^*$ origin (Table 1). In nickel(II) complex the new band at 510 nm corresponds to intra-ligand charge transfer transitions (ILCT) and well matched with calculated transition at 540 nm. The sharp band at 378 nm in the complex corresponds to the calculated transitions at 387 nm and 342 nm having ILCT in character.

5.4. Experimental

5.4.1 Materials and methods

p-Cresol and 2, 6- Diaminopyridine were purchased from Sigma Aldrich. All other organic chemicals and inorganic salts were available from Sisco Research Lab, Mumbai, India and used without further purification. Commercially available SRL silica gel (60–120 mesh) was used for column chromatography.

Elemental analysis was carried out in a 2400 Series-II CHN analyzer, Perkin Elmer, USA. HRMS mass spectra were recorded on Waters (Xevo G2 Q-TOF) mass spectrometer. Infrared spectra were taken on a RX-1 Perkin Elmer spectrophotometer with samples prepared as KBr pellets. Electronic spectral studies were performed on a Perkin Elmer Lambda 750 spectrophotometer. NMR spectra were recorded using a Bruker (AC) 300 MHz FTNMR spectrometer of ~0.05 M solutions of the compounds in CDCl₃. Magnetic susceptibilities were measured on a Gouy balance using Hg[Co(SCN)₄] as the calibrant. Diamagnetic correction was made using Pascal's constants.

5.4.2 Synthesis of the receptor H₂L

2, 6- Diaminopyridine (1.5 g, 13.745 mmol) was dissolved in 5 mL conc. HCl and 10 mL distilled water and cooled to 0°C. Sodium nitrite (2.276 g, 32.99 mmol) was dissolved in minimum volume of water and cooled to 0°C. The diazotized solution was added dropwise with constant stirring to *p*-

CHAPTER 5

cresol (2.87 ml, 27.49 mmol) dissolved in aqueous solution of sodium carbonate (3.0 g, 28.30 mmol). The product was purified by column chromatography using silica gel (60-120 mesh) and eluted by 30% (v/v) ethyl acetate petroleum ether mixture. Yield was, 3.6 g, 75%.

Anal. Calc. C₁₉H₁₇N₅O₂ (H₂L): C, 65.69; H, 4.93; N, 20.16 %. Found: C, 65.45; H, 4.82; N, 20.21%.

IR data (KBr, cm⁻¹): 3430 ν (O-H), 1585 ν (C=N); 1417 ν (N=N).

¹H NMR (CDCl₃, 300 MHz): δ (ppm): 14.50 (2H, s), 9.07 (2H, s), 8.16 (2H, d, J = 9.0 Hz), 7.69-8.84 (1H, t, J= 6.1 Hz), 6.94 (2H, d, J = 8.07 Hz), 6.63 (2H, d, J = 8.25 Hz), 2.17 (6H, s).

HRMS *m/z*, 370.4980 (calculated for C₁₉H₁₇N₅O₂ + Na⁺: 370.36), 348.4120(calculated for C₁₉H₁₇N₅O₂ + H⁺: 348.38).

5.4.3 Syntheses of the H₂L-Ni²⁺ complex

0.05 g (0.14 mmol) of H₂L was dissolved in CH₃CN-DMF (3:1, v/v) and the solution was stirred for 10 minutes. To it NiCl₂.6H₂O (0.33 g, 0.14 mmol) was added and further stirred for another 1 hour. The colour of the H₂L solution was green but on addition of Ni²⁺, colour instantaneously changed to deep red with the formation of deep red precipitate. The solution was filtered and the residue was washed with n-hexane, dried in a desiccator over anhydrous CaCl₂ under vacuum. The dried complex thus obtained was subjected to various spectroscopic analyses. The complex is air-stable, non-hygroscopic, soluble in MeOH, DMSO and DMF.

Anal. Calc. C₁₉H₁₅N₅O₂Ni (H₂L): C, 66.08; H, 4.38; N, 20.28 %. Found: C, 66.20; H, 4.42; N, 20.21%.

IR data (KBr, cm⁻¹): 1536 ν (C=N); 1407 ν (N=N).

HRMS *m/z*, 491.2237 (calculated for C₂₁H₂₃N₅NiO₄ + Na⁺: 491.12), 427.7238(calculated for C₁₉H₁₅N₅NiO₂ + Na⁺: 427.04). μ_{eff} (B.M.): 2.97.

5.4.4 General method for UV-Vis studies

CHAPTER 5

5.4.4.1 UV-Vis method

For UV-Vis titrations, stock solution of the sensor H₂L was prepared (*c* = 10 μM) in [(MeOH/H₂O), 1:1, v/v] (at 25°C) using HEPES buffered solution at pH = 7.4. The solution of the guest cations using their chloride salts in the order of 100 μM were prepared in deionized water. Solutions of various concentrations containing host and increasing concentrations of cations were prepared separately.

5.4.4.2 Job's plot by UV-Vis method

A series of solutions containing H₂L (10 μM) and NiCl₂ (100 μM) were prepared in such a manner that the sum of the total metal ion and H₂L volume remained constant (5 mL). MeOH:H₂O (1:1, v/v) was used as solvent at pH 7.4 using HEPES buffer. Job's plots were drawn by plotting (A-A₀) versus mole fraction of Ni²⁺ at 510 nm [A₀ = absorption intensity of the free receptor and A is the absorption intensity of H₂L after addition of Ni²⁺ at 510 nm].

5.4.4.3 Determination of Detection Limit

The detection limit was calculated based on the UV-Vis titration. To determine the S/N ratio, the absorption intensity of H₂L without any analyte was measured by 10 times and the standard deviation of blank measurements was found to be 2.7900×10⁻⁴.

The limit of detection (LOD) of HL for Ni²⁺ was determined from the following equation: LOD= K × SD/S, where K = 3 in this case, SD is the standard deviation of the blank solution and S is the slope of the calibration curve. From the graph we get slope = 1013.57576, and Sb₁ value is 2.7900×10⁻⁴ (Fig. 5.6). Thus using the formula, we get the LOD = 0.83 μM.

5.4.4.4 Determination of Association constant

Binding constant was calculated according to the Benesi-Hildebrand equation. *K_a* was calculated following the equation stated below.

$$1/(A-A_0) = 1/\{K(A_{\max}-A_0) [Ni^{2+}]_n\} + 1/[A_{\max}-A_0]$$

Here A₀ is the absorbance of receptor in the absence of guest, A is the absorbance recorded in the presence of added guest, A_{max} is absorbance in presence of added [Ni²⁺]_{max} and K_a is the association

CHAPTER 5

constant (M^{-1}). The association constant (K) could be determined from the slope of the straight line of the plot of $1/(A-A_0)$ against $1/[Ni^{2+}]_n$, $n=1$. The association constant (K_a) as determined by UV-vis titration method for sensor with Ni^{2+} is found to be $1.27 \times 10^5 M^{-1}$. (Fig. S6)

5.4.5 Computational method

All computations were performed using the Gaussian09 (G09) program [19]. The 6-31+G(d) basis set was assigned for C, H, N and O atoms [20]. The LANL2DZ basis set with effective core potential was employed for the nickel atom [21-23]. The vibrational frequency calculations were performed to ensure that the optimized geometries represent the local minima of potential energy surface and there are only positive Eigen-values. The vertical electronic excitations based on B3LYP optimized geometries were computed using the time-dependent density functional theory (TDDFT) [24-26] formalism using methanol as solvent for H_2L and H_2L-Ni^{2+} complex using conductor-like polarizable continuum model (CPCM) [27-29].

5.5. Conclusion

The sensing ability of the receptor H_2L for Ni^{2+} has been extensively studied using UV-Vis spectroscopy and several other spectroscopic tools. The synthesized chemosensor H_2L is highly efficient in detecting Ni^{2+} over other metal ions that commonly coexist with Ni^{2+} in physiological and environmental samples. H_2L also shows distinct colour change from light-green to deep red distinctly visible under naked eye due to specific binding with Ni(II). Thus H_2L provides a pathway for a very rapid, sensitive and selective detection of Ni^{2+} . Moreover, the pyridyl based framework H_2L has been synthesized using a very facile and economically cheap synthetic pathway.

5.6. Reference

1. L. Zeng, E.W. Miller, A. Pralle, E.Y. Isacoff, C.J. Chang, *J. Am. Chem. Soc.*, 2006, **128**, 10–11.
2. K. Hanaoka, K. Kikuchi, H. Kojima, Y. Urano, T. Nagano, *J. Am. Chem. Soc.*, 2004, **126**, 12470–12476.

CHAPTER 5

3. K.K. Das, S.N. Das, S.A. Dhundasi, *Indian J. Med. Res.*, 2008, **128**, 412-425.
4. X. Liu, X. Zhou, X. Shu, J. Zhu, *Macromolecules*, 2009, **42**, 7634-7637.
5. H.X. Wang, D.L. Wang, Q. Wang, X.Y. Li, C.A. Schalley, *Org. Biomol. Chem.*, 2010, **8**, 1017-1026.
6. L. Feng, Y. Zhang, L.Y. Wen, L. Chen, Z. Shen, Y.F. Guan, *Analyst*, 2011, **136**, 4197-4203.
7. N.W. Barnett, L.S. Chen, G.F. Kirkbright, *Anal. Chim. Acta.*, 1983, **149**, 115-121.
8. K. Ohta, K. Ishida, S.-I. Itoh, S. Kaneco, T. Mizuno, *Microchim. Acta*, 1998, **129**, 127-132.
9. A.M. Bond, G.G. Wallace, *Anal. Chem.*, 1983, **55**, 718-723.
10. A.M. Bond, G.G. Wallace, *Anal. Chem.*, 1984, **56**, 2085-2090.
11. N. Aksuner, E. Hendem, I. Yilmaz, A. Cukurovali, *Sens. Actuator B Chem.*, 2012, **166-167**, 269-274.
12. M.R. Ganjali, M. Hosseini, M. Motalebi, M. Sedaghat, F. Mizani, F. Faridbod, P. Norouzi, *Spectrochim. Acta A*, 2015, **140**, 283-287.
13. H. Haddou, S. Wiskur, V. Lynch, E.V. Anslyn, *J. Am. Chem. Soc.*, 2001, **123**, 11296-11297.
14. T. Gunnlaugsson, P. Kruger, P. Jensen, J. Tierney, H. Ali, G. Hussey, *J. Org. Chem.*, 2005, **70**, 10875-10878.
15. S. Goswami, S. Chakraborty, S. Paul, S. Halder, A. C. Maity, *Tet. Lett.*, 2013, **54**, 5075-5077.
16. D. Peralta-Domínguez, M. Rodríguez, G. Ramos-Ortíz, J. Luis Maldonado, M. A. Meneses-Nava, O. Barbosa-García, R. Santillan, N. Farfán, *Sens. Actuator B. Chem.*, 2015, **207**, 511-517.
17. J. Jiang, C. Gou, J. Luo, C. Yi, X. Liu, *Inorg. Chem. Commun.*, 2012, **15**, 12-15.
18. L. Wang, D. Ye, D. Cao, *Spectrochim. Acta A*, 2012, **90**, 40-44.
19. Gaussian 09, Revision D.01, M. J. Frisch, G. W. Trucks, H. B. Schlegel, G. E. Scuseria, M. A. Robb, J. R. Cheeseman, G. Scalmani, V. Barone, B. Mennucci, G. A. Petersson, H. Nakatsuji, M.

CHAPTER 5

Caricato, X. Li, H. P. Hratchian, A. F. Izmaylov, J. Bloino, G. Zheng, J. L. Sonnenberg, M. Hada, M. Ehara, K. Toyota, R. Fukuda, J. Hasegawa, M. Ishida, T. Nakajima, Y. Honda, O. Kitao, H. Nakai, T. Vreven, J. A. Montgomery, Jr., J. E. Peralta, F. Ogliaro, M. Bearpark, J. J. Heyd, E. Brothers, K. N. Kudin, V. N. Staroverov, R. Kobayashi, J. Normand, K. Raghavachari, A. Rendell, J. C. Burant, S. S. Iyengar, J. Tomasi, M. Cossi, N. Rega, J. M. Millam, M. Klene, J. E. Knox, J. B. Cross, V. Bakken, C. Adamo, J. Jaramillo, R. Gomperts, R. E. Stratmann, O. Yazyev, A. J. Austin, R. Cammi, C. Pomelli, J. W. Ochterski, R. L. Martin, K. Morokuma, V. G. Zakrzewski, G. A. Voth, P. Salvador, J. J. Dannenberg, S. Dapprich, A. D. Daniels, Ö. Farkas, J. B. Foresman, J. V. Ortiz, J. Cioslowski, and D. J. Fox, Gaussian, Inc., Wallingford CT, 2009.

20. T. Clark, J. Chandrasekhar, G.W. Spitznagel, P.V.R. Schleyer, *J. Comput. Chem.*, 1983, **4**, 294-301.

21. P.J. Hay, W.R. Wadt, *J. Chem. Phys.*, 1985, **82**, 270-283.

22. W.R. Wadt, P.J. Hay, *J. Chem. Phys.*, 1985, **82**, 284-298.

23. P.J. Hay, W.R. Wadt, *J. Chem. Phys.*, 1985, **82**, 299-310.

24. R. Bauernschmitt, R. Ahlrichs, *Chem. Phys. Lett.*, 1996, **256**, 454-464.

25. R.E. Stratmann, G.E. Scuseria, M.J. Frisch, *J. Chem. Phys.*, 1998, **109**, 8218-8224.

26. M.E. Casida, C. Jamorski, K.C. Casida, D.R. Salahub, *J. Chem. Phys.*, 1998, **108**, 4439-4449.

27. V. Barone, M. Cossi, *J. Phys. Chem. A.*, 1998, **102**, 1995-2001.

28. M. Cossi, V. Barone, *J. Chem. Phys.*, 2001, **115**, 4708-4717.

29. M. Cossi, N. Rega, G. Scalmani, V. Barone, *J. Comput. Chem.*, 2003, **24**, 669-681.

30. US EPA, EPA/Rod/R03-99/061, 1999.

CHAPTER 5

APPENDIX

CHAPTER 5

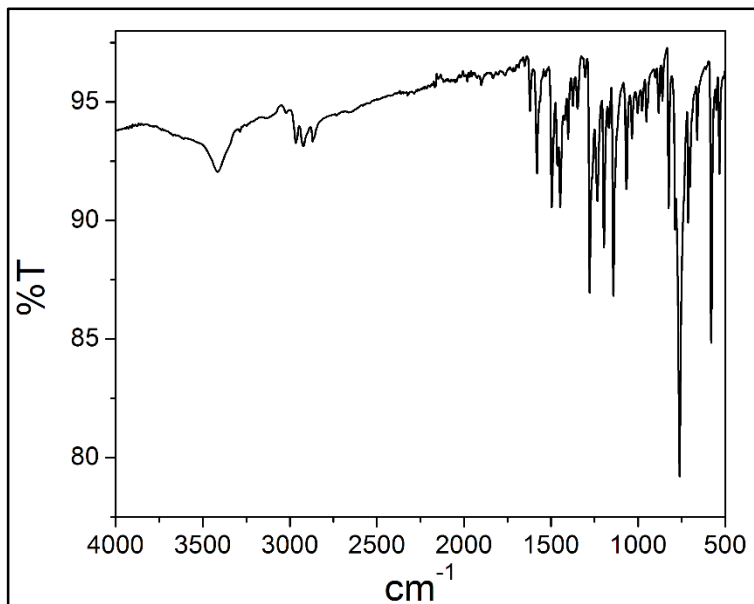


Fig. S1: IR spectrum of the receptor H₂L in KBr disk

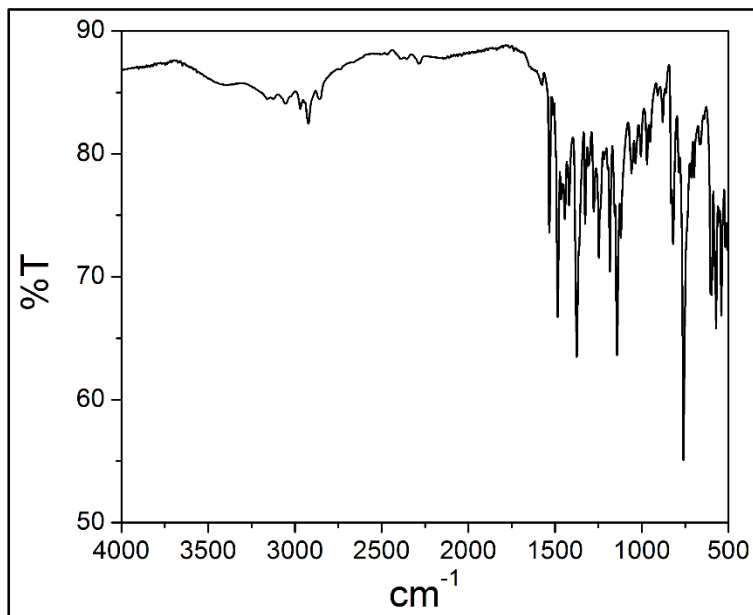


Fig. S2: IR spectrum of H₂L + Ni²⁺ in KBr disk

CHAPTER 5

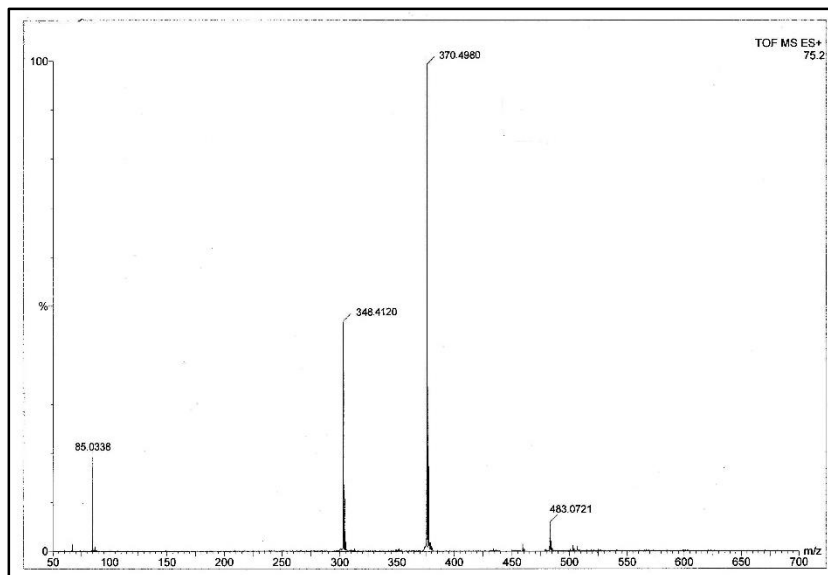


Fig. S3: HRMS spectra of the receptor H₂L.

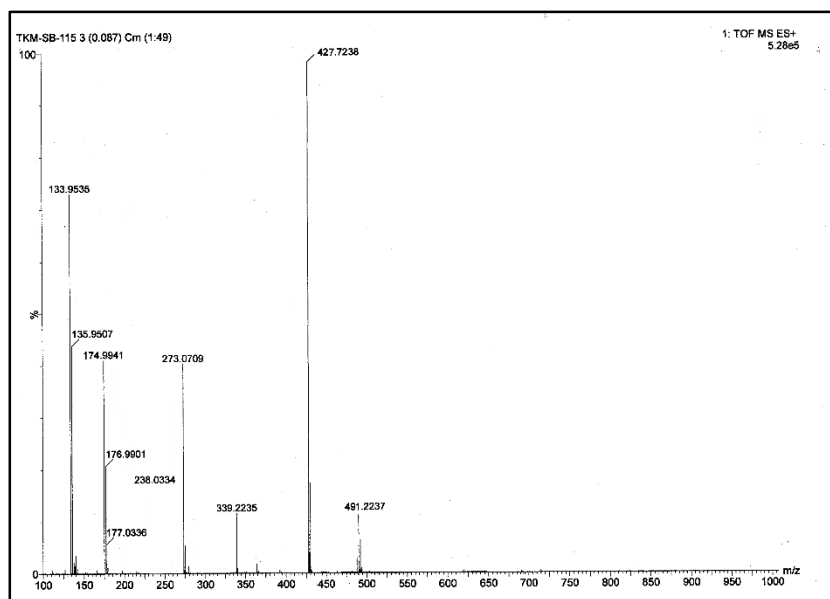


Fig. S4: HRMS spectra of the receptor H₂L-Ni²⁺ complex.

CHAPTER 5

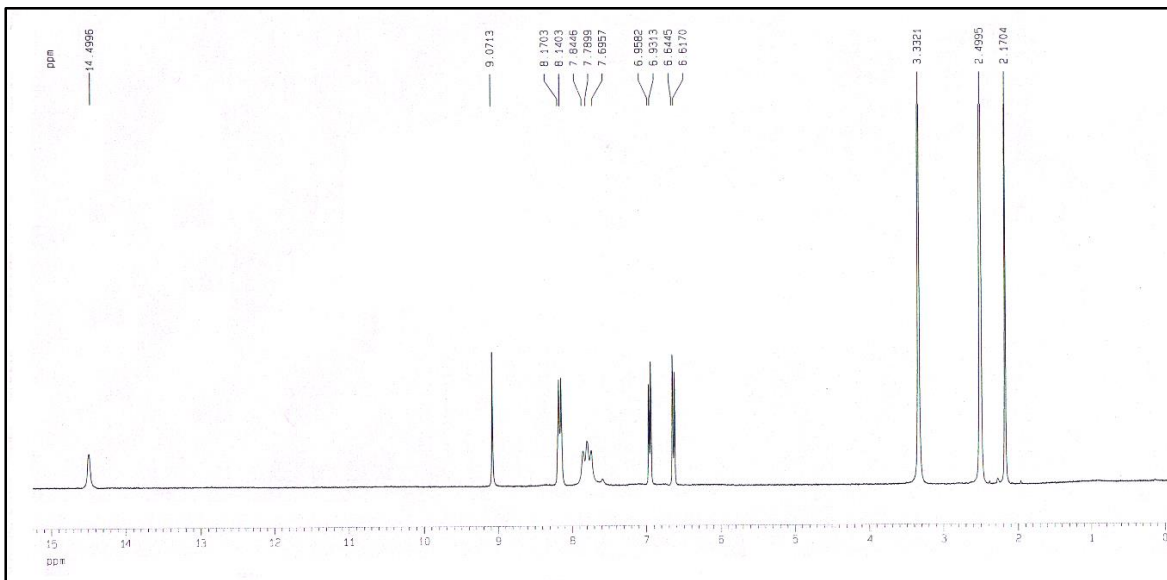


Fig. S5: ^1H -NMR spectra of the receptor H_2L

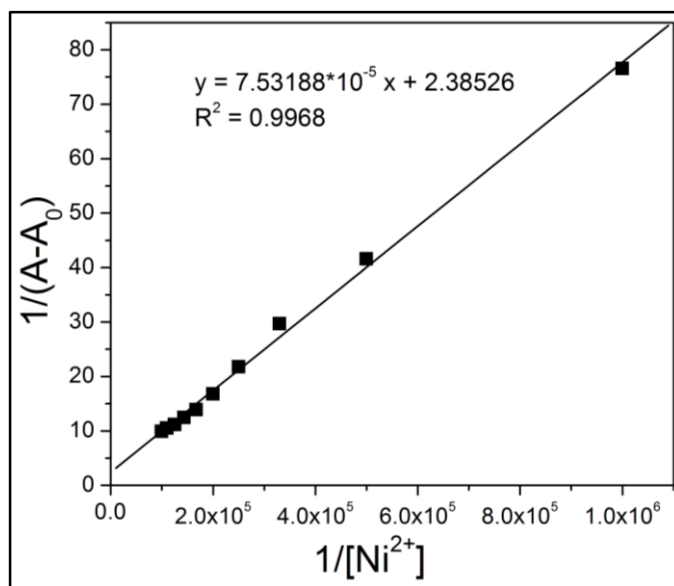


Fig. S6: Determination of binding constant of H_2L for Ni^{2+} from UV-Vis titration data

CHAPTER 5

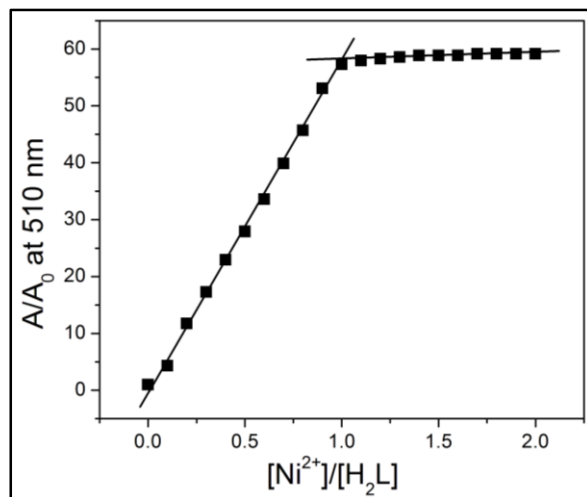


Fig. S7: Mole ratio plot of Ni²⁺ to the receptor H₂L

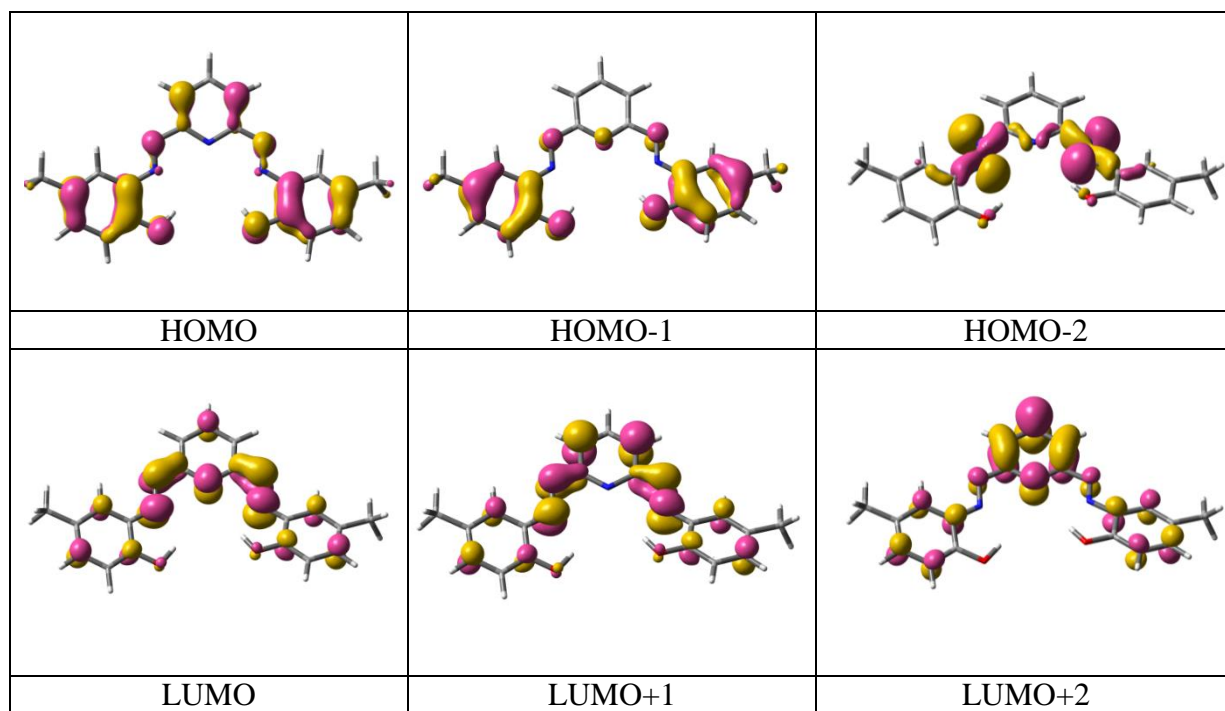


Fig. S8: Contour plots of selected molecular orbitals of chemosensor H₂L

CHAPTER 5

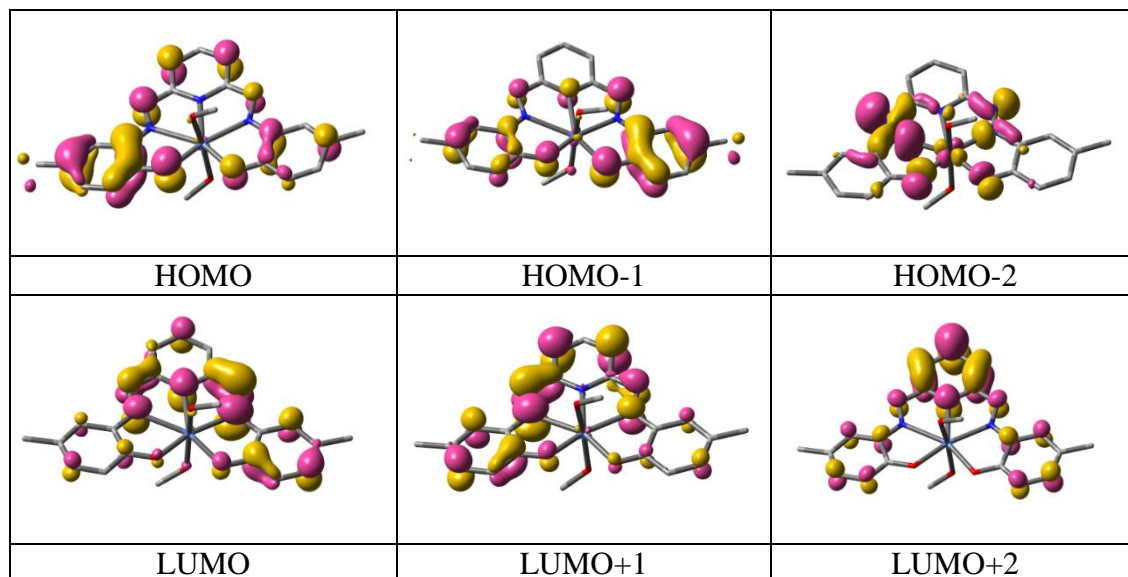


Fig. S9: Contour plots of some selected MOs (α -spin) of $\text{H}_2\text{L-Ni}^{2+}$ complex.

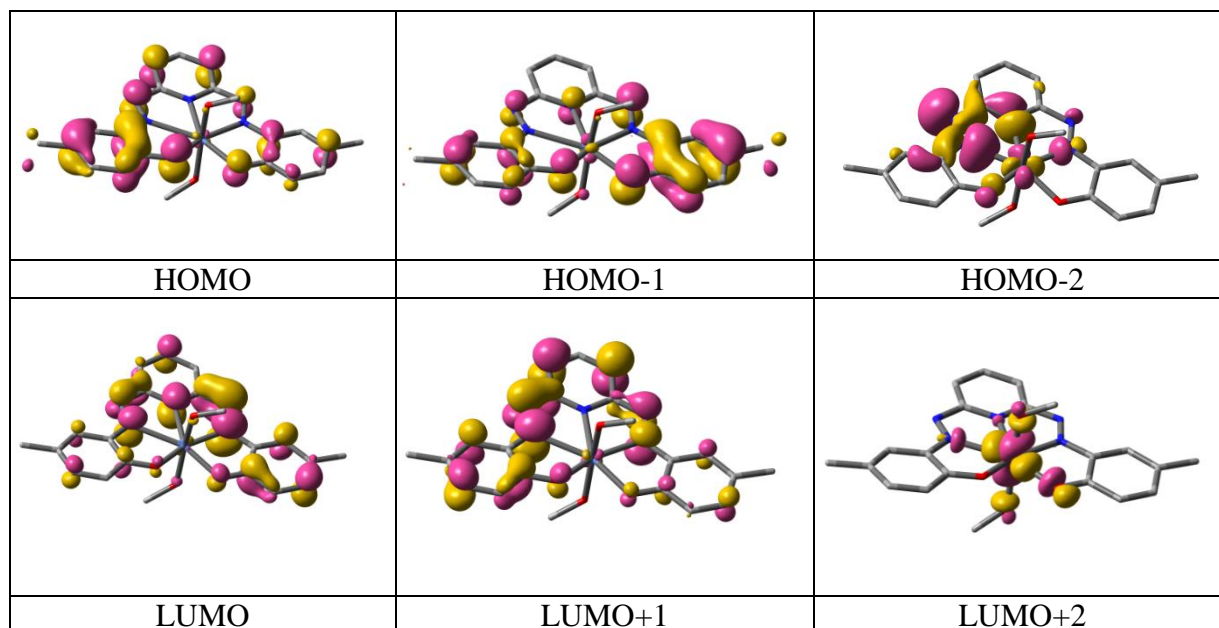


Fig. S10: Contour plots of some selected MOs (β -spin) of $\text{H}_2\text{L-Ni}^{2+}$ complex.

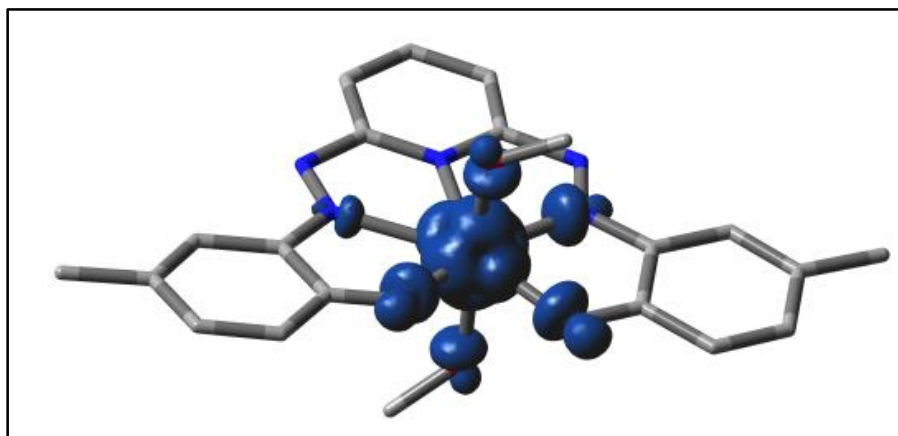


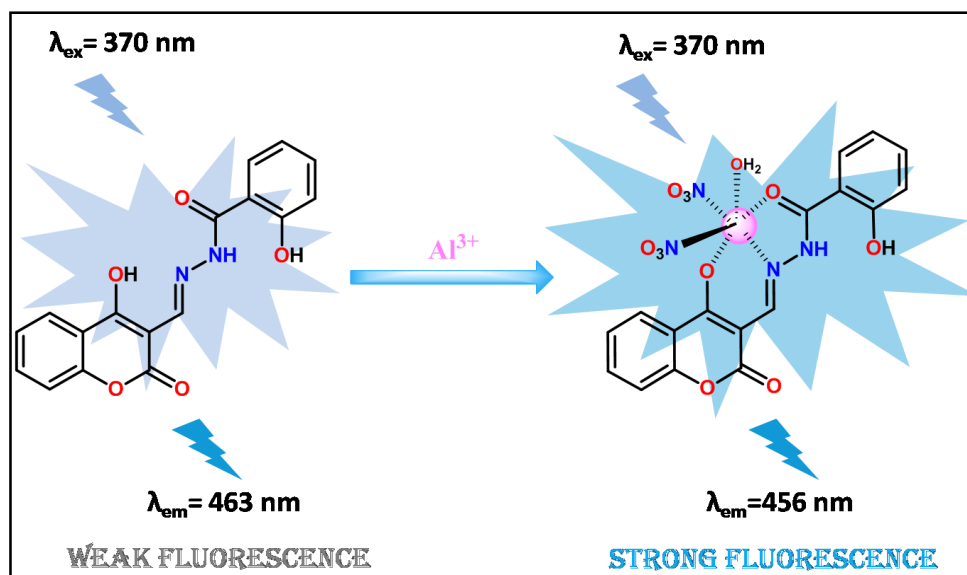
Fig. S11: Spin density plot of H_2L-Ni^{2+} complex

A new fluorescent “turn-on” switch based on coumarin for selective and distinct response towards Al^{3+}

Anewcoumarin-based “turn-on” probe for the selective and distinct fluorescence response towards Al^{3+}

Abstract

A new coumarin based fluorescent probe, HMBH was effectively fabricated and the structures are thoroughly characterized by NMR and HRMS spectroscopy. HMBH displays a selective and discrete “turn-on” fluorescence response for Al^{3+} in MeOH/ H_2O (1/9, v/v, pH=7.2) solution with almost 30-fold emission intensity over other analytes. No such changes in emission intensity were observed in case of other cations. HMBH shows a low detection limit of about 10^{-9}M which supports the fact that this newly developed probe can detect Al^{3+} in very tiny level. The stoichiometric ratio of the probe towards Al^{3+} was found to be 1:1 from Job’s plot experiment. The electronic structures of the sensor have been explained by DFT and TDDFT calculations.



CHAPTER 6

6.1. Introduction

Fabrication of fluorescent sensors for distinctive recognition of several analytes have been considered to be a noteworthy area of research for quite some time now owing to their amazing roles in numerous fields such as industry, biology, environment, medicines, living systems etc. [1-7]. This technique is chosen over other methods owing to their rapid response with high sensitivity, non-destructive appeal, good tunability etc. [8-12]. Among several biologically significant metal cations, discrimination of aluminium ion has drawn a massive interest of scientists towards itself owing to its daily use in human life as well as due to its toxic effects on human health [13-18]. Aluminium is acclaimed to be the third most abundant and most prevalent elements found in the lithosphere [19, 20] and regardless of its toxic nature, it has many advantages in our daily life as well as in industrial, biological and environmental arenas. The extensive use of aluminium in our everyday life, such as aluminium foil, cookware, as electronic components in several gadgets, the paper production, food additives and aluminium-based medicines results into a great exposure of this toxic metal to the environment as well as in human health [13, 21-24]. The acid rain causes the excess amount of aluminium in soil and water which eventually results into harmful consequences for the growth of the plants [25]. Aluminium is a crucial metal ion in the human body but can turn into a harmful element if accumulated in unregulated amounts which ultimately leads to several severe diseases and the permanent damage to central nervous system and immunity of our body [26, 27]. Aluminium is known as the neurotoxin that is supposed to be the root cause of Alzheimer's disease [28]. Its excessive toxicity also results in health hazards such as encephalopathy, dementia, osteomalacia, Parkinson's disease and breast cancer [29-32]. In addition, aluminium retains its concentration in the body tissues and cells for a longer time-period before expulsion from the body [19] which suggests us to take admissible quantities of aluminium only. The World Health Organization (WHO) approved the standard human consumption of aluminum to be around 3-10 mg day⁻¹ and allowable intake of aluminum in a week in the human body is predicted to be 7 mg kg⁻¹ body weight [33, 34]. Despite of its toxic and destructive nature, Al³⁺ cannot be kept away from our modern life which leads to the endangerment of human health as well as environment by its fatal toxicity. Thus, detection of Al³⁺ ions is an essential step to manage its adverse effects on human health as well as to the environment, industry, plant lives etc. Hence, designing a new switch for the detection of Al³⁺

CHAPTER 6

has an intense significance. Due to the fact that Al^{3+} is a hard-acid, it has been established that Al^{3+} favors to coordinate with donor sites like N and O atoms which are hard bases [35-40] and it is well known that schiff-bases are popular as hard bases which provides nitrogen-oxygen-rich coordination spheres for Al^{3+} . As an outcome, a great number of Schiff-base based probes have been fabricated for sensing Al^{3+} ion solely [41-44].

6.2. Basis of present work

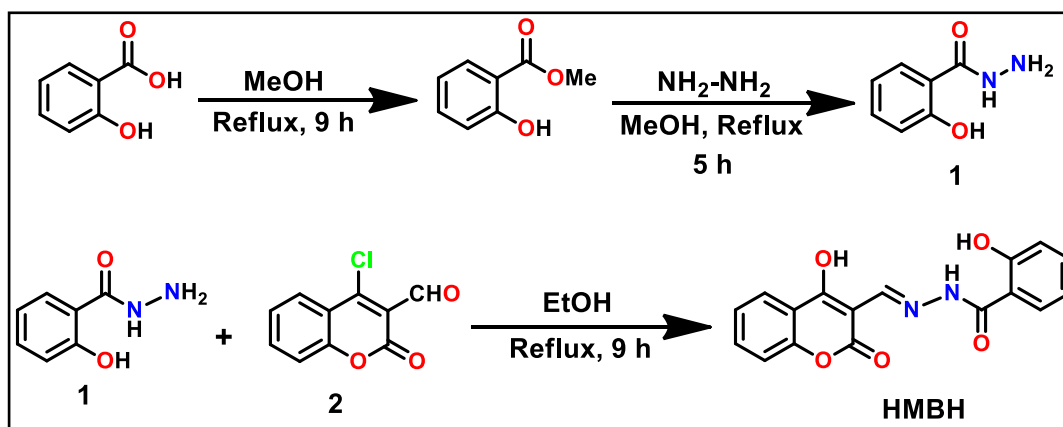
Due to the high demand of Al^{3+} sensors, there are some reports on fabrication of new sensors for selective recognition of aluminium over other cations. As for example, S. L. Hu et al. introduced a simple pyrazoline-based fluorescent probe that demonstrated fluorescence quenching pattern for Al^{3+} in aqueous solution [45]. T. H. Ma et al. gave a detailed account of a novel dual-channel fluorescent sensor for Al^{3+} [46]. Recently, Hwang et al. reported a simple Schiff base probe which selectively binds with aluminium with a very little detection limit of 290 nM and shows live cell imaging studies [47]. Another interesting report on aluminium sensors is found by Balamurugan et al. They synthesized a phenazine fluorophore based sensors which displays AIE effect selectively for Al^{3+} ion [48].

Herein, we investigated a new fluorescent probe, HMBH showing a sharp ‘turn-on’ emission response for Al^{3+} selectively. The synthesis of our target molecule, HMBH includes a very easy and economically inexpensive procedure. At first, compound **1** was obtained via a simple Schiff base condensation in methanol medium for 5 h. Then again a simple Schiff base condensation of compound **1** with 4-chloro-2-oxo-2H-chromene-3-carbaldehyde (**2**) was performed in ethanol under refluxing condition for 9 h which ultimately yield our highly fluorescent probe, HMBH. Fluorescence titration reveals that HMBH shows almost a ~30-fold “turn-on” emission enhancement upon addition of Al^{3+} in MeOH/ H_2O (1/9, v/v, pH=7.2) solution. The sensing aptitude of this newly developed probe (HMBH) in presence of other cations in MeOH/ H_2O (1/9, v/v, pH=7.2) solution has also been explored but there is barely any change in emission intensity observed in case of others.

6.3. Results and discussions

6.3.1 Synthesis of HMBH

The synthetic route of the probe (HMBH) is displayed in Scheme 6.1. The chemical structures of HMBH and its Al^{3+} complex is established by ^1H and ^{13}C NMR spectroscopy and ESI mass spectroscopic techniques (See appendix).



Scheme 6.1: Synthesis of chemosensor HMBH.

6.3.2 Spectral characterization and analysis of HMBH

FT-IR spectrum of HMBH is taken in KBr disk and it shows bands at 3271 and 3088 cm^{-1} which is due to the two free $-\text{OH}$ group stretching. The absorption band at 1679 cm^{-1} is due to the presence of $\text{C}=\text{O}$ stretching. The band at 1617 cm^{-1} indicates the presence of $-\text{C}=\text{N}$ stretching and the band at 1550 cm^{-1} accounts for the $-\text{NH}$ bending in HMBH. ^1H -NMR spectra are recorded in DMSO-d_6 for compound **1** and HMBH. In case of compound **1**, a singlet at δ 4.68 ppm is observed for NH_2 proton whereas NH proton appears at δ 10.08 ppm as another singlet and the last singlet due to the presence of $-\text{OH}$ proton appears at δ 12.50 ppm. The aromatic protons are found in the expected region of δ 6.82-7.83 ppm. In case of HMBH, the two $-\text{OH}$ protons appear at δ 12.54 and 12.62 ppm as singlet while another singlet appears at δ 9.95 ppm for the presence of $-\text{CH}=\text{N}$ imine proton along with the last singlet at δ 8.72 indicating the presence of $-\text{NH}$ proton. The aromatic protons are observed at the range of δ 6.99-7.96 ppm. ^{13}C -NMR spectrum of HMBH is recorded in DMSO-d_6 . Mass

CHAPTER 6

spectrum shows a peak corresponding to [Compound 1-H⁺] at (m/z) 153.1211 for compound 1 whereas the probe, HMBH displays a strong peak at 325.1012 corresponding to [HMBH+H⁺].

6.3.3 Cation sensing studies: UV-Vis spectroscopy studies

The probe shows a moderate absorbance band at 371 nm with a small shoulder hump at 388 nm in MeOH/H₂O (1/9, v/v) using 10 mM HEPES buffered solution at pH=7.2. Gradual addition of Al³⁺ into the solution of HMBH results in shifting of the band at 371 nm to 367 nm whereas the small hump at 388 nm appears to be distinct and sharper and it shifts to 385 nm (Fig. 6.1a) establishing the coordination of Al³⁺ to the probe. The changes of UV-Vis spectrum of HMBH are also explored in presence of other cations i.e., K⁺, Mg²⁺, Mn²⁺, Na⁺, Ca²⁺, Cr³⁺, Fe³⁺, Ni²⁺, Hg²⁺, Co²⁺, Zn²⁺, Cd²⁺, Pb²⁺ and Cu²⁺ and no noteworthy change is noticed for other metals (Fig. 6.1b).

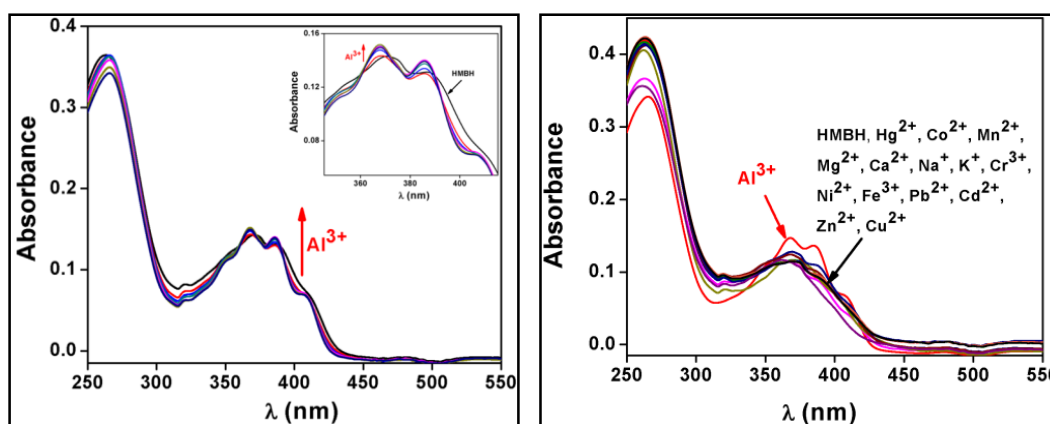


Fig. 6.1:(a) Change in UV-Vis spectrum of HMBH (20 μM) on gradual addition of Al³⁺ (40 μM) in MeOH/H₂O (1/9, v/v) using HEPES buffered solution at pH=7.2 and (b) UV-Vis spectra of HMBH (20 μM) upon addition of 2 equivalent of various cations i.e., Na⁺, K⁺, Mg²⁺, Mn²⁺, Co²⁺, Ni²⁺, Ca²⁺, Fe³⁺, Cr³⁺, Zn²⁺, Cu²⁺, Hg²⁺, Pb²⁺ and Cd²⁺ (40 μM) in MeOH/H₂O (1/9, v/v) using HEPES buffered solution at pH=7.2.

6.3.4 Cation sensing studies: Fluorescence emission studies

The fluorescence spectrum of the free probe (HMBH) displays a band with a very weak emission intensity with the maxima (F₀) emerging at 463 nm ($\lambda_{\text{excitation}}$, 370 nm) in MeOH/H₂O (1/9, v/v). On gradual addition of Al³⁺ to HMBH solution, an emission maximum is noticed at 456 nm along with a

CHAPTER 6

very slight blue shift which displays a sharp ~ 30 fold “turn-on” increment in fluorescence intensity (Fig. 6.2).

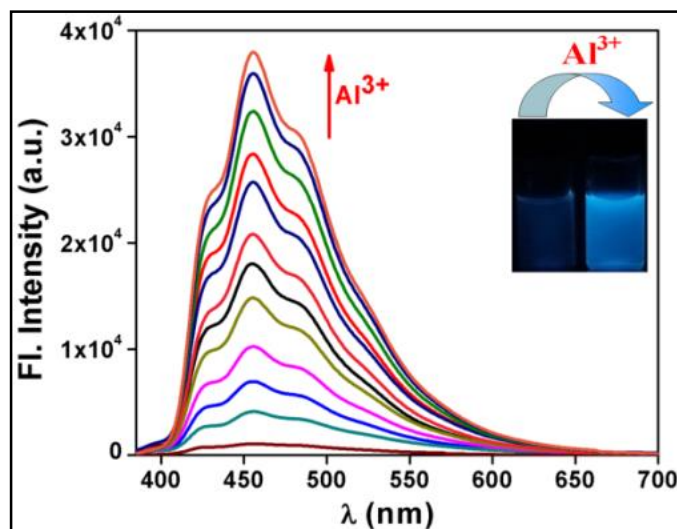


Fig. 6.2: Change in emission spectrum of HMBH (20 μM) upon gradual addition of Al^{3+} (40 μM) in MeOH/ H_2O (1/9, v/v). Inset shows effect of addition of Al^{3+} to HMBH upon UV radiation

The sensing capacity of this newly manufactured probe for Al^{3+} in presence of other cations like Ca^{2+} , Mg^{2+} , Na^+ , K^+ , Fe^{3+} , Cr^{3+} , Mn^{2+} , Ni^{2+} , Co^{2+} , Hg^{2+} , Zn^{2+} , Cu^{2+} , Pb^{2+} and Cd^{2+} (20 μM) in MeOH/ H_2O (1/9, v/v) are also studied (Fig. 6.3a) but there is no noticeable change in emission intensity of HMBH except a slight increase of emission intensity in case of Mg^{2+} . To explore the selectivity of HMBH for Al^{3+} , interference experiment is executed by recording the emission intensity of HMBH (10 μM) in presence of other cations like Ca^{2+} , Mg^{2+} , Mn^{2+} , Na^+ , K^+ , Co^{2+} , Ni^{2+} , Cr^{3+} , Fe^{3+} , Zn^{2+} , Hg^{2+} , Pb^{2+} , Cu^{2+} and Cd^{2+} (20 μM) before the addition of Al^{3+} in MeOH/ H_2O (1/9, v/v, pH=7.2) (Fig. 6.3b). It is noticed that a variety of competitive cations do not result in any noteworthy interference for Al^{3+} .

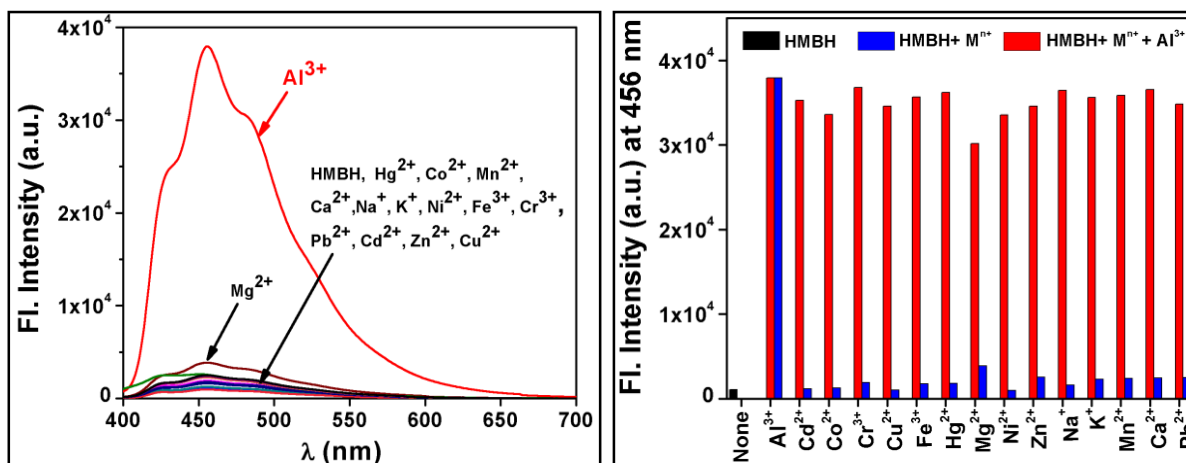


Fig. 6.3:(a) Emission intensity of HMBH (20 μM) upon addition of other cations like Mg²⁺, Mn²⁺, Na⁺, K⁺, Fe³⁺, Cr³⁺, Co²⁺, Ni²⁺, Ca²⁺, Cu²⁺, Hg²⁺, Zn²⁺, Pb²⁺ and Cd²⁺ (40 μM) in presence of Al³⁺(40 μM) in MeOH/H₂O (1/9, v/v) (pH=7.2) and (b) Emission intensity of HMBH (20 μM) (black bar). On addition of Mg²⁺, Mn²⁺, Na⁺, K⁺, Fe³⁺, Cr³⁺, Co²⁺, Ni²⁺, Ca²⁺, Cu²⁺, Hg²⁺, Zn²⁺, Pb²⁺ and Cd²⁺ (40 μM) in MeOH/H₂O (1/9, v/v) (pH=7.2) (red bars). Al³⁺ (40 μM) in presence of other cations (blue bars)

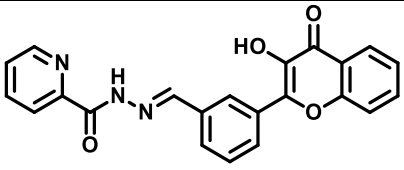
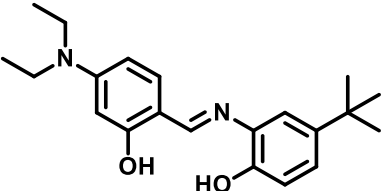
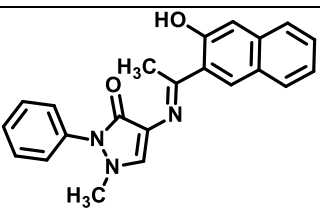
6.3.5 Binding studies of HMBH with Al³⁺

The mole ratio plot of HMBH demonstrates that the probe exhibits an enhancement in emission intensity till the ratio of HMBH-Al³⁺ attains the value of ~1 after which no further distinct increase in the emission intensity is seen (Fig. 6.4a). The emission intensity on addition of aluminum ion increased linearly with the amount added in between 0-9 μM which suggests that HMBH owned a linear response range towards Al³⁺ with R=0.995. Job's method for emission spectrum is performed and a maxima is observed in the plot corresponding to 0.5 mole fraction demonstrating 1:1 complexation of HMBH with Al³⁺ (Fig. 6.4b). From luminescence spectral change, limit of detection of the probe for Al³⁺ is calculated utilizing the equation $LOD = K \times SD/S$ where SD is the standard deviation of the blank solution and S is the slope of the linear response curve. The limit of detection

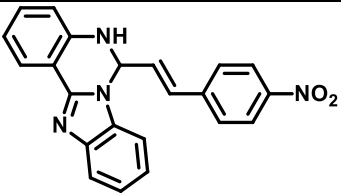
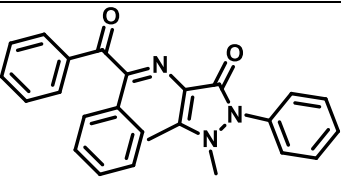
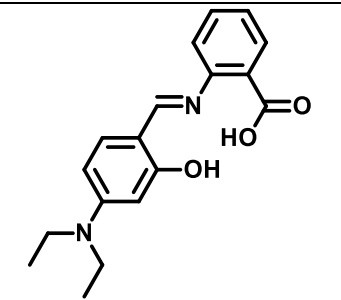
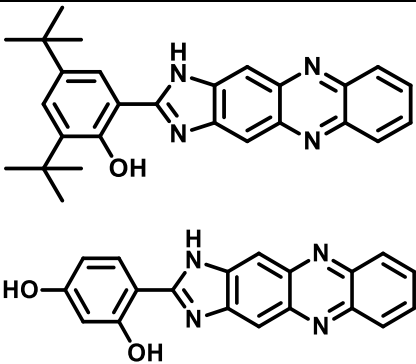
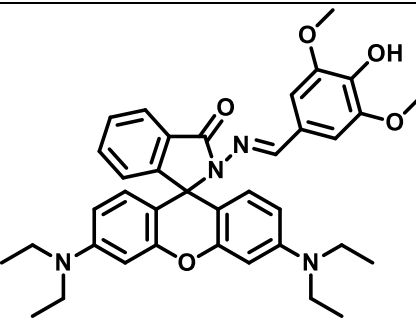
CHAPTER 6

for Al^{3+} is determined to be $3.16 \times 10^{-9} \text{ M}$ (Fig. 6.5a) which evidently reveals that the probe is vastly capable in identifying Al^{3+} even in very tiny level in the aqueous solution. The binding constant K_a is calculated by using the Benesi-Hildebrand equation. The ratio of intercept and slope of the plotted straight line yields the association constant. Plot of $1/[F-F_0]$ vs. $1/[\text{Al}^{3+}]$ gives a straight line signifying 1:1 complexation between HMBH and Al^{3+} . So from emission spectral titration, the association constant of HMBH with Al^{3+} is established to be $1.79 \times 10^5 \text{ M}^{-1}$ (Fig. 6.5b) indicating that the complexation of Al^{3+} with the probe, HMBH is sufficiently strong enough. A comparison study of LOD and binding constant is given in Table 6.1.

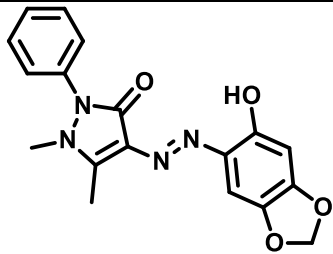
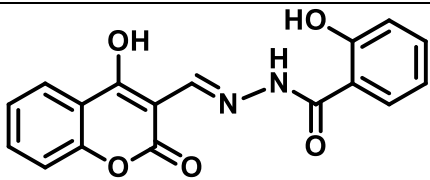
Table 6.1: Comparison of detection limit and binding constant (K_b) of some recently reported Al^{3+} sensors

Sl. No.	Chemosensors	Limit of detection (LOD)	Binding constant (K_b)	Refs
1.		$21.7 \times 10^{-6} \text{ M}$	Not reported	[49]
2.		$99.5 \times 10^{-9} \text{ M}$	$2.5 \times 10^4 \text{ M}^{-1}$	[50]
3.		$1 \times 10^{-5} \text{ M}$	$6.02 \times 10^3 \text{ M}^{-1}$	[51]

CHAPTER 6

4.		$9 \times 10^{-9} \text{ M}$	$2.8 \times 10^3 \text{ M}^{-1}$	[52]
5.		$0.49 \times 10^{-6} \text{ M}$	$4.58 \times 10^4 \text{ M}^{-1}$	[53]
6.		$2.9 \times 10^{-7} \text{ M}$	$3.1 \times 10^8 \text{ M}^{-1}$	[47]
7.		14 ppb 1.5 ppm	Not reported	[48]
8.		$1.05 \times 10^{-8} \text{ M}$	Not reported	[54]

CHAPTER 6

9.		$3.55 \times 10^{-7} \text{ M}$	$5.42 \times 10^5 \text{ M}^{-1}$	[55]
10.		$3.16 \times 10^{-9} \text{ M}$	$1.79 \times 10^5 \text{ M}^{-1}$	Present work

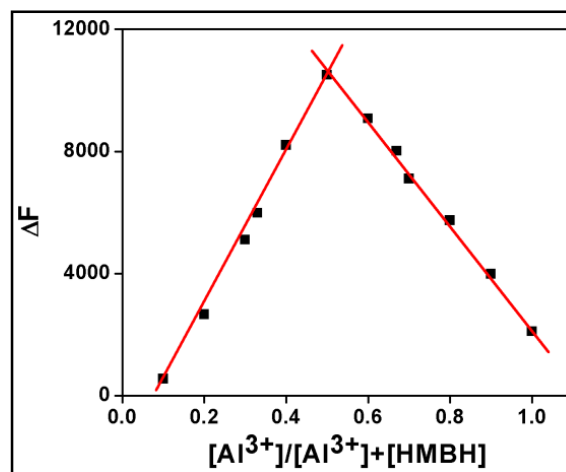
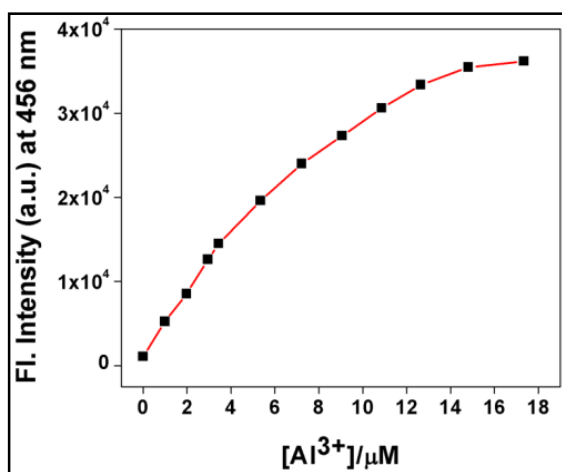


Fig. 6.4:(a) Mole ratio plot of HMBH for Al³⁺ and (b) Job's plot of the probe (HMBH) for Al³⁺ (where ΔF designates the change of emission intensity at 463 nm)

CHAPTER 6

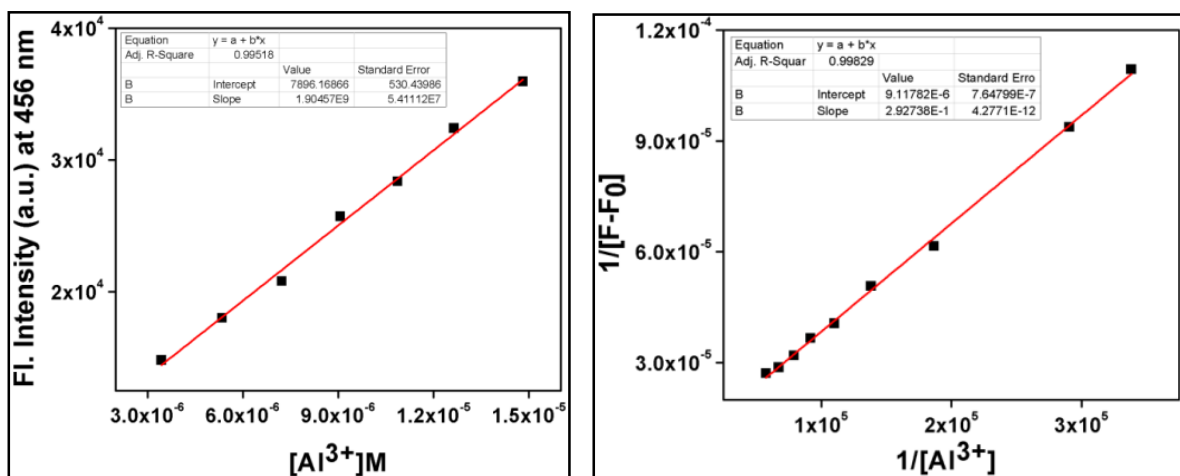


Fig. 6.5:(a) Linear response diagram of HMBH at 456 nm depending on the Al^{3+} concentration and (b) Association constant plot of HMBH for Al^{3+} from fluorescent titration data

6.3.6 Effect of pH on emission properties

Now the acid base titration was performed to explore the pH effect on the emission intensity of the probe (HMBH) with or without Al^{3+} . In case of HMBH, emission intensity remains almost same with increasing pH except showing slight increase in basic region whereas on addition of Al^{3+} , fluorescent intensity of HMBH increases in the pH range of 6.1-9.5 but in further basic region, the emission intensity decreases (Fig. 6.6) thereby stating the fact that HMBH can recognize Al^{3+} effectively into the pH range of 6-9. In the basic pH range, the -OH group is deprotonated driving the probe to dissociate and thereby resulting in the inability of HMBH in recognizing Al^{3+} . Hence the probe HMBH can identify Al^{3+} in the natural pH region with enough efficiency.

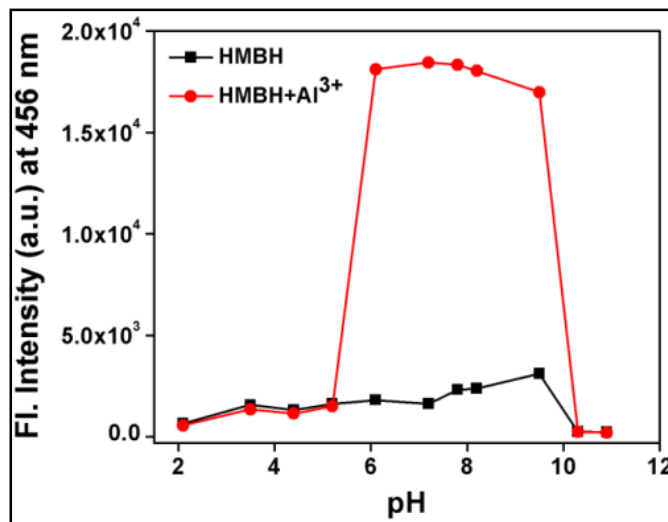


Fig. 6.6: Outcome of pH on emission intensity of HMBH (-■-■-) and HMBH+Al³⁺ (-●-●-)

6.3.7 Dip-stick experiment: Recognition of Al³⁺ using TLC plate

To exhibit some astounding applications of this probe (HMBH), an experiment was performed. It is popular as dipstick experiment. In this experiment the synthesized probe can act as a fluorescent portable kit which displays distinct sensing response towards a fixed analyte in solid state as well as solution state. This experiment is worth mentioning, as from this method, one can get vital qualitative data for the detection of Al³⁺ without even using any kind of instrumental techniques. So to carry out this experiment, a few thin-layer chromatography (TLC) plates were arranged and they are immersed into HMBH solution (2×10^{-4} M) in MeOH and then set aside for a short time to evaporate the solvent. Then the TLC plates are dipped into Al³⁺ (2×10^{-3} M) solution once and then the plates are set aside in order to dry them like before. This experiment helps us to ascertain the identification of Al³⁺ through bare eyes with much ease. The colour of the TLC plates confirms the change of the color from colorless to cyan in presence of Al³⁺ in the UV compartment (Fig. 6.7).

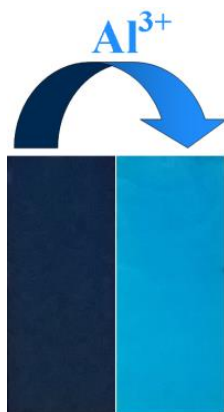
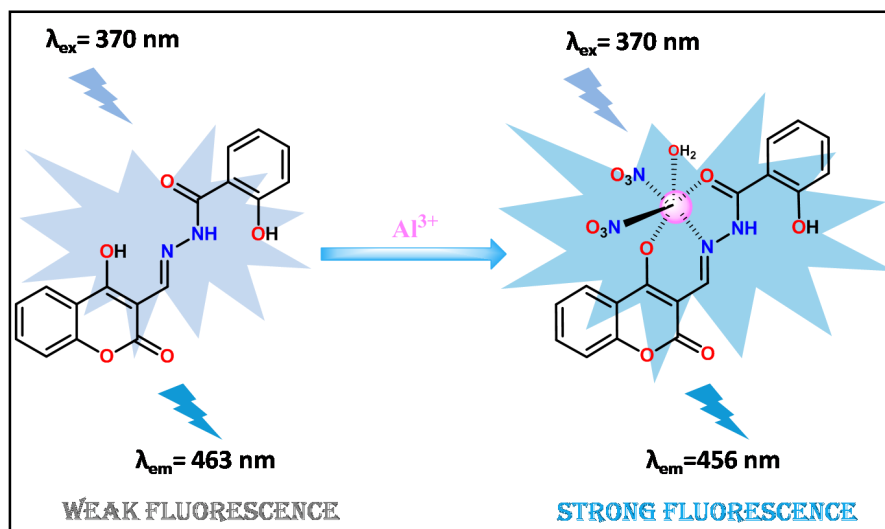


Fig. 6.7: TLC plates after dipping in HMBH-MeOH solution and in HMBH-Al³⁺-MeOH solution under UV compartment. [HMBH] = 2×10^{-4} M, [Al³⁺] = 2×10^{-3} M. Excitation wavelength of the UV light is 370 nm.

6.3.8 Plausible sensing mechanism

The sharp enhancement in the fluorescence intensity of the probe (HMBH), upon addition of Al³⁺ may be accredited to ESIPT turn-off and CHEF (Chelation induced fluorescence) process. When aluminium gets coordinated to HMBH, the hydroxyl proton on coumarin moiety disappears hence ESIPT is turned off. It is also found that in the complex, due to rigid binding with the metal the stiffness of the complex increases which restricts various bond rotations. This restriction of non-radiative processes clarifies the reason of the enhancement in emission intensity of HMBH after addition of aluminium. A plausible binding pattern of HMBH with Al³⁺ is shown in the illustration below (Scheme 6.2).



Scheme 6.2: Sensing mechanism of HMBH.

6.3.9 DFT calculations

To achieve profound knowledge about the electronic structure and electronic transition processes, geometry optimizations of HMBH and HMBH-Al³⁺ utilizing DFT/B3LYP method and TDDFT calculations have been executed. The optimized structures of the HMBH and HMBH-Al³⁺ complex are displayed in Fig. 6.8. The selected highest occupied molecular orbitals (HOMOs) and lowest unoccupied molecular orbitals (LUMOs) of HMBH and HMBH-Al³⁺ are also studied (see appendix). The energies and compositions of chosen molecular orbitals of HMBH-Al³⁺ is summarized in Tables 6.4 (Appendix). The HOMO-LUMO energy gap of HMBH (4.0 eV) is significantly diminished in the HMBH-Al³⁺ (3.67 eV), which is revealed in the shifting of low energy bands in the complexes. Additionally, to understand the electronic transitions, time dependent density functional theory (TDDFT) was utilized in the optimization of the geometries of the compounds. The low energy transition for HMBH at 342 nm ($\lambda_{\text{expt.}}$, 371 nm) corresponds to the HOMO-LUMO transition. For HMBH-Al³⁺ (Table 6.2), the low energy band shifted to 372 nm ($\lambda_{\text{expt.}}$, 367 nm) (Table 6.3- Appendix).

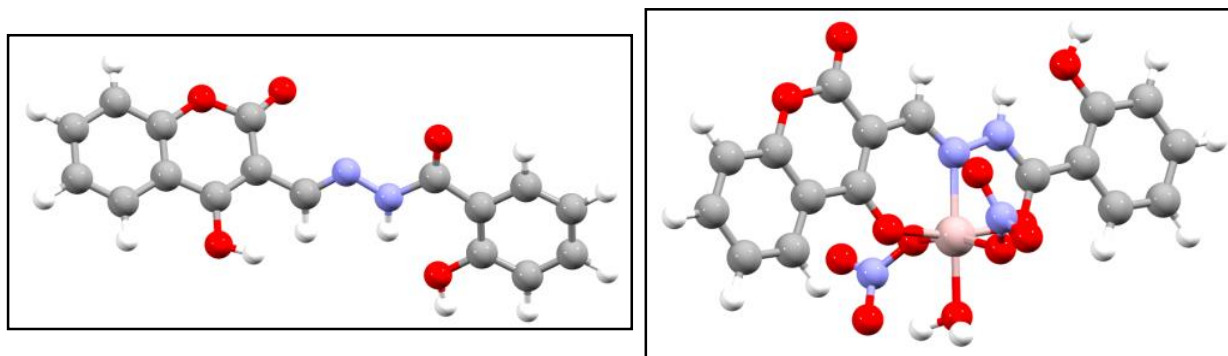


Fig.6.8: Optimized structure of (A) HMBH and (B) HMBH-Al³⁺ complex by DFT/B3LYP/6-31G(d,p) method.

6.4. Experimental

6.4.1 Materials and methods

4-hydroxycoumarin and salicylic acid were purchased from Sigma-Aldrich. Other inorganic salts and solvents were available from commercial suppliers.

Elemental analysis was executed in a 2400 Series-II CHN analyzer, Perkin Elmer, USA. Infrared spectra were recorded on a RX-1 Perkin Elmer spectrophotometer with samples arranged as KBr pellets. HRMS mass spectra were studied using Waters (Xevo G2 Q-TOF) mass spectrometer. Electronic spectral studies were carried out on a PerkinElmer Lambda 750 spectrophotometer. Luminescence property was studied using PerkinElmer LS 55 fluorescence spectrophotometer at room temperature (298 K). NMR spectra were studied and confirmed using a Bruker (AC) 300 MHz FTNMR spectrometer of ~0.05 M solutions of the compounds in CDCl₃ or in DMSO-d₆.

The luminescence quantum yield was calculated using Coumarin-120 laser dye as reference. The excitation wavelength of the compound and the reference dye were same, upholding almost the same absorbance (~0.1), and the emission spectra were recorded. The area of the emission spectrum was integrated with the help of the software accessible in the instrument and the quantum yield was determined according to the following equation:

CHAPTER 6

$$\phi_S/\phi_R = [A_S / A_R] \times [(Abs)_R / (Abs)_S] \times [\eta_S^2/\eta_R^2]$$

Here, ϕ_S and ϕ_R are the luminescence quantum yields of the sample and reference, respectively. A_S and A_R designate the areas under the emission spectra of the sample and the reference respectively, $(Abs)_S$ and $(Abs)_R$ indicate the respective optical densities of the sample and the reference solution at the wavelength of excitation, and η_S and η_R stand for the values of refractive index values for the respective solvent used for the sample and reference.

Fluorescence lifetimes were recorded with the help of a time-resolved spectrofluorometer from IBH, UK. The instrument uses a picoseconds diode laser (NanoLed-03, 370 nm) as the excitation source and the working principle of the instrument is time-correlated single photon counting. The goodness of fit was estimated by χ^2 criterion and visual assessment of the residuals of the fitted function to the data.

6.4.2 Synthesis of 2-hydroxybenzohydrazide (1)

$N_2H_4.H_2O$ (excess) was added to the solution of Methyl salicylate (1 g, 0.66 mmol) in methanol (10 ml). The mixture was stirred for 4 hours in refluxing condition. After cooling at room temperature, methanol was evaporated and water (10 ml) was added to the product and then extracted using dichloromethane (3×20 ml). Then the DCM portion was dried over the anhydrous sodium sulphate and evaporated. The evaporation of the solvent under reduced pressure affords an off-white compound (0.83 g, 83%). The compound is sufficiently pure and used straight for the next step without further purification.

Analytical data for $C_7H_8N_2O_2$: Calc. (%) C 55.31, H 5.26, N 18.36. Found (%), C 55.26, H 5.30, N 18.41.

1H NMR (DMSO- d_6 , 300 MHz): δ 4.68 (s, 2H), 6.82-6.95 (m, 2H), 7.39 (d, $J = 6.0$ Hz 1H), 7.83 (d, $J = 6.0$ Hz, 1H), 10.08 (s, 1H), 12.51 (s, 1H).

HRMS (ESI, positive): m/z , 153.0586 (calculated for $[C_7H_8N_2O_2 + H^+]$), found: 153.1211.

CHAPTER 6

6.4.3 Synthesis of (E)-2-hydroxy-N'-((4-hydroxy-2-oxo-2H-chromen-3-yl)methylene)benzohydrazide (HMBH)

2-hydroxybenzohydrazide(**1**) (0.07 g, 0.48 mmol) was added to the ethanolic solution of 4-chloro-2-oxo-2H-chromene-3-carbaldehyde(**2**) (0.1 g, 0.48 mmol) and the mixture was refluxed for about 9 hours. After the reaction reaches its end point, yellowish product was obtained which was put through to column chromatography furthermore to yield pure bright yellow solid. Yield was, 0.128 g, 80%.

Analytical data for C₁₇H₁₂N₂O₅: Calc. (%) C 62.91, H 3.78, N 8.68. Found (%), C 62.96, H 3.73, N 8.64.

¹H NMR (DMSO-d₆, 300 MHz):δ 6.99 (t, J = 6 Hz, 2H), 7.34 (t, J = 6.0 Hz, 2H), 7.45 (t, J = 6.0 Hz, 1H), 7.68 (t, J = 6.0 Hz, 1H), 7.83 (d, J = 9.0 Hz, 1H), 7.96 (d, J = 9.0 Hz, 1H), 8.72 (s, 1H), 9.95 (s, 1H), 12.54 (s, 1H), 12.62 (s, 1H) .

¹³C NMR (CDCl₃, 75 MHz):δ 97.5, 117.2, 117.3, 120.6, 123.8, 125.3, 128.6, 129.2, 134.5, 154.8, 157.3, 158.4, 161.4.

IR data (KBr, cm⁻¹): 3271 υ(-OH stretch), 3088 υ(-OH stretch), 1679 υ(-C=O stretch), 1617 υ(-C=N stretch), 1550 υ(-NH bending).

HRMS (ESI, positive):*m/z*, 325.0746 (calculated for [C₁₇H₁₂N₂O₅ + H⁺]), found: 325.1012.

6.4.4 General Method for UV-Vis and Fluorescence Titration

6.4.4.1 UV-Vis Method

Stock solution of the probe HMBH (20 μM) was prepared in MeOH/H₂O (1/9, v/v, 10 mM HEPES buffer, pH = 7.2). The solution of the guest cations were arranged utilizing their chloride salts in the order of 40 μM in deionized water. Solutions of diverse concentrations including host and increasing concentrations of cations were organized individually. The changes in UV-Vis spectra of the probe (20 μM) upon steady increasing concentration of cation solutions were recorded.

CHAPTER 6

6.4.4.2 Fluorescence Method

Stock solution of our probe, HMBH (10 μM) was prepared in MeOH/H₂O (1/9, v/v, 10 mM HEPES buffer, pH = 7.2). Fluorescence spectra were studied using chloride salts of different guest cations like Fe³⁺, Cr³⁺, Na⁺, Ca²⁺, Mg²⁺, K⁺, Mn²⁺, Co²⁺, Ni²⁺, Pb²⁺, Cu²⁺, Hg²⁺, Zn²⁺ and Cd²⁺. For competition studies, Al³⁺ (20 μM) solution was added to each of the probe-cation solutions and spectra were studied. The excitation wavelength used was 370 nm.

6.4.4.3 Job's Plot by Fluorescence Method

For Job's plot experiment, a sequence of solutions comprising HMBH (10 μM) and Al³⁺ (20 μM) were arranged in such a manner that the summation of the total metal ion and receptor volume remained invariable (2 ml). Fluorescence spectra was taken at room temperature by plotting ΔF versus mole fraction of Al³⁺ (ΔF = change of intensity of the emission spectrum at 370 nm).

6.4.5 Computational methods

All theoretical calculations were executed with the aid of the Gaussian09 (G09) program [56]. Full geometry optimization of HMBH was executed using the DFT method with Becke's three parameterized Lee-Yang-Parr (B3LYP) exchange functional level [57, 58] with the 6-31+G(d) basis set which was allotted for C, N, H and O atoms. The vertical electronic excitations were observed by means of the time-dependent density functional theory (TDDFT) formalism [59-61] in methanol. The solvent effect was considered by the help of conductor-like polarizable continuum model (CPCM) [62-64] with similar B3LYP level and basis sets. The GaussSum 2.2 was utilized to estimate the contributions of molecular orbitals in electronic transitions [65].

6.5. Conclusions

Herein a coumarin based "turn-on" fluorescence switch (HMBH) was reported which selectively detects Al³⁺ among other cations. All the UV-Vis and emission studies show the desired change that confirmed the sensing property of HMBH. The fluorescence study reveals that HMBH displays a sharp "turn-on" enhancement in the emission intensity with a noteworthy emission leap of about 30

CHAPTER 6

folds. The structure of the fabricated fluorescent switch has also been confirmed by several other elemental analyses and the possible binding modes of the probe with aluminium were also studied through DFT and TDDFT methods. The lower LOD value than WHO level (7.41×10^{-6} M) also corresponds to the fact that HMBH can detect aluminium in very minute level.

6.6. References

1. C. Liang, W. Bu, C. Li, G. Men, M. Deng, Y. Jiangyao, H. Sun, S. Jiang, *Dalton Trans.* 2015, **44**, 11352-11359.
2. H. Wang, B. Wang, Z. Shi, X. Tang, W. Dou, Q. Han, Y. Zhang, W. Liu, *Biosens. Bioelectron.*, 2015, **65**, 91-96.
3. C. Li, J. Qin, G. Wang, B. Wang, A. Fu, Z. Yang, *Inorg. Chim. Acta*, 2015, **430**, 91-95.
4. R. R. Koner, S. Sinha, S. Kumar, C. K. Nandi and S. Ghosh, *Tetrahedron Lett.* 2012, **53**, 2302-2307.
5. S. Sinha, T. Mukherjee, J. Mathew, S. K. Mukhopadhyay, S. Ghosh, *Anal. Chim. Acta*, 2014, **822**, 60-68.
6. Z. Liu, C. Zhang, Y. Li, Z. Wu, F. Qian, X. Yang, W. He, X. Gao, Z. Guo, *Org. Lett.*, 2009, **11**, 795-798.
7. X. Qu, C. Li, H. Chen, J. Mack, Z. Guo, Z. Shen, *Chem. Commun.*, 2013, **49**, 7510-7512.
8. X. Lou, D. Ou, Q. Li, Z. Li, *Chem. Commun.*, 2012, **48**, 8462-8477.
9. Y. Zhou, J. Yoon, *Chem. Soc. Rev.*, 2012, **41**, 52-67.
10. S. Das, S. Guha, A. Banerjee, S. Lohar, A. Sahana, D. Das, *Org. Biomol. Chem.*, 2011, **9**, 7097-7104.
11. V. Amendola, L. Fabbrizzi, F. Forti, M. Licchelli, C. Mangano, P. Pallavicini, A. Poggi, D. Sacchi, A. Taglietti, *Coord. Chem. Rev.*, 2006, **250**, 273-299.
12. K. Rurack, U. Resch-Genger, *Chem. Soc. Rev.*, 2002, **31**, 116-127.
13. P. Nayak, *Environ. Res.*, 2002, **89**, 101-115.
14. N. Fimreite, O. O. Hansen, H. C. Pettersen, *Bull. Environ. Contam. Toxicol.*, 1997, **58**, 1-7.
15. A. Salifoglou, *Coord. Chem. Rev.*, 2002, **228**, 297-317.

CHAPTER 6

16. M. E. Percy, T. P. A. Kruck, A. I. Pogue, W. J. Lukiw, *J. Inorg. Biochem.*, 2011, **105**,1505-1512.
17. G. D. Fasman, *Coord. Chem. Rev.*, 1996,**149**, 125-165.
18. D. Krewski, R. A. Yokel, E. Nieboer, D. Borchelt, J. Cohen, J. Harry, S. Kacew, J. Lindsay, A. M. Mahfouz, V. Rondeau, *J. Toxicol. Environ. HealthPart B*, 2007,**10**, 1-269.
19. Z. Krejpcio, R. W. P. Wojciak, *Pol. J. Environ. Stud.*, 2002,**11**, 251-254.
20. J. Barcelo, C. Poschenrieder, *Environ. Exp. Bot.*, 2002, **48**, 75-92.
21. N. Fimreite, O. O. Hansen, H. C. Pettersen, *Bull. Environ. Contam. Toxicol.*, 1997, **58**, 1-7.
22. D. Maity, T. Govindaraju, *Chem. Commun.*,2010, **46**, 4499-4501.
23. A. Sahana, A. Banerjee, S. Lohar, A. Banik, S. K. Mukhopadhyay, D. A. Safin, M. G. Babashkina, M. Bolte, Y. Garcia, D. Das, *Dalton Trans.*, 2013, **42**, 13311-13314.
24. A. Banerjee, A. Sahana, S. Das, S. Lohar, B. Sarkar, S. K. Mukhopadhyay, A. K. Mukherjee, D. Das, *Analyst*, 2012, **137**, 2166-2175.
25. E. Delhaize, P. Ryan, *Plant Physiol.*, 1995,**107**,315-321.
26. N. A. Muma, S. M. Singer, *Neurotoxicol. Teratol.*, 1996, **18**, 679-690.
27. Y. Z. Zhu, Y. F. Li, L. G. Miao, Y. P. Wang, Y. H. Liu, X. J. Yan, X. Z. Cui, H. T. Li, *Immunotoxicity of aluminum*, 2014,**104**, 1-6.
28. (a) D. R. Crapper, S. S. Krishnan, A. J. Dalton, *Science* ,1973, **180**, 511-513; (b) D. P. Perl, A. R. Brody, *Science*, 1980, **208**, 297-299; (c) E. House, J. Collingwood, A. Khan, O. Korchazkina, G. Berthon, C. Exley, *J. AlzheimersDis.*, 2004, **6**, 291-301.
29. W. F. Forbes, J. F. Gentleman, C. J. Maxwell, *Exp. Gerontol.*, 1995, **30**, 23-32.
30. A. I. Arieff, *Am. J. Kidney Dis.*, 1985,**6**, 317-321.
31. P. F. Good, C. W. Olanow, D. P. Perl, *Brain Res.*, 1992, **593**, 343-346.
32. P. D. Darbre, F. Mannello, C. Exley, *J. Inorg. Biochem.*,2013, **128**, 257-261.
33. J. Barcelo and C. Poschenrieder, *Environ. Exp. Bot.*, 2002,**48**, 75-92.
34. K. K. Upadhyay, A. Kumar, *Org. Biomol. Chem.*, 2010,**8**, 4892-4897.
35. A. Sahana, A. Banerjee, S. Lohar, B. Sarkar, S. K. Mukhopadhyay, D. Das, *Inorg. Chem.*, 2013,**52**, 3627-3633.
36. S. Das, S. Goswami, K. Aich, K. Ghoshal, C. K. Quah, M. Bhattacharyya, H. K. Fun, *New J. Chem.*,2015, **39**,8582-8587.

CHAPTER 6

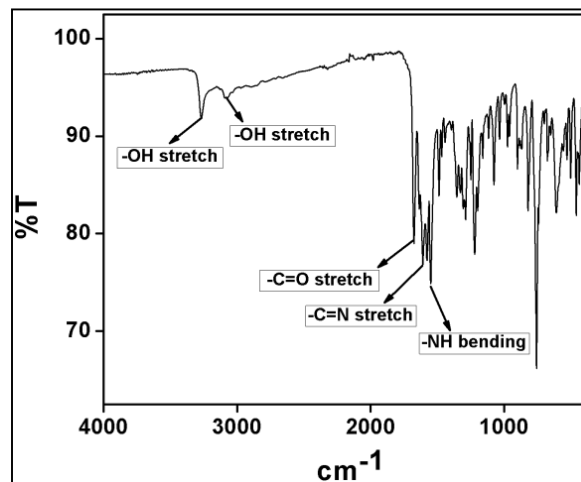
37. S. Das, A. Banerjee, S. Lohar, D. A. Safin, M. G. Bashkina, M. Bolte, Y. Garcia, I. Hauli, S. K. Mukhopadhyay, D. Das, *Dalton Trans.*, 2013, **42**, 4757-4763.
38. S. Kim, J. Y. Noh, K. Y. Kim, H. K. Kang, S. W. Nam, S. H. Kim, S. Park, C. Kim, J. Kim, *Inorg. Chem.*, 2012, **51**, 3597-3602.
39. M. Shellaiah, Y.H. Wu, H.C. Lin, *Analyst*, 2013, **138**, 2931-2942.
40. L.-m. Liu, Z.-y. Yang, *Inorg. Chim. Acta*, 2018, **469**, 588-592.
41. T. Liua, X. Wana, Y. Yao, *Sens. Actuators B*, 2018, **254**, 1094-1100.
42. A. K. Saini, K. Natarajan, S. M. Mobin, *Chem. Commun.*, 2017, **53**, 9870-9873.
43. O. Alici, S. Erdemir, *Sens. Actuators B*, 2015, **208**, 159-163.
44. M. Maniyazagana, R. Mariadasse, M. Nachiappan, J. Jeyakanthan, N. K. Lokanath, S. Naveen, G. Sivaraman, P. Muthuraja, P. Manisankar, T. Stalin, *Sens. Actuators B*, 2018, **254**, 795-804.
45. S. L. Hu, J. J. Song, G. Y. Wu, C. X. Cheng, Q. Gao, *Spectrochim. Acta Part A*, 2015, **136**, 1188-1194.
46. T. H. Ma, M. Dong, Y. M. Dong, Y. W. Wang, Y. Peng, *Chem.-Eur. J.*, 2010, **16**, 10313-10318.
47. I. H. Hwang, Y. W. Choi, K. B. Kim, G. J. Park, J. J. Lee, L. Nguyen, I. Noh and C. Kim, *New J. Chem.*, 2016, **40**, 171-178.
48. G. Balamurugan, S. Velmathi, N. Thirumalaivasan, S. P. Wu, *Analyst*, 2017, **142**, 4721-4726.
49. J. Zhao, Y. Zhao, S. Xu, N. Luo, R. Tang, *Inorg. Chim. Acta*, 2015, **438**, 105-111.
50. P. Torawane, K. Tayade, S. Bothra, S. K. Sahoo, N. Singh, A. Borse, *Sens. Actuators B*, 2016, **222**, 562-566.
51. G. T. Selvan, M. Kumaresan, R. Sivaraj, I. V. M. V. Enoch, *Sens. Actuators B*, 2016, **229**, 181-189.
52. M. Mukherjee, B. Sen, S. Pal, A. Maji, D. Budhadev, P. Chattopadhyay, *Spectrochim. Acta Part A*, 2016, **157**, 11-16.
53. L. K. Kumawat, N. Mergu, M. Asif, V. K. Gupta, *Sens. Actuators B*, 2016, **231**, 847-859.
54. T. Liua, X. Wana, Y. Yao, *Sens. Actuators B*, 2018, **254**, 1094-1100.
55. G. Bartwal, K. Aggarwal, J. M. Khurana, *New J. Chem.*, 2018, **42**, 2224-2231.

CHAPTER 6

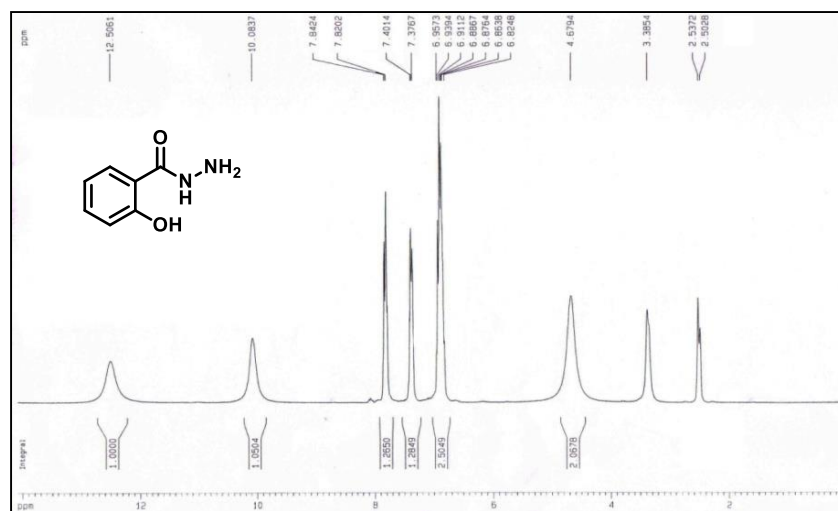
56. Gaussian 09, Revision D.01, M. J. Frisch, G. W. Trucks, H. B. Schlegel, G. E. Scuseria, M. A. Robb, J. R. Cheeseman, G. Scalmani, V. Barone, B. Mennucci, G. A. Petersson, H. Nakatsuji, M. Caricato, X. Li, H. P. Hratchian, A. F. Izmaylov, J. Bloino, G. Zheng, J. L. Sonnenberg, M. Hada, M. Ehara, K. Toyota, R. Fukuda, J. Hasegawa, M. Ishida, T. Nakajima, Y. Honda, O. Kitao, H. Nakai, T. Vreven, J. A. Montgomery, Jr., J. E. Peralta, F. Ogliaro, M. Bearpark, J. J. Heyd, E. Brothers, K. N. Kudin, V. N. Staroverov, R. Kobayashi, J. Normand, K. Raghavachari, A. Rendell, J. C. Burant, S. S. Iyengar, J. Tomasi, M. Cossi, N. Rega, J. M. Millam, M. Klene, J. E. Knox, J. B. Cross, V. Bakken, C. Adamo, J. Jaramillo, R. Gomperts, R. E. Stratmann, O. Yazyev, A. J. Austin, R. Cammi, C. Pomelli, J. W. Ochterski, R. L. Martin, K. Morokuma, V. G. Zakrzewski, G. A. Voth, P. Salvador, J. J. Dannenberg, S. Dapprich, A. D. Daniels, Ö. Farkas, J. B. Foresman, J. V. Ortiz, J. Cioslowski, and D. J. Fox, *Gaussian Inc.*, 2009, Wallingford CT.
57. A. D. Becke, *J. Chem. Phys.*, 1993, **98**, 5648-5652.
58. C. Lee, W. Yang, R.G. Parr, *Phys. Rev. B*, 1988, **37**, 785-789.
59. R. Bauernschmitt, R. Ahlrichs, *Chem. Phys. Lett.*, 1996, **256**, 454-464.
60. R. E. Stratmann, G. E. Scuseria, M. J. Frisch, *J. Chem. Phys.*, 1998, **109**, 8218-8224.
61. M. E. Casida, C. Jamorski, K. C. Casida, D. R. Salahub, *J. Chem. Phys.*, 1998, **108**, 4439-4449.
62. V. Barone, M. Cossi, *J. Phys. Chem. A*, 1998, **102**, 1995-2001.
63. M. Cossi, V. Barone, *J. Chem. Phys.*, 2001, **115**, 4708-4717.
64. M. Cossi, N. Rega, G. Scalmani, V. Barone, *J. Comput. Chem.*, 2003, **24**, 669-681.
65. N. M. O'Boyle, A. L. Tenderholt, *J. Comput. Chem.*, 2008, **29**, 839-845.

APPENDIX

CHAPTER 6

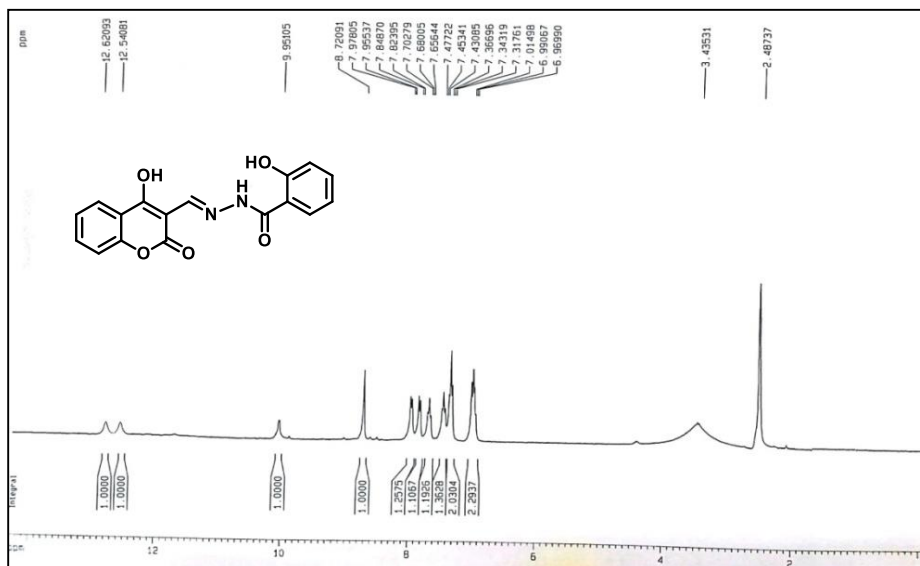


IR spectrum of **HMBH** in KBr disk

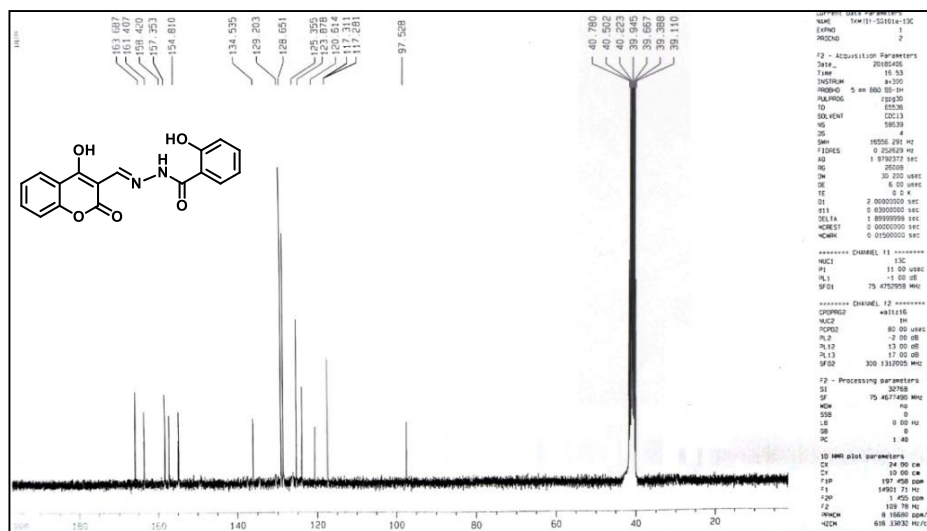


¹H-NMR (300 MHz) spectra of **Compound 1** in DMSO-d₆

CHAPTER 6

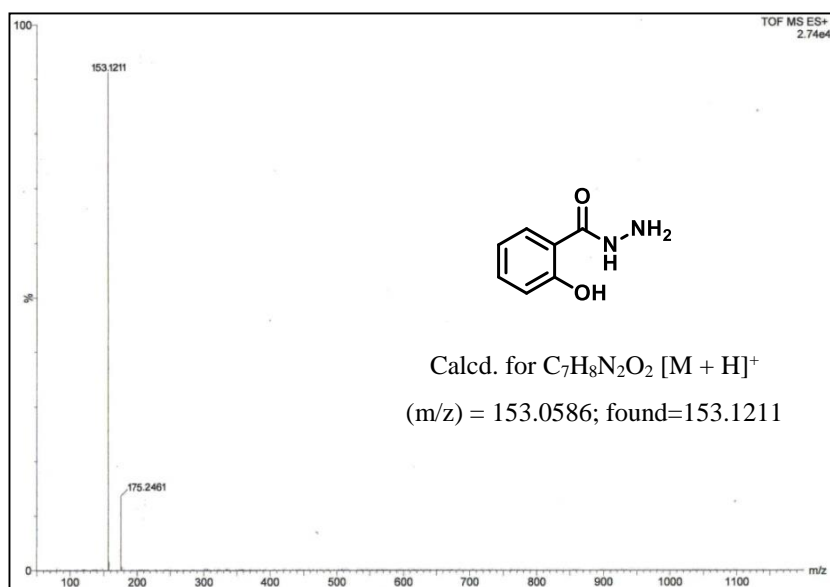


¹H-NMR (300 MHz) spectra of HMBH in DMSO-d₆

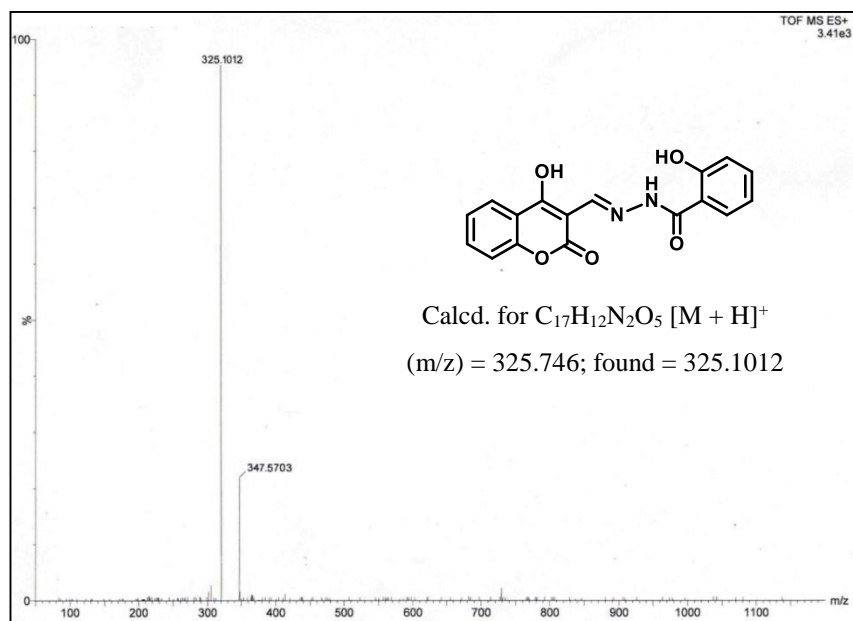


¹³C-NMR (75 MHz) spectra of HMBH in DMSO-d₆

CHAPTER 6

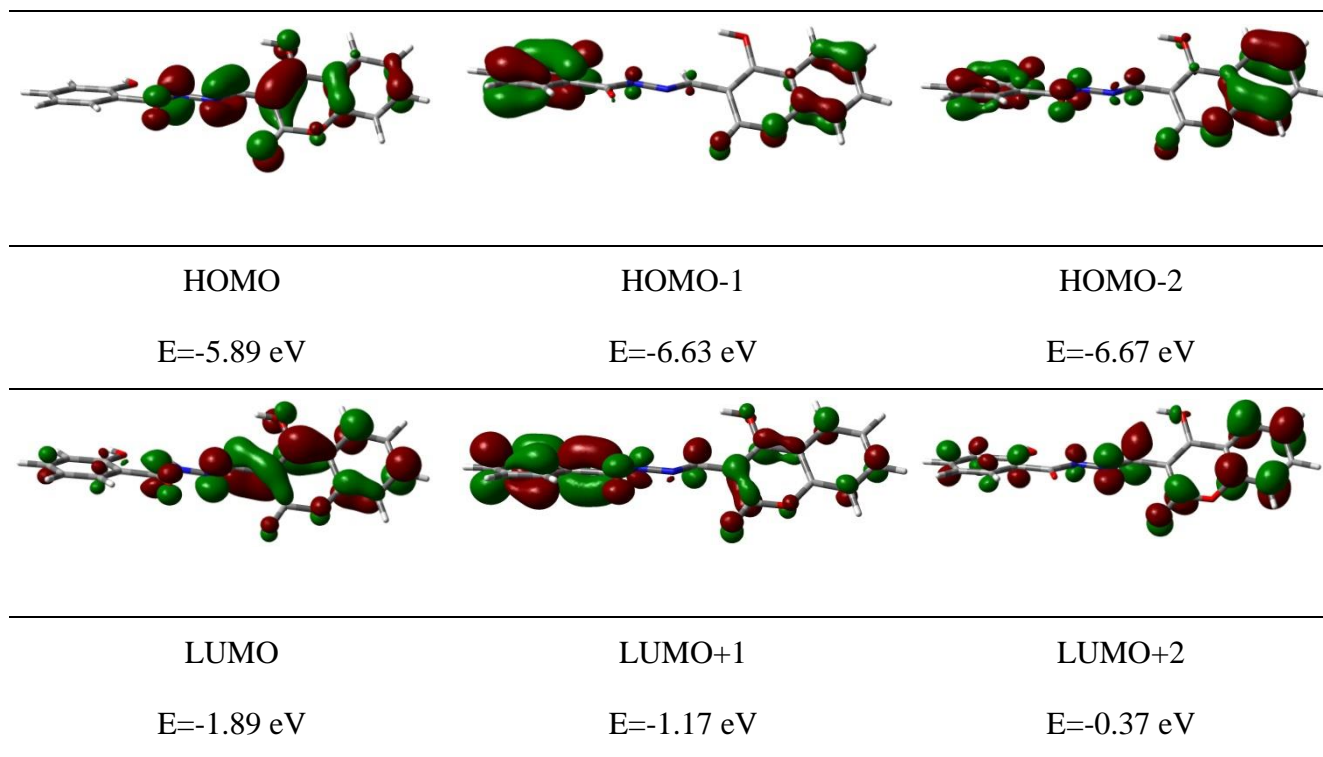


HRMS spectra of the **Compound 1**



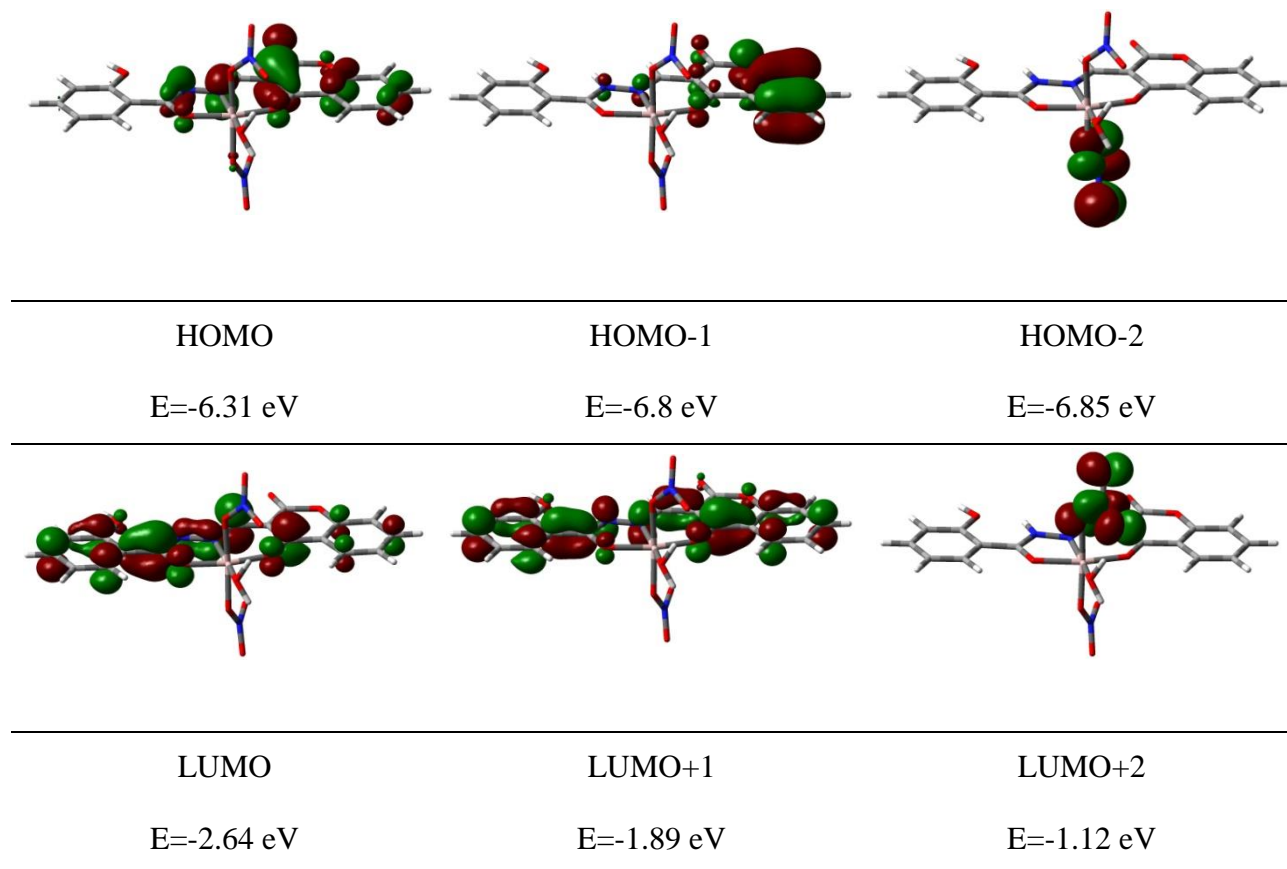
HRMS spectra of the receptor **HMBH**

CHAPTER 6



Contour plots of some selected molecular orbitals of HMBH

CHAPTER 6



Contour plots of some selected molecular orbitals of HMBH-Al³⁺

Table 6.2: Vertical electronic transitions calculated by TDDFT/B3LYP/CPCM method for HMBH

Energy (eV)	Wavelength (nm)	Osc. strength (f)	Key transitions	Character
3.6181	342.67	0.9506	(97%) HOMO→LUMO	$\pi(L) \rightarrow \pi^*(L)$
4.0689	304.71	0.0116	(92%) HOMO-1→LUMO	$\pi(L) \rightarrow \pi^*(L)$
4.2062	294.77	0.0786	(85%) HOMO-2→LUMO	$\pi(L) \rightarrow \pi^*(L)$

CHAPTER 6

4.3285	286.44	0.0304	(85%) HOMO→LUMO+1	$\pi(\text{L}) \rightarrow \pi^*(\text{L})$
4.4113	281.06	0.0124	(70%) HOMO-4→LUMO	$\pi(\text{L}) \rightarrow \pi^*(\text{L})$

Table 6.3: Vertical electronic transitions calculated by TDDFT/B3LYP/CPCM method for HMBH-Al³⁺ adduct

Energy (eV)	Wavelength (nm)	Osc. strength (f)	Key transitions	Character
3.3307	372.25	0.8924	(98%) HOMO→LUMO	$\pi(\text{L}) \rightarrow \pi^*(\text{L})$
3.7768	328.27	0.0547	(78%) HOMO-1→LUMO	$\pi(\text{L}) \rightarrow \pi^*(\text{L})$
3.8838	319.24	0.0300	(77%) HOMO-2→LUMO	$\pi(\text{L}) \rightarrow \pi^*(\text{L})$
4.1236	300.67	0.0028	(70%) HOMO→LUMO+2	$\pi(\text{L}) \rightarrow \pi^*(\text{L})$
4.6075	269.09	0.0358	(75%) HOMO-1→LUMO+1	$\pi(\text{L}) \rightarrow \pi^*(\text{L})$

CHAPTER 6

Table 6.4: Energy and compositions of some selected molecular orbitals of HMBH-Al³⁺

MO	Energy (eV)	% of composition	
		Al	HMBH
LUMO+5	-0.57	2	98
LUMO+4	-0.69	1	99
LUMO+3	-0.9	0	100
LUMO+2	-1.12	2	98
LUMO+1	-1.89	0	100
LUMO	-2.64	0	100
HOMO	-6.31	0	100
HOMO-1	-6.8	0	100
HOMO-2	-6.85	1	99
HOMO-3	-7.4	1	99
HOMO-4	-7.43	0	100
HOMO-5	-7.53	0	100
HOMO-6	-7.59	0	100
HOMO-7	-7.78	0	100
HOMO-8	-8.08	0	100
HOMO-9	-8.17	0	100
HOMO-10	-8.26	1	99

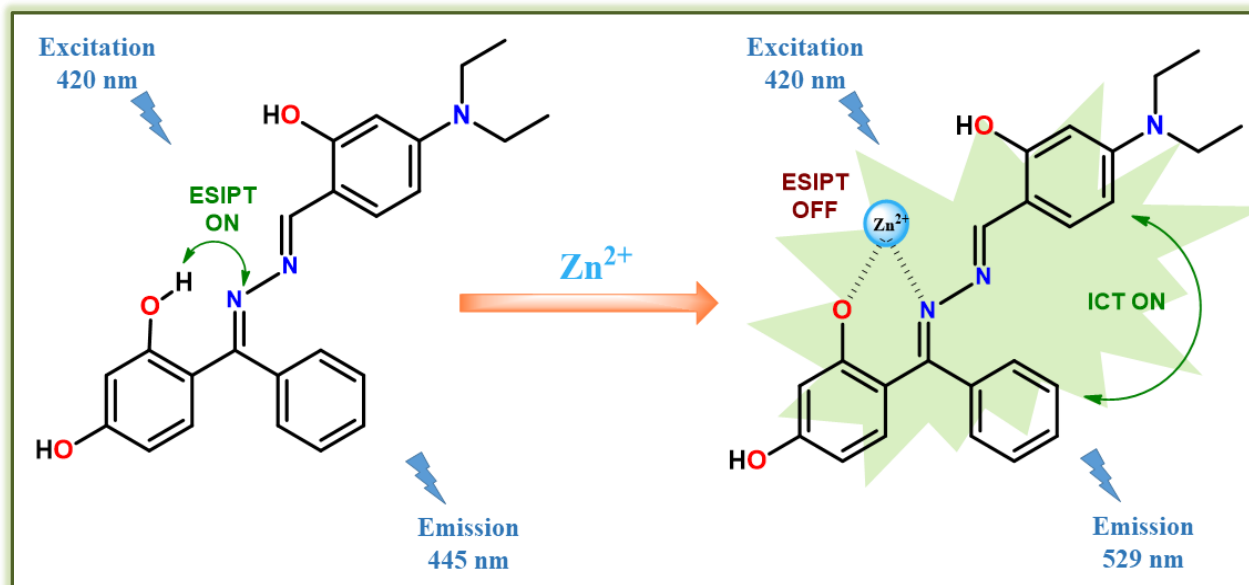
A new ESIPT-ICT mediated dual channel fluorescence “turn-on” switch for selective and sequential detection of Zn²⁺

CHAPTER 7

A new ESIPT-ICT mediated dual channel fluorescence “switch-on” probe for specific detection of Zn²⁺

Abstract

A highly fluorescent probe (HBSA) was synthesized and characterized by varieties of spectroscopic techniques. Fluorescence titration clearly states that HBSA acts as a “turn-on” fluorescent probe for the detection of Zn²⁺ with slight blue shift in emission intensity in MeOH/H₂O (1/1, v/v, pH=7.2) solution over other analytes. Though there is hardly any change in emission intensity observed in case of others. The limit of detection is in the order of 10⁻⁹ M for Zn²⁺ which clearly indicates high efficiency of HBSA in detecting them in minute quantity. DFT and TDDFT calculations are done to interpret electronic structure and sensing mechanism.



7.1. Introduction

Zinc gathers its maximum attention probably as the second most significant nutrient after Vitamin D among the several note worthy trace elements in our body, appearing in the enzymes circulated all over the human body.[1-3] Compounds derived from zinc are broadly utilized in medical grounds as anticancer agents, radio-protective agents, tumor photosensitizers and insulin mimetic to fight diabetes mellitus. Besides, zinc performs numerous roles in human physiopathology. [4-7] Moreover the additional Zn^{2+} ions existing in water and soil may diminish the microbial activity of soil, triggering phytotoxic effect thereby resulting in muddy and smelly water. [5,8] Zinc being the second most abundant and essential element among the physiologically vital trace elements in human body has drawn much attention due to its crucial and active role in various biological processes like gene transition, oxygen transport, neural signal transmission, cellular metabolism and apoptosis [9-11]. Although a deficiency of zinc in human body can cause an uncontrolled metabolism which actually can stimulate high blood cholesterol and various neurological diseases such as Alzheimer's disease, Parkinson's disease, ischemic stroke, infantile diarrhea and epilepsy [12-14] As per the WHO rules, the allowed limit of Zn^{2+} consumption in drinking water is 76 μM . [15] Besides Zn^{2+} regulates brain excitability and acts as a crucial factor in synaptic plasticity. [16, 17] In addition, an excess of zinc in the environment may reduce the soil microbial activity thereby acting as a pollutant. [18, 19] For these reasons, the scheme and fabrication of a selective and non-interfering method to detect free zinc ions is still extremely desirable.

Fluorescent probes are generally designed in such a fashion that the fluorescence response they show is caused by some proposed mechanisms such as intermolecular charge transfer (ICT) [20-22], excited-state intramolecular proton transfer (ESIPT) [23], chelation-induced enhanced fluorescence (CHEF) [24], photo-induced electron transfer (PET) [25], excimer/exciplep formation [26, 27] and fluorescence resonance energy transfer (FRET). [28-30] Among them, ESIPT mediated probes can exhibit large stroke shifts and brilliant light stability owing to its keto-enol tautomerism. [31, 32] On the other hand, the ICT mechanism would cause blue shift of the emission

CHAPTER 7

spectra of the probe as it binds with metal ions thereby causing adequate enhancement in the emission profile.

7.2. Basis of present work

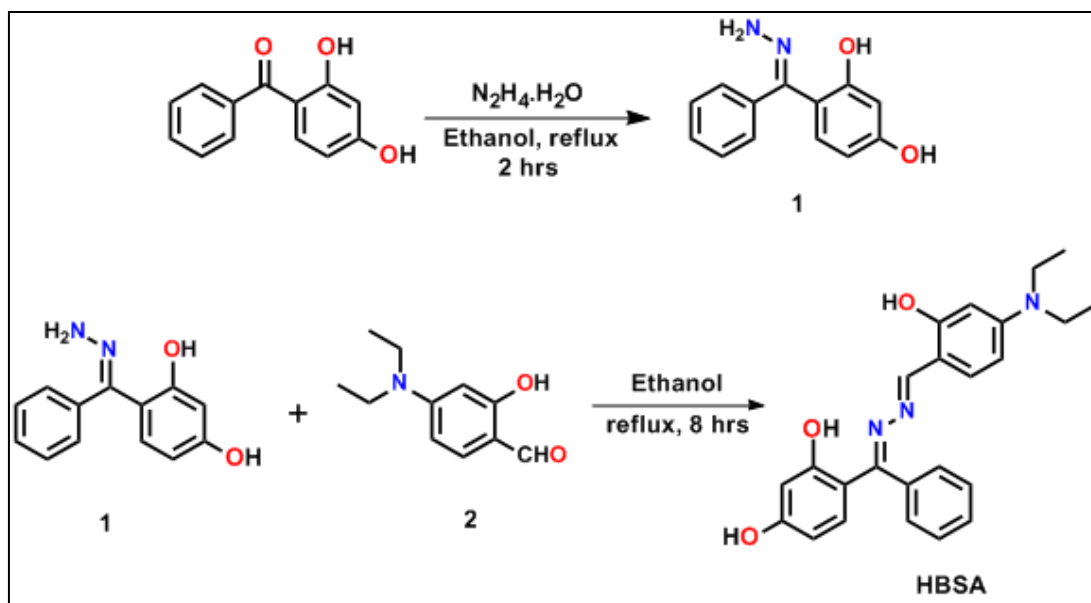
During the last few decades, several analytical tools have been reported for the exploration of ions. Among these methods, detection of ions by a colorimetric and fluorescent technique has been of a great attraction owing to its advantages of selective sensing, high sensitivity and easy modus operandi. [33-35] Due to the high demand of zinc sensors, many fluorescent probes were being reported, mainly based on Schiff bases, polythiacrown ethers etc. [36-42] Although in most of the report, the detections have suffered from the interference of Cd^{2+} and sometimes from Ca^{2+} . [43-50] Schiff base fluorescent sensors have attracted several researchers' attention owing to their simple synthetic route with diverse singular structures and cost effective precursor materials. [51,52-56] In spite of low yields in various circumstances and tiresome workup procedure, Schiff bases have several advantages, comprising high sensitivity, low price, rapid detection and easy-to-synthesize protocol. [57,58] Schiff bases can be useful as a chelating agent for the recognition of numerous metal ions. The foremost disadvantage of some previous procedures like ICP-AES and ICP-MS is they identify total metal ions without oxidation state and proper environment of coordination state along with the much expensive, time consuming, low infrastructural backup and high skill necessities for any operation which greatly restricted their application for routine analysis of countless samples. [59-61] So, in this consequence, in pursuit of precise sensitivity, easy-to-use, low cost and experimental effortlessness, we design and present a simple new fluorescent probe, HBSA showing distinctive 'turn-on' emission properties for Zn^{2+} . Synthetic route towards our target molecule, HBSA simply involves the schiff base condensation of (E)-4-(hydrazono(phenyl)methyl)benzene-1,3-diol (**1**) with 4-(diethylamino) salicylaldehyde (**2**) in ethanol solvent under refluxing condition. Fluorescence titration reveals that HBSA acts as a "turn-on" fluorescent probe for the detection of Zn^{2+} in MeOH/H₂O (1/1, v/v, pH = 7.2) solution. The sensing capacity of the developed sensor (HBSA) in presence of other cations and anions in MeOH/H₂O (1/1, v/v, pH = 7.2) solution are also studied but there is hardly any change in emission intensity observed in case of other ions.

CHAPTER 7

7.3. Results and discussions

7.3.1 Synthesis of HBSA

The synthetic route of HBSA is portrayed in Scheme 7.1. The chemical structures of HBSA and its Zn^{2+} complex is confirmed by 1H and ^{13}C NMR spectroscopy and ESI mass spectroscopic techniques (See appendix).



Scheme 7.1: Synthesis of chemosensor HBSA.

7.3.2 Spectral characterization and analysis of HBSA

1H -NMR spectra are recorded in $DMSO-d_6$ for **compound 1** whereas in $CDCl_3$ for **HBSA**. In case of the former, a singlet at δ 5.95 ppm is observed which is due to the presence of $-NH_2$ proton. The aromatic ring protons appear as expected in the region of δ 6.09-7.54 ppm. The two singlets for the two $-OH$ protons appear at δ 10.69 and 12.92 ppm respectively. In case of **HBSA**, the three $-OH$ protons appear at δ 10.72, 11.09 and 13.57 ppm respectively as singlets while the other singlet at

CHAPTER 7

δ 1.13 ppm accounts for the presence of six $-\text{CH}_3$ protons and another singlet at δ 3.32 ppm appears for four $-\text{CH}_2$ protons. The aromatic protons appear at the range of δ 6.05-8.45 ppm. ^{13}C -NMR spectra is recorded in CDCl_3 for **HBSA**. FT-IR spectrum of **compound 1** taken in KBr disk and exhibits bands at 3338 and 3258 cm^{-1} which is due to the free $-\text{OH}$ group stretches. The absorption band at 1620 cm^{-1} is due to the presence of $\text{C}=\text{N}$ stretching. The band at 2915 cm^{-1} indicates the presence of $\text{C}-\text{H}$ stretch in compound 1. Similarly, in case of **HBSA**, the IR spectrum which was also taken in KBr disk shows 3528 and 3329 cm^{-1} owing to the free $-\text{OH}$ stretches. The band at 3061 cm^{-1} confirms the presence of $=\text{C}-\text{H}$ stretch. The band at 2972 cm^{-1} indicates the presence of $\text{C}-\text{H}$ stretch and 1637 cm^{-1} accounts for the $\text{C}=\text{N}$ stretch present as the imine group in **HBSA**. Mass spectrum shows a peak corresponding to $[\text{Compound1}-\text{H}^+]$ at (m/z) 229.1097 for compound 1 whereas the probe, HBSA shows a strong peak at 404.1244 corresponding to $[\text{HBSA}+\text{H}^+]$.

7.3.3 Cation sensing studies: UV-Vis spectroscopy studies

The probe HBSA (10 μM) shows a strong absorbance band at 414 nm and at 265 nm in $\text{MeOH}:\text{H}_2\text{O}$ (1/1, v/v) using 10 mM HEPES buffered solution at $\text{pH} = 7.2$. Gradual addition of Zn^{2+} into the probe solution showed a decrease of the band at 414 nm to 431 nm with two new band formations at 333 nm and 465 nm (Fig. 7.1a). Two distinct isosbestic points were observed at 371 nm and 444 nm respectively. The changes of UV-Vis spectrum of HBSA are also studied in presence of other cations like Na^+ , K^+ , Ca^{2+} , Mg^{2+} , Mn^{2+} , Fe^{3+} , Cr^{3+} , Al^{3+} , Co^{2+} , Ni^{2+} , Cu^{2+} , Cd^{2+} and Hg^{2+} (Fig. 7.1b).

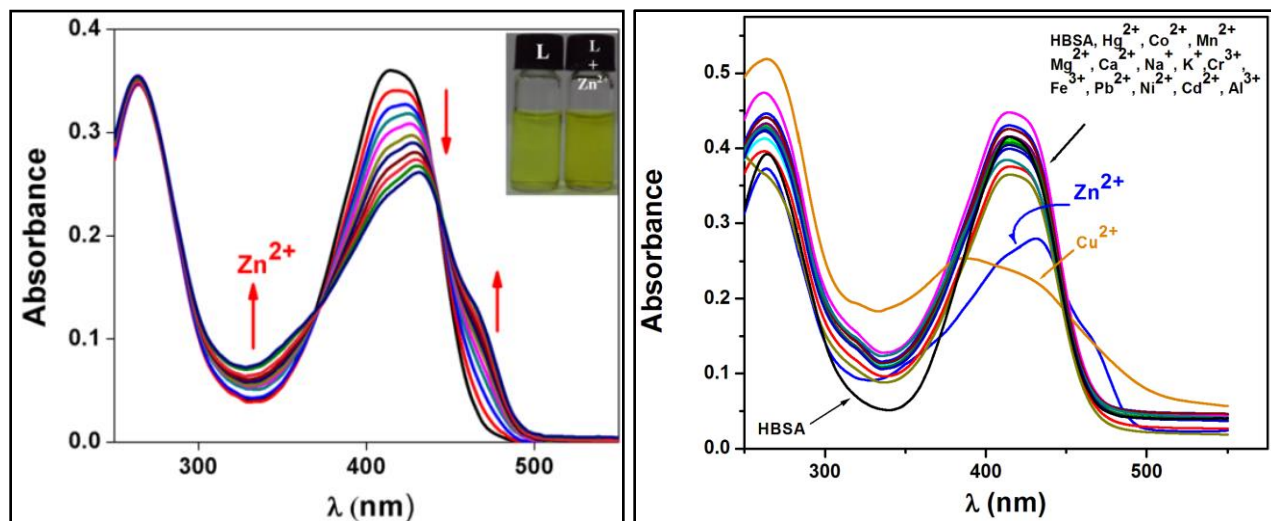


Fig. 7.1:(a) Change in UV-Vis spectrum of HBSA (10 μM) upon gradual addition of Zn^{2+} (40 μM) in $\text{MeOH}/\text{H}_2\text{O}$ (1/1, v/v) using HEPES buffered solution at $\text{pH}=7.2$ and (b) UV-Vis spectra of chemosensor (HBSA) (20 μM) upon addition of 2 equivalent of various cations i.e., Na^+ , K^+ , Ca^{2+} , Mg^{2+} , Mn^{2+} , Fe^{3+} , Cr^{3+} , Al^{3+} , Co^{2+} , Ni^{2+} , Cu^{2+} , Cd^{2+} and Hg^{2+} (40 μM) in $\text{MeOH}/\text{H}_2\text{O}$ (1/1, v/v) using HEPES buffered solution at $\text{pH}=7.2$.

7.3.4 Cation sensing studies: Fluorescence emission studies

In the absence of the ions, the emission spectrum of the probe exhibits a band with moderately weak emission intensity with the maxima (F_0) appearing at 545 nm ($\lambda_{\text{excitation}}$, 420 nm) in $\text{MeOH}/\text{H}_2\text{O}$ (1/1, v/v) with an emission quantum yield (f) of 0.01. Upon addition of Zn^{2+} to the probe solution, an emission maximum was observed at 529 nm having a blue shift with a sharp increase in emission intensity having emission quantum yield, $\phi = 0.29$ (Fig. 7.2).

CHAPTER 7

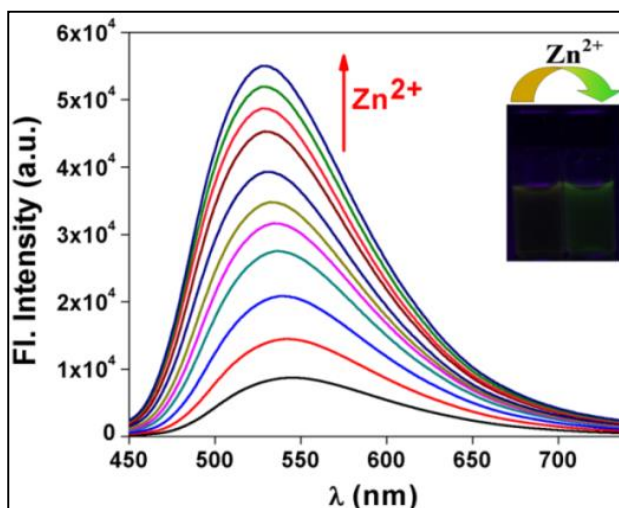


Fig. 7.2: Change in emission spectrum of HBSA (10 μM) upon gradual addition of Zn^{2+} (40 μM) in MeOH/ H_2O (1/1, v/v). Inset shows effect of addition of Zn^{2+} to HBSA upon UV radiation

The sensing capacity of the developed probe for Zn^{2+} in presence of other respective cations in MeOH/ H_2O (1/1, v/v) are also studied (Fig. 7.3a) but there is hardly any change in emission intensity of HBSA. To investigate the selectivity of HBSA for Zn^{2+} , interference experiment is carried out by recording the emission intensity of HBSA (10 μM) in presence of other cations like Na^+ , K^+ , Ca^{2+} , Mg^{2+} , Mn^{2+} , Fe^{3+} , Cr^{3+} , Al^{3+} , Co^{2+} , Ni^{2+} , Cu^{2+} , Cd^{2+} and Hg^{2+} (20 μM) before the addition of Zn^{2+} (Fig. 7.3b) in MeOH/ H_2O (1/1, v/v, pH=7.2) respectively. It is observed that the various competitive ions do not cause any significant interference for Zn^{2+} .

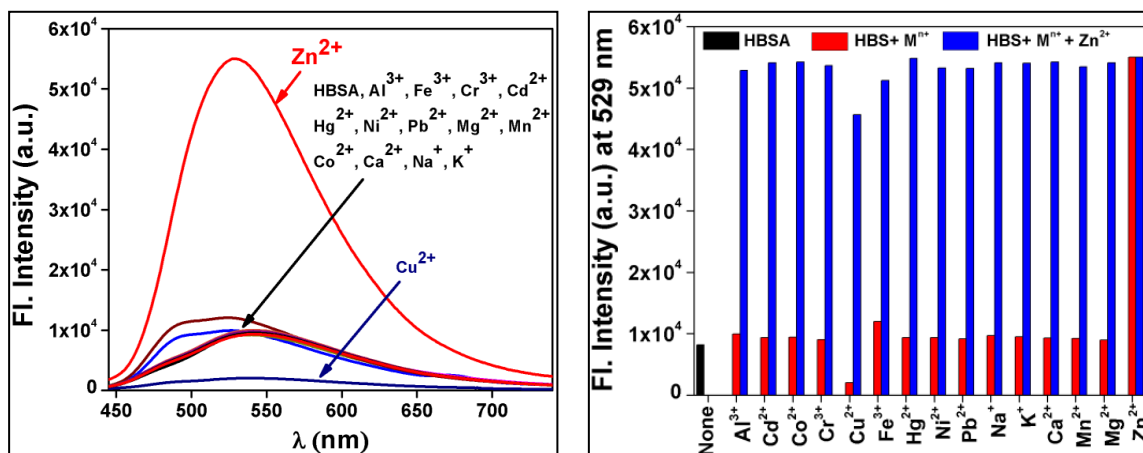


Fig. 7.3:(a)Emission intensity of HBSA (10 μM) upon addition of other cations like Na^+ , K^+ , Ca^{2+} , Mg^{2+} , Mn^{2+} , Pb^{2+} , Fe^{3+} , Cr^{3+} , Al^{3+} , Co^{2+} , Ni^{2+} , Cu^{2+} , Cd^{2+} and Hg^{2+} (40 μM) in $\text{MeOH}/\text{H}_2\text{O}$ (1/1, v/v) (pH=7.2) and (b)Emission intensity of HBSA (20 μM) (black bar). Upon addition of Na^+ , K^+ , Ca^{2+} , Mg^{2+} , Mn^{2+} , Fe^{3+} , Cr^{3+} , Al^{3+} , Co^{2+} , Ni^{2+} , Cu^{2+} , Cd^{2+} and Hg^{2+} (40 μM) in $\text{MeOH}/\text{H}_2\text{O}$ (1/1, v/v) (pH=7.2) (red bars). Zn^{2+} (40 μM) in presence of other cations (blue bars)

7.3.5 Binding studies of HBSA with Zn^{2+}

Mole ratio plot obtained from the emission study indicates that the probe, HBSA shows an increase in emission intensity till the ratio of HBSA- Zn^{2+} reach at ~ 1 , after that there is hardly any increase in emission intensity (Fig. 7.4a). Job's plot analysis was carried out which revealed that the maxima appears at a mole fraction of 0.5 for HBSA- Zn^{2+} thereby establishing the fact that HBSA is bonded to Zn^{2+} in 1:1 complex formation (Fig. 7.4b). From the emission spectra, the detection limit of HBSA for Zn^{2+} is ascertained. The equation $\text{LOD} = K \times \text{SD}/S$ is used, where SD is the standard deviation of the blank solution and S is the slope of the linear response curve. The limit of detection for Zn^{2+} is found to be 3.07×10^{-9} M (Fig. 7.5a) which clearly demonstrates that the probe is highly efficient in sensing Zn^{2+} even in very minute level. The plot shows a good linear relationship suggesting 1:1 complex formation of HBSA with both Zn^{2+} with $R = 0.989$. The binding constant

CHAPTER 7

K_a is determined from the ratio of intercept and slope of Benesi-Hildebrand plot. Plot of $1/[F-F_0]$ vs. $1/[Zn^{2+}]$ gives a straight line indicating 1:1 complexation between HBSA and Zn^{2+} . So from fluorescent spectral titration the association constant of HBSA with Zn^{2+} is found to be $6.48 \times 10^4 M^{-1}$ (Fig. 7.5b).

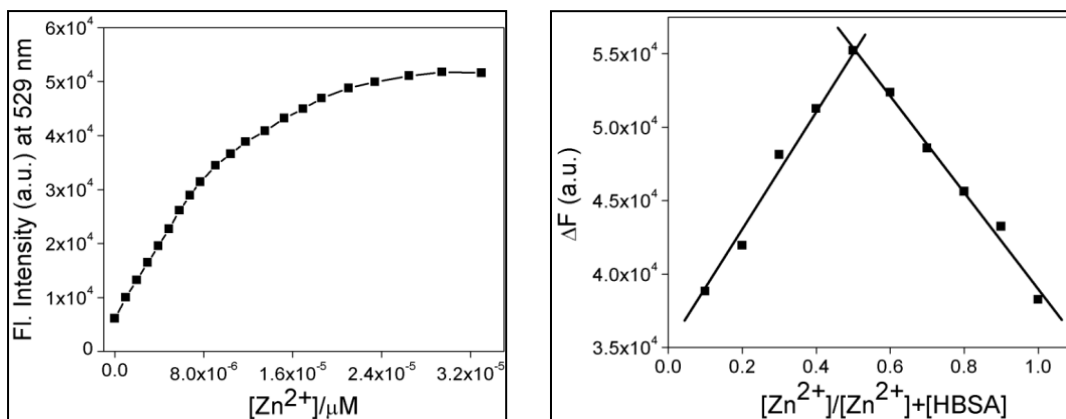


Fig. 7.4: (a) Mole ratio plot of HBSA for Zn^{2+} and (b) Job's plot diagram of the receptor (HBSA) for Zn^{2+} (where ΔF indicates the change of emission intensity at 529 nm)

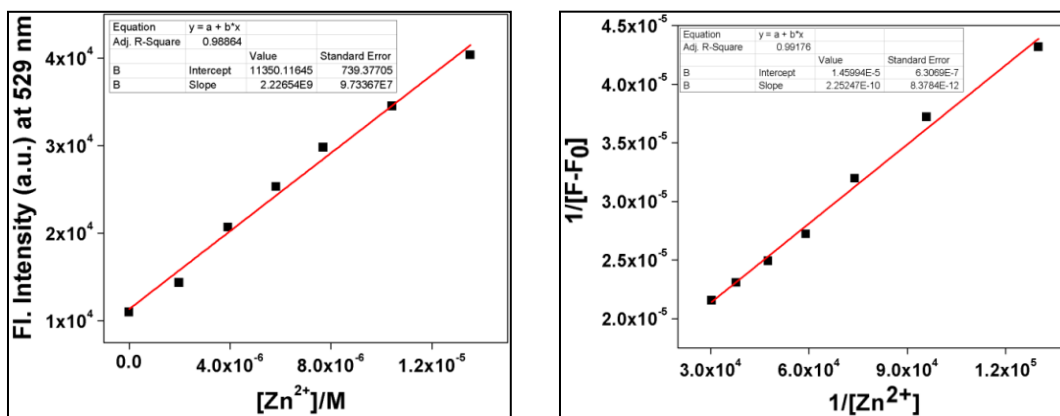


Fig. 7.5: (a) Linear response curve of HBSA at 529 nm depending on the Zn^{2+} concentration and (b) Determination of association constant of HBSA for Zn^{2+} from fluorescent titration data

7.3.6 Effect of pH on emission properties

The effect of pH on the emission intensity of the probe (HBSA) in absence and presence of Zn^{2+} is studied. In case of HBSA, emission intensity increases in the pH range of 2-4 but on pH 5.7, there is a sharp decrease in the emission intensity of HBSA which on further increase of pH shows almost no change. Now on addition of Zn^{2+} the fluorescent intensity sharply increases in the pH range of almost 2-6. On further increasing pH in the range of 7-10, the fluorescence intensity remains almost same (Fig. 7.6).

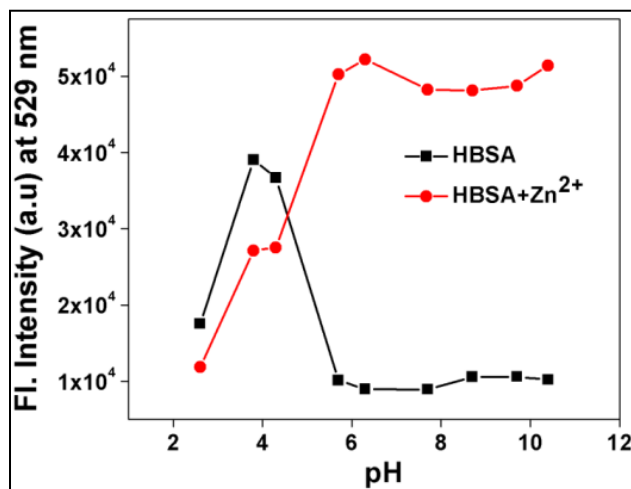


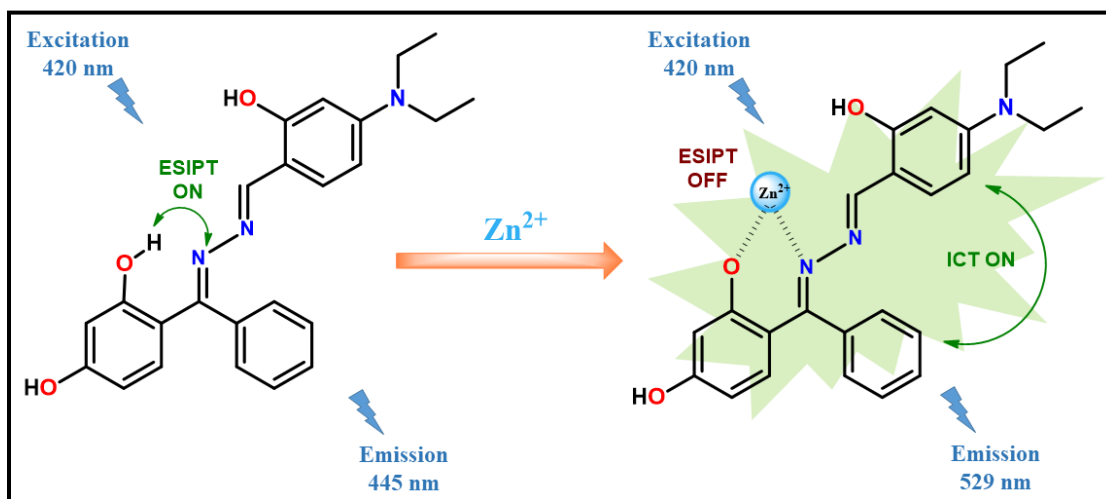
Fig. 7.6: pH dependence of fluorescence intensity of HBSA and after addition of Zn^{2+}

7.3.7 Probable sensing mechanism

Upon gradual addition of Zn^{2+} to the solution of HBSA, an emission maximum was blue shifted at 529 nm with a sharp increase in emission intensity. The enhancement in the emission intensity of HBSA after addition of Zn^{2+} may be attributed to the mechanism named ESIPT (Excited state intramolecular proton transfer) process [62]. At first, HBSA itself exhibited slightly moderate emission intensity as ESIPT was 'on' as the transferable hydrogen remained free and could be transferred to give two desired 'keto-enol' tautomers (Scheme 7.2). But after incorporation of Zn^{2+} ,

CHAPTER 7

as it binds to HBSA, the tautomerization gets inhibited thereby ‘switching off’ the ESIPT process which accounts for the enhancement and blue shift in emission intensity. This blue shift may also be due to the internal charge transfer (ICT).



Scheme 7.2: Sensing mechanism of HBSA.

7.3.8 DFT calculations

To explain the electronic structure and electronic transition processes, geometry optimizations of HBSA and its complex with Zn²⁺ using DFT/B3LYP method and TDDFT calculations have been carried out on the optimized geometries. The optimized structures of HBSA and HBSA-Zn²⁺ are shown in Fig. 7.7a and Fig. 7.7b. All the contour plots of the HOMO and LUMO of HBSA and HBSA-Zn²⁺ are summarized (see appendix). The HOMO-LUMO gap of HBSA is decreased from 3.56 eV to 3.29 eV in the Zn²⁺ complex which suggests the shifting of low energy band in the complex thereby indicating to the fact that a new band was formed at longer wavelength after addition of Zn²⁺ into HBSA solution which was due to the HBSA-Zn²⁺ complex formation. The intense band at 414 nm in methanol for HBSA corresponds to HOMO → LUMO transition (calculated $\lambda = 417$ nm, $f = 1.41$) (Table 7.1), while the HOMO → LUMO transition for the HBSA-Zn²⁺ complex is obtained at 433 nm ($f = 1.10$) (Table 7.2) corresponding to the experimental absorption band 431 nm in methanol.

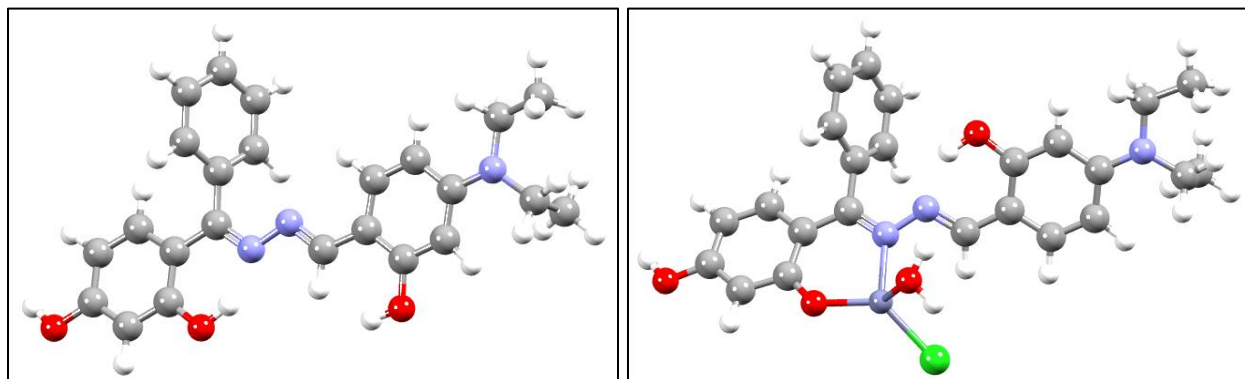


Fig.7.7: Optimized structure of (A) HBSA and (B) HBSA-Zn²⁺ complex by DFT/B3LYP/6-31G(d,p) method.

7.4. Experimental

7.4.1 Materials and methods

4-(diethylamino)salicylaldehyde and (2,4-dihydroxyphenyl)(phenyl)methanone were purchased from Sigma-Aldrich. All other organic chemicals and inorganic salts were available from commercial suppliers and used as it is without any further purification.

7.4.2 Synthesis of (E)-4-(hydrazono(phenyl)methyl)benzene-1,3-diol (**1**)

N₂H₄.H₂O (excess) was added to the solution of (2,4-dihydroxyphenyl)(phenyl)methanone (1.0 g, 4.66 mmol) in ethanol (10 ml). The mixture was stirred for 2 hour in refluxing condition. After cooling at room temperature, the solvent was evaporated under reduced pressure and water (10 ml) was added to the crude product and extracted the organic part using dichloromethane (3 × 20 ml). The DCM portion was dried over anhydrous sodium sulphate and evaporated to get yellow solid (0.92 g, 86%). The compound is pure enough and used directly for the next step without further purification.

CHAPTER 7

Analytical Data for C₁₃H₁₂N₂O₂: Calc. (%) C 68.41, H 5.30, N 12.27. Found (%), C 68.39, H 5.20, N 12.17.

IR Data (KBr, cm⁻¹): 3338 ν (-OH stretch), 3258 ν (-OH stretch), 2915 ν (C-H stretch), 1620 ν (C=N stretch).

¹H NMR (CDCl₃, 300 MHz): δ 5.95 (s, 2H), 6.09 (dd, J₁ = 2.1 Hz, J₂ = 2.1 Hz, 1H), 6.24 (s, 1H), 6.31 (d, J = 8.5 Hz, 1H), 7.23 (d, J = 6.7 Hz, 3H), 7.54 (m, 3H), 10.69 (s, 1H), 12.92 (s, 1H).

HRMS(ESI, positive): m/z , 229.0977 (calculated for [C₁₃H₁₃N₂O₂ + H⁺]), found: 229.1041.

7.4.3 Synthesis of 4-((Z)-((E)-(4-(diethylamino)-2-hydroxybenzylidene)hydrazono)(phenyl) methyl)benzene-1,3-diol (HBSA)

4-(diethylamino)-2-hydroxybenzaldehyde (**2**) (0.1g, 0.517 mmol) was added to the ethanolic solution of 4-(hydrazono(phenyl)methyl)benzene-1,3-diol (**1**) (0.12 g, 0.525 mmol) and the mixture was refluxed for about 7 hours. After completion of the reaction, yellowish orange product was obtained which was subjected to column chromatography furthermore to yield pure orange solid. Yield was, 0.143 g, 81%.

Analytical Data for C₂₄H₂₅N₃O₃: Calc. (%) C 71.44, H 6.25, N 10.41. Found (%), C 71.40, H 6.22, N 10.39.

¹H NMR (CDCl₃, 300 MHz): δ 1.13 (t, J = 6.9 Hz, 6H), 3.32 (q, J = 7.02 Hz, 4H), 6.05 (s, 1H), 6.19-6.27 (m, 2H), 6.51 (s, 1H), 6.83 (d, J = 8.7 Hz, 1H), 7.06 (d, J = 8.7 Hz, 1H), 7.28 (s, 1H), 7.29 (s, 1H), 7.52 (d, J = 6.3 Hz, 3H), 8.45 (s, 1H), 10.72 (s, 1H), 11.09 (s, 1H), 13.57 (s, 1H).

¹³C NMR (CDCl₃, 75 MHz): δ 12.6, 44.6, 97.8, 103.7, 104.2, 106.9, 107.3, 113.0, 128.0, 128.5, 128.9, 133.5, 134.7, 151.6, 159.7, 161.1, 161.4, 162.4, 169.0.

CHAPTER 7

IR data (KBr, cm^{-1}): 3528 ν (-OH stretch), 3329 ν (-OH stretch), 3061 ν (=C-H stretch), 2972 ν (C-H stretch), 1637 ν (C=N stretch).

HRMS (ESI, positive): m/z , 404.1974 (calculated for $[\text{C}_{24}\text{H}_{25}\text{N}_3\text{O}_3 + \text{H}^+]$), found: 404.1244.

7.4.4 General Method for UV-Vis and Fluorescence Titration

7.4.4.1 UV-Vis Method

Stock solution of the receptor HBSA (10 μM) in [(MeOH/H₂O), 1:1, v/v] (at 25°C) using HEPES buffered solution at pH = 7.2 was prepared. The solution of the guest cations and anions using their chloride and sodium salts respectively in the order of 1×10^{-5} M were prepared in deionised water in HEPES buffer. Solutions of a number of concentrations containing the probe and increasing concentrations of cations and anions were prepared separately. The changes in UV-Vis spectra of receptor (10 μM) upon gradual addition of both the solutions were recorded.

7.4.4.2 Fluorescence Method

Stock solution of the receptor HBSA (10 μM) in [(MeOH/H₂O), 1:1, v/v] (at 25°C) using HEPES buffered solution at pH = 7.2 was prepared. Fluorescence spectra were recorded using chloride salts of different guest cations such as Na⁺, K⁺, Ca²⁺, Mg²⁺, Mn²⁺, Fe³⁺, Cr³⁺, Al³⁺, Co²⁺, Ni²⁺, Cu²⁺, Cd²⁺ and Hg²⁺. For competition studies, Zn²⁺ (40 μM) solution was added to probe-cation solution and spectra were recorded. The excitation wavelength used was 420 nm.

7.4.4.3 Job's Plot by Fluorescence Method

For Job's plot experiment, a series of solutions containing HBSA (10 μM) and Zn²⁺ (40 μM) were prepared in MeOH:H₂O (1:1, v/v) solution using HEPES buffer at pH 7.2 in such a manner that the sum of the total metal ion and receptor volume remained constant (2 ml). Job's plots were drawn

CHAPTER 7

by plotting ΔF versus mole fraction of Zn^{2+} (ΔF = change of intensity of the emission spectrum at 529 nm).

7.4.5 Computational methods

All computations were executed using the Gaussian09 (G09) program [63]. The calculations were executed by the Gauss View visualization program. Complete geometry optimization of HBSA was carried out using the DFT method at the B3LYP level of theory [64, 65]. The 6-31+G(d) basis set was assigned for C, H, N and O atoms. The vibrational frequency calculations were completed to ascertain that the optimized geometries signify the local minima and there are only positive Eigen values. The lowest 40 singlet-singlet vertical electronic excitations based on B3LYP optimized geometries were computed using the time-dependent density functional theory (TDDFT) formalism [66-68] in methanol using conductor-like polarizable continuum model (CPCM) [69-71] with the same B3LYP level and basis sets.

7.5. Conclusions

Thus in this present work a “turn-on” fluorescence probe (HBSA) was fabricated which selectively and distinctly detects Zn^{2+} among other cations. All the UV-Vis and fluorescence studies demonstrate the anticipated change that confirmed the sensing property of HBSA. The structure of the developed chemosensor has also been confirmed by several other elemental analyses and also pH study has been done. The LOD value also corresponds to the fact that HBSA can detect Zn^{2+} in very minute level. 1H -NMR spectra of the free ligand and complex was also carried out to confirm the binding of Zn^{2+} with HBSA (Fig. S4 and S5).

7.6. References

1. T. Anand, A. K. Sk and S. K. Sahoo, *Photochem. Photobiol. Sci.*, 2018, **17**, 414–422.
2. A. Mayor-Ibarguren, C. Busca-Arenzana and A. Robles Marhuenda, *Front. Immunol.*, 2020, **11**, 1736.
3. Y. Upadhyay, T. Anand, L. Thilak Babu, P. Paira, G. Crisponi, A. K. Sk, R. Kumar and S. K. Sahoo, *Dalton Trans.*, 2018, **47**, 742–749.
4. M. Kiani, M. Bagherzadeh, S. Meghdadi, N. Rabiee, A. Abbasi, K. Schenk-Joß, M. Tahriri, L. Tayebi and T. J. Webster, *New J. Chem.*, 2020, **44**, 11841–11852.
5. K. Tayade, B. Bondhopadhyay, H. Sharma, A. Basu, V. Gite, S. Attarde, N. Singh and A. Kuwar, *Photochem. Photobiol. Sci.*, 2014, **13**, 1052–1057.
6. M. Maares and H. Haase, *Nutrients*, 2020, **12**, 762.
7. A. Maji, S. Pal, S. Lohar, S. K. Mukhopadhyay and P. Chattopadhyay, *New J. Chem.*, 2017, **41**, 7583–7590
8. V. Kumar, A. Kumar, U. Diwan and K. K. Upadhyay, *Dalton Trans.*, 2013, **42**, 13078–13083
9. J. F. Kerr, A. H. Wyllie, A. R. Currie, *Br. J. Cancer*, 1972, **4**, 239-257.
10. E. Loisel, L. Jacquamet, L. Serre, C. Bauvois, J. L. Ferrer, T. Vernet, A. M. D. Guilmi, C. Durmort, *AdcAII, J. Mol. Biol.*, 2008, **381**, 594-606.
11. D. J. Bobilya, J. T. Reynolds, K. L. Faia, M. B. Anderson, P. G. Reeves, *J. Nutr. Biochem.*, 1999, **10**, 139-145.
12. M. Maes, N. D. Vos, P. Demedts, A. Wauters, H. Neels, *J. Affective Disord.*, 1999, **56**, 189-194.

CHAPTER 7

13. D. J. Bobilyaa, N. A. Gauthiera, S. Karkia, B. J. Olleya, W. K. Thomas, *J. Nutr. Biochem.*, 2008, **19**, 129-137.
14. J. Lai, A. Moxey, G. Nowak, K. Vashum, K. Bailey, M. McEvoy, *J. Affective Disord.*, 2012, **136**, 31-39.
15. T. Tulchinsky, *Public Health Rev.*, 2010, **32**, 243-255.
16. J. H. Weiss, S. L. Sensi, J. Y. Koh, *Trends Pharmacol. Sci.*, 2000, **21**, 395-401.
17. B. K. Bitanhirwe, M. G. Cunningham, Zinc: the brain's dark horse, *Synapse*, 2009, **63**, 1029-1049.
18. E. Zhang, E. Lui, J. Shen, Y. Cao, Y. Li, *J. Environ. Sci.*, 2012, **24**, 1189-1196.
19. J. Cherif, C. Mediouni, W. B. Ammar, F. Jemal, *J. Environ. Sci.*, 2011, **23**, 837-844.
20. Z. Xu, Y. Xiao, X. Qian, J. Cui, Dawei Cui, *Org. Lett.*, 2005, **7**, 889-892.
21. J. B. Wang, X. F. Qian, J. N. Cui, *J. Org. Chem.*, 2006, **71**, 4308-4311.
22. S. Goswami, S. Das, K. Aich, *Tetrahedron Lett.*, 2013, **54**, 4620-4623.
23. S. Goswami, S. Das, K. Aich, B. Pakhira, S. Panja, S. K. Mukherjee, S. Sarkar, *Org. Lett.*, 2013, **15**, 5412-5415.
24. N. C. Lim, J. V. Schuster, M. C. Porto, M. A. Tanudra, L. Yao, H. C. Freake, C. Bruckner, *Inorg. Chem.*, 2005, **44**, 2018-2030.
25. T. Gunnlaugsson, A. P. Davis, J. E. O'Brien, M. Glynn, *Org. Lett.*, 2002, **4**, 2449-2452.
26. J.-S. Wu, J.-H. Zhou, P.-F. Wang, X.-H. Zhang, S.-K. Wu, *Org. Lett.*, 2005, **7**, 2133-2136.
27. A. Banerjee, A. Sahana, S. Guha, S. Lohar, I. Hauli, S. K. Mukhopadhyay, J. S. Matalobos, D. Das, *Inorg. Chem.*, 2012, **51**, 5699-5704.
28. S. Das, K. Aich, S. Goswami, C. K. Quah, H. -K. Fun, *New J. Chem.*, 2016, **40**, 6414-6420.

CHAPTER 7

29. A. E. Albers, V. S. Okreglak, C. J. Chang, A FRET-based approach to ratiometric fluorescence detection of hydrogen peroxide, *J. Am. Chem. Soc.*, 2006, **128**, 9640-9641.
30. P. Mahato, S. Saha, E. Suresh, R. D. Liddo, P. P. Parnigotto, M. T. Conconi, M. K. Kesharwani, B. Ganguly, A. Das, *Inorg. Chem.*, 2012, **51**, 1769-1777.
31. S. Goswami, A. Manna, S. Paul, A. K. Das, K. Aich, P. K. Nandi, *Chem. Commun.*, 2013, **49**, 2912-2914.
32. J. Nie, N. Li, Z. Ni, Y. Zhao, L. Zhang, *Tetrahedron Lett.*, 2017, **58**, 1980-1984.
33. J. Y. Jung, M. Kang, J. Chun, J. Lee, J. Kim, J. Kim, Y. Kim, S. Kim, C. Lee, J. Yoon, *Chem. Commun.*, 2013, **49**, 176-178.
34. C. Jin, M. Zhang, C. Deng, Y. F. Guan, J. Gong, D. R. Zhu, Y. Pan, J. L. Jiang, L. Y. Wang, *Tetrahedron Lett.*, 2013, **54**, 796-801.
35. M. Xue, X. Zhong, Z. Shaposhnik, Y. Q. Qu, F. Tamanoi, X. F. Duan, J. I. Zink, *J. Am. Chem. Soc.*, 2011, **23**, 8798- 8801.
36. K. D. Belfield, M. V. Bondar, A. Frazer, A. R. Morales, O. D. Kachkovsky, I. A. Mikhailov, A. E. Masunov, O. V. Przhonska, Fluorene-Based Metal-Ion Sensing Probe with High Sensitivity to Zn²⁺ and Efficient Two-Photon Absorption, *J. Phys. Chem.B*, 2010, **114**, 9313-9321.
37. H. M. Chawla, S. Richa, P. Shubha, Preferential recognition of zinc ions through a new anthraquinonoidal calix[4]arene, *Tetrahedron Lett.*, 2012, **53**, 2996-2999.
38. T. B. Wei, P. Zhang, B. B. Shi, P. Chen, Q. Lin, J. Liu, Y. M. Zhang, A highly selective chemosensor for colorimetric detection of Fe³⁺ and fluorescence turn-on response of Zn²⁺, *Dyes & Pigm.*, 2013, **97**, 297-302.

CHAPTER 7

39. K. Du, S. Niu, L. Qiao, Y. Dou, Q. Zhu, X. Chen, P. Zhang, A highly selective ratiometric fluorescent probe for the cascade detection of Zn^{2+} and H_2PO_4^- and its application in living cell imaging, *RSC Adv.*, 2017,**7**, 40615-40620.
40. J. J. Lee, S. A. Lee, H. Kim, L. Nguyen, I. Noh, C. Kim, A highly selective CHEF-type chemosensor for monitoring Zn^{2+} in aqueous solution and living cells, *RSC Adv.*, 2015, **5**, 41905-41913.
41. Soumya Sundar Mati, Saugata Konar and Bobby Samai, Synthesis of an unprecedented H-stitched binuclear crystal structure based on selective fluorescence recognition of Zn^{2+} in newly synthesized Schiff base ligand with DFT and imaging application in living cells, *New J. Chem.*, 2021, **45**, 18459-18471.
42. Sukanya Paul, Suwendu Maity, Satyajit Halder, Basudeb Dutta, Srikanta Jana, Kuladip Jana and Chittaranjan Sinha, Idiosyncatic recognition of Zn^{2+} and CN^- using pyrazolyl-hydroxycoumarin scaffold and live cell imaging: depiction of luminescent Zn(II) - metallocryptand, *Dalton Trans.*, 2022, **51**, 3198-3212.
43. P. Jiang, Z. Guo, Fluorescent detection of zinc in biological systems: recent development on the design of chemosensors and biosensors, *Coord. Chem. Rev.*, 2004, **248**, 205-229.
44. N. C. Lim, H. C. Freake, C. Bruckner, Illuminating Zinc in Biological Systems, *Chem. Eur. J.*, 2004,**11**, 38-49.
45. Z. C. Liu, B. D. Wang, Z. Y. Yang, T. R. Li, Y. Li, A novel fluorescent chemosensor for Zn(II) based on 1,2-(2'-oxoquinoline-3'-yl-methylideneimino)ethane, *Inorg. Chem. Commun.*, 2010, **13**, 606-608.
46. A. R. Kay, Evidence for Chelatable Zinc in the Extracellular Space of the Hippocampus, But Little Evidence for Synaptic Release of Zn, *J. Neuroscience*, 2003,**23**, 6847-6855.

CHAPTER 7

47. J. Zhao, B. A. Bertoglio, K. R. Gee, A. R. Kay, The zinc indicator FluoZin-3 is not perturbed significantly by physiological levels of calcium or magnesium, *Cell Calcium*, 2008, **44**, 422-426.
48. S. C. Burdette, C. J. Frederickson, W. M. Bu, S. J. Lippard, ZP4, an improved neuronal Zn²⁺ sensor of the Zinpyr family, *J. Am. Chem. Soc.*, 2003, **125**, 1778-1787.
49. E. M. Nolan, S. C. Burdette, J. H. Harvey, S. A. Hilderbrand, S. J. Lippard, Synthesis and characterization of zinc sensors based on a monosubstituted fluorescein platform, *Inorg. Chem.*, 2004, **43**, 2624-2635.
50. C. J. Chang, E. M. Nolan, J. Jaworski, S. C. Burdette, M. Sheng, S. J. Lippard, Bright Fluorescent Chemosensor Platforms for Imaging Endogenous Pools of Neuronal Zinc, *Chem. Biol.*, 2004, **11**, 203-210.
51. X. Peng, X. Tang, W. Qin, W. Dou, Y. Guo, J. Zheng, W. Liu and D. Wang, *Dalton Trans.*, 2011, **40**, 5271–5277.
52. A. Gomathi, P. Viswanathamurthi and K. Natarajan, *J. Photochem. Photobiol. A*, 2019, **370**, 75–83.
53. S. J. Malthus, S. A. Cameron and S. Brooker, *Inorg. Chem.*, 2018, **57(5)**, 2480–2488.
54. U. A. Fegade, S. K. Sahoo, A. Singh, N. Singh, S. B. Attarde and A. S. Kuwar, *Anal. Chim. Acta*, 2015, **872**, 63–69.
55. T. Anand, A. K. Sk and S. K. Sahoo, *Chemistry Select*, 2017, **2**, 7570–7579.
56. S. Chall, S. S. Mati, S. Konar, D. Singharoy and S. Chandra Bhattacharya, *Org. Biomol. Chem.*, 2014, **12**, 6447–6456
57. M. M. Rahman, M. M. Hussain, M. N. Arshad, M. R. Awual and A. M. Asiri, *New J. Chem.*, 2019, **43**, 9066–9075.

CHAPTER 7

58. V. K. Gupta, A. K. Singh and L. K. Kumawat, *Sens. Actuator B Chem.*, 2014, **204**, 507–514
59. T. A. Sheikh, M. N. Arshad, M. M. Rahman, A. M. Asiri, H. M. Marwani, M. R. Awual and W. A. Bawazir, *Inorg. Chim. Acta*, 2017, **464**, 157–166.
60. R. M. Kamel, A. Shahat, W. H. Hegazy, E. M. Khodier and M. R. Awual, *J. Mol. Liq.*, 2019, **285**, 20–26.
61. M. R. Awual, M. M. Hasan, J. Iqbal, A. Islam, M. A. Islam, A. M. Asiri and M. M. Rahman, *Microchem. J.*, 2020, **154**, 104585.
62. S. Goswami, S. Das, K. Aich, B. Pakhira, S. Panja, S. K. Mukherjee, S. Sarkar, A Chemodosimeter for the Ratiometric Detection of Hydrazine Based on Return of ESIPT and Its Application in Live-Cell Imaging, *Org. Lett.*, 2013, **15**, 5412-5415.
63. Gaussian 09, Revision D.01, M. J. Frisch, G. W. Trucks, H. B. Schlegel, G. E. Scuseria, M. A. Robb, J. R. Cheeseman, G. Scalmani, V. Barone, B. Mennucci, G. A. Petersson, H. Nakatsuji, M. Caricato, X. Li, H. P. Hratchian, A. F. Izmaylov, J. Bloino, G. Zheng, J. L. Sonnenberg, M. Hada, M. Ehara, K. Toyota, R. Fukuda, J. Hasegawa, M. Ishida, T. Nakajima, Y. Honda, O. Kitao, H. Nakai, T. Vreven, J. A. Montgomery, Jr., J. E. Peralta, F. Ogliaro, M. Bearpark, J. J. Heyd, E. Brothers, K. N. Kudin, V. N. Staroverov, R. Kobayashi, J. Normand, K. Raghavachari, A. Rendell, J. C. Burant, S. S. Iyengar, J. Tomasi, M. Cossi, N. Rega, J. M. Millam, M. Klene, J. E. Knox, J. B. Cross, V. Bakken, C. Adamo, J. Jaramillo, R. Gomperts, R. E. Stratmann, O. Yazyev, A. J. Austin, R. Cammi, C. Pomelli, J. W. Ochterski, R. L. Martin, K. Morokuma, V. G. Zakrzewski, G. A. Voth, P. Salvador, J. J. Dannenberg, S. Dapprich, A. D. Daniels, Ö. Farkas, J. B. Foresman, J. V. Ortiz, J. Cioslowski, and D. J. Fox, Gaussian, Inc., Wallingford CT, 2009.

CHAPTER 7

64. A. D. Becke, Density-functional thermochemistry. III. The role of exact exchange, *J. Chem. Phys.*, 1993, **98**, 5648-5652.
65. C. Lee, W. Yang, R.G. Parr, Development of the Colic-Salvetti correlation-energy formula into a functional of the electron density, *Phys. Rev. B*, 1988, **37**, 785-789.
66. R. Bauernschmitt, R. Ahlrichs, Treatment of electronic excitations within the adiabatic approximation of time dependent density functional theory, *Chem. Phys. Lett.*, 1996, **256**, 454-464.
67. R. E. Stratmann, G. E. Scuseria, M. J. Frisch, An efficient implementation of time-dependent density-functional theory for the calculation of excitation energies of large molecules, *J. Chem. Phys.*, 1998, **109**, 8218-8224.
68. M. E. Casida, C. Jamorski, K. C. Casida, D. R. Salahub, Molecular excitation energies to high-lying bound states from time dependent density-functional response theory: Characterization and correction of the time-dependent local density approximation ionization threshold, *J. Chem. Phys.*, 1998, **108**, 4439-4449.
69. V. Barone, M. Cossi, Quantum Calculation of Molecular Energies and Energy Gradients in Solution by a Conductor Solvent Model, *J. Phys. Chem. A*, 1998, **102**, 1995-2001.
70. M. Cossi, V. Barone, Time-dependent density functional theory for molecules in liquid solutions, *J. Chem. Phys.*, 2001, **115**, 4708-4717.
71. M. Cossi, N. Rega, G. Scalmani, V. Barone, Energies, structures, and electronic properties of molecules in solution with the C-PCM solvation model, *J. Comput. Chem.*, 2003, **24**, 669-681.

CHAPTER 7

APPENDIX

CHAPTER 7

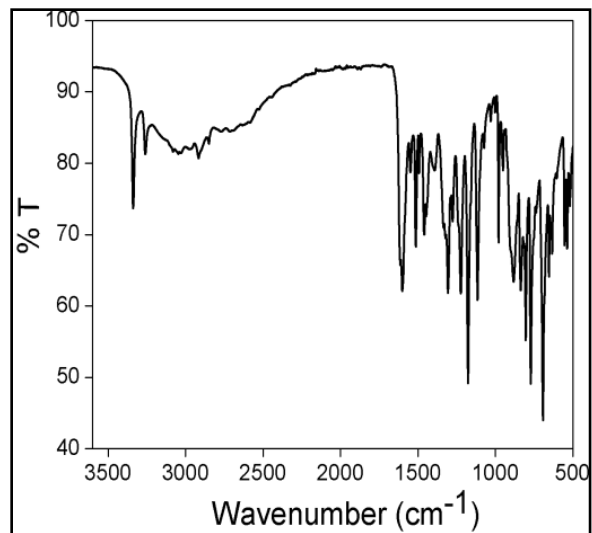


Figure S1: IR spectrum of Compound 1 in KBr disk

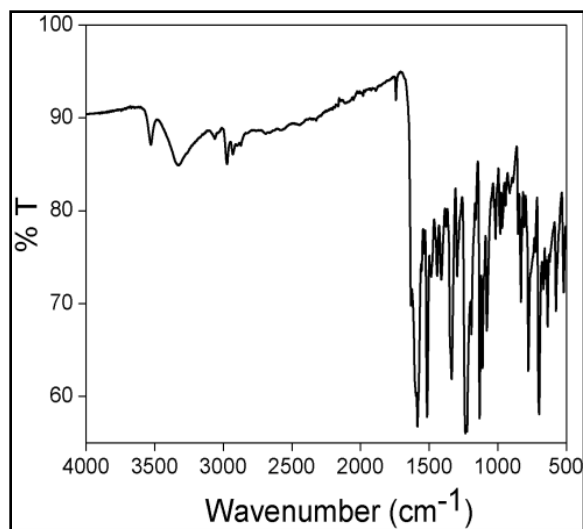


Figure S2: IR spectrum of **HBSA** in KBr disk

CHAPTER 7

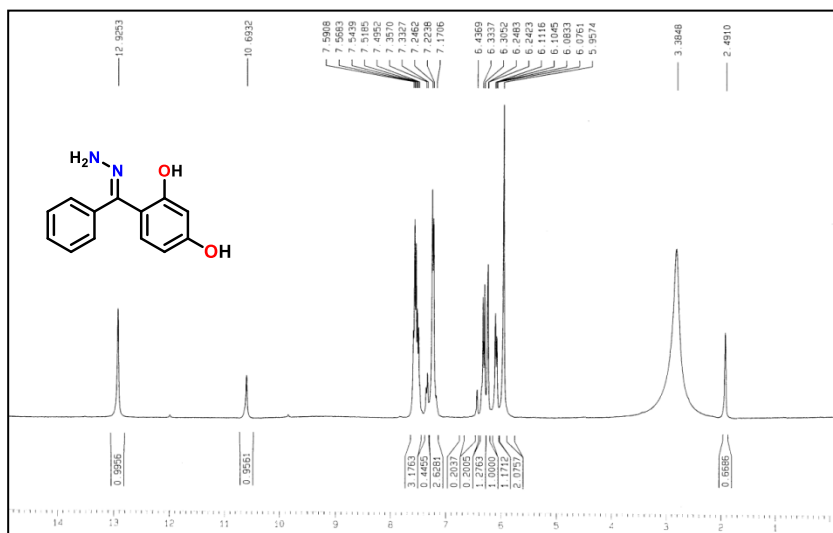


Figure S3: ¹H-NMR (300 MHz) spectra of **Compound 1** in DMSO-d₆

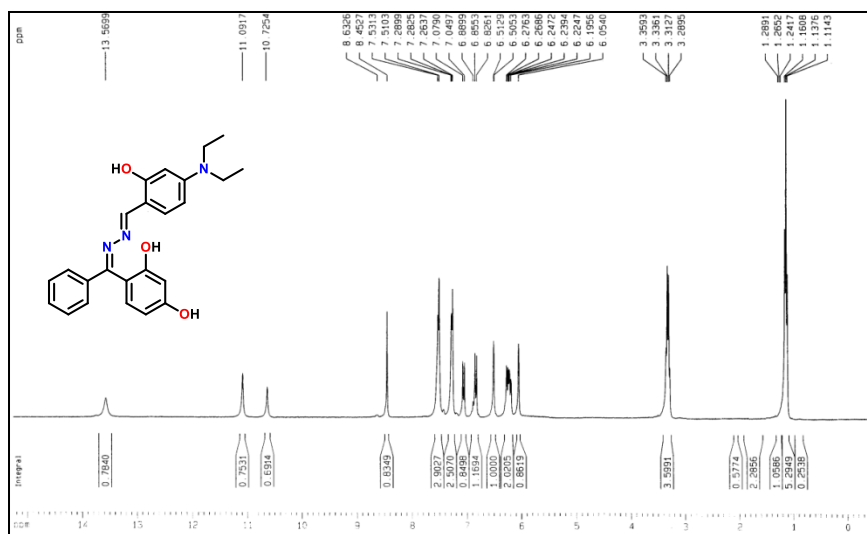


Figure S4: ¹H-NMR (300 MHz) spectra of **HBSA** in CDCl₃

CHAPTER 7

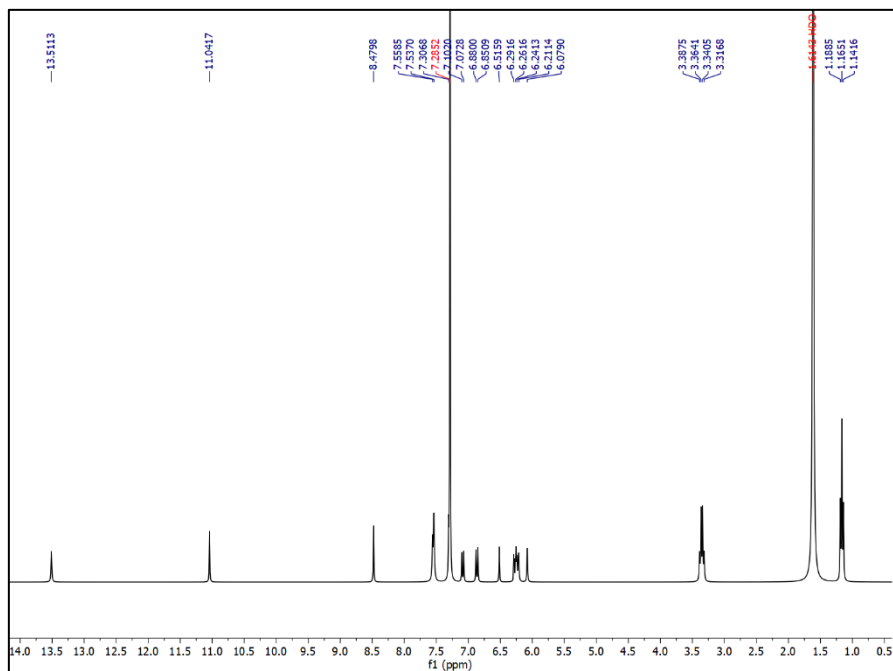


Figure S5: ^1H -NMR (300 MHz) spectra of **HBSA-Zn²⁺** complex in CDCl_3

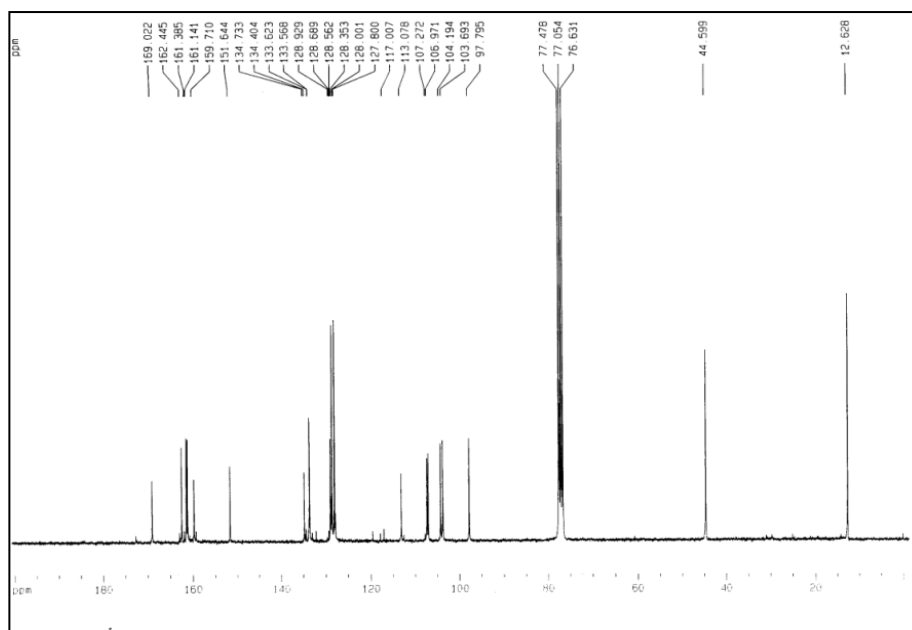


Figure S6: ^{13}C -NMR (75 MHz) spectra of **HBSA** in CDCl_3

CHAPTER 7

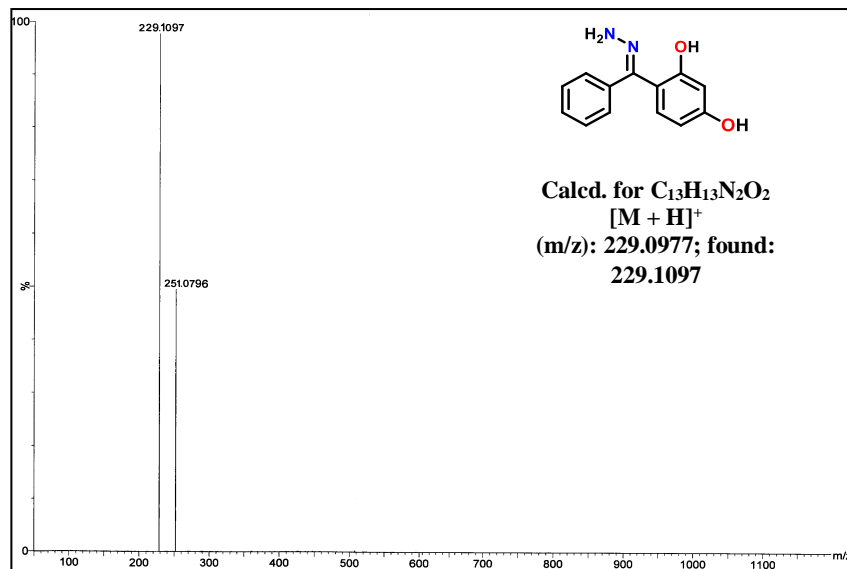


Figure S7: HRMS spectra of the **Compound 1**

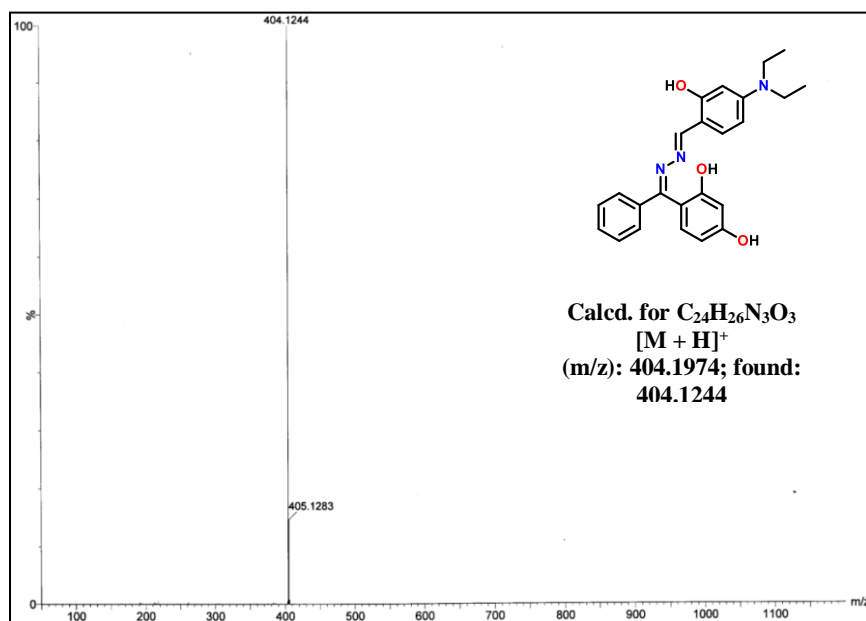


Figure S8: HRMS spectra of the receptor **HBSA**

CHAPTER 7

Table S1: Contour plots of some selected molecular orbitals of HBSA

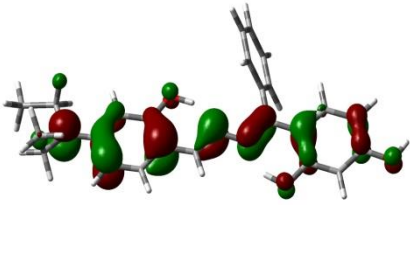
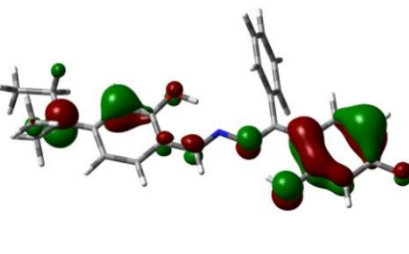
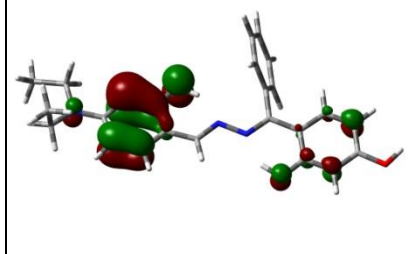
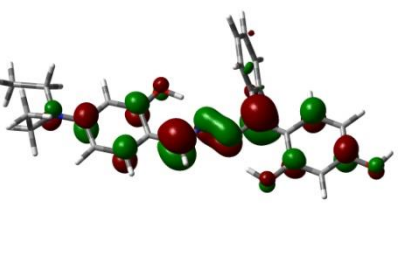
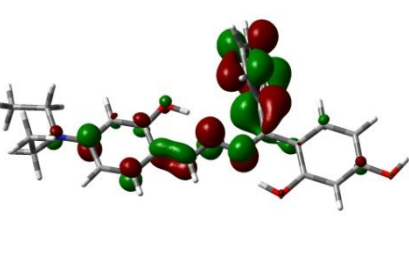
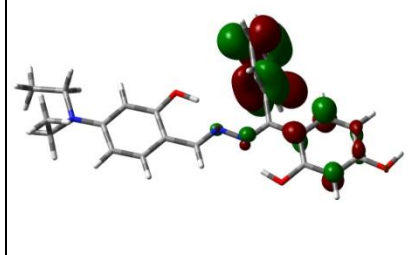
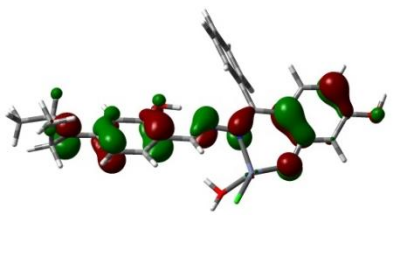
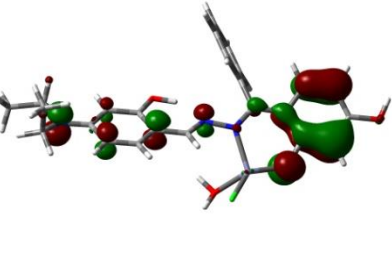
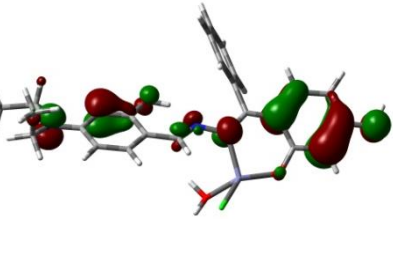
		
HOMO E=-4.97 eV	HOMO-1 E=-5.78 eV	HOMO-2 E=-5.91 eV
		
LUMO E=-1.6 eV	LUMO+1 E=-0.3 eV	LUMO+2 E=-0.13 eV

Table S2: Contour plots of some selected molecular orbitals of HBSA-Zn²⁺

		
HOMO E = -5.18 eV	HOMO-1 E = -5.63 eV	HOMO-2 E = -6.07 eV

CHAPTER 7

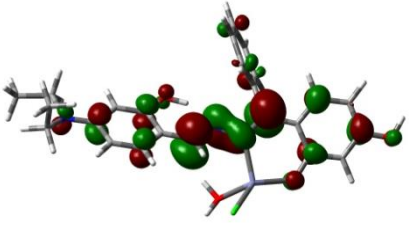
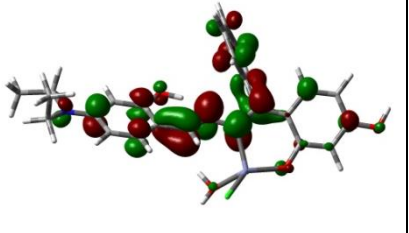
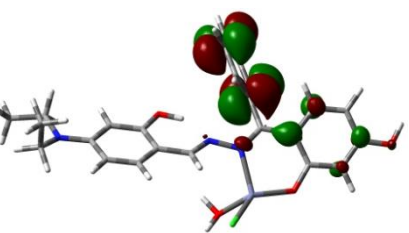
		
LUMO E = -1.89 eV	LUMO+1 E = -0.78 eV	LUMO+2 E = -0.35 eV

Table S3: Vertical electronic transitions calculated by TDDFT/B3LYP/CPCM method for HBSA

Energy(eV)	Wavelength (nm)	Osc. strength (f)	Key transitions
2.9712	417.28	1.4123	(99%) HOMO→LUMO
3.7171	333.55	0.0267	(83%)HOMO-1→LUMO
3.7765	328.31	0.0176	(73%) HOMO-2→LUMO
3.8198	324.58	0.0013	(61%) HOMO-4→LUMO
4.0709	304.56	0.1856	(70%) HOMO-3→LUMO

CHAPTER 7

Table S4: Vertical electronic transitions calculated by TDDFT/B3LYP/CPCM method for HBSA-
Zn²⁺

Energy (eV)	Wavelength (nm)	Osc. strength (f)	Key transitions
2.8576	433.87	1.1060	(98%) HOMO→LUMO
3.3542	369.64	0.0350	(93%) HOMO-1→LUMO
3.7182	333.45	0.0092	(85%) HOMO-2→LUMO
3.7882	327.29	0.2512	(65%) HOMO-3→LUMO
4.0522	305.97	0.0043	(54%) HOMO→LUMO+1
4.2901	289.00	0.0547	(93%) HOMO→LUMO+2

Table S5: Energy and compositions of some selected molecular orbitals of HBSA -Zn²⁺

MO	Energy (eV)	% of composition		
		Cl	Zn	HBSA
LUMO+5	0.23	1	29	71
LUMO+4	0.11	0	26	74
LUMO+3	-0.24	0	2	98
LUMO+2	-0.35	0	3	97
LUMO+1	-0.78	0	3	97

CHAPTER 7

LUMO	-1.89	0	1	99
HOMO	-5.18	0	1	99
HOMO-1	-5.63	0	1	99
HOMO-2	-6.07	0	0	100
HOMO-3	-6.18	0	0	100
HOMO-4	-6.74	10	2	88
HOMO-5	-6.98	5	0	95
HOMO-6	-7.07	1	0	99
HOMO-7	-7.25	68	2	30
HOMO-8	-7.27	91	2	6
HOMO-9	-7.51	4	0	95
HOMO-10	-7.7	26	6	68

LIST OF PUBLICATIONS

List of publications

Thesis works:

1. An Efficient Fluorescence “Turn-On” Chemosensor Comprising of Coumarin and Rhodamine Moieties for Al³⁺ and Hg²⁺, **S. Acharyya**, S. Gharami, L. Patra and T. K. Mondal, *J. Fluoresc.*, 2017, **27**, 2051.
2. A thioether containing reversible fluorescence “turn-on” chemosensor for selective detection of zinc(II): Applications in live cell imaging and inhibit logic gate,
S. Acharyya, S. Gharami, D. Sarkar, P. Ghosh, N. Murmu and T. K. Mondal, *J. Mol. Struct.*, 2021, **1224**, 129179.
3. Novel pyridyl based azo-derivative for the selective and colorimetric detection of nickel(II), S. Biswas, **S. Acharyya**, D. Sarkar, S. Gharami and T. K. Mondal, *Spectrochim. Acta, Part A*, 2016, **159**, 157.

Other works:

4. A Phenanthraquinone Based Fluorescent Probe for Sequential Detection of Cu²⁺ and SO₃²⁻, S. Gharami, D. Sarkar, **S. Acharyya** and T. K. Mondal, *J. Fluoresc.*, 2016, **26**, 2113.
5. A coumarin based azo-phenol ligand as efficient fluorescent “OFF-ON-OFF” chemosensor for sequential detection of Mg²⁺ and F⁻: Application in live cell imaging and as molecular logic gate, S. Gharami, D. Sarkar, P. Ghosh, **S. Acharyya**, K. Aich, N. Murmu and T. K. Mondal, *Sens. Actuators, B*, 2017, **253**, 317.

An Efficient Fluorescence “Turn-On” Chemosensor Comprising of Coumarin and Rhodamine Moieties for Al³⁺ and Hg²⁺

Samik Acharyya¹ · Saswati Gharami¹ · Lakshman Patra¹ · Tapan Kumar Mondal¹

Received: 30 March 2017 / Accepted: 18 July 2017 / Published online: 19 August 2017
© Springer Science+Business Media, LLC 2017

Abstract A potent fluorescence ‘turn-on’ receptor (HL) based on rhodamine and coumarin moieties for the detection of Hg²⁺ and Al³⁺ is synthesized by condensation of rhodamine 6G hydrazide and 4-hydroxy-3-acetylcoumarin. In presence of Al³⁺ and/or Hg²⁺ the receptor (HL) exhibits deep pink colouration and a sharp band at 528 nm is appeared in UV–vis titration. Upon gradual addition of Al³⁺ and/or Hg²⁺ to the solution of HL significant enhancement of fluorescence intensity is observed at 564 nm in MeCN:H₂O (1:5, v/v) medium. The receptor is strongly bound to Al³⁺ and/or Hg²⁺ and the association constants (K_a) are found to be 1.74 × 10⁴ and 1.04 × 10⁴ M⁻¹ for Al³⁺ and Hg²⁺ respectively.

Keywords Fluorescence turn-on sensor · Rhodamine-coumarin based chemosensor · Detection of Hg²⁺ and Al³⁺ · DFT calculation

Introduction

Mercury is considered to be one of the most toxic heavy metals and can cause serious environmental and health problem [1, 2]. It may have adverse effect on human nervous system, digestive and immune systems including lungs, kidneys, skin, eyes, brain and nervous system [3–5]. According to the Environmental Protection Agency (EPA) the limit of inorganic mercury(II)

level in drinking water should be less than 2 ppb [6, 7]. On the other hand aluminum is one of the most common metals in nature and has abundant use in electrical, food packaging and food processing industry which causes easy bioaccumulation of the metal in human body and plants [8–11]. Aluminium has neurotoxic effects and has long been suspected as one of the factors causing the Alzheimer’s and Parkinson’s disease [12]. Al³⁺ can cause osteomalacia [13] and also acts as a metalloestrogen facilitating the gene-expression in breast cancer cell and therefore its growth [14–17]. The World Health Organization (WHO) prescribed the average human intake of aluminium as around 3–10 mg/day and its limit in drinking water should be less than 7.41 μM [18–21]. Therefore facile and financially viable methods of detecting Hg²⁺ and Al³⁺ in environmental and biological samples has become a matter of utmost interest. Detection by measuring luminescence property is simple, highly sensitive, quick and reversible in nature [22–24].

Till date very few chemosensors are reported comprising of coumarin and rhodamine moieties that can detect Al³⁺ and/or Hg²⁺ [25–28]. Herein, the reported chemosensor, 3-(1-(rhodamine-6G-hydrazidimino)ethyl)-4-hydroxy-2H-chromen-2-one (HL) was synthesized following an economically cheap route. It can detect both Al³⁺ and Hg²⁺ with high selectivity in solution phase and also has the benefit of being reversible. Both the metal ions i.e., Hg²⁺ and Al³⁺ induce huge increase in emission intensity, but the emission intensity is quenched significantly in presence of F⁻ and S²⁻ for Al³⁺ and Hg²⁺ respectively.

Electronic supplementary material The online version of this article (doi:10.1007/s10895-017-2144-9) contains supplementary material, which is available to authorized users.

✉ Tapan Kumar Mondal
tapank.mondal@jadavpuruniversity.in

¹ Department of Chemistry, Jadavpur University, Kolkata 700032, India

Experimental

Materials and Methods

Rhodamine-6G hydrochloride and 4-hydroxycoumarin were purchased from Sigma Aldrich. All other organic



A thioether containing reversible fluorescence “turn-on” chemosensor for selective detection of zinc(II): Applications in live cell imaging and inhibit logic gate

Samik Acharyya^a, Saswati Gharami^a, Deblina Sarkar^b, Paramita Ghosh^c, Nabendu Murmu^c, Tapan Kumar Mondal^{a,*}

^a Department of Chemistry, Jadavpur University, Kolkata 700032, India

^b Department of Chemistry, Bagnan College, Howrah, WB 711303, India

^c Department of Signal Transduction and Biogenesis Amines (STBA), Chittaranjan National Cancer Institute, Kolkata 700026, India

ARTICLE INFO

Article history:

Received 25 July 2020

Revised 22 August 2020

Accepted 30 August 2020

Available online 1 September 2020

Keywords:

Chemosensor for Zn²⁺

MTT assay

Live cell imaging studies

INHIBIT logic gate

DFT calculation

ABSTRACT

A new fluorescence probe (H₂L) is designed and synthesized for efficient and selective detection of Zn(II). H₂L exhibits a “turn-on” fluorescence response with substantial enhancement of emission intensity with Zn²⁺ even in presence of other coexisting cations found in various environmental and biological samples. The calculated value of limit of detection (LOD) is 1.73×10^{-9} M. Exploiting the reversibility of the probe in presence of EDTA, an INHIBIT logic gate is constructed with Zn²⁺ and EDTA as chemical inputs. DFT and TDDFT calculations are used to interpret electronic structures and elucidate the sensing mechanism. Cytotoxicity study by MTT method with human breast cancer cell lines (MCF-7) reveals that H₂L has negligible toxicity in low concentration levels and can be effectively used for live cell imaging.

© 2020 Elsevier B.V. All rights reserved.

1. Introduction

Zn(II) is the second most abundant transition metal in human body after iron [1,2] and plays indispensable roles in biological systems including regulation of cell growth, apoptosis, neural signal transmissions and catalysis [3,4]. Disturbance of zinc level in the human body may cause a series of diseases, parkinson's disease, alzheimer's disease, metabolic disorder, prostate cancer etc. [5–7]. Excess intake of Zn(II), also may lead to diabetes, superficial skin diseases and even prostate cancer [5]. The above facts strongly advocate for the necessity of developing new and cost effective methods for efficient detection minuscule level of Zn(II) in biological samples. Fluorescent technique has gain profound recent attention as a powerful detection tool for non-invasive detection of metal ions because of its simplicity, sensitivity and reversible nature [8–10]. Recently, a good number of fluorescent probes are designed, based mostly on quinoline [11,12], coumarin [12,13], BINOL [14], fluorescein [15,16] and bipyridyl [17] fluorophores for effective detection of Zn(II). However, many of them require complex synthesis procedures involving drastic reaction conditions and expensive chemi-

cals. The present chemosensor (H₂L) is prepared by simple Schiff base condensation reaction of 3,5-dichlorosalicylaldehyde and 2,2'-(butane-1,4-diylbis(sulfanediy))dianiline in methanol. Schiff bases are known to be a good complexing agent and extensively used for fluorogenic detection of metal ions [18,19] and anions [20–22]. In recent years, Schiff bases of salicylidene derivatives are extensively used for the recognition of metal ions and anion sensing [23–25]. Moreover, the thioether containing fluorescence probes are known to be very efficient for selective detection of Zn(II) [26,27]. In the present case the thioether containing chemosensor, H₂L exhibits significant and selective fluorescence enhancement in presence of Zn(II) in DMSO:H₂O (1:5, v/v) solution at pH 7.2. In presence of Zn(II), fluorescence intensity of H₂L enhanced significantly at 490 nm and an intense green fluorescence is observed under UV light. The structure of L-Zn²⁺ is confirmed by single crystal X-ray diffraction method. The cytotoxicity of the present probe towards human breast cancer cell lines (MCF-7) is studied and the probe is utilized for fluorescence live cell imaging.

2. Results and discussion

2.1. Synthesis and formulation

Synthetic procedure of formation of H₂L involves two very economic viable and easy steps. In the first step 2-aminothiophenol is

* Corresponding author.

E-mail address: tapank.mondal@jadavpuruniversity.in (T.K. Mondal).



Novel pyridyl based azo-derivative for the selective and colorimetric detection of nickel(II)



Sujan Biswas, Samik Acharyya, Deblina Sarkar, Saswati Gharami, Tapan Kumar Mondal *

Department of Chemistry, Jadavpur University, Kolkata 700032, India

ARTICLE INFO

Article history:

Received 17 September 2015
Received in revised form 16 January 2016
Accepted 23 January 2016
Available online 26 January 2016

Keywords:

Pyridyl based chemosensor for Ni²⁺
Colorimetric sensor
Naked eye detection
Spectral characterization
DFT calculation

ABSTRACT

A highly sensitive and selective pyridyl based colorimetric chemosensor (H₂L) for the efficient detection of Ni²⁺ has been reported. The synthesized chemosensor H₂L is highly efficient in detecting Ni²⁺ even in the presence of other metal ions that commonly co-exist with Ni²⁺. H₂L also shows distinct color change from green to deep red visible under naked eye due to specific binding with Ni²⁺. This color change is due to formation of a new band at 510 nm upon gradual addition of Ni²⁺. The association constant has been found to be $1.27 \times 10^5 \text{ M}^{-1}$ with limit of detection (LOD) of $8.3 \times 10^{-7} \text{ M}$. Electronic structure of the H₂L–Ni²⁺ complex and sensing mechanism have been interpreted theoretically by DFT and TDDFT calculations.

© 2016 Elsevier B.V. All rights reserved.

1. Introduction

Recognition and sensing of metal ions has become an active field of research owing to its potential application in several fields which includes chemistry, bio-medicine, and environmental studies [1,2]. Detection of nickel(II) is highly important due to its toxic nature [3] and widespread use in various industrial and catalytic processes. Increased exposure to nickel(II) causes several diseases such as pneumonitis, dermatitis, asthma, several problems of the central nervous system and even cancer of the nasal cavity and lungs [4–6]. Thus the detection of nickel(II) is of utmost importance in several biological, industrial and food samples. Most of the industrial methods for detection of nickel(II) are time consuming and depends on the involvement of sophisticated analytical techniques which includes atomic absorption or emission spectrometry [7,8], liquid chromatography [9,10] and fluorometric chemosensors [11,12]. In spite of the fact that these methods are highly sensitive, they are not convenient for “in-the-field” detection as they require expensive instruments which are very difficult to carry. Hence detection of nickel(II) using a very simple-to-use method which is rapid and also of low cost, is of utmost demand.

Colorimetric sensors comprise a class of reagent which shows a distinctive color change visible under ‘naked eye’, on selectively binding with certain specific analytes without the employment of sophisticated and expensive equipment [13,14]. Thus the development of colorimetric sensor for the easy and rapid detection of nickel(II) is a demanding field of research as only a few have been reported till date. A quinoxaline

based colorimetric and ratiometric chemosensor for the detection of nickel(II) has been reported by S. Goswami et al. [15]. Besides, Peralta-Domínguez et al. reported a Schiff base derivative of cinnamaldehyde, used for efficient detection of nickel(II) by colorimetric method [16]. Several coumarin based colorimetric chemosensors for nickel(II) have been reported so far by Jiang et al. and Wang et al. [17,18].

In our previous work we have reported new benzimidazole based colorimetric sensor for nickel(II) [19]. In continuation to develop new colorimetric sensor, we have synthesized new pyridyl based azo derivative (H₂L) for the selective, sensitive and rapid recognition of nickel(II). The cation binding property has been mainly investigated by UV–Vis spectroscopy and naked-eye detection. The chemical, electronic structure and photo physical properties have been studied by various spectroscopic analyses abetted with DFT and TDDFT calculations.

2. Experimental

2.1. Materials and methods

p-Cresol and 2, 6-Diaminopyridine were purchased from Sigma Aldrich. All other organic chemicals and inorganic salts were available from Sisco Research Lab, Mumbai, India and used without further purification. Commercially available SRL silica gel (60–120 mesh) was used for column chromatography.

Elemental analysis was carried out in a 2400 Series-II CHN analyzer, Perkin Elmer, USA. HRMS mass spectra were recorded on Waters (Xevo G2 Q-TOF) mass spectrometer. Infrared spectra were taken on a RX-1 Perkin Elmer spectrophotometer with samples prepared as KBr pellets. Electronic spectral studies were performed on a Perkin Elmer Lambda

* Corresponding author.

E-mail address: tkmondal@chemistry.jdvu.ac.in (T.K. Mondal).

A Phenanthraquinone Based Fluorescent Probe for Sequential Detection of Cu^{2+} and SO_3^{2-}

Saswati Gharami¹ · Deblina Sarkar¹ · Samik Acharyya¹ · Tapan Kumar Mondal¹

Received: 8 July 2016 / Accepted: 4 August 2016 / Published online: 12 August 2016
© Springer Science+Business Media New York 2016

Abstract Herein we report the selective detection of Cu^{2+} and SO_3^{2-} by phenanthraquinone thiosemicarbazone (PQTSC) chemosensor. The chemosensor is efficient in detecting Cu^{2+} over other metal ions, while the PQTSC- Cu^{2+} complex selectively sense SO_3^{2-} over other anions. On addition of Cu^{2+} to the receptor solution, quenching of emission intensity is observed by 16 folds and upon gradual addition of SO_3^{2-} to this solution, the emission intensity increases and the maxima is regained. The limit of detection for Cu^{2+} detection calculated from fluorescence titration is 1.06×10^{-8} M and the association constant of PQTSC with Cu^{2+} is found to be 2.18×10^5 .

Keywords Phenanthraquinone thiosemicarbazone (PQTSC) · Chemosensor · Fluorescent turn-off sensor · Copper sensor

Introduction

Metal ions in well-balanced concentration benefit the ecosystem and human health whereas their abnormal concentration will be very much dangerous towards eco-system. Therefore, simple and selective methods for the determination of metal ions have attracted considerable amount of attention [1]. Copper (II) after iron and zinc, ranks the third most

abundant essential trace element in the human body and plays an important role in many important physiological processes in organisms [2]. Because of its role as catalyst in a variety of biological processes, copper is required by nearly every living organism [3]. Its biochemical activity involves oxygen transportation, hormone maturation, signal transduction etc. [4]. Copper (II) also plays a significant role in biological, environmental and chemical systems [5, 6]. Copper is an essential element for the formation of hemoglobin, red blood cells and bones of the human system [7]. Nevertheless, copper ion at excessive concentration is very toxic. Copper is also treated as a remarkable metal pollutant due to its enormous use [8]. Some copper catalyzed reactions usually lead to liver damage especially for infants [9]. Its maximum tolerable level is 2.0 mg L^{-1} in drinking water (WHO, 1993). The disorder in Cu(II) metabolism may lead to severe neurodegenerative diseases, such as Alzheimer's and Wilson's diseases, amyotrophic lateral sclerosis, Menke's syndrome and hematological manifestations [10–14]. Hence, to monitor and to regulate the concentration of copper ion is essential for organisms.

Considerable efforts had been taken to develop selective sensors for copper ions in the past few decades [15, 16]. Among the numerous analytical methods that are available for the detection of copper ions, fluorescent sensors offer distinct advantages such as high sensitivity, selectivity along with some biological activities [17–19].

Due to its simplicity, sensitivity and tenability, the artificial chemosensors have been classified to be an effective tool for detection of selective metal ions by fluorescence technique. Recently, several reported molecules have the capability to detect copper by quenching of fluorescent intensity [20, 21]. This is because Cu^{2+} ion shows an inherent fluorescence quenching property as a paramagnetic species [8].

For anion recognition, substantial efforts have been made to develop selective and efficient fluorescent sensors as the

Electronic supplementary material The online version of this article (doi:10.1007/s10895-016-1907-z) contains supplementary material, which is available to authorized users.

✉ Tapan Kumar Mondal
tkmondal@chemistry.jdvu.ac.in

¹ Department of Chemistry, Jadavpur University, Kolkata -700032, India



A coumarin based azo-phenol ligand as efficient fluorescent “OFF-ON-OFF” chemosensor for sequential detection of Mg^{2+} and F^- : Application in live cell imaging and as molecular logic gate

Saswati Gharami^a, Deblina Sarkar^b, Paramita Ghosh^b, Samik Acharyya^a, Krishnendu Aich^a, Nabendu Murmu^{b,*}, Tapan Kumar Mondal^{a,*}

^a Department of Chemistry, Jadavpur University, Kolkata 700032, India

^b Department of Signal Transduction and Biogenesis Amines (STBA), Chittaranjan National Cancer Institute, Kolkata 700026, India

ARTICLE INFO

Article history:

Received 30 December 2016
Received in revised form 20 June 2017
Accepted 21 June 2017
Available online 23 June 2017

Keywords:

Coumarin based azo-phenol ligand
Fluorescence turn-on chemosensor for Mg^{2+}
Detection of F^-
A549 lung cancer cell line
Live cell imaging
DFT calculation

ABSTRACT

A novel coumarin based azo-phenol ligand (H_2L) has been synthesized and characterized by several spectroscopic techniques. An almost 16 fold enhancement of emission intensity has been observed upon gradual addition of Mg^{2+} to H_2L in DMSO:H₂O (1:5 v/v) medium while it has no significant effect in emission intensity even in presence of other metal ions. The emission intensity of L- Mg^{2+} complex has almost quenched on gradual addition of F^- to it. The limit of detection for both Mg^{2+} and F^- are of 10^{-8} M order, hence the newly developed chemosensor is highly efficient in detecting Mg^{2+} and F^- in very minute levels. The chemosensor can even detect Mg^{2+} in the intracellular region of human lung cancer cells (A549 cells).

© 2017 Elsevier B.V. All rights reserved.

1. Introduction

Magnesium is one of the most abundant divalent intracellular cation present in the human body [1–3] and it is considered as an important and essential element for all biological living things [4]. After potassium, magnesium is the most predominant cation in living cells, which plays an important role in many enzymatic systems in human body [5]. Magnesium also controls neuronal activity, neuromuscular transmission and cardiac excitabilities [6–8] along with some cellular functions like DNA and protein synthesis, membrane stabilization, proliferation of cells and also cell death [9]. Generally 3.0–4.3 mg/kg/day of magnesium should be considered for a human body from the food sources like meat, fish, seafood, dairy products etc. [10–12]. But excessive as well as low intake of magnesium can play an etiological role in several severe diseases. Low intake of this metal cation can lead to some rigorous diseases like acute migraine, cardiac diseases, high blood pressure, osteoporosis, diabetes whereas presence of excess magnesium in our body

can cause coma, even death [13]. Therefore a simple and convenient method for the detection of Mg^{2+} in biological, industrial and environmental field as well as its estimation in food sources have much importance nowadays. Sometimes under intracellular conditions, Ca^{2+} interferes with Mg^{2+} [14] and as a result Mg^{2+} detection becomes hard enough to perform. So our aim here is to fabricate such an efficient probe that will selectively detect Mg^{2+} in presence of other metal ions along with Ca^{2+} .

Development of chemosensors for the detection of anions has also become an interesting field of research from past few years for their importance in various biological as well as in environmental sciences [15–18]. Among them, the detection of fluoride is of great interest due to its important roles in many diseases and environmental pollutants [19–21]. Fluoride is used in dental cure and in treatment of osteoporosis and also in detection of residue of some nerve gases [22]. However, a high intake of fluoride can lead to several diseases like kidney malfunction, gastric disorders and skeletal fluorosis [23–27]. So the detection of fluoride is very much needed for the sake of environment and human health.

During the past few decades fluorescent chemosensors are widely used for the detection of metal ions [28,29]. Few fluorescent probes which were designed for Mg^{2+} detection in the past few years, were mainly based on metal chelating structures like crown

* Corresponding authors.

E-mail addresses: nabendu.murmu@cnci.org.in (N. Murmu), tapank.mondal@jadavpuruniversity.in (T.K. Mondal).